Experimental and Numerical Studies of the Fundamental Flame Speeds of Methane/Air and Syngas (H2/CO)/Air Mixtures

Nicolas Bouvet

To cite this version:

Nicolas Bouvet. Experimental and Numerical Studies of the Fundamental Flame Speeds of Methane/Air and Syngas (H2/CO)/Air Mixtures. Electric power. Université d'Orléans, 2009. English. NNT : . tel-00473266

HAL Id: tel-00473266
https://theses.hal.science/tel-00473266
Submitted on 15 Apr 2010

UNIVERSITÉ D'ORLÉANS

PUCVL
Pôle Universités
Centre Val de Loire

UNIVERSITE D'ORLEANS

ÉCOLE DOCTORALE SCIENCES ET TECHNOLOGIES

LABORATOIRE ICARE

PENNSTATE

THÈSE

présentée par :

Nicolas BOUVET

soutenue le : **17 décembre 2009**

pour obtenir le grade de : **Docteur de l'université d'Orléans**

Discipline : Mécanique des Fluides, Énergétique, Thermique, Combustion, Acoustique

Experimental and Numerical Studies of the Fundamental Flame Speeds of Methane/Air and Syngas (H_2/CO)/Air Mixtures

THÈSE dirigée par :

Mr. Iskender GÖKALP	Directeur de Recherche / ICARE-CNRS

RAPPORTEURS :

Mr. Alexander KONNOV	Professeur / Lund University
Mr. Geoff SEARBY	Directeur de Recherche / IRPHÉ-CNRS

JURY :

Mme Christine ROUSSELLE	Professeur / Université d'Orléans, Présidente
Mr. Alexander KONNOV	Professeur / Lund University
Mr. Geoff SEARBY	Directeur de Recherche / IRPHÉ-CNRS
Mr. Robert J. SANTORO	Professeur / Penn State University
Mr. Daniel DUROX	Ingénieur de Recherche / EM2C-CNRS
Mr. Bruno RENOU	Professeur / INSA de Rouen
Mr. Christian CHAUVEAU	Chargé de Recherche / ICARE-CNRS
Mr. Iskender GÖKALP	Directeur de Recherche / ICARE-CNRS

Abstract

In the context of CO_2 emission reduction, the present study is devoted to the development of a laminar flame speed measurement methodology, using the Digital Particle Image Velocimetry (DPIV) diagnostic. The latter is applied to stagnation flow flames, seen to have considerable assets for such studies. Indeed, flames stabilized in these diverging flows are planar, steady and in near-adiabatic conditions, while subtraction of strain effects on flame is intrinsically allowed. The methodology developed herein has been applied to the well-characterized methane/air mixtures for validation. An extensive comparison with the literature datasets has been provided. Both 1D (PREMIX, OPPDIF) as well as 2D (Fluent©) numerical tools have been used to confirm the reliability and accuracy of the developed approach. A particular attention has been given to the characterization of the seeding particle motion within the diverging flow, with consideration of the often-neglected thermophoretic force. Fundamental flame velocities of various syngas (H_2+CO) mixtures have been investigated using multiple experimental approaches including the aforementioned counterflow methodology as well as spherical and conical flame configurations. Performed measurements from the different approaches have been confronted and flame sensitivities to stretch have been characterized for a wide range of equivalence ratios (E.R.=0.4 to 5.0) and mixture compositions (5/95 to 50/50 % H_2/CO).

Table of Contents

List of Figures

List of Tables

Introduction

How to face up the worldwide constantly-increasing demand for energy, while meeting the most stringent environmental standards aiming at minimizing climate changes? An intricate problem if recent statistics are considered. From 1971 to 2007, the world total fuel consumption, mainly relying on fossil sources, has roughly doubled (see Figure 0.1). At a larger scale, the exponential rise of CO_2 emissions from fossil-fuel burning that started during the Industrial Revolution does not seem to find any substantial abatement in the past few decades, reaching an alarming 29 Gigatons (Gt) in 2007 (see Figure 0.2). Recently, the Intergovernmental Panel on Climate Change (IPCC) reported that "Observational evidence from all continents and most oceans shows that many natural systems are being affected by regional climate changes". These observations are based on notable evolutions of: the global average surface temperature (increase of 1°C/150 years), the global average sea level (increase of ≈ 2 cm/130 years) and the Northern Hemisphere snow cover (decrease of ≈ 2 million km^2) (see Figure 0.3). In October 2009, the World Energy Outlook projects that if no new initiative is taken in the incoming years, the critical level of 40 Gt of CO_2 emissions would be reached in 2030, with serious environmental and health problems (Reference Scenario, Figure 0.4 (a)). An alternate scenario has been considered for which the long-term green house gas concentration is stabilized at a 450 ppm CO_2-equivalent level (450 Scenario, Figure 0.4, a). This second approach would require harsh CO_2-emission savings through massive investments to reach energy efficiency at both industrial and end-use level, with an increased use of renewable energies, biofuels, nuclear power and implementation of CO_2 capture and storage facilities for existing power generation plants (See table, Figure 0.4 (a)). As such, the global temperature increase would be limited to 2°C in the horizon of 2030.

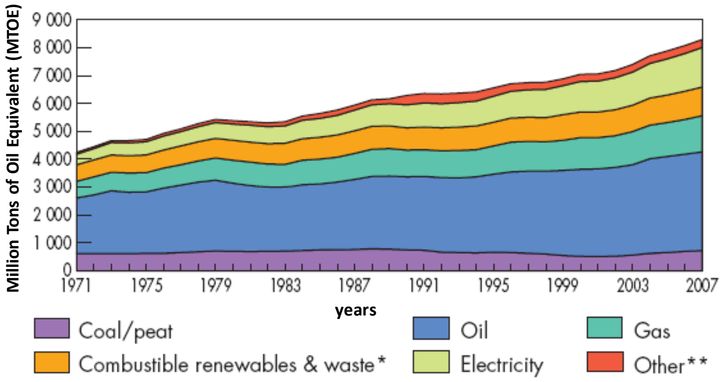

Figure 0.1 Evolution of the world total fuel consumption by type from 1971 to 2007 - * Estimated before 1994, ** "Other" include geothermal, solar, wind, heat, etc. (Adapted from ref. [1]).

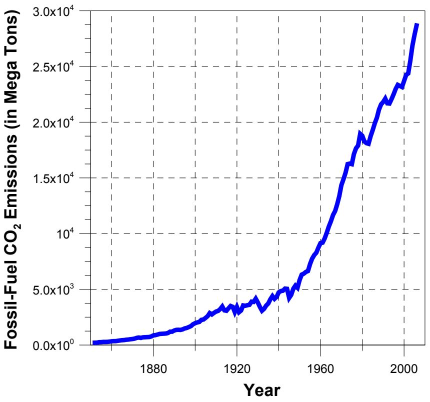

Figure 0.2 Global CO_2 emissions from fossil-fuel burning (the Carbon Dioxide Information Analysis Center, Oak Ridge National Laboratory, April 2009)

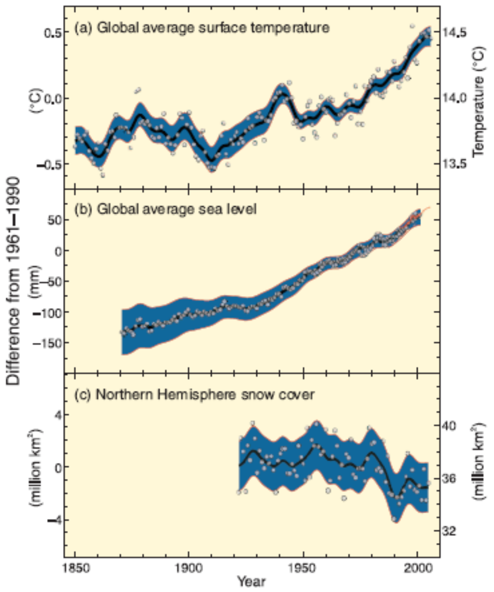

Figure 0.3 Changes in temperature, sea level and Northern Hemisphere snow cover (Graphic from ref. [2]).

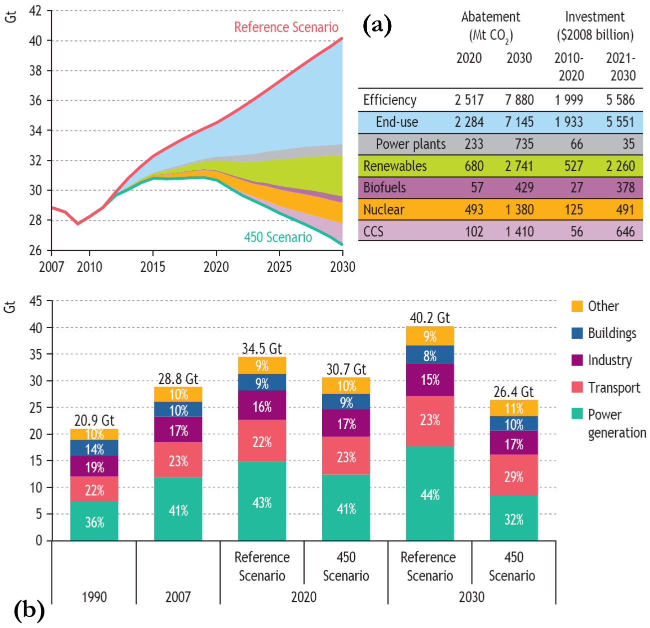

	Abatement (Mt CO_2)		Investment ($2008 billion)	
	2020	2030	2010-2020	2021-2030
Efficiency	2 517	7 880	1 999	5 586
End-use	2 284	7 145	1 933	5 551
Power plants	233	735	66	35
Renewables	680	2 741	527	2 260
Biofuels	57	429	27	378
Nuclear	493	1 380	125	491
CCS	102	1 410	56	646

Figure 0.4 World energy-related CO_2 emissions: (a) the CO_2 emissions (in Gigatons) for the reference and 450 Scenario (Table: CO_2 abatement and corresponding investment in 2008 US dollars to yield the 450 scenario target), (b) CO_2 emissions (in Gt) by sector and predicted scenario (Graphics from ref. [3]).

In this challenging context, both transport and power generation sectors, historically heavily relying on fossil energies, will have to operate a profound mutation to reach the 450 scenario expectancies (See Figure 0.4, b).

The power generation field deserves a particular attention since considerable efforts towards zero-emission goals have been already engaged in the past 15 years, especially for the reduction of nitrogen oxide (NO_x) emissions in thermal power plants [4]. Important changes still have to be operated but the demonstrated wide fuel capabilities of heavy duty gas turbines, complying with both alternative gaseous and liquid fuels, is a major asset [5]. To date, this fuel flexibility is a key aspect for the innovative Integrated Gasification Combined Cycle (IGCC) power plants. These facilities are merging various technologies, including for instance gasification, gas cleaning, steam and combustion turbines and carbon sequestration to produce a clean and affordable energy (see Figure 0.5). In 2003, the U.S. Department of Energy announced an ambitious $1 billion industry partnership for the creation of a pilot "FutureGen" IGCC plant with 60 % efficiency (HHV), $4 per million-Btu hydrogen and CO_2 sequestration [6]. If the great variety of allowed carbon-based feedstock, including coal, biomass, wastes etc., seem to be the highlight of such power plants, the composition of resulting synthesis gases (H_2+CO mainly) that are produced and burned in combustion turbines can greatly vary (see Figure 0.6). Often, hardware adaptations are required to ensure safe and efficient burning operations, particularly for synthesis gases with higher hydrogen contents [7]. To do so, fundamental properties of syngas mixtures, and in general, of any potential alternative fuel, are needed.

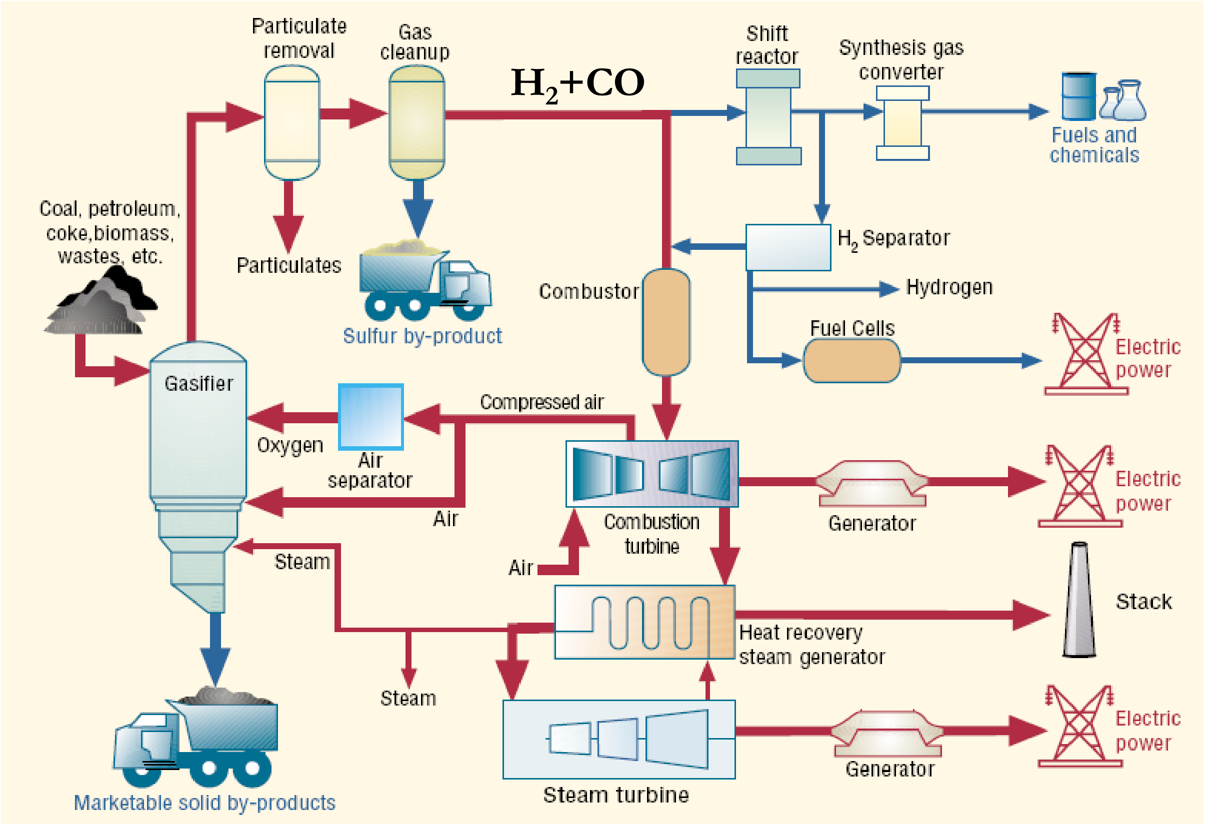

Figure 0.5 IGCC Principles: from raw feedstock to final marketable products (Adapted from ref. [8]).

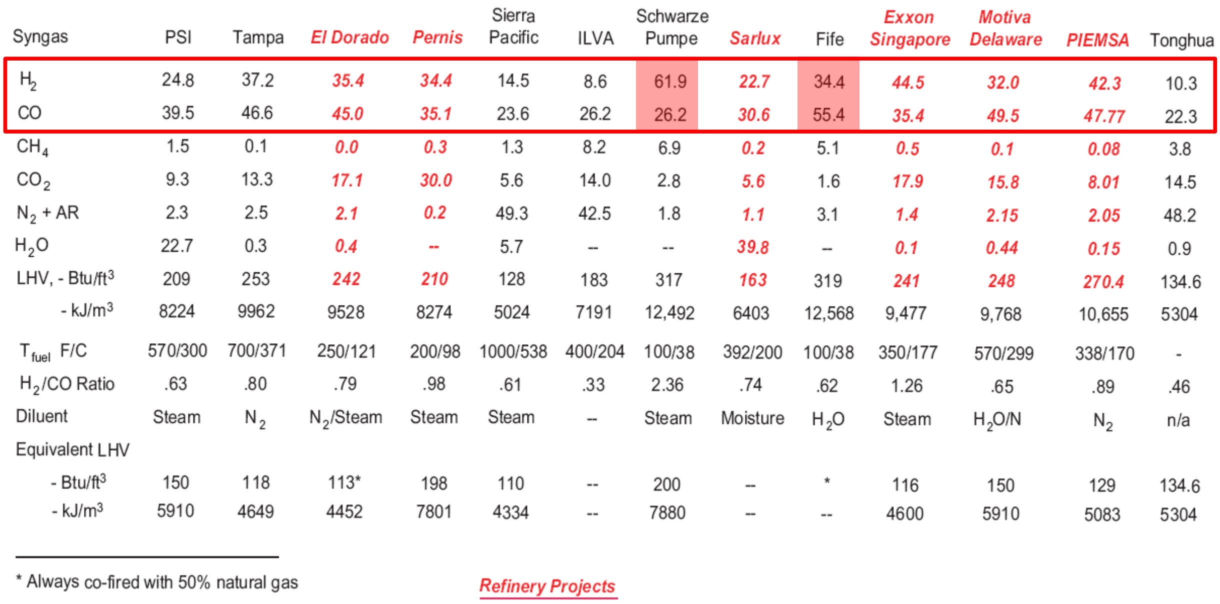

Syngas	PSI	Tampa	*El Dorado*	*Pernis*	Sierra Pacific	ILVA	Schwarze Pumpe	*Sarlux*	Fife	*Exxon Singapore*	*Motiva Delaware*	*PIEMSA*	Tonghua
H_2	24.8	37.2	*35.4*	*34.4*	14.5	8.6	61.9	*22.7*	34.4	*44.5*	*32.0*	*42.3*	10.3
CO	39.5	46.6	*45.0*	*35.1*	23.6	26.2	26.2	*30.6*	55.4	*35.4*	*49.5*	*47.77*	22.3
CH_4	1.5	0.1	*0.0*	*0.3*	1.3	8.2	6.9	*0.2*	5.1	*0.5*	*0.1*	*0.08*	3.8
CO_2	9.3	13.3	*17.1*	*30.0*	5.6	14.0	2.8	*5.6*	1.6	*17.9*	*15.8*	*8.01*	14.5
N_2 + AR	2.3	2.5	*2.1*	*0.2*	49.3	42.5	1.8	*1.1*	3.1	*1.4*	*2.15*	*2.05*	48.2
H_2O	22.7	0.3	*0.4*	*--*	5.7	--	--	*39.8*	--	*0.1*	*0.44*	*0.15*	0.9
LHV, - Btu/ft³	209	253	*242*	*210*	128	183	317	*163*	319	*241*	*248*	*270.4*	134.6
- kJ/m³	8224	9962	9528	8274	5024	7191	12,492	6403	12,568	9,477	9,768	10,655	5304
T_{fuel} F/C	570/300	700/371	250/121	200/98	1000/538	400/204	100/38	392/200	100/38	350/177	570/299	338/170	-
H_2/CO Ratio	.63	.80	.79	.98	.61	.33	2.36	.74	.62	1.26	.65	.89	.46
Diluent	Steam	N_2	N_2/Steam	Steam	Steam	--	Steam	Moisture	H_2O	Steam	H_2O/N	N_2	n/a
Equivalent LHV													
- Btu/ft³	150	118	113*	198	110	--	200	--	*	116	150	129	134.6
- kJ/m³	5910	4649	4452	7801	4334	--	7880	--	--	4600	5910	5083	5304

* Always co-fired with 50% natural gas

Refinery Projects

Figure 0.6 Examples of Syngas composition variability for GE gas turbines operating on refinery residues: H_2 and CO contents can vary from 8.6 to 61.9 % and 22.3 to 55.4 respectively (Adapted from ref. [9]).

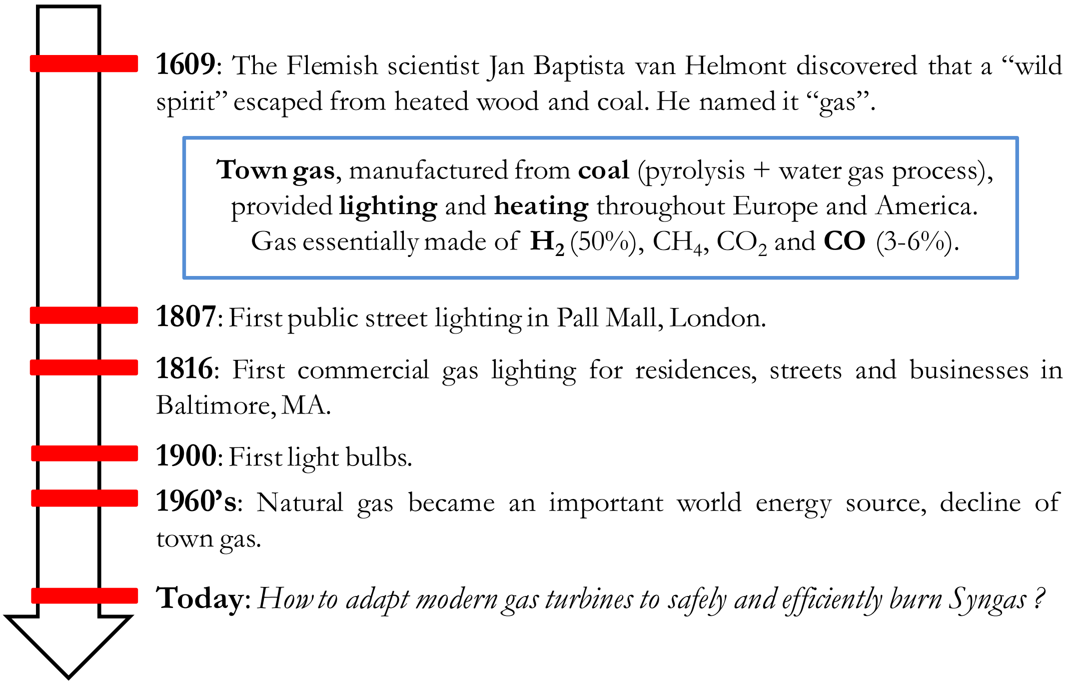

1609: The Flemish scientist Jan Baptista van Helmont discovered that a “wild spirit” escaped from heated wood and coal. He named it “gas”.

Town gas, manufactured from **coal** (pyrolysis + water gas process), provided **lighting** and **heating** throughout Europe and America. Gas essentially made of $\mathbf{H_2}$ (50%), CH_4, CO_2 and **CO** (3-6%).

1807: First public street lighting in Pall Mall, London.

1816: First commercial gas lighting for residences, streets and businesses in Baltimore, MA.

1900: First light bulbs.

1960’s: Natural gas became an important world energy source, decline of town gas.

Today: *How to adapt modern gas turbines to safely and efficiently burn Syngas ?*

Figure 0.7 The use of “synthetic” gases over the years: from Town gas to Syngas.

Although “burning Syngas” is not an entirely new concept (see the historical outlines provided in Figure 0.7), the demanding heavy duty gas turbine application led the combustion community to carry out extensive research to study properties of syngas fuels, including: inflammability limits, autoignition delays, flame flashback and blowoff propensities, and fundamental flame speed. The latter is one of the most important properties in combustion since it is providing essential information about thermochemical processes arising during fuel combustion. It is also extensively used for flame modeling purposes.

In this particular context, the present study is devoted to the development of a laminar flame speed determination methodology, using the Digital Particle Image Velocimetry (PIV) diagnostics. The latter is applied to stagnation flow flames, seen to have considerable assets in comparison with other flame configurations. Indeed, flames stabilized in such diverging flows are planar, steady and in near-adiabatic conditions while subtraction of strain effects on flame is allowed. The methodology developed herein has been applied to the well-characterized methane/air mixtures for validation. Laminar flame velocities of various syngas mixtures (H_2+CO) have been investigated using multiple experimental approaches including the counterflow, spherical and conical flame configurations.

These experimental studies have been performed at the “Institut de Combustion, Aérothermique, Réactivité et Environnement” (ICARE) of the CNRS-Orléans, the Propulsion Engineering Research Center (PERC) of the Pennsylvania State University and the “Institut Pluridisciplinaire de Recherche en Ingénierie des Systèmes, Mécanique et Énergétique” (PRISME) of Orléans University.

The present work is divided into 6 chapters including:

- **Chapter I**: **Fundamentals of Laminar Premixed Combustion**.

  Definitions relevant to laminar premixed combustion are recalled. Governing equations of models used in this investigation are presented.

- **Chapter II**: **Laminar Flame Speed Determination in Reactive Stagnation Flows: A Review.**

  Governing equations of particle motion in viscous fluids are recalled. Thermophoretic effects in counterflow premixed and non-premixed flames are discussed. A detailed review of Laser Doppler and Particle Image Velocimetry experiments in stagnation flows is provided. Issues related to the choice of a reference plane for flame parameter extraction and the influence of the nozzle separation distance on flame speed measurements are discussed. Literature investigations using the stagnation plate flame setup are detailed with inclusion of the stagnation-to-conical flame transition methodology.

- **Chapter III: Digital Particle Image Velocimetry for Laminar Flame Speed Determination: Principles and Application to Stagnation Flow Flames.**

  Main Digital Particle Image Velocimetry (DPIV) principles are recalled. The following methodological steps are detailed and discussed: 1/ Choice of the PIV processing algorithms, 2/ Choice of seeding material including trial tests and particle concentration estimations, 3/ Relevance of peak-locking effects and influence on strain rate determinations, 4/ Algorithm developed for DPIV images post-processing including laminar flame speed extraction and data reduction procedures, 5/ Estimations of uncertainties on extrapolated velocities with relative influence of the extrapolation main parameters.

- **Chapter IV: Laminar Strained Flames in CH_4/Air Mixtures in Stagnation Flow Configurations: Experimental and Numerical Studies.**

  CH_4/air laminar strained flame are experimentally (PART I) and numerically (PART II) investigated for both stagnation plate flame and counterflow twin flame configurations. In the first part, experimental setups are presented along with the protocol for data acquisition. Feasibility of the planar-to-conical flame transition methodology is discussed. Laminar flame speeds results obtained in the counterflow configuration are compared with various literature data sets and predictions of several kinetic mechanisms for validation. The second part is devoted to the 1D and 2D simulations of chosen experimental cases to assess the compatibility of both numerical approaches. For the stagnation plate flame case, the particle dynamics in the diverging flow is analyzed including relevant

Stokes drag, gravity and thermophoretic forces. The different possible definitions for the applied flame strain rate are assessed in the light of the counterflow 2D simulation results.

- **Chapter V: Laminar Flame Speeds of Syngas/Air Mixtures in the Counterflow Twin Flame Configuration.**

  This chapter is devoted to the determination of laminar flame speeds of various syngas/air mixtures with H_2 contents up to 50%. Modifications of the burner apparatus of chapter IV as well as new flow control and gas supply systems are presented. Results are confronted to the literature datasets as well as predictions of two leading mechanisms for syngas combustion.

- **Chapter VI: Laminar Flame Speeds of Syngas/Air Mixtures: Comparison with the Bunsen and Outwardly Propagating Flame Approaches.**

  Laminar flame speeds of syngas mixtures have been investigated for two alternate experimental configurations, i.e. the outwardly propagating and the burner rim-stabilized conical flames. Each individual setups and methodological approaches are detailed and results are individually compared to literature datasets and numerical predictions. The confrontation of measurements from the three different experimental approaches is provided.

I. Fundamentals of Laminar Premixed Combustion

I.1 Introduction and Objectives

The present chapter intends to provide basic definitions related to laminar premixed combustion. In a first part, the laminar flame speed and flame stretch definitions are recalled. A comparison of methodologies available for the laminar flame speed determination is provided. The second part is devoted to the presentation of both 1D (PREMIX, OPPDIF) and 2D (Fluent) combustion codes to be used in the later sections. Corresponding conservation equations and related approximations are detailed, and transport properties of both 1D and 2D codes are confronted to identify potential dissimilarities between both formulations.

I.2 On the Determination of Laminar Flame Speeds

I.2.1 Laminar Flame Speed Definition

The laminar flame speed – also widely called laminar flame velocity or laminar burning velocity – is conventionally defined as the speed at which a flame front is moving with respect to the fresh gases in a one dimensional geometry [10]. This definition is illustrated Figure I.1.

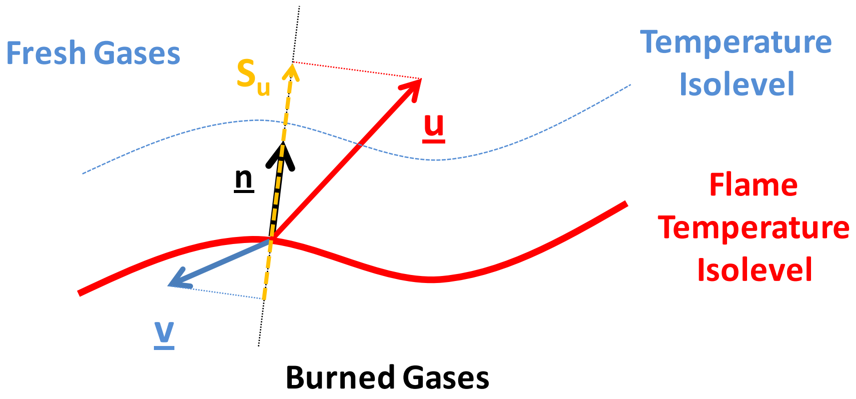

Figure I.1 Illustration of the laminar flame speed determination with ***n***, normal to the flame front oriented towards fresh gases, ***u***, local flame velocity vector evaluated on the flame temperature isolevel, ***v***, local flow velocity vector evaluated at a chosen fresh gas temperature isolevel, S_u, resulting laminar flame speed.

The laminar flame speed S_u is defined as:

$$S_u = (\boldsymbol{u} - \boldsymbol{v}).\boldsymbol{n} = u_n - v_n \qquad \text{(I-1)}$$

with ***n***, the normal to the flame front oriented towards the fresh gases, ***u***, the local flame velocity vector evaluated on the flame temperature isolevel, ***v***, the local flow velocity vector evaluated at a chosen fresh gas temperature isolevel, u_n, the absolute speed at which the flame front is moving with respect to the laboratory frame (this speed is often referred to as the "flame propagation speed") and v_n, the fresh gas inlet speed with respect to the laboratory frame. An important shortcoming of the present definition is that S_u is not unique for a fixed mixture composition and fixed temperature and pressure conditions. Indeed, flame stretch effects, including for instance flame curvature and aerodynamic straining (to be defined in a later section) as well as flame cooling effects (heat transfers to the flame surroundings) can significantly modify this value. Therefore, most combustion studies have oriented their efforts towards the determination of reference speeds that are free from the aforementioned effects. These are the so-called fundamental flame speeds S_u^0, corresponding to the speeds of laminar 1D planar adiabatic unstretched freely-propagating flames. Such flames are however idealistic and can hardly be achieved in practice since the upstream flow is rarely totally uniform, and thus the flame rarely planar. Note here that, in absence of any other stabilizing effects, the free propagation of a slightly curved/wavy flame will be significantly influenced by hydrodynamic instabilities due to the gas expansion through the flame front (See ref. [11], chapter V). That is why laboratory experiments have been essentially devoted to the determination of laminar flame speeds for either stretched or heat stabilized flames from which fundamental flame speeds are ultimately deduced.

I.2.2 Flame Stretch

Definition

The flame stretch is defined as the fractional rate of change of a flame surface element. Various derivations of the flame stretch can be found in the literature, see for instance ref. [12-14]. We recall here the formulation proposed by Chung and Law [12] for a flame surface velocity $\boldsymbol{u}$, a flow velocity $\boldsymbol{v}$ and the unit vector of the elemental surface pointing in the flame propagation direction $\boldsymbol{n}$:

$$K = \frac{1}{A}\frac{dA}{dt} = \underbrace{\nabla\cdot\boldsymbol{v}_{s,t}}_{\mathbf{1}} + \underbrace{(\boldsymbol{u}\cdot\boldsymbol{n})(\nabla\cdot\boldsymbol{n})}_{\mathbf{2}} = \underbrace{\nabla\cdot[\boldsymbol{n}\times(\boldsymbol{v}_s\times\boldsymbol{n})]}_{\mathbf{1}} + \underbrace{(\boldsymbol{u}\cdot\boldsymbol{n})(\nabla\cdot\boldsymbol{n})}_{\mathbf{2}} \qquad \text{(I-2)}$$

With A, an infinitesimal element of the flame surface and $\boldsymbol{v}_s$, the tangential velocity component of the flow velocity at the flame. The term 1 embodies effects of both flow nonuniformity ($\boldsymbol{v}_s$) and flame curvature ($\boldsymbol{n}$). Note here that the flow velocity should be oblique to the flame surface, the term $\boldsymbol{v}_s\times\boldsymbol{n}$ will vanish otherwise. The term 2 is accounting for a stretch felt by a non stationary flame ($\boldsymbol{u}$), that is simultaneously experiencing curvature, else $\nabla\cdot\boldsymbol{n} = 0$. Thus, it is conventionally admitted that flames are submitted to three types of stretch effects, individually referred to as aerodynamic straining, flame curvature and flame motion.

As discussed earlier, the flame speed of a stretched flame (either strained or curved or both) will be depending on the importance of aforementioned stretch effects. In the limit of weakly stretched flames, the following linear relation, partly based on the early flame speed formulation proposed by Markstein [15] for curved flames, is generally assumed [10]:

$$S_u = S_u^0 - LK \qquad \text{(I-3)}$$

with L, the Markstein length characterizing the flame sensitivity to stretch. Expression (I-3) may be recast in the following form:

$$\frac{S_u}{S_u^0} = 1 - Ma\,Ka \tag{I-4}$$

with Ma, the Markstein number and Ka, Karlovitz number, both defined as:

$$Ma = \frac{L}{\delta} \quad \text{(I-5)} \qquad\qquad Ka = \frac{\delta}{S_u^0} K \quad \text{(I-6)}$$

where δ given by expression (I-7): $\delta = D_T / S_u^0$ is the unstretched flame thickness defined as the ratio of the mixture thermal diffusivity D_T to the fundamental flame speed S_u^0. Various expressions have been derived in the literature for the Markstein numbers. For a flame with variable density and a one-step overall chemical reaction, the following Markstein number expression is provided by Clavin and Joulin in ref. [16]:

$$Ma = \frac{1}{\gamma} ln\left(\frac{1}{1-\gamma}\right) + \beta \frac{(Le-1)}{2}\left(\frac{1-\gamma}{\gamma}\right)\int_0^{\frac{\gamma}{1-\gamma}} \frac{ln(1+x)}{x}\,dx \tag{I-8}$$

with β, the reduced activation energy, γ, the gas expansion parameter, and Le the mixture Lewis number defined as:

$$\gamma = 1 - \frac{\rho_b}{\rho_u} < 1 \quad \text{(I-9)} \qquad\qquad Le = \frac{D_T}{D_{mol}} \quad \text{(I-10)}$$

With ρ_b and ρ_u, the burned and unburned gas densities respectively, and D_{mol}, the species diffusivity. It is important to recognize from expression (I-8) that depending on the Lewis number, Ma can be either positive or negative. In fact, most hydrocarbon/air flames have positive Ma numbers and a change of sign is only to be expected for mixtures with Lewis numbers significantly departing from unity, i.e. $Le \ll 1$ (For example, lean fuel blends with highly diffusive species such as H_2, He, etc).

I.2.3 Methodologies for Experimental Determination of Laminar Flame Speeds

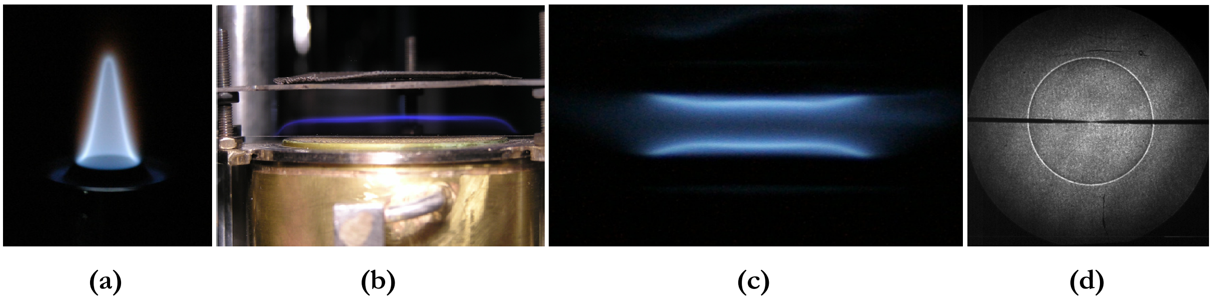
(a) **(b)** **(c)** **(d)**

Figure I.2 Laminar flame configurations for flame speed studies: (a) Rim-stabilized conical flame, (b) Heat flux-stabilized flat flame, (c) Counterflow flames, (d) Spherically expanding flame (shadowgraph).

The methodologies for fundamental flame speed determination involve flames that are, in the laboratory frame, either stationary, i.e. $u_n = 0$ and $v_n \neq 0$, or propagating with respect to a quiescent unburned mixture, i.e. $v_n = 0$ and $u_n \neq 0$. The former include conical, flat and counterflow flames and the latter spherically expanding flames. All configurations are briefly described in the remaining part of the present section and compared in Table I.1.

The rim-stabilized conical flame method (Figure I.2, a)

In this method, the premixed reactants flow towards the exit of a cylindrical tube where a conical flame is anchored. Various techniques (Schlieren, Shadows, Chemiluminescence) can be used to visualize and record the cone boundaries from which laminar flame speeds are deduced (see chapter VI for additional information concerning the detailed flame speed extraction procedures). The major drawback of the present configuration is that the burning velocity is not constant over the entire flame cone. It is indeed affected by: i/ heat losses at the burner rim; ii/ a burning intensity increase or decrease at the flame cone apex, depending on the flame tip curvature and the importance of nonequidiffusive effects for the mixture of interest. Furthermore, the choice of a reference surface to yield the laminar flame speed following the flame surface area procedure (S_u = volume flow rate/flame cone area) has been the source of a great controversy [17]. An overall accuracy of ±20 % has to be expected according to ref. [18].

The flat flame and heat flux method (Figure I.2, b)

The original method was proposed by Botha and Spalding [19]. A flat flame is stabilized downstream of a water-cooled porous plate by adjusting the corresponding cooling water flow rate. The extracted heat and non adiabatic flame speed (assumed to be equal, when stability is reached, to the average flow rate divided by the burner surface area) can thus be determined. The operation is reiterated for various inlet velocity conditions. The fundamental flame speed is then found by linear extrapolation to the "zero-extracted-heat" state. A major drawback of this methodology is that the increase of the water cooling temperature is rather small which worsen the accuracy of the determined fundamental flame speeds. To circumvent this problem, a new burner design was proposed by Van Maaren et al. [20] for which the flame is stabilized on a perforated brass plate. The latter is heated (typically around 85 °C), warming up fresh gases flowing through. Thus, the flame is losing heat at the burner plate and gaining some from the heat transfer to the unburned reactants. The net difference between the heat loss and the heat gain is responsible for the radial temperature distribution of the perforated plate, observed thanks to series of thermocouples. By tuning the fresh gases inlet velocity, an adiabatic state can be reached for which the heat loss exactly compensates the heat gain. This state is achieved when the temperature reach a constant value across the entire burner plate. Additional details on the methodology can be found in ref. [21-22].

The counterflow flame method (Figure I.2, c)

The counterflow flame methodology for laminar flame speed determination was first introduced by Wu and Law [23] in 1984. By impinging two identical laminar reactive jets onto each other, a stagnation plane is formed, with flat flames stabilized on both sides in the divergent jets. After injection, both flows are strongly decelerating before reaching the flame preheat zones. In this region, fresh gases are experiencing a strong thermal expansion and therefore a steep flow velocity increase is observed. The flow axial velocities finally decrease upon combustion completion when the stagnation plane is approached. Such flow velocity profiles can be used to determine a reference velocity $S_{u,ref}$, usually taken at the unburned upstream edge of the flame. Its associated stretch rate is conventionally defined as the axial velocity gradient K in the hydrodynamic zone of the jet. Notice here that the flames are only subjected to aerodynamic straining, characterized by the parameter K. The latter can be independently varied by changing the inlet flow rates or the nozzle separation distance. Plotting the various $S_{u,ref}$ velocities versus corresponding strain rates allow for a linear extrapolation to be performed, yielding the fundamental laminar flame speed for $K \rightarrow 0$. This value is obtained under quasi-adiabatic conditions, since upstream heat losses are small (nozzle-generated jet), and downstream ones negligible due to the symmetry. Additional details on the methodology will be provided in the course of chapters III & IV.

The spherically expanding flame method (Figure I.2, d)

In this approach, a spherical chamber is filled with the quiescent combustible mixture to be studied. The laminar flame is ignited at the center of the chamber and propagates in the outward direction. If the flame radius is not to large, the chamber pressure and temperature of fresh gases ahead of the flame are similar to those measured in the initial state. Pressure and fresh mixture temperature should be separately recorded otherwise. The temporal evolution of the flame front (visualized thanks to Schlieren, shadow, etc. techniques) allow for the determination of a stretched laminar flame propagation speed and its associated stretch rate at each time step. Similarly to the counterflow flame method, an extrapolation is performed to yield the unstretched flame propagation speed, subsequently rescaled by the burned-to-unburned gas density ratio. The final velocity value obtained is the fundamental laminar flame speed of interest. It is worth to mention that, contrary to counterflow flames, spherical flames are subjected to stretch effects arising from both aerodynamic straining and flame curvature. Studies of Bradley et al. [24], Gu et al. [25] and Groot et al. [26] should be consulted for additional details on the appropriate separation of both stretch contributions for spherically expanding flames. An important statement formulated in ref. [26] is that Markstein numbers for flow straining are strongly dependant on the chosen isotherm at which they are evaluated.

	Rim-Stabilized Conical Flames	Flat Flames/Heat Flux	Counterflow Flames	Spherically Expanding Flames
	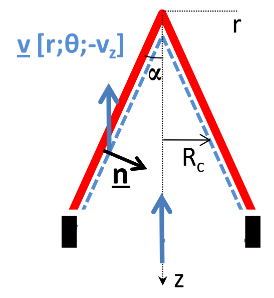	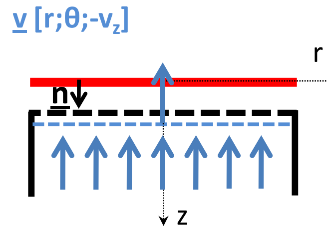	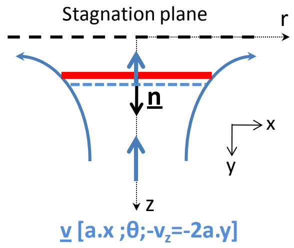 (Assuming potential flow)	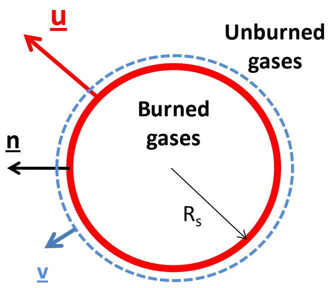
Flame Front Absolute Speed	$u_n = 0$	$u_n = 0$	$u_n = 0$	u_n measured
Fresh Gases Speed	$v_n = -v_z \sin\alpha$	$v_n = -v_z$	$v_n = -v_z = -2a.y$	v_n: dependant of the chosen isotherm
Laminar Flame Speed	$S_u = -v_n = v_z \sin\alpha$	$S_u = -v_n = v_z$	$S_u = -v_n = v_z = 2a.y$	$S_u = \frac{\rho_b}{\rho_u}(u_n + v_n) = \frac{\rho_b}{\rho_u}\frac{dR_S}{dt}$
Stretch Influence	Yes: Flow straining + Curvature	Negligible	Yes: Flow Straining	Yes: Flow straining + Curvature
Stretch Expression (expression (I-2))	$K = -\frac{v_z \sin(2\alpha)}{2 R_c}$ (v_z and α constants)	×	$K = 2a$	$K = \frac{2}{R_s}\frac{dR_s}{dt}$
Heat Loss Influence	Yes (No compensation)	Yes (Possible compensation)	Quasi-adiabatic	Quasi-adiabatic
Methodology Merits	● Simple and flexible burner setup. ● Easy burner operation.	● Flame can be considered as adiabatic (for the heat compensation case). ● Interpolation is done for S_u^0 determination (for the heat compensation case). ● Ultra-low stretch achieved ≈o(1 s^{-1}). ● Adapted for low pressure measurements.	● Flames stabilized far from the burner heads = quasi-adiabatic conditions. ● Flow straining can be easily varied. ● Ideal to perform multi-diagnostics approaches including laser-based diagnostics for velocimetry and flame species measurements.	● Simple design. ● Fast operation. ● Continuous record of the flame front evolution ensures that (K;S_u) pairs are extracted for the same initial conditions. ● Only small volume of gases are needed. ● Intrinsically adapted for rich flames.

			● Aerodynamic straining has a stabilizing effect for cellular instabilities. ● Adapted for high pressure measurements.	● Easy extraction of burned Markstein lengths. ● Adapted for high pressure measurements.
Methodology Drawbacks	● Wall quenching effects never completely eliminated. ● Influence of straining and curvature effects generally not subtracted. ● Steady source of gas supply needed. ● Alteration of the fuel equivalence ratio at the flame base through diffusional interchange of chemical species present in the flame surroundings. ● The flame cone can act as a lens in shadow measurements causing uncertainties in the determination of the real size of the cone. ● Increased flame propensity to flashback for large burner I.D. ● Choice of different unburned reference surface can lead to disparities in measurements. ● Ambiguous experimental determination of the flame boundary at the cone base. ● Burner housing is required for rich cases.	● Steady source of gas supply needed. ● Complex burner setup for the heat flux compensation case. ● Indirect evaluation of S_u^0. ● Proximity of the flame to the burner plate renders laser-based measurements difficult. ● Flame edge effects at higher burner inlet velocity might be non negligible.	● Steady source of gas supply needed. ● Steady/continuous source of seeding tracers needed (+ Cleaning!) ● Complex burner operation. ● Need for extrapolation to a zero strain rate state to yield S_u^0. ● Non negligible PIV computation times for the velocity vector fields. ● Instabilities: possible Helmholtz resonance for the nozzle burner (See Chapter IV). ● Choice of a reference plane needed: ambiguity of interpretation for the flame strain sensitivity (See discussion Chapter II). ● Burner housing is required for rich cases.	● Need for extrapolation to the zero stretch rate state to yield the unstretched flame propagation speed S_b^0. ● Need to "rescale" S_b^0 by a calculated burned to unburned gas density ratio. ● Heavy processing steps. ● Influence of the initial energy deposition. ● Influence of the electrodes (heat loss at the initial stage of the flame propagation). ● Influence of the confined domain. ● Distortion of the flame shape due to buoyancy effects (essentially for weakly burning flames).

Table I.1 Comparison of various methodologies for the determination of fundamental flame speeds.

I.3 Numerical Tools for Reacting Flow Simulations

I.3.1 General Formulation of the Conservation Equations for Reacting Flows

Derivations of the conservation equations for reacting flows can be found in the literature, for instance in the book of Kuo [18]. General forms of these equations, widely implemented in combustion codes, were commented by Poinsot and Veynante in ref. [10] and are recalled as such in Table I.2. These equations are including:

- **The mass conservation equation** (I-11): with ρ, the mixture density and u_i , the flow velocity in the direction i.
- **The momentum conservation equation** (I-12): with p, pressure, Y_k , mass fraction of the species k, $f_{k,j}$, the volume force acting on species k in the j direction, τ_{ij} , the viscous tensor, μ , the dynamic viscosity and δ_{ij} , the Kronecker symbol.
- **The species conservation equation** (I-14): with $V_{k,i}$, the diffusion velocity of the species k in the direction i and $\dot{\omega}_k$, the reaction rate of species k.
- **The energy conservation equation** (I-15): with C_p , the mixture mass heat capacity, T, the mixture temperature, $\dot{\omega}_T$, the heat release, λ , the mixture thermal conductivity, $C_{p,k}$, the mass heat capacity of species k and Q , the heat source term, for example due to an electric spark.
- **The equation of state** (I-16): with R , the perfect gas constant and W, the mean molecular weight of the mixture.

Mass Conservation	$\frac{\partial \rho}{\partial t} + \frac{\partial \rho u_i}{\partial x_i} = 0$	(I-11)
Momentum Conservation	$\frac{\partial}{\partial t}\rho u_j + \frac{\partial}{\partial x_i}\rho u_i u_j = -\frac{\partial p}{\partial x_j} + \frac{\partial \tau_{ij}}{\partial x_i} + \rho \sum_{k=1}^{N} Y_k f_{k,j}$ $With \quad \tau_{ij} = -\frac{2}{3}\mu \frac{\partial u_k}{\partial x_k}\delta_{ij} + \mu\left(\frac{\partial u_i}{\partial x_j} + \frac{\partial u_j}{\partial x_i}\right)$	(I-12) (I-13)
Species Conservation	$\frac{\partial \rho Y_k}{\partial t} + \frac{\partial}{\partial x}\left(\rho\left(u_i + V_{k,i}\right)Y_k\right) = \dot{\omega}_k$	(I-14)
Energy Conservation (Temperature Equation)	$\rho C_p \frac{DT}{Dt} =$ $\dot{\omega}_T + \frac{Dp}{Dt} + \frac{\partial}{\partial x_i}\left(\lambda \frac{\partial T}{\partial x_i}\right) - \left(\rho \sum_{k=1}^{N} C_{p,k} Y_k V_{k,i}\right)\frac{\partial T}{\partial x_i} + \tau_{ij}\frac{\partial u_i}{\partial x_j} + Q + \rho \sum_{k=1}^{N} Y_k f_{k,i} V_{k,i}$	(I-15)
Equation of State	$p = \rho \frac{R}{W} T$	(I-16)

Table I.2 General conservation and state equations for reacting flows involving N individual species.

I.3.2 1D Simulation Codes

Two one-dimensional codes have been considered in the present investigation and will be briefly presented herein. These are:

- PREMIX, a code widely used among the combustion community to compute species and temperature profiles for steady-state burner-stabilized and freely propagating premixed laminar flames. This numerical tool has been involved in numerous studies aiming at developing kinetic mechanisms to accurately predict combustion characteristics of various fuel/oxidant systems.
- OPPDIF, a program computing solutions for steady non-premixed and premixed flames stabilized in the counterflow configuration. Velocity, temperature and species profiles can be determined in the core flow between two opposing nozzles.

Both programs are included in the CHEMKIN collection suite. The next two sections will present the governing equations as well as leading assumptions involved in the resolution of related problems. For additional details on program structures, numerical solution methods or user-specified options, readers will redirected to the original Sandia reports for both PREMIX [27] and OPPDIF [28] codes. Note however that both approaches have a common general architecture requiring a gas phase chemistry input and related thermodynamic and transport data as well as user inputs for the cases of interest.

PREMIX

Governing equations for the PREMIX code are detailed in Table I.3. These expressions are obtained from the general formulations presented in Table I.2 with the following additional assumptions:

- The flame is calculated for a steady state condition: derivative in time are removed.
- The flame is propagating in only one direction, x for the present example.
- For subsonic combustion with low Mach numbers, pressure variations can be neglected: the Dp/Dt term in equation (I-15) can be set to zero. The same assumption applies to the viscous heating term $\tau_{ij}\,(\partial u_i/\partial x_j)$ of equation (I-15).
- Volume forces acting on individual species are set to zero: the last term of equation (I-15) is removed.
- No external source of energy is provided to the system: the term Q in (I-15) is set to zero.

The heat release term of equation (I-15) can be expressed as the sum of the products of specific enthalpies and reaction rates of each individual species, i.e.:

$$\dot{\omega}_T = -\sum_{k=1}^{N} h_k \dot{\omega}_k \tag{I-17}$$

Note that the momentum equation (I-12) is not included in the set of equations presented in Table I.3. It can eventually be used to compute the pressure field and verified that the pressure jump through the flame front is effectively small [10].

Mass Conservation	$\rho u = cste$	(I-18)
Species Conservation	$\rho u \frac{dY_k}{dx} + \frac{d}{dx}\rho Y_k V_k = \dot{\omega}_k \quad k = 1, \dots, N$	(I-19)
Energy Conservation (Temperature Equation)	$\frac{d}{dx}\left(\lambda \frac{dT}{dx}\right) - \rho u\, C_p \frac{dT}{dx} - \left(\rho \sum_{k=1}^{N} C_{p,k} Y_k V_k\right)\frac{dT}{dx} = \sum_{k=1}^{N} h_k \dot{\omega}_k$	(I-20)
Equation of State	$p = \rho \frac{R}{W} T$	(I-21)

Table I.3 PREMIX conservation and state equations.

The PREMIX code was essentially used in the present investigation in the freely propagating flame configuration for which laminar flame velocities were calculated for inlet pressure, temperature and mixture composition as main input parameters. Contrary to burner-stabilized flames for which heat losses might have an important influence on flame temperature, computations are assuming adiabatic conditions and the temperature distribution is determined through the energy conservation equation (I-20).

OPPDIF

Governing equations for the OPPDIF code are detailed in Table I.4. Additional details for the mathematical formulation of the problem as well as equation derivations can be found in the works of Kee et al. [29] and Dixon-Lewis [30]. Only the general outline will be emphasized here. The conservation of mass in cylindrical coordinates for a steady state case yields the expression (I-23), with *u*, normal velocity and *v*, tangential velocity and *r*, radial coordinate. Two stream functions *G* (I-25) and *F* (I-26*)* satisfying (I-23) can be defined to yield the simplified continuity equation (I-24). This definition directly implies that:

- *u* and *ρ* are functions of *x* only,
- *v* is linearly depending on the radial coordinate *r*, i.e. the radial velocity gradient *a* defined as:

$$a = \frac{v}{r} \tag{I-22}$$

is constant for a fixed *x*.

Additional assumptions are made:

- The temperature *T* and the species mass fraction Y_k are depending on *x* only.
- Similarly to the PREMIX case, the small Mach number assumption is used, leading to the suppression of the third term in equation (I-15). However pressure gradient terms are still present in the axial and radial momentum equations. It can be found [29] that the term *1/r (∂p/∂r)* is a constant and represent an eigenvalue of the 1D problem. This term is calculated as a part of the numerical solution. By further introducing expressions (I-25), (I-26) and (I-28) in the radial momentum equation, expression (I-27) is obtained.

The species and energy conservation equations (I-29) and (I-30) are similar to those presented for the PREMIX case and are established for identical assumptions.

Mass Conservation	(I-23) $\frac{\partial}{\partial x}\rho u + \frac{1}{r}\frac{\partial}{\partial r}\rho r v = 0 \quad \Leftrightarrow \quad G(x) = \frac{dF(x)}{dx}$ (I-24) $With \quad G(x) = -\frac{\rho v}{r}$ (I-25) $\quad F(x) = \frac{\rho u}{2}$ (I-26)
Perpendicular Momentum Conservation	$H - 2\frac{d}{dx}\left(\frac{FG}{\rho}\right) + \frac{3G^2}{\rho} + \frac{d}{dx}\left[\mu\frac{d}{dx}\left(\frac{G}{\rho}\right)\right] = 0$ (I-27) $With \quad H = \frac{1}{r}\frac{\partial p}{\partial r} = cste$ (I-28)
Species Conservation	$\rho u\frac{dY_k}{dx} + \frac{d}{dx}\rho Y_k V_k = \dot{\omega}_k \qquad k = 1, \dots, N$ (I-29)
Energy Conservation (Temperature Equation)	$\frac{d}{dx}\left(\lambda\frac{dT}{dx}\right) - \rho u\, C_p\frac{dT}{dx} - \left(\rho\sum_{k=1}^{N} C_{p,k}Y_k V_k\right)\frac{dT}{dx} = \sum_{k=1}^{N} h_k\dot{\omega}_k$ (I-30)
Equation of State	$p = \rho\frac{R}{W}T$ (I-31)

Table I.4 OPPDIF conservation and state equations.

An interesting implication of expression (I-24) is that there is a direct relation between the strain rate and the axial and radial velocity gradients in the cold flow regions of the counterflow flames. Taking the general strain rate form for the variable density stagnation point flows of Dixon-Lewis [30] and introducing the formalism of expression (I-22) for the radial gradient velocity, expression (I-32) is obtained:

$$K = -\left(\frac{1}{\mathrm{\rho}}\right)\frac{d\rho u}{dx} = -\frac{du}{dx} = -\frac{2}{\rho_u}\frac{dF}{dx} = 2a \qquad \text{(I-32)}$$

With ϱ_u, the unburned mixture density. Thus, the strain rate in the hydrodynamic zone can either be characterized thanks to the normal velocity gradient or twice the radial velocity gradient. Another remarkable implication of (I-24) is that a general derivation of the simplified mass conservation equation yields a first order differential equation for $\varrho(x)$, valid over the entire domain:

$$\frac{d}{dx}\rho(x) + \epsilon(x)\rho(x) = 0 \qquad \text{(I-33)}$$

$$with \quad \epsilon(x) = \frac{1}{u(x)}\left(\frac{du(x)}{dx} + 2a(x)\right) \qquad \text{(I-34)}$$

The function ϵ depends only on x and could be determined for a practical case (again if (I-24) is assumed!) if 2D velocity measurements are performed. A direct analytic solution of equation (I-33) is however excluded due to complex variations of the function ϵ. Numerical methodologies would have to be implemented to compute the flow field density from the velocity measurements.

The OPPDIF code allows the simulation of two types of inlet flow conditions. These are: i/the potential flow condition, characterized by a constant axial velocity gradient and hence a linearly decreasing axial velocity in the hydrodynamic region of the reactive jet and ii/the plug flow condition, for which the axial velocity gradient is constantly decreasing and therefore axial velocity is describing a parabolic shape. Both cases can be modeled through specifications of adapted boundary conditions at the burner inlet: for the plug flow condition, the axial injection velocity *u(0)* as well as the radial velocity gradient *a(0)* are both required. Note that the pure plug flow condition corresponds to the *a(0) = 0* case. For the potential flow case, a "fully developed" potential flow velocity gradient a_p definition has to be introduced [30]:

$$a_p(x) = \sqrt{\frac{-H}{\rho(x)}} \tag{I-35}$$

This gradient, that is associating the eigenvalue H defined in (I-28) and the density ρ, is a function of local conditions in the counterflow flames. Contrary to the plug flow approach, the potential flow condition requires the single parameter $a_p(0)$ to be specified and the following relation is assumed:

$$a_p(0) = -\frac{1}{\rho_u}\frac{dF}{dx}\bigg|_{x=0} \tag{I-36}$$

i.e.

$$a_p(0) = \sqrt{\frac{-H}{\rho_u}} = -\frac{1}{2}\frac{du}{dx}\bigg|_{x=0} = -\frac{1}{\rho_u}G(0) = a(0) \tag{I-37}$$

As such, the eigenvalue of the 1D problem is known, no extra equation is involved and the inlet velocity *u(0)* is found during the computational procedure.

I.3.3 2D Simulation Code

FLUENT

Fluent is a Computational Fluid Dynamics (CFD) commercial code allowing for the multi-dimensional (2D, 3D) simulation of complex reacting flows. It typically solves the general equations presented in Table I.2, without simplifying assumptions as previously discussed for the classical 1D models. Table I.5 provides further comparisons for standard options relative to mixture transport properties for both 1D (PREMIX, OPPDIF) and 2D (Fluent) codes, with:

- The mixture viscosity μ (Expression (I-38) and (I-39) from the Wilke Formula [31]) with μ_k, X_k and W_k respectively the viscosity, the molar fraction, and the molar mass of the k^{th} species and N, the number of species.
- The mixture thermal conductivities λ (Expressions (I-40) from ref. [32] and (I-41) from Fluent formalism) with λ_k, thermal conductivity of the k^{th} species.

- The diffusion mass fluxes $J_{k,i}$ and $J'_{k,i}$ (Expressions (I-42)/(I-44) from ref. [31] and (I-43)/(I-45) from Fluent formalism) with *W*, the mean molar mass of the mixture, x_i, the spatial coordinate in the i^{th} direction (axial or radial), Y_k, the species mass fraction; d_k and d'_k, the diffusion coefficients of the k^{th} species in the gas mixture; D_{lk}, the binary diffusion coefficient for the l^{th} and k^{th} species.

Mixture Transport Properties	**1D Codes** **PREMIX-OPPDIF**	**2D Codes** **FLUENT**
Viscosity	$\mu = \sum_{k=1}^{N}\left[X_k \mu_k \left(\sum_{l=1}^{N} X_l \phi_{kl}\right)^{-1}\right]$ (I-38) $with \quad \phi_{kl} = \frac{1}{\sqrt{8}}\left(1+\left(\frac{\mu_k}{\mu_l}\right)^{1/2}\left(\frac{W_l}{W_k}\right)^{1/4}\right)^{2}\left(1+\frac{W_l}{W_k}\right)^{-1/2}$ (I-39)	
Thermal Conductivity	$\lambda = \frac{1}{2}\left(\sum_{k=1}^{N} X_k \lambda_k + \left(\sum_{k=1}^{N}\frac{X_k}{\lambda_k}\right)^{-1}\right)$ (I-40)	$\lambda = \sum_{k=1}^{N}\frac{X_k \lambda_k}{\sum_{l=1}^{N} X_l \phi_{kl}}$ (I-41)
Diffusion Mass Fluxes	$J_{k,i} = -\rho d_k \frac{W_k}{W}\frac{\partial X_k}{\partial x_i}$ (I-42) $d_k = (1-Y_k)\left(\sum_{l\neq k}\frac{X_k}{D_{lk}}\right)^{-1}$ (I-44)	$J'_{k,i} = -\rho d'_k \frac{W_k}{W}\frac{\partial Y_k}{\partial x_i}$ (I-43) $d'_k = (1-X_k)\left(\sum_{l\neq k}\frac{X_k}{D_{lk}}\right)^{-1}$ (I-45)

Table I.5 Comparison of conventional mixture transport property options of 1D-(PREMIX, OPPDIF) and 2D-(FLUENT) codes.

II. Laminar Flame Speed Determination in Reactive Stagnation Flows: A Review

II.1 Introduction and Objectives

The present chapter intends to give an insight into the determination of laminar flame velocities in the stagnation flow configuration using flow tracers. It is divided into three main parts including:

- *The presentation of the general equations governing particle motions in fluids.* Relevant Stokes drag and gravity forces are presented and responsity of seeding particles is evaluated for the specific case of the stagnation flow. A detailed literature review on thermophoretic effects on particles seeded in premixed and non-premixed counterflow flames is provided. The importance of other additional forces is discussed.
- *The presentation of laminar flame speed investigations using Laser Doppler Velocimetry (LDV) and Particle Image Velocimetry (PIV) and the stagnation flow configuration.* This part summarizes all available experimental investigations of the literature dedicated to laminar flame speed determination in both single and opposed jet reactive flows. A particular emphasis is set on each individual flame configuration to provide a global overview on important experimental parameters ruling the methodology (i.e. strain rate ranges, nozzle burner separation distances, etc.). Summaries can be found in Table II.2 and Table II.3.
- *The presentation of specific issues related to the laminar flame speed determination in the stagnation flow configuration.* Long standing issues concerning the choice of a reference plane for strained flame speed evaluation as well as influence of nozzle burner separation distances on flame velocity measurements are reviewed. Experimental investigations using stagnation plate setups and the recent stagnation-to-conical flame transition methodology are addressed.

II.2 On the Importance of Particle Motion in Seeded Fluids for Velocimetry Diagnostics

II.2.1 Formulation of the General Equation of Motion of Seeding Particles in Viscous Fluids

The formulation of the equation of motion of a spherical particle in a stationary viscous fluid of infinite extent was first introduced by Basset in 1888 for a stagnant flow. For a moving fluid, the equation can be expressed as follow [33-36]:

$$\underbrace{\frac{\pi d_p^3}{6}\rho_p \frac{dv_p}{dt}}_{\substack{\textit{Particle accelerating}\\ \textit{force}}} = \underbrace{-3\pi\mu d_p\left(v_p - v_f\right)}_{\textit{Stokes drag force}} + \underbrace{\frac{\pi d_p^3}{6}\rho_f \frac{dv_f}{dt}}_{\substack{\textit{Pressure gradient}\\ \textit{force on fluid}}} \underbrace{-\frac{1}{2}\frac{\pi d_p^3}{6}\rho_f \frac{d\left(v_p - v_f\right)}{dt}}_{\substack{\textit{Fluid resistance to}\\ \textit{accelerating sphere}}} \underbrace{-\frac{3}{2} d_p^2 \sqrt{\pi\mu\rho_f} \int_{t_0}^{t} \frac{d\left(v_p - v_f\right)}{d\omega} \frac{d\omega}{\sqrt{(t-\omega)}}}_{\substack{\textit{Drag force associated with unsteady}\\ \textit{motion}\\ \textit{(``Basset history integral'')}}} \tag{II-1}$$

with d_p particle diameter, μ fluid dynamic viscosity, v velocity, ϱ density, t time, "*f*" and "*p*" subscripts corresponding to fluid and particle respectively. The first two terms represent the acceleration force and the viscous resistance according to Stokes law. The third term accounts for forces arising from fluid acceleration, creating a pressure gradient in the vicinity of the particle. The fourth term stands for the resistance of an inviscid fluid to the acceleration of a spherical particle. The last term represents the Basset history integral accounting for an additional resistance due to flow unsteadiness. It is worth to emphasize that combining terms 1, 3 and 4 yields a force balance describing the acceleration of a spherical particle whose mass is increased by an additional virtual mass corresponding to half the mass of the displaced fluid by the sphere. Extensive studies on the approximations involved in the formulation of the present equation yielded two necessary conditions to confirm (II-1) validity [33]:

$$\frac{\rho_f {d_p}^2}{\mu}\frac{\partial v_f}{\partial x} \ll 1 \qquad \text{(II-2)} \qquad\qquad \frac{v_f}{{d_p}^2}\frac{1}{\left(\frac{\partial^2 v_f}{\partial x^2}\right)} \gg 1 \qquad \text{(II-3)}$$

As conventional seeding powders for combustion environments have densities considerably higher than studied gas flows, terms containing the fluid density ϱ_f in equation (II-1) can be neglected. This leads to the following simplified formulation:

$$\frac{\pi d_p^3}{6}\rho_p\frac{dv_p}{dt} = -3\pi\mu d_p\left(v_p - v_f\right) \qquad \text{(II-4)}$$

However, equation (II-4) needs further modifications to accurately describe the motion of micron and submicron particles typically used in combustion experiments. Especially, the Stokes drag force formulation needs to be corrected. Additional forces acting on the particles, such as gravitational or phoretic forces should also be considered. These modifications are addressed below.

II.2.2 Stokes Drag Force

Formulation

The Stokes drag force arises from a difference in the particle and fluid instantaneous velocity. It is considered to apply when the particle Reynolds number Re_p is smaller than unity [36]:

$$Re_p = \frac{\rho_f d_p \left|v_p - v_f\right|}{\mu} \leq 1 \qquad \text{(II-5)}$$

For finite Reynolds numbers, the deviation from the Stokes drag law can be corrected using a Re_p dependant correction factor, as mentioned in ref. [37-38]. The Stokes drag formulation of equations (II-1) and (II-4) assumes a no-slip boundary condition for the fluid at the particle surface. This hypothesis is particularly correct for particle motions in liquid medium. However, this is no longer accurate for small particle displacements in gaseous medium, where a velocity discontinuity is observed at the surface of the moving particle. Therefore, a correction term is required to modify Stokes drag force F_{SD} expression [39]:

$$F_{SD} = \frac{-3\pi\mu d_p\left(v_p - v_f\right)}{C} \qquad \text{(II-6)}$$

with *C*, the Cunningham slip correction factor following the Knudsen-Weber form:

$$C = 1 + Kn\left[\alpha + \beta exp\left(\frac{-\gamma}{Kn}\right)\right] \qquad \text{(II-7)}$$

and

$$Kn = \frac{2\lambda}{d_p} \qquad \text{(II-8)}$$

α, *β* and *γ* are characteristic parameters depending on particle surface and gas specificities and are generally determined through experimentation [39]. *Kn* is the particle Knudsen number and *λ* is the mean free path of the gaseous molecules. *λ* is related to the fluid dynamic viscosity *μ* as follows:

$$\mu = \phi\, \rho_f\, \bar{c}\, \lambda \qquad \text{(II-9)}$$

with ϕ a dimensionless parameter given by the kinetic theory, typically 0.491 for the considered cases and $\bar{c}$ the mean velocity of the gas molecules.

It should be emphasized that accuracy of the slip correction detailed above clearly depends on *α*, *β* and *γ* parameters of the Cunningham correction factor. Using an improved Millikan apparatus, Allen and Raabe [39] measured slip correction factors for an extensive number of solid spherical particles yielding the following values for the Knudsen-Weber parameters:

$$\alpha = 1.142\ (\pm 0.0024), \quad \beta = 0.558\ (\pm 0.0024) \quad \text{and} \quad \gamma = 0.999\ (\pm 0.0212) \qquad \text{(II-10)}$$

Assuming a mean free path of 0.0673 μm for air at sea level and 23°C with viscosity of 183.245 micropoise, the investigated Knudsen numbers spanned a 0.03 to 7.2 range for particle diameters from 0.79 to 4.6 μm. This particle diameter range typically encompasses particle diameters of conventional powders used in combustion experiments, therefore expression (II-7) along with slip parameters (II-10) have been previously used in computational studies of seeded reactive flows (See for example ref. [38, 40-41]).

Application to the Stagnation Flow Case: Responsivity of Seeded Particles

An important matter in velocimetry related experiments is the choice of the particle tracers that will have to closely follow the flow. This is of prime importance in stagnation flow configurations where particles will be confronted to steep velocity gradients. Sung and coworkers proposed a convenient way to evaluate particle responsivities in such flows [35]. Equation (II-4) can further be expressed as:

$$m_p \frac{dv_p}{dt} = \frac{\left(v_f - v_p\right)}{B} \qquad \text{(II-11)}$$

With $m_p = \varrho_p \pi d_p^3/6$, particle mass and $B = \left(3\pi\mu d_p\right)^{-1}$, particle mobility. Making the assumption that v_f and v_p have the same order of magnitude, e.g. $v_f \approx v_p \gg \left(v_f - v_p\right)$, it can then be assumed that:

$$\frac{dv_p}{dt} \approx \frac{dv_f}{dt} = v_f \frac{dv_f}{dx} = v_f K \tag{II-12}$$

With $K = dv_f/dx$, the axially determined strain rate. Equation (II-11) becomes:

$$FVL\ (\%) = 100 \times m_p BK = 100 \times \frac{\left(v_f - v_p\right)}{v_f} \tag{II-13}$$

The non-dimensional Fractional Velocity Lag (*FVL*) of particles can be therefore easily evaluated knowing the characteristic strain rate of the seeded flow. For instance, micron-size zirconium particles (5.0 g.cm^{-3}) seeded in an isothermal air flow (300K) would lag the flow by about 1.2 % at K = 800 s^{-1} (See Table II.1), which is deemed acceptable for stagnation flow studies. Assuming a local fluid velocity of 1 m.s^{-1}, all calculated particle Reynolds numbers are considerably smaller than unity, confirming in turn the validity of using the Stokes drag forms (II-6) for the particle sizes and velocity lags discussed herein. However, this approach should be reconsidered for larger particles ($d_p \geq 5$ µm) and higher strain rates (K = 500-800 s^{-1}) for which hypothesis (II-12) ceases to be true (See values in parenthesis in the Table II.1).

Particle Diameter		K = 100 s^{-1}	K = 500 s^{-1}	K = 800 s^{-1}
0.3 µm	*FVL (%)*	0.01	0.07	0.11
	Re_p	2.60E-06	1.30E-05	2.08E-05
1 µm	*FVL (%)*	0.15	0.76	1.21
	Re_p	9.65E-05	4.82E-04	7.72E-04
5 µm	*FVL (%)*	3.78	(18.90)	(30.34)
	Re_p	1.21E-02	(6.03E-02)	(9.65E-02)

Table II.1 Fractional Velocity Lag (FVL) in % and corresponding particle Reynolds number Re_p (based on v_f = 1 m.s^{-1}) for various zirconium oxide particles seeded in an ambient air stream (300 K) for different strain rates K = 100, 500 and 800 s^{-1}. For values between parentheses, expression (II-12) has to be reconsidered.

II.2.3 Gravitational Force

The gravitational force F_G on each particle of the seeded flow is given by:

$$F_G = -m_p g \tag{II-14}$$

With $g = 9.81$ m.s^{-2}, the gravitational acceleration under normal gravity conditions. This quantity can generally be neglected in many practical situations [34, 42]. For instance, Egolfopoulos and Campbell [38] studied the influence of the gravitational force on Al_2O_3 spherical particles of different diameters, seeded in strained laminar premixed hydrogen/air flames. For an inlet velocity of 14 cm.s^{-1}, the gravitational force was found to have no major effect for particles under 5 μm. As recalled by Bergthorson and Dimotakis [41], seeded particles in laminar flames are subject to accelerations 10 to 1000 times larger than the gravitational acceleration. Therefore, classical micron and submicron particles used in combustion experiments are not expected to depart from the flow motion under normal gravity conditions.

In the case of a continuously accelerating flow and assuming that the particle velocity step response follows an exponential law (i.e. ϱ_p much larger than ϱ_f), a particle relaxation time τ_s can be defined [42]:

$$\tau_s = d_p^2 \frac{\rho_p}{18\mu} \tag{II-15}$$

This relaxation time is a useful indication of the particle tendency to reach the actual flow velocity value under gravity conditions. For a micron size zirconium oxide particle (5.0 g.cm^{-3}) seeded in an isothermal air flow (300 K), τ_s is about 15 μs.

II.2.4 Additional Forces

Various additional external forces have been mentioned in the literature to have an effect on particle motion and therefore create a deviation of seeded particles from the fluid motion. These are for instance electrostatic, centrifugal or acoustic forces [34]. Also, phoretic effects, including diffusiophoresis, photophoresis and thermophoresis should also be considered [43-44].

Among all of them, thermophoretic effects are of crucial importance for flame-related experiments implying velocity measurements. The steep temperature gradient, characteristic of the narrow thermal expansion zone of a flame, will give rise to a thermophoretic force, opposite to the temperature gradient. Depending on the flow direction, seeded particles will experience an acceleration or deceleration, and measured velocities will consequently be higher or lower than the actual flow velocity value.

The Thermophoretic Force

Formulation

The thermophoretic force acting on a spherical particle due to a temperature gradient ∇T in the near continuum limit ($Kn < 1$) was introduced by Brock [45]. A fitting formula, in accordance with a large number of experimental data and validated over a wide range of Knudsen number, was subsequently proposed by Talbot and coworkers [46]:

$$F_T = \frac{-6\pi\mu\eta d_p C_s \left(\frac{k_f}{k_p} + C_t Kn\right)\frac{\nabla T}{T_0}}{(1+3C_m Kn)\left(1+2\frac{k_f}{k_p}+2C_t Kn\right)} \tag{II-16}$$

With $\eta = \mu/\varrho_f$, kinematic viscosity, k, thermal conductivity, ∇T, temperature gradient in the gas, T_0, mean gas temperature in the vicinity of the particle, C_s, C_t and C_m constants with values equal to 1.17, 2.18 and 1.14 respectively. Expression (II-16) is a widely applied formulation even though practical investigations do not necessarily involved spherical particles. Theoretical investigations, however, suggest that non-spherical particles, such as spheroid [47], sphero-cylindrical [48] or bispherical [49] particles are likely to behave differently while subjected to the same temperature gradient. An excellent thorough review of theories associated with thermophoretic effects can be found in ref. [50] for additional details. Along with expression (II-16), one can define the "particle drift velocity" v_t induced by the thermophoretic force [44]:

$$v_t = -D_t\left(\frac{\nabla T}{T_0}\right) \tag{II-17}$$

With D_t, thermophoretic diffusivity. As recalled by Gomez and Rosner [44], the latter diffusivity plays an important role in many practical applications involving high temperature environments and dusty flows (high temperature gas filtration, turbine operations with ash-containing fuels, etc…) and also in fundamental investigations (deposition and combustion experiments).

Experimental and Numerical Evidences of Thermophoretic Effects for Laminar Non-premixed and Premixed Counterflow Flames

A crucial matter in the velocimetry-related experiments in reactive stagnation flows is to assess the importance of the induced thermophoretic velocity drift and ultimately correct measurements if needed. While most studies have readily neglected the phenomenon, only few investigations tried to evaluate the impact of thermophoresis on the particle velocities, they will be discussed in this section.

In 1993, Gomez and Rosner [44] used the counterflow diffusion flames as a benchmark approach to determine the thermophoretic diffusivity of TiO_2 particles. CH_4/O_2/inert diffusion flames were stabilized at very low strains close to the Gas Stagnation Plane (GSP). Particles moving towards this plane were gradually affected by the thermophoretic force due to the presence of the flame and eventually stopped in a Particle Stagnation Plane (PSP) for which the particle axial velocity and the thermophoretic velocity would exactly counterbalance each other. As a result, a particle-free zone could be observed on each side of the flame confirming the phase separation phenomenon. By measuring temperatures, thickness of the dust-free zones, measuring and computing the axial convective velocities at the PSP position, authors were able to calculate the thermophoretic diffusivity of TiO_2 particles. For N_2 diluted flame, it was found that the gaseous velocity in the PSP was 1.8 $cm.s^{-1}$ and the thermophoretic diffusivity 1.3 $cm^2.s^{-1}$, a value in excellent agreement with the classical kinetic theory. Interestingly, this value is expected to hold for a very large range of particle diameter (from 2 nm to 0.4 μm). Results obtained on

He-diluted flames, however, did not yield satisfactory results, presumably due to gas composition uncertainties and diffusiophoretic effects.

Further motivated by experimental evidences of velocity drifts, potentially due to thermophoretic effects, observed in the counterflow premixed nitrogen-diluted methane/air flame of Sung and Law [51] and the counterflow methane/air diffusion flame of Chelliah and coworkers [52], Sung et al. [35] numerically investigated the motion of seeding particles in the counterflow flames of ref. [51] (E.R.= 0.95, N_2/O_2=5). First neglecting thermophoretic effects, it was shown that, for highly strained flames (569 s^{-1}), particles with primary diameters larger than 2 µm would start to lag the flow ahead of the flame. Inclusion of thermophoretic effects at an intermediate strain (240 s^{-1}) demonstrated that if small particles (0.3 µm Al_2O_3) perfectly follow the flow in the upstream part of the velocity profile, a consequent lag was observed in the fast expanding region of the flame, somehow independent of the particle diameter. A maximum 15 $cm.s^{-1}$ discrepancy was found for both 0.3 and 5 µm particles at a fluid local velocity of about 60 $cm.s^{-1}$. LDV data of Sung and Law [51] were successfully modeled at moderate strains of 240 s^{-1} and 348 s^{-1}, therefore emphasizing on the non-negligible effects of thermophoresis in counterflow flame experiments. The authors suggested that biased measurements could be corrected if the thermophoretic drift velocity is known. Two different ways were proposed herein: i/ making a steady-state approximation on the particle motion equation yields an expression for the thermophoretic velocity that can be calculated thanks to the expression of the thermophoretic force and the Cunningham slip correction factor, ii/ v_t can be evaluated using expression (II-17) provided that the thermophoretic diffusivity of the particles is known. Applying Gomez and Rosner [44] diffusivity coefficient to their own case indicated that TiO_2 particles would reach a velocity 14 $cm.s^{-1}$ lower than the fluid velocity for the steepest temperature gradient within the flame region. The present investigation concluded that micron-size particles could be used in most stagnation flames studies of hydrocarbon/air mixtures, but LDV measurements should be limited to the flow region upstream of the preheat zone of the flame if thermophoretic effects are not accounted for.

Willing to extend previous observations of thermophoresis effects in counterflow flames, Sung and coworkers [40] experimentally and numerically studied flow and particle velocity profiles for different laminar premixed and diffusion methane flames. It was subsequently found that thermophoresis effects were stronger for laminar premixed flames (E.R. = 0.69 and 0.8) while strain was increased, i.e. for flames located very close to the stagnation plane. On the other hand, diffusion flames formed close to the stagnation surface presented peculiarities in velocity profiles with important discrepancies noticed in comparison with flow calculations. Especially, critically cases were achieved where LDV data could not be taken due to the lack of particles in a wide zone close to the stagnation plane. This particle-free zone coincides with earlier observations of Pandya and Weinberg [53] in ethylene/O_2/N_2 diffusion flames and of Kim and coworkers [54] in counterflow polymer diffusion flames. It has been used, as mentioned previously, by Gomez and Rosner [44] in their methodology of thermophoretic diffusivity determination.

This phenomenon clearly underlines the importance of thermophoretic effects in counterflow laminar diffusion flames and difficulties in obtaining reliable velocity profiles within the flame region.

Egolfopoulos and Campbell [38] conducted a detailed numerical study of dynamics and thermal response of Al_2O_3 particles seeded in hydrogen/air counterflow flames. A considerable improvement over preceding numerical investigations of seeded reacting flows [35, 40] is the inclusion of thermal coupling between the gas and solid phases, including conductive/convective heat exchange between phases as well as particle absorption, emission and radiation. The Stokes drag, gravitational and thermophoretic forces were also included in this approach. While 0.3-μm particles closely followed the flow in the hydrodynamic zone, it was found that they would substantially lag the flow (up to≈ 9 cm.s^{-1}) in the preheat zone of an H_2/air flame at an equivalence ratio of 0.25. However, a reverse trend was observed for larger particles (5 μm) that departed from the flow in the decelerating cold region due to inertia effects, but seemed to be less affected by thermophoretic effects in the vicinity of the flame. A careful analysis of the expression of the particle spatial velocity v_p revealed that inertia, leading to a larger difference between fluid and particle velocities for large particles, contributed to the increase of the drag in the fast expanding region of the flame. Consequently, thermophoresis effects were found to be preponderant for small particles and low particle velocities in the preheat zone of the flame which corroborates results established in ref. [35].

Recently, Bergthonson and Dimotakis [41] developed a particle streak velocimetry diagnostic that was applied to laminar strained flames stabilized against a stagnation plate. Particle motions were experimentally recorded and 1D modeling was performed including Stokes drag and thermophoretic effects, while gaseous phase simulation was performed with the Cantera software package [55]. Results obtained for various methane/air flames (E.R. = 0.7, 0.9, 1.3) indicated that measured velocity profiles, were, for all cases, largely overestimated by simulations of the fluid motion. Inclusion of thermophoretic effects were seen to have a noticeable influence on the velocity gradient in the fast accelerating region of the preheat zone of the flame, resulting in a better concordance with experimental data. However, consequent discrepancies still remained, particularly for lean flames for which velocity lags up to 35 cm.s^{-1} could be observed. This observation generally holds for complementary results available for ethane/air and ethylene/air flames in ref. [56].

On the Importance of Other Forces

Numerous external forces can be considered as mentioned above. However, their impact on particle motion can generally be neglected for the classical stagnation flow configuration. These are for instance:

- ✓ Electrostatic forces - For the typical concentration of seeding material in velocimetry related experiment, direct electrostatic interaction between particles can be neglected, the importance of electrostatic forces being largely encompassed by gravitational forces [34].
- ✓ Centrifugal forces - They should be only considered in the case of strong rotating vortex for which body forces can influence particle motion: for example, 2 μm seeding particles were deemed

unacceptable for a 9000 rpm air vortex [34]. These conditions are of course not met in common stagnation flame configurations.

- ✓ Acoustic forces - Acoustic fields can have an impact on particle motion and their coagulation rate at substantially high levels of perturbations (140-150 dB) [34] that are not relevant to applications discussed herein.
- ✓ Other Phoretics effects including:
  - ▪ Electrophoresis - It corresponds to an additional force acting on charged particles in presence of an external electrostatic field and is not likely to apply, as explained in ref. [44].
  - ▪ Photophoresis - This phenomenon induces a particle drift due to impact of gas molecules on a particle receiving asymmetric radiative heating. It has also been shown to have negligible effects on particle motion [44].
  - ▪ Diffusiophoresis - A particle seeded in an isothermal gaseous flow will tend to drift relative to the mean mass motion of the mixture at a so-called diffusiophoretic velocity [44]. If this effect was found to be negligible for N_2-diluted diffusion flames, the diffusiophoretic velocity was found to be on the order of the thermophoretic velocity for He-diluted flames studied in ref. [44]. In Egolfopoulos and Campbell study of lean laminar premixed flames [38], trial calculations, bases on ref. [44] assumptions, yielded diffusiophoretic velocities on the order of 1.4 $cm.s^{-1}$ and 0.4 $cm.s^{-1}$ for hydrogen/air flames at an equivalence ratio of 0.57 and 0.25 respectively. These drifts were considered as minor in comparison to other velocities and diffusiophoretic effects were not considered in the rest of the study.

II.3 Laminar Flame Speed Determination over the Years

II.3.1 Laser Doppler Velocimetry (LDV) Investigations

The stagnation flow experiment for laminar flame velocity measurements was first introduced in 1984 by Wu and Law [23]. Laminar premixed flame of different hydrocarbon-air mixtures were formed using a contraction nozzle impinging on a water-cooled brass plate. Extracted velocity profiles at the centerline of the flames suggested that the first local minimum could represent the beginning of the preheat zone with a good degree of approximation, particularly for the lower strain cases. Therefore, unburned upstream velocity values could be clearly characterized along with their associated strain rates defined as the negative slopes of the potential flow-like part of the centerline velocity profiles. As suggested by previous theoretical studies, linear dependence of the reference velocity with the strain rate was revealed for methane, propane, butane, and hydrogen-air mixtures. It was consequently proposed to linearly extrapolate the observed trends to the 0-strain case, yielding by definition the one-dimensional unstrained flame velocities. This methodology was applied to methane and hydrogen-air mixtures to successfully determine laminar flame velocities for a wide range of equivalence ratios. Non-unity Lewis number effects were also mentioned and characterized for several propane and butane-air mixtures, confirming enhancement and decrease of the burning intensity for mixtures with respectively $Le < 1$ and

Le >1. Further investigations confirmed that the nature of the stagnation surface, either created by an opposite cold jet (air or nitrogen) or a similar reactive jet, did not have an influence on the extracted reference velocities. According to the authors, boundary layer effects could be neglected for flames stabilized far from the stagnation plate, as shown in their previous works [57]. Although slightly dished-shaped flames were obtained away from the stagnation surface, flames were deemed acceptable for study provided that the center portion was planar and perpendicular to the centerline stream tube.

The aforementioned technique was further employed by Yu and coworkers [58] for the determination of methane and propane-air flame including addition of small amounts of hydrogen. The experimental set-up was modified using a counterflow twin flame system therefore eliminating any potential downstream heat losses that could arise while using a solid stagnation plate. Nitrogen shrouds surrounding the main reactive flows were added and found to significantly improve the flame stability, particularly for rich flames prone to external disturbances. The linear dependence of the reference velocity with the strain rate was confirmed for various methane-air mixtures including equivalence ratio ranging from 0.59 to 1.36 and strain rates up to 330 s^{-1}. The validity of the linear extrapolation methodology was further assessed calculating a nondimensionnal strain rate parameter for typical mixtures used in their experiment. This parameter, later known as the Karlovitz number, was found to be on the order of 0.1 implying that involved strain rates were sufficiently low for the linear extrapolation to be used accurately in accordance with theoretical developments of Matalon and Matkovskii [59]. The authors even emphasize on the fact that linearity seems to hold even for Karlovitz numbers on the order of 1, suggesting an extension of the validity of previous analytical works.

In 1986, Law and coworkers reiterated their experimental studies on methane and propane-air premixed mixtures, complemented with extinction stretch rate determinations [60]. The same counterflow twin flame set-up and methodology were used to obtain fundamental flame velocities along with flame velocities at the state of extinction. Large strain rates (≈1500 s^{-1}) were achieved for strongly burning flames close to stoichiometry, with $Ka < 1$ for all cases. Linear evolutions of the reference velocities with strain were confirmed for all mixtures except for strongly stretched near-stoichiometric flames with a Lewis number (*Le*) lower than 1. However, they did only exhibit a monotonic increase with strain which did not conform with theoretical analysis mentioned by the authors [59, 61], predicting opposite trends for Lewis number mixture values departing from unity. According to Law and coworkers, it was not clear why such a contradiction occurred.

The counterflow twin flame setup was further used by Zhu and coworkers [62] for the determination of laminar flame velocities of methane/(Ar, N_2, CO_2)-Air mixtures. This investigation essentially aimed at providing accurate data in order to validate selected C_1 and C_2 kinetic mechanisms. Three independent parameters were chosen: the mixture equivalence ratio, the pressure and flame adiabatic temperature. The latter was tuned by substituting various amount of nitrogen present in the air by argon or carbon dioxide. The counterflow burners were housed in a continuously ventilated stainless steel chamber where ignition was achieved using high energy sparks. The "classical" methodology was applied with reported uncertainties on the order of ± 1.5 cm.s^{-1} for flame velocity measurements and ±0.01 for the equivalence ratio, which constitute, according to the authors, an improvement over precedent reported data. A similar investigation was led by Egolfopoulos and coworkers [63] for methane/air flames for pressures up to 3 atmospheres, yielding comparisons with numerical predictions obtained with various kinetic mechanisms developed for C_1 and C_2 combustion.

Further motivated by large scatters in hydrogen/air flame velocity measurements, a consequent lack of data for ultra-lean mixtures, and consequently, an important need for validation of related mechanisms, Egolfopoulos and Law [64] investigated laminar flame velocities of hydrogen/air mixtures with the oxygen molar concentration in (O_2+N_2) varied from 7.4 to 30 %, and equivalence ratio ranging from 0.153 to 2.2. Suppression of cellular instabilities due to positive stretched was confirmed for all stabilized flames, including very lean mixtures close to flammability limits. Reported accuracy of LDV measurements were on the order of 1 to 2 cm.s^{-1} for the lowest flames (<60 cm.s^{-1}), up to 10 cm.s^{-1} for the fastest (> 170 cm.s^{-1}). Experimental data were confronted to various kinetic scheme predictions with final conclusions emphasizing on the importance of H_2O_2 and HO_2 chemistry for weakly burning flames and higher pressure conditions. Similar investigations by the same authors can be found in [65] for ethane, ethylene, and acetylene flames with oxygen and nitrogen. All reported flame velocity data were mentioned to be reproducible and accuracy of measurements yielding 1-2 cm.s^{-1} for the slowest flames (< 50 cm.s^{-1}) to 2-5 cm.s^{-1} for the fastest (> 70 cm.s^{-1}).

Laminar flame velocities of liquid fuels in the counterflow configuration were first reported by Egolfopoulos et al. in 1992 for methanol/air [66] and ethanol/air [67] mixtures. Both studies aimed at developing comprehensive oxidation mechanisms for methanol and ethanol combustion, with validation of numerical models against a large amount of data obtained for burner-stabilized flames, flow reactors and shock tubes. These investigations required modifications of the original counterflow setup with the inclusion of a continuous-flow evaporator, achieved thanks to liquid fuel impingement on a hot plate. Electrically-heated gas delivery lines along with heating of the burner inner surface with a surrounding hot water jacket were provided. Adiabatic flame velocities were obtained through the usual linear extrapolation to zero strain, although some theoretical studies, for instance ref. [68], indicated overestimation of the adiabatic flame velocity through the conventional methodology. Since any systematic study on non-linear effects at low strain rates was available at the time and discrepancies mentioned to be less than 5 to 10 %, the authors confirmed with confidence the accuracy of their measurements.

An experimental investigation of laminar flame velocities of methane and methyl chloride with air was initiated by Yang and Puri [69] in 1993. Their counterflow burner consisted of two facing straight ducts with nitrogen shrouds. The upper burner was equipped with a water-cooled jacket to decrease the hot product temperature prior to ventilation from the building. Strained and fundamental flame velocity values were extracted using the conventional methodology established by Law and coworkers [23, 58]. Reported uncertainty on extrapolated flame velocities was on the order of 10 % for the slowest flames and 5 % for the fastest. Pure methyl chloride-air mixtures were shown to be extremely sensitive to straining, with low strain rates at extinction, resulting in a very limited number of data points for the extrapolation plots.

Laminar flame velocities and extinction strain rates of carbon monoxide-air mixtures with hydrogen and methane additions were investigated by Vagelopoulos and Egolfopoulos in 1994 [70]. Aware of finite domain effects leading to over predictions of true laminar flame velocities and further comforted by their parametric study on the influence of the nozzle separation distance on flame velocity determination in the counterflow configuration [71], laminar flame velocities were extracted using a nozzle separation distance of 22 mm. According to the authors, considerable efforts were involved to reach the lowest possible strain rates in order to ensure the most accurate linear extrapolations. The present study concluded on the importance of the CO oxidation reaction when traces of hydrogen or methane were added, while the chemistry seemed to shift to the additives kinetics when large amounts were added.

An extensive investigation of laminar flame velocities of various C_1 to C_8 hydrocarbons/air mixtures was led by Davis and coworkers in the counterflow configuration. The following hydrocarbons were considered: benzene and toluene [72-73], iso-octane and n-heptane [74], propyne [75], propene [76], n-butane, iso-butane, 1-butene, iso-butene, 1,3-butadiene, n-pentane, cyclopentane, n-hexane, cyclohexane [73]. Laminar flame velocities were determined for a wide range of equivalence ratios (0.7 to 1.7 for almost all mixtures) at room temperature and atmospheric pressure. In order to minimize linear extrapolation errors, 14 mm I.D. nozzles were used with a 16.1 mm nozzle separation distance for all cases. A detailed comparison of extrapolated velocity values between linear and non-linear methodologies was performed using Tien and Matalon non-linear formulation [68]. Non-linear results were shown to be generally 1 to 2 cm.s^{-1} lower than linearly extrapolated ones, with the maximum decay of 3 cm.s^{-1} for the rich weakly-burning mixtures. Associated Karlovitz numbers could not be maintained close to 0.1 for these mixtures and reached values on the order of 0.2 to 0.3. Furthermore, the non-linear flame behavior was not observed experimentally due to a lack of data points at very low strain rates. As the non-linear approach only relied on theoretical considerations and that the apparent extent of deviation between both methodologies was on the order of experimental uncertainties, the linear approach was here favored. Discrepancies up to 10-15 cm.s^{-1} could be found between stretch-compensated results of the present study and former investigations on various configurations (for instance Bunsen flames), therefore emphasizing on the importance of strain, non-adiabaticity and non equidiffusion effects while measuring flame velocities. Details of the experimental apparatus and compilation of the aforementioned results can be found in [77].

Laminar flame velocities of methanol, ethanol, n-heptane and iso-octane with air have been reported by Wang and Wang [78] in the stagnation plate configuration similar to that of Wu and Law [23]. Strain rates from 100 to 300 s^{-1} were achieved for mixture equivalence ratios between 0.7 and 1.4 and unburned reactant temperatures from 323 to 413 K. As only natural cooling of the plate was involved, the authors considered that the downstream heat losses were negligible and that the subsequent flame velocity extractions were done under adiabatic conditions. Velocity measurement accuracy of the LDA system was carefully checked using a motor driven rotational disc and estimated to be on the order of ±0.3 % for the

0.4 to 2 m.s^{-1} velocity range. In 1998, the same author [79] investigated laminar burning velocities and extinction stretch rates of benzene/air mixtures using the counterflow technique. Strain rates could be varied between 150 and 350 s^{-1} for mixture initial temperatures between 348 and 398 K. Mixtures strain sensitivities were in accordance with the theoretical Lewis number interpretations, especially for very rich or ultra lean mixtures, where reference velocities displayed a marked increase or decrease with the strain rate respectively. It was also reported that reference velocities were quite insensitive to strain for near stoichiometric mixtures. The standard deviation of the linear extrapolation used in the present study was on the order of 1%, with Karlovitz numbers ranging from 0.02 to 0.08. Non-linear extrapolation procedures were not attempted as a large nozzle separation distance was used (18mm). Laminar flame velocities extracted from the upper flame of the twin flame system were shown to be slightly higher (4%) than those extracted from the lower one, therefore underlining the importance of buoyancy effects on this specific flame configuration. Further attention has been devoted to the characterization of downstream heat loss impact on the laminar flame velocity, by replacing the upper counterflowing jet by a cold nitrogen or air flow. In almost all cases, resulting flame velocities were found to be lower, with a maximum discrepancy of about 6 cm.s^{-1}, clearly suggesting that downstream heat losses involved had a marked influence on the flame propagation.

Due to their potential use for fire suppression purposes and the consequent lack of unbiased experimental data for kinetic mechanism developments, laminar flame velocities of chlorinated and fluorinated hydrocarbon mixtures were studied more recently in the counterflow twin flame configuration. This investigations included mixtures such as: chloromethane [80], dichloromethane and trichloromethane [81], tetrachloromethane [82], trifluoromethane [83], all blended with methane and air (with extra diluents), and hydrogen/chlorine/nitrogen blends [84]. Important modifications of the classical counterflow setup were provided so as to minimize hydrogen chloride impact on the environment. This included, for instance, a new burner fiberglass housing, a gas scrubber and an acid neutralizer system. All reported laminar flame velocities mentioned herein were obtained through linear extrapolation to the zero strain rate state, being systematically higher than non-linearly extrapolated values by 1 to 3 cm.s^{-1}. Reported strain rates achieved for the trifluoromethane-methane mixtures were typically between 200 and 450 s^{-1} for strong flames and 100 to 250 s^{-1} for weaker flames. Experimental results essentially contributed to the improvement of existing kinetic mechanisms and comprehension of the chlorinated and fluorinated mixture oxidation main steps.

More recently, Natarajan and coworkers [85-86] investigated lean hydrogen/carbon monoxide/carbon dioxide/nitrogen and air mixtures (syngas mixtures) laminar flame velocities for high pressure and high reactant preheat conditions. The Bunsen flame approach was chosen for these measurements while a limited number of data points was obtained using the stagnation plate flame configuration with the LDV diagnostics. The latter setup consisted of nozzle of different I.D. (6.25 to 12.5 mm) impinging on a rounded stainless steel plug mentioned to consequently improve the flame stability for the highest velocity conditions (higher reactant preheat temperature and high hydrogen content mixtures). However, development of vortex shedding at the periphery of the diverging jet could not be avoided for these conditions which consequently worsen flames steadiness. Therefore, an alternative approach was to stabilize button-shaped flames by totally cutting off the nitrogen shroud for the high preheat reactant cases. Wall stagnation flame results were essentially analyzed in term of strain sensitivities of the different mixtures, which all displayed a velocity increase with strain, the leanest mixtures being systematically the most strain-sensitive. Reported strained flame velocities were overall in very high strain rate ranges, typically from 1000 to 10000 s^{-1}. The agreement of linearly extrapolated velocity values with the Bunsen flame ones was somehow mitigated. For instance, while a very good agreement was found within 3 % for lean $H_2/CO/CO_2$ (40/40/20 %) mixtures at ambient temperature and atmospheric pressure, differences up to 20 % were mentioned for lean 50/50 % H_2/CO mixtures at 1 atmosphere and 700 K preheat temperature. Related Karlovitz numbers were however not mentioned for the present study which does not allow any conclusion on the legitimacy of the linear extrapolation methodology. Numerical simulations using the Chemkin OPPDIF code [28] were performed for nitrogen diluted hydrogen/air flames (700K preheat temperature, equivalence ratio: 0.8) in the counterflow and stagnation wall configuration respectively. They confirmed that heat losses at the stagnation wall did not alter the value of the flame velocity at the reference location prescribed by the classical methodology, even for flames located within two flame thicknesses from the solid wall. The reference velocity was found to be quite insensitive to the inlet nozzle boundary conditions, the potential and plug flow approaches leading to a 2 % difference for velocities calculated within the 1000-3500 s^{-1} strain rate range. Discrepancies up to 10 % were reported between 1D flame velocities calculated with the Chemkin PREMIX code [27] and linearly extrapolated velocities from OPPDIF calculations. According to the authors, this difference would be due to the arbitrary definition of the unburned reference flame velocity location. Additional details on the present experimental works can be found in ref. [87-88].

Authors Year	**Conf.**	**Mixtures**	**T [K]**	**P [atm]**	**L/D**	**Nozzle Diameter D [mm]**	**Seeded Particles**	**Ref.**
Wu and Law 1984	SP (Brass)	CH_4/Air H_2/Air	Amb.	1	Close to 2	40, 30, 20, 10, 7, 5	1 µm MgO	[23]
Yu et al. 1986	CTF	CH_4/Air (+H_2) C_3H_8/Air (+H_2)	Amb.	1	About 1	30, 20, 14, 10	1 µm MgO	[58]
Law et al. 1986	CTF	CH_4/Air C_3H_8/Air	Amb.	1	About 1	30 to 7	1 µm MgO	[60]
Zhu et al. 1988	CTF	CH_4/(Ar, N_2, CO_2)-Air	Amb.	0.25 to 2	×	14, 10, 7	0.3 µm Al_2O_3	[62]
Egolfopoulos et al. - 1989	CTF	CH_4/Air	Amb.	0.25 to 3	×	7 and 14	0.3 µm Al_2O_3	[63]
Egolfopoulos and Law - 1990	CTF	$H_2/O_2/N_2$	Amb.	0.2 to 2.25	×	23, 14, 12, 10, 7, 5	×	[64]
Egolfopoulos et al. - 1990	CTF	C_2H_6, C_2H_4, C_2H_2, C_3H_8 /Air	Amb.	0.25 to 3	×	×	×	[65]

Egolfopoulos et al. - 1992	CTF	CH_3OH/Air	318 to 368	1	×	×	×	[66]
Egolfopoulos et al. - 1992	CTF	C_2H_5OH/Air	363 to 453	1	×	×	×	[67]
Yang and Puri 1993	CTF	CH_4/CH_3Cl/Air CH_3Cl/Air	Amb.	1	0.55	25.4 (Straight ducts)	1-5 µm MgO	[69]
Vagelopoulos and Egol. - 1994	CTF	$CO/H_2/CH_4$ /Air	Amb.	1	× L=22mm	×	×	[70]
Vagelopoulos et al - 1994	CTF	H_2/Air [Lean] CH_4/Air C_3H_8 /Air	Amb.	1	1 L=22mm	×	×	[71]
Vagelopoulos and Egol. - 1998	SP (Tran. Meth.)	CH_4/Air, C_2H_6/Air, C_3H_8/Air	Amb.	1	1.5-2.5	14, 22, 30	×	[89]
Davis et al. 1996	CTF	C_6H_6 /Air $C_6H_5CH_3$ /Air	Amb.	1	×	×	×	[72]
Davis and Law 1998	CTF	iso-Octane, C_8H_{18} n-Heptane, C_7H_{16} +Air	Amb.	1	×	×	×	[74]
Davis et al. 1998	CTF	C_3H_4 /Air	Amb.	1	×	×	×	[75]
Davis and Law 1998	CTF	Benzene, C_6H_6 Toluene, $C_6H_5CH_3$ n-Butane, C_4H_{10} iso-Butane, C_4H_{10} 1-Butene, C_4H_8 iso-Butene, C_4H_8 1,3-Butadiene, C_4H_6 n-Pentane, C_5H_{12} Cyclopentane, C_5H_{10} n-Hexane, C_6H_{14} Cyclohexane, C_6H_{12} +Air	Amb.	1	1.15	14	0.3 µm Al_2O_3	[73]
Davis et al. 1999	CTF	C_3H_6 /Air	Amb.	1	×	×	×	[76]
Wang and Wang 1997	SP	Methanol, CH_3OH Ethanol, C_2H_5OH iso-Octane, C_8H_{18} n-Heptane, C_7H_{16} +Air	323 to 413	1	×	18	0.1-1 µm MgO	[78]
Wang et al. 1998	CTF	Benzene, C_6H_6 +Air	348 to 398	1	1	18	0.1-1 µm MgO	[79]
Wang et al. 1996	CTF	CH_3Cl+CH_4/Air	Amb.	1	1	25	0.3 µm Al_2O_3	[80]

Leylegian et al. 1998	CTF	CH_2Cl_2 $CHCl_3$ + CH_4/Air	Amb.	1	1	13.4 (Straight ducts)	0.3 μm Al_2O_3	[81]
Leylegian et al. 1998	CTF	CCl_4+CH_4/Air	Amb.	1	1	13.4 (Straight ducts)	0.3 μm Al_2O_3	[82]
Saso et al. 1998	CTF	CHF_3+CH_4+O_2 +diluents (N_2 , Ar)	Amb.	1	1	14	0.3 μm Al_2O_3	[83]
Leylegian et al. 2005	CTF	H_2/Cl_2/N_2	Amb.	1	×	×	×	[84]
Natarajan et al. 2007	SP	H_2/CO/CO_2/Air	Up to 700	1 to 5	1 to 2	6.25, 9, 12.5	1-2 μm Al_2O_3	[85-88]

Table II.2 Summary of experimental investigations of laminar flame speeds in stagnation flames using the LDV diagnostic (Conf.: Configuration, T: Temperature, P: Pressure, L: Distance between nozzles or twice the burner-to-stagnation plate distance, D: Burner diameter, Ref.: References. In "Conf.": SP = Stagnation Plate, CTF = Counterflow Flames, Tran. Meth. = Transition Methodology. "×": not mentioned).

II.3.2 Particle Image Velocimetry (PIV) Investigations

The use of Digital Particle Image Velocimetry (DPIV) for laminar flame velocity determination in the counterflow configuration was first introduced by Hirasawa and coworkers in 2002 for binary fuel blends, including ethylene, n-butane and toluene [90-91]. According to the authors, the advantage of using DPIV over the classical LDV diagnostics is twofold: (a) the complete mapping of the two-dimensional flow is less time-consuming than point-based laser diagnostics, (b) the positioning accuracy is increased as no translation of the measurement probe is needed, therefore ensuring an optimal extraction of the reference velocity and its associated strain rate. The experimental setup was identical to the aforementioned experiments: two nitrogen-shrouded convergent nozzle burners were used to create the counterflow premixed twin flames. The flow was seeded with droplets of liquid silicone with a boiling point above 570K, indicating that seeded particles would not survive in the post flame region. Interestingly, axial velocity profiles presented herein showed a consequent lack of data after the reference velocity, suggesting an early depletion of seeded droplets due to vaporization in the preheat zone. However, liquid particles were mentioned not to clog or pollute the burners, which represented an important improvement over preceding studies using solid particles. A detailed analysis of the measurement accuracy of the extracted reference velocities was performed and found to be in the range of 0.83 to 1.16 %. Strain rates were unambiguously determined from radial velocity gradient of the tangential velocities taken at the point of reference, showing an evident linear trend compared to the conventional calculated strain rates in the axial direction. Fundamental flame velocities were subsequently determined using linear [91] and non-linear [90] extrapolation procedures. Typical ranges of strain rates achieved for ethylene/air flames yielded 100 to 150 s^{-1} with maximal relative deviations in the reference velocities and strain rates of 1.3 and 1.7 % respectively, therefore indicating a good degree of steadiness for the stabilized flames. Reported measurements compared fairly well with existing LDV experimental data, and therefore provided a reasonable validation for the DPIV approach. The same counterflow setup was further used in 2005 by Ibarreta et al. [92-93] for burning velocity measurements of ethylene/air sooting flames. It was found that the appearance of the soot layer clearly depended on the mixture equivalence ratio and applied strain rates. Critically cases were reached for higher equivalence ratios (>2.4) for which, for all strain rates, twin flames would merge together, going eventually unstable at lower strain rates, rendering the extrapolation procedure impossible. Authors concluded that the counterflow twin flame configuration was not suitable for flame velocity measurements of highly sooting flames.

Dong and coworkers [94] conducted experiments in the stagnation flow configuration using the planar to Bunsen flame transition methodology of Vagelopoulos and Egolfopoulos [89] with the DPIV diagnostic. Laminar flame velocities of methane and ethane with hydrogen, oxygen, nitrogen and helium additions were measured just before the state of transition. Associated Karlovitz numbers being less than 8.0×10^{-3} s^{-1}, extracted reference velocities were considered as the true fundamental flame velocities, without any further extrapolation procedure. Strain rates were directly derived from the gradient of the tangential velocity profile along the flame surface, a definition somehow different from the investigation of Hirasawa et al. [90-91] where a factor of 2 was mentioned to equate the axially determined strain rate. However, due to the extremely low strain rates reported, it is not clear whether this factor was included or not, although the authors are quoting Hirasawa and coworkers [91] for the strain determination methodology. Data for methane/air flames were in close agreement with measurement performed by Vagelopoulos and Egolfopoulos [89] on the same experimental setup, although slightly higher on the rich branch.

Laminar flame velocities of primary reference fuels (n-heptane and iso-octane blends) with additions of first stage reformer gas ($H_2/CO/N_2$, 28/25/47 % by volume) were studied by Huang and coworkers [95-99]. The main features of the present experiment including burner setup, PIV diagnostic and data analysis are similar to those mentioned in ref. [90-91]. Stability of the studied flames was once again demonstrated with a relative deviation of strain rates under 1.4% while that of the reference flame speeds was no more than 2%. In most cases, related Karlovitz number were kept under 0.1 with differences of linearly and non-linearly extrapolated velocity values on the order of 1-2 cm s^{-1}. Strain rate spans mentioned for iso-octane/air flames are typically 200-600 s^{-1} for rich flames (*E.R.* = 1.4), and 80-130 s^{-1} for lean flames (*E.R.* = 0.7). Errors related to extrapolation procedures were studied in detail and it was shown that if the number of data points was greater than 100, the uncertainty of the extrapolated value was around 2% with a 95% confidence interval. Effects of seeding particle concentration were also investigated for three different particle mass loadings, respectively corresponding to 6.3, 9.9 and 16.8 particles per subregion. No noticeable difference was obtained between the different mass loading cases, and experiments were consequently run for a number of particles around 10 per interrogation spot. Similar measurements were performed by Freeh and coworkers [100] on preheated iso-octane/air and n-decane/air at atmospheric pressure. The aforementioned setup [96] was modified to accommodate a secure mixture preheating system. For most conditions mentioned for iso-octane/air mixtures, *Ka* was kept under 0.08 with a maximum discrepancy between linear and non-linear procedures around 2 cm.s^{-1}.

Zhao and coworkers used the single jet stagnation flame configuration to determine laminar flame velocities of several mixtures including dimethyl ether/air [101-102], propane/air [103] and n-decane/air [104]. Their experimental setup included a silica foam stagnation plate, chosen for its low heat conductivity and capacity, located far downstream from the burner exit (25 mm). A PIV diagnostic along with an autocorrelation processing code were used to extract reference velocities and their associated axially determined strain rates, following the classical methodology. All laminar flame speeds reported herein were based on linear extrapolation methodologies. Typical reported uncertainties for propane/air mixtures were on the order of ± 1.25 % for raw velocity data, and 5 % for extrapolated velocity values. A detailed analysis of the conventional linear extrapolation method and its associated uncertainty was proposed and it was shown that uncertainty of extrapolated values could be decreased following 3 general ways: 1/ increase the number of data points taken, 2/ increase the quality of measurements, in other words, decrease the individual standard deviation of each point, 3/ get the lowest possible strained data. As such, for a lowest strain achieved at 100 s^{-1}, a 2.5 % standard deviation in the raw data and 16 points, a laminar flame speed uncertainty of 2.8 % was obtained. It was subsequently shown that the uncertainty of the extrapolated velocity value is always larger than uncertainties of individual measurements. A similar attempt to determine Markstein length uncertainty in the aforementioned conditions yielded a 27.1 % deviation, a value somehow much larger than extrapolated velocity ones, which largely explained the important scatter of Markstein lengths available in the literature. Results discussed in this series of experimental works are compiled in ref. [105].

Recently, Kumar and coworkers studied laminar flame speeds of various mixtures including: iso-octane/O_2/N_2 and n-heptane/O_2/N_2 [106], n-decane/O_2/N_2 and n-dodecane/O_2/N_2 [107-108] and ethylene/O_2/N_2 [109-110]. The experimental set-up, DPIV features and methodologies were essentially identical to those previously mentioned in ref. [95-99]. Again, discrepancies found between linear and non-linear extrapolation yielded 1 to 3 cm.s^{-1}. All stabilized flames had a corresponding Karlovitz number being less than 0.1 apart from lean equivalence ratios of ethylene mixtures reaching *Ka* numbers around 0.15-0.21. Non equidiffusion effects are here clearly illustrated for lean n-heptane and iso-octane mixtures (E.R.= 0.7, ref. [106]) and lean n-decane (E.R. = 0.8, ref. [107]) mixtures with strain sensitivities in adequacy with associated Lewis numbers inferior to unity. Experimental works of Kumar are gathered in ref. [111].

Authors Year	Conf.	Mixtures	T [K] P [atm]	L/D D [mm]	Seeded Particles	DPIV C. Type I.C.S. [Pixel] S.R. [μm]	Ref.
Hirasawa et al. 2002	CTF	Ethylene, C_2H_4 n-Butane, C_4H_{10} Toluene, $C_6H_5CH_3$ +Air	Amb. 1	1.14 10.5	0.3-0.5 μm Silicone fluid particles	Cross.C. 32×32 188	[90-91]
Dong et al. 2002	SP	CH_4, C_2H_6 + H_2,O_2,N_2 and He	Amb. 1	1.5 14, 22, 35	1-5 μm Al_2O_3	Cross.C. × 500-1000	[94]
Huang et al. 2004	CTF	n-Heptane, C_7H_{16} iso-Octane, C_8H_{18} +H_2/CO/N_2 (Blends)	Amb. 1	1.14 10.5	0.5-1.1 μm Silicone fluid particles	Cross.C. 32×32 188	[95-99]
Freeh et al. 2004	CTF	iso-Octane, C_8H_{18} n-Decane, $C_{10}H_{22}$ +Air	323-400 1	× ×	Up to 2 μm Silicone fluid particles	× × ×	[100]
Zhao et al. 2004	SP	DME, CH_3OCH_3 +Air	Amb. 1	1.79 14	0.3-1.1 μm BN (Boron Nitride)	Auto C. 64×64 ×	[101-102]
Zhao et al. 2004	SP	Propane, C_3H_8 +Air	Amb., 500, 600 1	1.79 14	0.3-1.1 μm BN (Boron Nitride)	Auto C. 64×64 ×	[103]
Zhao et al. 2005	SP	n-Decane, $C_{10}H_{22}$ +Air	500 1	× 14	0.3-1.1 μm BN (Boron Nitride)	Auto C. 64×64 ×	[104]
Ibarreta et al. 2005	CTF	Ethylene, C_2H_4 +Air (Sooting)	Amb. 1	1.14 10.5	×	× × ×	[92-93]
Kumar et al. 2007	CTF	iso-Octane, C_8H_{18} n-Heptane, C_7H_{16} +O_2/N_2	Amb., 360,400, 470 1	1 13	Up to 2 μm Silicone fluid particles	Cross.C. 32×32 144	[106]
Kumar et al. 2007	CTF	n-Decane, $C_{10}H_{22}$ n-Dodecane, $C_{12}H_{26}$ +Air	360-470 1	1 13	Up to 2 μm Silicone fluid particles	Cross.C. 32×32 ×	[107-108]
Kumar et al. 2007	CTF	Ethylene, C_2H_4 +O_2/N_2	298-470 1	1 13	Silicone fluid particles	× × ×	[109-110]

Table II.3 Summary of experimental investigations of laminar flame speeds in stagnation flames using the PIV diagnostic (Conf.: Configuration, T: Temperature, P: Pressure, L: Distance between nozzles or twice the burner-to-stagnation plate distance, D: Burner Diameter, C. Type: Correlation Type, I.C.S.: Interrogation Cell Size, S.R.: Spatial Resolution, Ref.: References. In “Conf.”: CTF = Counterflow Flames, SP = Stagnation Plate. “×”: not mentioned).

II.4 About the Methodology: Towards Optimization and Improvements

II.4.1 Choice of the Reference Velocity for Laminar Flame Speed Determination and Necessity of Non-Linear Extrapolation Methodologies

An important issue in laminar flame speed determination studies is the choice of the relevant location at which flame related parameters have to be extracted. For experimental investigations, this location is fixed according to remarkable points that are easily identified on measured quantities: for instance, the first minimum of the axial velocity profile in the counterflow flames has been selected by Wu and Law [23] and widely used in similar studies as detailed above. This is however not compulsory and other choices have been done in the past.

Daneshyar and coworkers [112] experimentally defined the reference flame velocity by linearly extrapolating the axial velocity profile in the hydrodynamic zone to a plane corresponding to the maximum of the velocity profile, or alternatively in ref. [113], by rescaling this maximum velocity thanks to the burned to unburned temperature ratio. According to the latter definition, their theoretical study [113] showed that strain fields could affect the flame by reducing its burning velocity and eventually reach the flame extinction state. A flame speed increase was not observed for mixtures with Lewis numbers under unity, and it was seen that the Lewis number would only affect the rate of the velocity decrease. However, the temperature in the plane of reference was found to increase or decrease for $Le<1$ or $Le>1$ respectively. By changing the reference plane to the minimum velocity point upstream of the flame, increasing trends were found for propane/air mixtures, a result in accordance with observations of ref. [23].

In 1989, Smith and coworkers [114] found that depending on the location of the reference plane, being either upstream or downstream of the flame, linear extrapolation to zero strain rate performed on reference velocities yielded different unstrained flame speed values and strain sensitivities. Comparison with experimental results obtained for spherically expanding flames led the authors to conclude that the hot boundary of the flame was the appropriate location for laminar flame speed studies. This observation was at the time reinforced by earlier numerical results of Dixon-Lewis and Islam [115] on methane and hydrogen 1D flames, showing that reference planes for burning velocity measurements were all positioned close to the maximum reaction rate.

In 1990, Deshaies and Cambray investigated stretched flames by both strain and curvature effects in a stagnation flow experiment [116]. Laminar flame speeds were extracted from experimental measurements by linearly extrapolating the velocity profiles of the cold hydrodynamic zone to a computed plane of reference similar to the asymptotic reaction zone defined in the work of Clavin and Joulin [16]. Strain sensitivities were found for lean propane/air flames in an apparent contradiction with the works of Wu and Law [23] that obtained burning velocities moderately increasing with strain. It was argued that this contradiction arose from the choice of different flame burning velocity definition that could not only lead to different fundamental flame speeds evaluations but also reverse the flame sensitivity dependence to stretch. This assumption was further validated by processing results of ref. [23] in the manner those of ref. [116] and an identical Markstein number was recovered for both set of data.

In an attempt to reconcile all aforementioned experimental observations, Tien and Matalon [68] and Matalon [117] developed expressions for the dependence of laminar burning velocities with strain based on the various definitions that could be useful in experimental investigations. Their numerical analysis essentially relied on earlier analytical developments of: i/ Matalon and Matkowsky [59] for a general flame asymptotic formulation assuming large activation energies and weak strain. The flame typically shrinks to a single surface known as the "reaction sheet" and the outer flow is considered as an inviscid and incompressible flow, ii/ Eteng et al. [118] who proposed the outer flow field formulation for a flame in the stagnation point flow configuration. In ref. [68], a particular attention was brought to the formulation of the inner structure of the flame, still characterized by a single reaction sheet, but with a finite thickness incorporating expansion effects due to the presence of the preheat zone. Burning velocity dependence with strain was derived for several points of reference including:

- The 1% temperature rise at the upstream edge of the flame: a linear increase of the laminar flame speed is predicted with strain for almost all Lewis numbers.
- The local velocity minimum at the upstream edge: the following approximate non-linear relation is obtained:

$$S_{u,ref} = S_u^0 \left(1 - Ka\,Ma + Ka\,ln\left[\frac{1-\sigma}{Ka}\right]\right) \qquad \text{(II-18)}$$

  where σ is the thermal expansion parameter i.e. the burned to unburned gas temperature ratio or unburned to burned gas density ratio. This formulation is applicable for strain rates up to 1000 s^{-1} and a decreasing dependence of the velocity with strain is predicted only for mixtures with Lewis numbers that are large enough. This somehow corresponds to experimental observations of Wu and Law [23].
- The local maximum temperature at the downstream edge of the flame: again, a linear dependence of the flame velocity with strain rate is obtained and, according to this definition, $S_{u,ref}$ values are seen to increase or decrease for mixtures with Le <1 or Le >1 respectively. It is argued in ref. [68] and [117] that these trends are in accordance with results presented in ref. [113] which seems to be inaccurate if final conclusion of the authors are considered.

Additional works were performed by Chao and coworkers [119] on the dependence of flame velocity with strain in the counterflow twin flame configuration for a realistic finite domain with plug flow boundary conditions. It was shown that the conventional linear extrapolation based on $S_{u,ref}$ strained velocities overestimates the fundamental flame velocity due to the existence of a non-linear dependence at lower strains. This non-linearity was however found to be weak if a sufficient nozzle separation distance is used and hence it was concluded that linear extrapolation in these conditions would provide a flame speed with sufficient accuracy.

Non-linear effects on flame propagation were recently analyzed by Kelley and Law [120-121] for outwardly propagating flames. In these studies, a general formulation, taking into account the flame speed non-linear dependence with strain, is proposed:

$$\left(\frac{S_u}{S_u^0}\right)^2 ln\left(\frac{S_u}{S_u^0}\right)^2 = -2\frac{L_u K}{S_u^0} \tag{II-19}$$

With L_u, the unburned Markstein length, S_u, the upstream flame speed and K, the strain rate. Expression (II-19) is expected to hold for the upstream flame velocity of the counterflow flame [121] and has been applied in ref. [120] to counterflow flame data points of n-butane/air mixtures yielding lower extrapolated flame speed values in comparison to the commonly used linear extrapolation procedure.

An alternate location for the evaluation of flame properties is the plane of the maximum heat release rate. This point of reference has been investigated by Sun et al. [122] in an flame integral analysis of weakly stretched flames allowing for non-unity Le numbers as well as an accurate description of the temperature variations throughout the flame front. A linear expression linking the axial flow velocity S_b at the point of maximum heat release with the strain rate was derived:

$$S_b = S_b^0 + \left[\frac{Ze(1-Le)}{2} - 1\right]\Delta K\delta \tag{II-20}$$

with S_b^0, the linearly extrapolated "burned" velocity value, Ze, the Zeldovich number, Le, the mixture Lewis number, $\Delta=1+\ln\left[\sigma+\left(1-\sigma\right)e^{-1}\right]$, a factor accounting for the thermal expansion, itself depending on a thermal expansion factor σ, K, the strain rate and δ, the flame thickness. Interestingly, it was shown from computational results that extracted Lewis numbers for the three different flame configurations studied including inwardly, outwardly propagating and counterflow flames were similar, therefore demonstrating the general nature of nonequidiffusive effects in the propagation of weakly stretched flames. Numerical studies of laminar premixed counterflow propane/air flames were initiated by Davis and coworkers [123] for both potential and plug flow velocity inlet conditions. It was shown that flames submitted to the same hydrodynamic strain (matched upstream axial velocity gradients $K = du/dx$) but different inlet velocity formulations would display noticeable differences in their structure with: i/different flame standoff distances to the stagnation plane, ii/ consequent discrepancies for the strains evaluated close to or at the location of the chemically reacting zone. Matching the strain rate values of both approaches close to the plane of maximum flame reactivity gave however identical flame responses which led the authors to conclude that the classical strain evaluation at the upstream edge of the flame is not an appropriate indicator of the strain really felt by the flame. Thus, the choice of a reference plane located close the reaction zone was recommended. This observation was further supported by computational and analytical works of the same authors [124]. Following the recommendation of ref. [123] and assuming plug flow conditions, a methodology of parabolic extrapolation is proposed in order to evaluate both unburned and burned counterflow flame properties (reference velocities and corresponding strains) for a reference plane located at the maximum flame heat release. Evolutions of both unburned and burned Markstein numbers throughout the flame front found a good agreement with theoretically predicted values by the asymptotic theory in a reference plane close to the barycenter of the flame heat release. This confirmed the importance of evaluating flame properties close to the chemical zone. Subsequent investigations of Davis et al. [125] and Davis and Searby [126] were devoted to Markstein numbers determinations for counterflow methane and propane/air flames as well as hydrogen/air flames respectively. Choosing a reference plane close to the maximum heat release peak, burned and unburned Markstein numbers were computed, showing a reasonable agreement with experimentally-deduced values in the outwardly propagating flame configuration, hence confirming equal flame answers to weak stretch arising from either curvature or straining.

II.4.2 Nozzle Separation Distance and Finite Domain Effects for Counterflow Flames

The first evocation of the importance of the nozzle separation distances in counterflow experiments appeared in the pioneer numerical investigation of Kee and coworkers [29]. Simulations were performed to reproduce experimental results of Law et al. on extinction limits of CH_4/air mixtures [60]. Both plug flow and potential approach were tested for a relatively small burner separation distance (7mm) while extinction strain rates were calculated from the axial velocity gradient K ahead of the first local velocity minimum. It was found that the traditional potential flow approach failed to accurately describe extinction behavior with equivalence ratio while the plug flow formulation yielded excellent agreement with experimental data for the lean mixture cases. A comparison of axial velocity profiles for the two formulations revealed that the single parameter K as computation input was not sufficient to uniquely characterize the strain field: thus, it was shown that extinction limit computations were strongly dependant on fluid mechanical formulations which considerably complicated direct comparison between numerical and experimental results. It was suggested, to circumvent this problem, to lead independent measurements of both radial and axial velocities to remove any ambiguity and fully characterize the flow. Three possible reasons were mentioned to explain remaining discrepancies: i/radial spread at the inlet was not taken into account, i.e. by default, the radial gradient a was set to 0 at the burner inlet which might not correspond to practical cases, ii/ the determination of strain rates involving "best fit" procedures was found to be prone to important scatters even for numerically determined profiles where variations up to 100 s^{-1} were observed depending on the chosen methodology, iii/ solution might depend on the nozzle separation distance. The latter is confirmed by J.S. Tien (see ref. [29], Comments section) mentioning, from experimental observations, that "…the burning rate are constant if the ratio of nozzle separation distance to the nozzle diameter is between one and three. When the ratio is smaller than one, the stagnation flow region is squeezed and nozzle exit flow is perturbed. When this ratio is greater than three, ambient entrainment becomes important".

In 1990, Dixon-Lewis [30] numerically investigated stoichiometric methane-air flame in the counterflow planar axisymetric configuration for various nozzle separation distances (L = 7, 16 and 30 mm). It was found that the nozzle separation distance had no influence on linearly extrapolated velocities. However, it was noticed that extrapolated value would lie above the 1D calculation by about

3 cm.s^{-1} for the same reaction mechanism and rate parameters, implying an "unknown" flame behavior at lower strains.

The influence of the nozzle separation distance was further investigated by Egolfopoulos in ref. [127] for which computed extinction strain rates with classical methodologies were compared to the experimental data of Law et al. [60]. It was observed that, depending on nozzle-burner distances L (7 or 14 mm), discrepancies up to 200 s^{-1} could be obtained. It was then decided to analyze this "finite domain effect" by computing premixed methane/air flames (E.R.=1) submitted to the same axial velocity gradient K (1500 s^{-1}) for different nozzle burner distances (7, 14 and 22 mm). Instead of the conventional comparison of axial velocities, the weighted strain rate variable $-G$ as defined in equation (I-25) is monitored. As mentioned by the author, this variable is accounting for the radial mass flux gradient in the flame which is directly related to the local burning rate. For the same applied strain rate, it was found that calculations would predict lower radial fluxes for larger distances L while the smaller separation gap was characterized by an overall increased value of G, hence an increased value of the strain felt by the flame, and, in return, an earlier flame extinction state. This observation clearly corroborates Kee et al. [29] conclusions on the fact that the stagnation flame dynamics is not governed by the single parameter K. In practice this could have serious implications on laminar flame speed studies, as demonstrated below.

Vagelopoulos and coworkers [71] studied the influence of the nozzle separation distance on laminar flame speed determination for counterflow flames of weakly burning hydrogen flames (E.R.= 0.3 and 0.35), as well as methane-propane/air mixtures. For hydrogen mixtures, numerical simulations were performed assuming plug flow condition with zero velocity gradient used at the nozzle exit for nozzle separation distances L ranging from 7 to 50 mm. It was globally shown that, for these weakly burning hydrogen flames, smaller burner separation distances would lead to higher $S_{u,ref}$ values due to enhance effects of the thermal expansion "more readily felt by the flow". This effect was found to diminish for larger L values, especially 14 and 22 mm for which $S_{u,ref}$ evolutions were almost superimposed. These numerical results were confirmed by experimental observations conducted for nozzle-separation-distance to burner-diameter ratios equal to 1. Another important conclusion drawn by the authors is that the linear extrapolation procedure to the zero strain state seemed to be accurate, according to the 1D independently calculated flame velocity, only if small Karlovitz numbers, typically on the order of 0.1, are reached. In the light of previous observations, new laminar flame speed datasets for methane and propane flames were obtained for a 22 mm nozzle separation distance and, as expected, lower velocity values were found. Similar works were led by Chao and coworkers for methane/air flames (E.R.=1) [119] with nozzle separation distances of 14 and 22 mm. Both numerical and experimental approaches did not display any significant difference in $S_{u,ref}$ evolutions with strain, indicating that any intermediate value between 14 and 22 mm would be appropriate for atmospheric CH_4/air flames.

II.4.3 The Stagnation Plate Flame and the Direct Determination of Laminar Flame Speeds

As seen earlier, an alternative setup to the classical counterflow burner can be obtained creating a stagnation flame by impinging a reactive jet on the flat surface. This stagnation plate configuration considerably simplifies the classical counterflow twin flame approach as: i/a single reactive jet is controlled, ii/ gas consumption is significantly reduced which in return complies with more drastic safety issues, iii/ the stagnation plane is unambiguously identified, iiii/ the complex insulation required to have an adiabatic upper burner is avoided and renders the experimental apparatus more flexible. Early developments of the plate setup were essentially oriented towards heat transfer issues, see for example the works of Milson and Chigier [128] on turbulent methane/air flames impacting on a cold plate, and some attempts to numerically and experimentally characterize flame extinction behavior as well as quantify heat fluxes to the stagnation wall readily appeared [129-130]. Later on, the experimental investigation of Law et al. [57] on extinction and stability of stretched premixed propane/air flames in the single jet stagnation flow configuration concluded that the nature of the solid plate and particularly its temperature had a negligible influence on the determination of extinction limits. Following studies by Ishizuka and Law [131] and Ishizuka et al. [132] insisted on the role of preferential diffusion in extinction phenomena with an increased importance of downstream heat losses for mixtures Lewis number <1. This fact was clearly demonstrated in ref. [131] where extinction data for adiabatic counterflow twin flames and plate stabilized flames were confronted. The stagnation plate configuration was also used by Vlachos and coworkers [133-134] in numerical studies of methane and hydrogen/air mixtures in order to assess the influence of surfaces on combustion processes, including catalytic effects. High wall temperatures were found to promote radical wall destruction and hence altering extinction characteristics compared to counterflow flames. Only recent studies by Egolfopoulos and coworkers [135] and Zhang [136] are addressing in detail the wall effects on the propagation properties of steady strained laminar premixed flames, particularly the impact of downstream heat losses on the evaluation of laminar flame speeds. In this work, the propagation of laminar methane/air flames was numerically and experimentally studied for the heated stagnation plate configuration. Results showed that as far as low strains are considered, i.e. flames are not close to the stagnation plate, downstream heat losses are not “felt” by the flame and single and opposed jet experiments yield comparable results. The authors concluded on the viability of the stagnation plate methodology as an alternative setup to the classical counterflow twin flame configuration. They also recommended the use of high plate temperatures combined with large burner-to-plate distances to minimize the bending behavior of $S_{u,ref}$ profiles observed at intermediate strains due to the progressive influence of heat transfers to the plate.

It is worth to mention here that several flame speed investigations, including those listed in Table II.2 and Table II.3, are studying strained planar flames stabilized against either non-heated [78, 86, 94] or water-cooled [23, 56, 105, 137] stagnation plates. Interestingly, heated plates have not been considered for laminar flame speed determination purposes. The main reproach that could be formulated here is that these investigations rarely assess interactions occurring with the stagnation plates. Especially the influence of downstream heat losses on the flame speed measurements is often assumed to be negligible when a thorough comparison with counterflow flame data, as presented in ref. [135-136], would be required.

An original methodology for direct laminar flame speed measurement was proposed by Vagelopoulos and Egolfopoulos [89, 138] using a stagnation plate combined with large burner-to-plate separation distances ($1.5 < L_{sp}/D < 2.5$). Aware that very low strains could not be reached keeping the usual moderate burner-to-plate separation distance while lowering the inlet velocity, the authors investigated stagnation flame stabilized for large L/D ratios. It was noticed that a gradual decrease of the burner flow rate would lead to a smooth transition from a planar positively stretched to a conical Bunsen-type negatively stretched flame. Based on this observation, a technique was developed to isolate a "near-zero strain" situation and perform LDV measurements while the flame undergoes this unassisted transition. Although flame stability complications seem to arise for specific mixtures due to thermodiffusional and gravitational effects, this methodology is very attractive since no extrapolation procedure is needed. Indeed, flame velocities are extracted for ultra low strains, typically on the order of 10 to 20 s^{-1}, therefore extracted values are assumed to be representative of the unstrained fundamental laminar flame speeds. This experimental approach was numerically supported by Cuenot at al. [139] who showed that during the transition, the flame is experiencing a zero strain state for which the flame velocity equalize the fundamental laminar flame speed.

II.5 Summary

General equations governing the particle motion in viscous fluids have been presented along with the relevant Stokes drag, gravity and thermophoretic force formulations. A detailed literature review on seeded premixed and non-premixed counterflow flames indicated that thermophoresis potentially plays an important role for moving particles in the vicinity of the flame plane. This underlined the importance of characterizing particle thermophoretic drifts that could arise in practical situations to account for discrepancies between experimental and numerical results.

A thorough review of laminar flame speed experiments in stagnation flow configurations has been proposed. Both LDV and PIV investigations were detailed. Several points of interest should be underlined:

- Almost all studied flames were stabilized for weak strain rates with corresponding Karlovitz numbers Ka usually lower than or equal to 0.1. Only lean and rich weakly burning flames were studied for Ka numbers above 0.1.
- Uncertainties on unstrained extrapolated flame speeds are rarely mentioned. Few estimates found among cited references seem to indicate that the final flame speed uncertainty is on the order of 1 to 10 % of the extrapolated value.
- Extrapolation procedures following non-linear formulations (i.e. Tien and Matalon [68]) typically yields unstrained flame speeds from 1 to 3 $cm.s^{-1}$ lower than the conventional linear methodology.

- For counterflow flames, the apparent flame sensitivity to strain is strongly dependant on the reference location at which flame properties ($S_{u,ref}$, K) are evaluated. Therefore, care should be taken, since it has been noticed that different reference location in the flame (for instance, the upstream or downstream edges) can possibly lead to reverse interpretations.
- For stagnation flow experiments, the nozzle separation distance L, or alternatively the burner-to-plate distance L_{sp}, and the burner diameter D are important parameters. Although controversial, experimental and numerical observations seem to indicate that L/D ratios on the order of one (or slightly higher) are well adapted for laminar flame speed studies, provided that L is not too small [71]. Nozzle separation distances from 14 to 22 mm were found to be well-adapted to this specific application.

In the last section, key investigations with stagnation flame plate setups have been presented. This configuration, allowing for a simplified burner operation, was deemed acceptable for use in laminar flame speed studies provided that the stabilized flame is not too close to the burner plate. The recent planar-to-conical flame transition methodology developed by Vagelopoulos and Egolfopoulos [89] has been presented. By isolating a near-zero strain state during the flame transition, the fundamental flame speed is directly deduced form LDV measurements without any extrapolation procedure.

III. Digital Particle Image Velocimetry for Laminar Flame Speed Determination: Principles and Application to Stagnation Flow Flames

III.1 Introduction and Objectives

One of the prime objectives of the present experimental work was to adapt the Digital Particle Image Velocimetry (DPIV) technique to fundamental flame speed determination in reactive stagnation flows. The DPIV diagnostic was found to be very challenging in this particular context. Especially, seeding-related issues had to be dealt with, including, for instance, selection of a powder adapted to high velocity gradient situations, control of seeding densities for optimized vector calculations, etc. Choices and individual influences of PIV-related parameters, such as laser pulse delays *(Δt)* or advanced algorithm for image processing had also to be investigated. Another important aspect of the present methodology is the large amount of data generated through 2D velocity mapping for the various experimental conditions of interest. Clearly, automated procedures are needed to extract useful information, such as reference velocities and their associated strain rates, and avoid human bias that could be introduced by manually selecting the information. The last crucial point to be mentioned is the evaluation of uncertainties related to extrapolation methodologies necessary to yield unstrained flame velocities. They have been a long time overlooked in the literature and need to be addressed.

From DPIV practical implementation considerations to the final data extrapolation procedure, this chapter intends to give an insight into choices that were made for the development of this methodology. For sake of clarity, the main principles of PIV will be first recalled, followed by diagnostic setups and specifications of the present study. Then, the choice of seeding material, as well as particle density observed on PIV images will be discussed. Finally, routines developed for the extraction of useful information on post-treated PIV images will be presented, including the final extrapolation procedure to yield unstrained flame speed values.

III.2 About DPIV

III.2.1 Principles and Rules of Thumb

Particle image velocimetry, referred as PIV, has known considerable developments over more than two decades, from analog recording and treatment methodologies to modern digital techniques including powerful computer acquisition possibilities and elaborated processing options. The present section is devoted to recall the main principles of Digital PIV (DPIV) as well as rules of thumb generally useful in experimental approaches. An exhaustive review of the DPIV technique is clearly out of scope of the present work and readers interested in specific DPIV aspects will be redirected to archival literature. The latter includes: the Ph.D. thesis and related works of J. Westerweel on theoretical fundamentals of PIV [140-141], detailed papers by, for instance, Willert and Gharib [142], Keane and Adrian [143-144] or

Grant [145] providing comprehensive overviews and optimization guidelines for the technique. An updated review of Particle Image Velocimetry is proposed by Raffel and co-authors in their book “Particle Image Velocimetry – A Practical Guide” covering theoretical backgrounds as well as state of art developments and implementations of DPIV [42].

The DPIV methodology relies on the displacement of small tracers seeded in the medium that needs to be characterized. A pulsed laser plane is used to illuminate the flow, generally twice, within a short period of time Δt. Provided that seeded particles follow Mie scattering theory, i.e., making the assumption of sphericity and making sure that particle diameter d_p is larger than the light source wavelength, scattered light can be recorded thanks to an appropriate CCD camera, see Figure III.1 (a). Image pairs are further processed to yield the entire velocity field of investigated area within the flow, as shown Figure III.1 (a-b): they are first divided into cells, referred as “interrogation spots”, which constitutes a processing unit. Statistical methods, nowadays mostly cross correlations, are then used to locate individual units of the first frame (Image A) on the second frame (Image B). Most probable displacements are found for all interrogation areas and velocity mapping of the entire region of interest is rendered possible knowing the time interval Δt and the optical system magnification M.

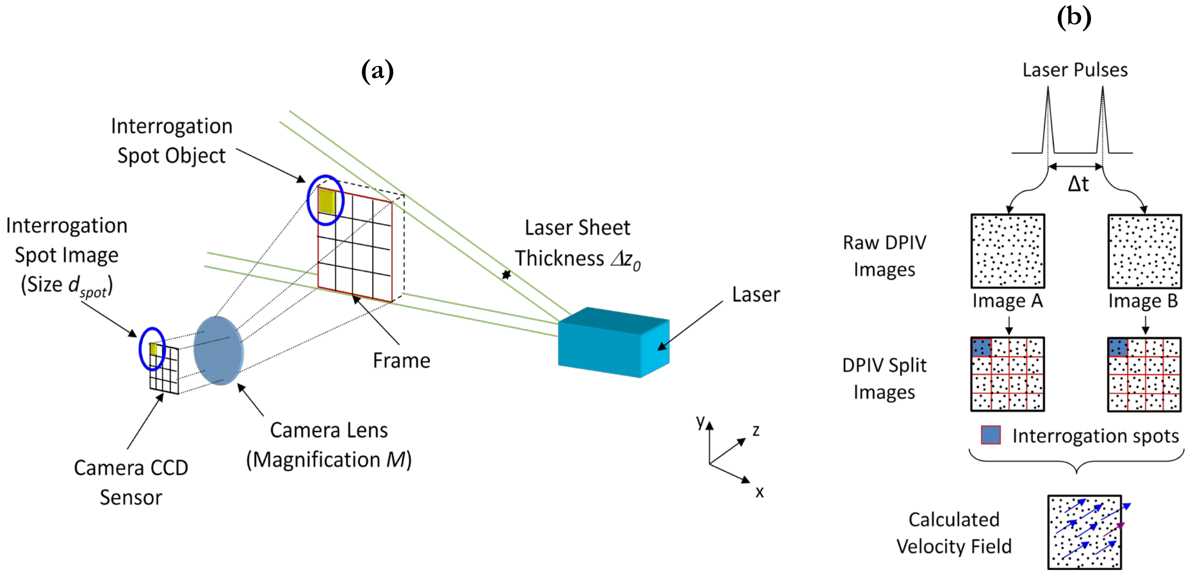

Figure III.1 Schematic of the DPIV diagnostic: (a) Setup and visualization of the interrogated zone, (b) Image computation process.

Keane and Adrian [143] studied the influence of various parameters on PIV performances through Monte Carlo simulations. Results of their study provided useful recommendations that are still commonly applied in two pulse PIV methods. These are listed Table III.1.

	Recommendations	Expression
I.	The **particle image density** N_p should be at least **15** for optimized correlation. (The particle image density corresponds to the mean number of particles per interrogation spot).	$N_p \geq 15$
II.	The velocity gradient $\Delta \boldsymbol{u}$ within an interrogation spot should be **small enough** to avoid statistical bias and improve correlation (with M, optical system magnification, Δt laser pulse interval and d_{spot}, size of the interrogation spot).	$\frac{M\|\Delta u\|\Delta t}{d_{spot}} < 0.05$
III.	The particle displacement $\Delta \boldsymbol{x}$ within an interrogation spot should be **small enough** to avoid lost pairs during the Δt time interval. This yields the classical **¼*d_{spot} maximum allowed displacement** rule, widely applied in PIV.	$\frac{\Delta x}{d_{spot}} \leq 0.25$
IV.	The particle transverse displacement Δz (i.e. out-of-plane motion) should be **small enough** to avoid lost pairs and improve correlation (with w, transverse velocity component and Δz_0, laser sheet thickness).	$\frac{\|w\|\Delta t}{\Delta z_0} \leq 0.25$
V.	Detectability threshold D_0 should be **lower than 1.5** and **greater than 1.2**. (The detectability threshold is the ratio of the first tallest peak to the second tallest peak on the correlation map, it is an important parameter during the final processing phase).	$1.2 \leq D_0 \leq 1.5$

Table III.1 PIV recommendations by Keane and Adrian [143].

III.2.2 Processing Methodology

Overview

PIV processing is characterized by the following "generic" steps:

- ✓ **Image conditioning**: this step aims at subtracting a background file to DPIV raw images in order to improve correlation features. Specifically, zones displaying strong reflections of the laser light can be systematically subtracted to improve local velocity evaluation by suppressing correlation noise.
- ✓ **Grid generation**: a grid engine is used to split image pairs into interrogation spots. Numerous spot shapes can usually be adapted; moreover, they do not need to be of the same size on both frames. Modern algorithms generally include special features such as multiple pass interrogation, grid refining schemes and more recently image deformation schemes.
- ✓ **Spot Masking**: This step corresponds to spot enhancement to improve the signal-to-noise ratio of the correlation map. Typically, interrogation spots are filtered using intensity criteria on contained pixels.

- ✓ **Correlation**: This step computes displacements of interrogation spots within a maximal allowed translation (See criterion III, Table III.1). For each interrogation area, a correlation map is calculated and the location of the highest correlation peak is assumed to give the particle image displacement. Other peaks will be regarded as noise resulting from random pairing of particles on both frames. Thus, a detectability threshold is needed to discriminate clearly calculated displacements, i.e. a single correlation peak of higher amplitude among small secondary peaks, or ambiguous ones, i.e. several peaks of the same amplitude (See criterion V, Table III.1). The latter will not be validated. A remarkable aspect of the present step is the possibility to locate the highest peak maximum thanks to methodologies able to yield displacement with subpixel accuracy.
- ✓ **Validation**: this step usually involves user-defined filters to remove spurious vectors on calculated velocity fields.

All classical PIV software on the market are usually providing dedicated algorithms for each one of the 5 aforementioned steps. Two of them have a particular importance in the PIV processing: these are the grid generation and the correlation steps. Erroneous or unsuitable parameter inputs while initializing these particular phases can considerably affect DPIV calculations. In the remainder of the section, details on the main principles of each step will be recalled. They will be illustrated with technical solutions provided by the TSI software Insight™ 6.0 used for the present study. As such, processing parameters used in the course of the present investigation will be fully characterized.

The Grid Generation Step

As recalled earlier, a grid engine is used to split images into interrogation spots whose displacements will be further assessed. A compromise has to be found: selecting large interrogation area sizes will lead to an “easier” correlation process while sacrificing the spatial resolution. Also, in case of a strong velocity gradient within the interrogation spot, i.e. violation of criterion II (Table III.1), the calculated velocity might be considerably biased by computing an average velocity for all particles present in the area. On the contrary, choosing very small interrogation cells might render the correlation process impossible due to lack of particle in spot pairs, in turn violating criterion I (Table III.1). A basic approach of the grid generation consists of using a single pass grid, i.e. images pairs are divided just once, using the same mesh, applying criterion III (Table III.1). As seen Figure III.2, it results in particle pair losses outside interrogation spot. An optimized approach is to use multiple pass grids: the first pass is used to compute an average displacement field. During the second pass, interrogation windows are translated by this mean displacement, allowing a close match of particles from both spots, hence increasing the signal-to-noise ratio of the correlation process [42, 146]. The multiple grid algorithms can be significantly improved by downsizing interrogation spots at each pass, therefore authorizing the use of smaller spot sizes which was not allowed at the beginning of the process due to proportionally large displacements (They would indeed introduce a considerable noise during the correlation process !). As such, the dynamic spatial range, defined as the largest to the smallest length scales observed within the flow, is seen to be consequently increased [42]. It is clear that this interesting scheme combination is particularly suitable for dense PIV images and flows with important velocity variations, conditions that are both met in the present stagnation flame experiments.

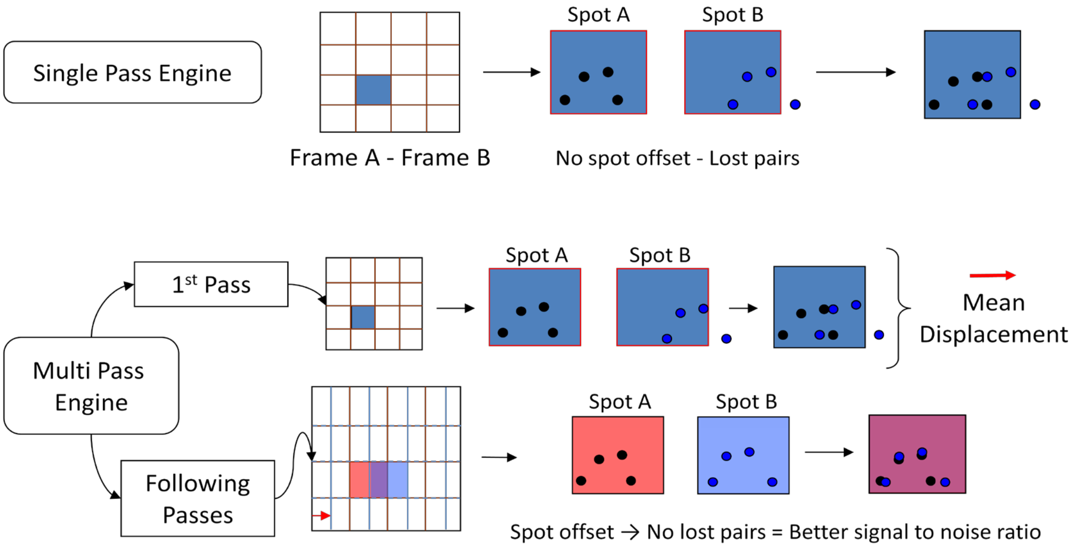

Figure III.2 Illustration of the single and multiple pass grid engines.

A practical implementation of such elaborated schemes is proposed in the commercial software used in the present study. A “Recursive Nyquist Grid” can be selected to split image pairs following Nyquist sampling criterion, i.e. a 50% grid overlap is introduced, therefore doubling interrogation spots that will be processed. A first pass is then computing integer pixel displacements and the resulting velocity field can be edited through user-defined filters saved in a pass validation file. The second pass uses the optimized displacement fields by offsetting individual spots. As such, the highest correlation peak is expected to be within a half pixel of the correlation map center. The grid is finally refined according to the user spot size specifications.

Another advanced feature of modern grid engines, however not used in the course of this work, is the possibility to select grid deformation schemes that will enhance correlation processes for flows characterized by important velocity gradients at the interrogation spot scale [147]. It somehow relaxes recommendation II of Table III.1 by deforming cells according to the flow pattern, which was shown to increase robustness and accuracy of velocity estimations in highly sheared and turbulent flows [42]. If grid deformation schemes present numerous advantages, the main drawback to be mentioned is the considerably increased computation time that makes such schemes difficult to apply when large series of PIV images have to be processed.

The Correlation Step

The basic underlying concept of correlation in DPIV is to match particle samples contained in an interrogation area of the first image to particle samples contained in a spot size cell on the second image, within a maximum "authorized" displacement (See criterion III, Table III.1). This can be done through the discrete cross-correlation function *C* [42, 141], expressed herein for a *N*×*N* pixel interrogation spot:

$$C(x, y) = \sum_{i=1}^{N} \sum_{j=1}^{N} I(i, j)\, I'(i + x, j + y) \qquad \text{(III-1)}$$

With (x, y) coordinates of the displacement vector, I and I', intensity of a pixel contained in the computed spot on the first image and a pixel contained in the displaced spot on the second image. The (i, j) coordinates indicate the location of a pixel within the interrogation spot of chosen size. Once all possible displacement are "scanned", a correlation map is established: as mentioned earlier, the highest obtained cross-correlation peak gives the best matching location of the displaced particle sample present in the original spot. This process is illustrated Figure III.3 for a 4 pixel size spot (N=4) and a maximum authorized displacement of 4 pixels.

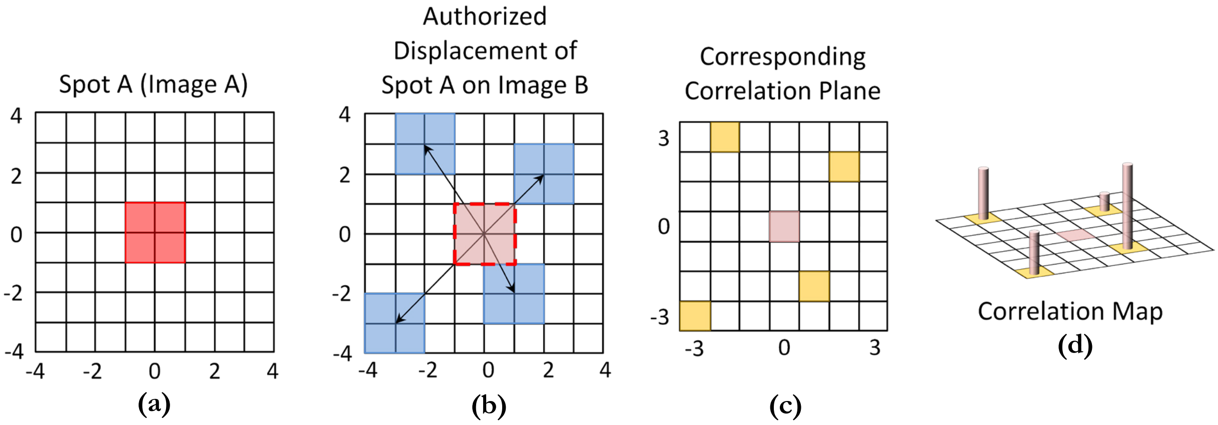

Figure III.3 Illustration of the correlation process for a four pixel interrogation spot and a maximum four pixel authorized displacement: (a) Spot A on a portion of image A, (b) Examples of authorized displacements of spot A on a portion of image B, (c) Corresponding 2D correlation plane, (d) 3D correlation map.

This correlation process is generally referred as direct correlation and is implemented in Insight™ 6.0 under the Hartcorrelator and Direct Correletor denominations. The Hartcorrelator typically applies expression (III-1) only for the most significant pixels of the interrogation spots: the limit can be user-defined through a compression ratio. The Direct Correlator computes all pixels present in the interrogation areas with two extra features: average intensities of spots are subtracted in expression (III-1) and the correlation map is corrected thanks to an autocorrelation factor for increased measurement accuracy. It is clear, looking at expression (III-1), that direct correlation processes require considerable computation efforts that end up being extremely time-consuming. An alternate approach, widely used, is to switch to the frequency domain. Taking advantage of the theorem stating that cross correlation of two functions is equivalent, in the frequency domain, to the complex conjugate product of their Fourier transforms, cross correlation can be processed much faster. Indeed, Fast Fourier Transform (FFT) of interrogation spots from both images is taken, the complex conjugate multiplication performed, and a final inverse FFT applied to yield the cross correlation data. This type of correlation engine, referred as FFT Correlator in Insight™ 6.0, requires the processed spots to be square powers of 2. Other spot sizes might be patched using the zero pad mask technique.

The final important phase of the correlation step concerns the validation and accurate localization of the highest correlation peak on the cross-correlation map. The ratio of the highest peak correlation coefficient (potential displacement) to the second highest peak coefficient (noise due to random pairing of particles) is computed and compared to the user-defined detectability threshold value (See recommendation V, Table III.1). If the displacement peak stands clearly above the noise, it will be selected and further processed. If not, weak confidence is accorded to the selection process and data is usually discarded. The second task to be performed is the accurate evaluation of the position of the displacement peak. If a raw analysis of the cross-correlation map gives a displacement with a ±1 pixel accuracy, much more information is actually contained on the correlation map by considering the correlation information of neighborhood pixels. Typically, subpixel accuracy, in a range of 1/10th to 1/20th of a pixel for a 32×32 interrogation spot (8 bit digital images), can be achieved [42]. This is rendered possible through fitting procedures on the pixel with the highest intensity and its closest neighbors. Table III.2 presents two classical three-point estimators that were used in the present study. They usually perform well for particles images displayed on 2-3 pixels. For wider particle images, cross-correlation values of the highest peak and direct neighbors are too close to give a reliable shift. On the opposite, for too small particle images (i.e. ≈1 pixel), neighborhood correlation values are lost in the background noise and uncertainty in the location of the displacement considerably increases.

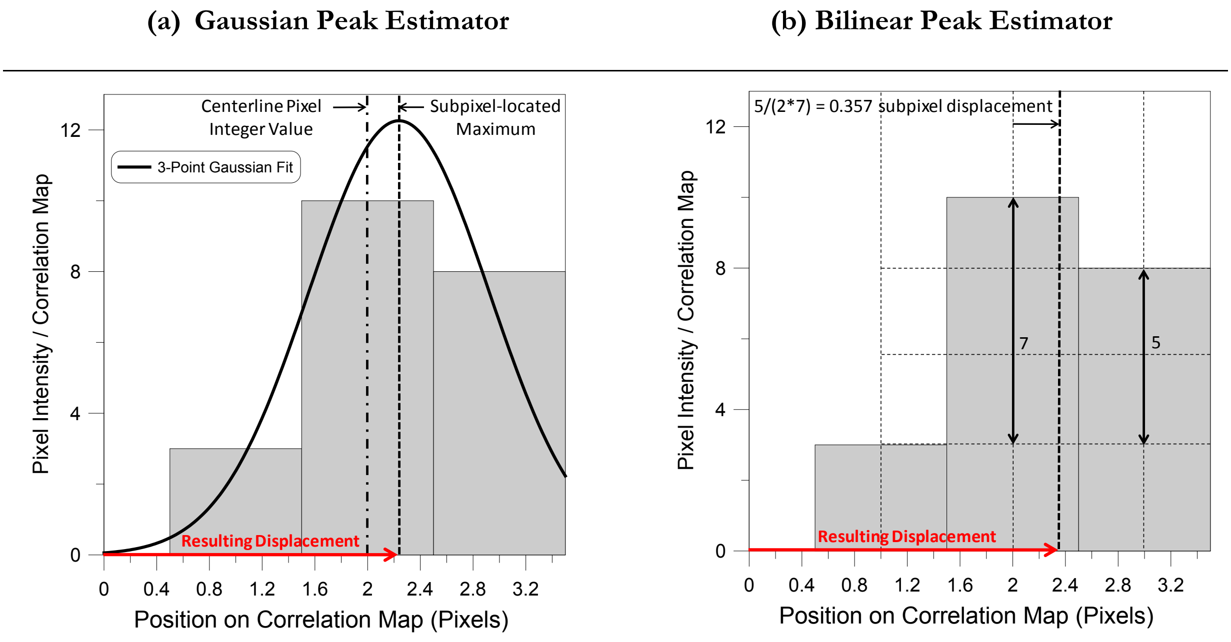

$$x_0 = \tilde{\imath} + \frac{\log C_{(\tilde{\imath}-1,\tilde{\jmath})} - \log C_{(\tilde{\imath}+1,\tilde{\jmath})}}{2\log C_{(\tilde{\imath}-1,\tilde{\jmath})} - 4\log C_{(\tilde{\imath},\tilde{\jmath})} + 2\log C_{(\tilde{\imath}+1,\tilde{\jmath})}}$$

$$y_0 = \tilde{\jmath} + \frac{\log C_{(\tilde{\imath},\tilde{\jmath}-1)} - \log C_{(\tilde{\imath},\tilde{\jmath}+1)}}{2\log C_{(\tilde{\imath},\tilde{\jmath}-1)} - 4\log C_{(\tilde{\imath},\tilde{\jmath})} + 2\log C_{(\tilde{\imath},\tilde{\jmath}+1)}}$$

$$x_0 = \tilde{\imath} + \frac{C_{(\tilde{\imath}+1,\tilde{\jmath})} - C_{(\tilde{\imath}-1,\tilde{\jmath})}}{2\max\left\{C_{(\tilde{\imath},\tilde{\jmath})} - C_{(\tilde{\imath}-1,\tilde{\jmath})}\,,\ C_{(\tilde{\imath},\tilde{\jmath})} - C_{(\tilde{\imath}+1,\tilde{\jmath})}\right\}}$$

$$y_0 = \tilde{\jmath} + \frac{C_{(\tilde{\imath},\tilde{\jmath}+1)} - C_{(\tilde{\imath},\tilde{\jmath}-1)}}{2\max\left\{C_{(\tilde{\imath},\tilde{\jmath})} - C_{(\tilde{\imath},\tilde{\jmath}-1)}\,,\ C_{(\tilde{\imath},\tilde{\jmath})} - C_{(\tilde{\imath},\tilde{\jmath}+1)}\right\}}$$

Table III.2 Two of the 3-points estimators used in the present study: (a) Gaussian Peak Estimator, (b) Bilinear Peak Estimator. The coordinates $(\tilde{\imath},\tilde{\jmath})$ indicates the highest peak location on the cross correlation map, (x_0, y_0) are the coordinates of the total displacement.

III.3 Application to Stagnation Flow Flames

The DPIV technique, as described above, has been applied to several reactive stagnation flows in order to determine the fundamental flame speeds of various methane/air (Chapter IV) and syngas/air mixtures (Chapter V). Unless otherwise stated, global parameters related to experimental results that will be presented herein are indicated in the figure captions between parentheses. These parameters are including: the mixture blend (*MB*), the Equivalence Ratio of the studied mixture (*ER*), the Burner exit Inside Diameter (*BID*), the Burner Configuration (*BC*) being either the Stagnation Plate (SP) or Counterflow (CT) setups, the burner-to-plate (L_{sp}) or burner-to-burner (L) distances, and finally the Main Flow Rate (*MFR*) and Coflowing inert Flow Rate (*CFR*). Specifications related to experimental setups will be developed in detail in the course of Chapter IV.

III.3.1 Diagnostics Setup and PIV Specifications

The velocity measurements were performed in the vertical plane passing through the burner axis. In this plane, a laser sheet was created using a twin-head 532 nm Nd-Yag Continuum Minilite, providing nominal pulse energy of 25 mJ for a pulse duration of 5 ns. An optical system including a spherical lens (f=500 mm for CH_4/air flame setup and 592 mm for the syngas flame setup) and a plano-cylindrical lens (*f* =-25.4 mm) were set to respectively focus and expand the laser beam at the region of interest. The nominal thickness of the light sheet was on the order of 200 μm in the measurement zone. Particle image pairs were recorded via a CCD camera, TSI PIVCAM, on a 1008 × 1018 pixel matrix, at the maximum allowed frequency of 14 Hz. The camera was placed at a 90° angle with respect to the laser sheet plane and equipped with a Nikon objective (*f* =105mm, f/2.8D) combined with a Kenko MC7 conversion lens (AF 2×). A synchronizer, TSI Laser Pulse, was used to synchronize the laser pulses with the camera acquisition phases. Based on 32×32 pixels interrogation cells, a magnification ratio of 0.72 and 50% overlap grid spacing, a typical spatial resolution achieved for the velocity vector grid was 200 μm in both directions. The delay between laser pulses Δt was adjusted to resolve the entire flow field while observing the rule of thumb of the ¼ spot size maximum displacement. Note here that the maximum number of velocity vectors within a methane/air flame thermal thickness is evaluated to be on the order of 2 for the strongest flames, e.g. E.R.=1.0, to 5 for the weakest ones, e.g. E.R.=0.6 (see Table III.3 for additional details).

Flame Thicknesses in μm	*Diffusion Th.* $\delta = \frac{D_T}{S_u^0}$	*Thermal Th.* $\delta_{th} = \frac{T_b - T_u}{max\,\{dT/dx\}}$	*Chemical Th.* $\delta_{ch} = \frac{\delta_{th}}{Ze}$	PIV Spatial Resolution in μm
E.R. = 0.6	192	1067	103	≈ 200
E.R. = 1.0	57	471	42	

Table III.3 Examples of methane/air flame thicknesses (All parameters calculated with the PREMIX code [27] along with the GRI-Mech. 3.0 [148] kinetic mechanism and related thermodynamics and transport properties, parameters are : D_T, mixture thermal diffusivity, T_b, temperature of burned gases, T_u, temperature of fresh gases, *Ze*, Zeldovich number).

The flowchart of the typical algorithm combination used for the vector processing step is shown Figure III.4. Input images were first split into 64 pixel square spots to compute the intermediate vector velocity field. The latter was used in a second pass to optimize displacement calculations as discussed above. The correlation step was accomplished through FFT correlation which considerably decreased computation time compared to direct correlation processes. Gaussian correlation peak localization, supposed to improve peak locking issues [141], was also selected. Two user-defined files could be specified: the pass validation file, filtering the intermediate velocity vector field, was usually set to remove outliers and fill up resulting holes in the velocity grid. The second file, related to the final vector validation, was typically chosen to remove the last spurious vectors. Consequently, the final velocity field was obtained without any filtering, such as smoothing or averaging, therefore conserving integrity of raw velocity measurements defined in the second pass. As such, series of 250 image pairs were usually computed within 30~40 minutes.

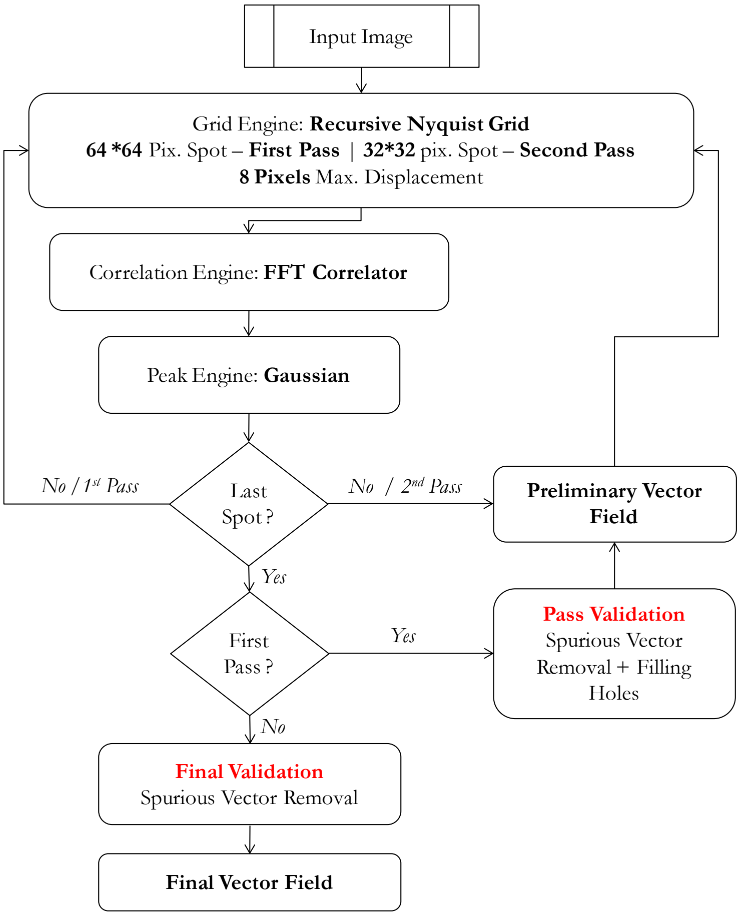

Figure III.4 Processing flowchart.

III.3.2 Choice of Seeding Material for the Present Application

As discussed in the precedent chapter, this issue is of prime importance as measurements directly rely on the capacity of seeded particles to closely follow the flow. Details on appropriate seeding materials for PIV applications can be found in ref. [36] and combustion related issues in ref. [149]. A conventional practice, widespread in combustion experiments, is to select micron and submicron particles according to manufacturer's primary diameter specifications. Based on previous experimental reports, it is then assumed that chosen particles are suitable for intended applications. However, the tendency of submicron particles to agglomerate is often overlooked. For instance, it has been shown that SiO_2 nanoparticles, prone to agglomerating fluidization, cannot be characterized by their primary particle size: their hydrodynamic behavior has to be related to physical properties of agglomerates [150]. This result is of particular interest in the present experiment as the seeded flow is driven through various channels and seeding devices that might enhance the buildup of cohesive forces between individual particles.

Aware of these possible agglomeration problems, it was decided to perform trial tests to help in the choice of seeding materials that would further be used. This study was performed in the stagnation plate configuration (Burner I.D.: 7mm), using nitrogen inert jets and reactive methane/air jets. Studied particles, primary particle sizes and the test matrix are displayed Table III.4. The entire burner setup and ducts were cleaned between each experimental set to avoid any interference. For each case, 300 image pairs were taken and an identical processing step was performed. As a result, averaged normal velocity profiles in the centerline of the jets were computed and compared for the inert (Figure III.5) and reactive cases (Figure III.6) respectively.

Particle type	Particle Diameter (μm)	Manufacturer	NON-REACTIVE CASES (N_2 JET)			REACTIVE CH_4/Air E.R.=1
			2.5 L/min	3 L/min	5.5 L/min	
Al_2O_3	0.32-0.43	ALPHA AESAR	●	●	●	●
Al_2O_3	0.44-1.67	ALPHA AESAR		●	●	●
TiO_2	1.22	ALPHA AESAR			●	
ZrO_2	1.8	VWR-PROLABO	●	●	●	●
Al_2O_3	2.07	ALPHA AESAR			●	
Al_2O_3	20-50	ALPHA AESAR	●	●		●

Table III.4 Tested particle matrix.

For the non-reactive cases, it can be seen that for the 3 different flow rates 2.5, 3 and 5.5 L/min, corresponding to maximal velocity gradients of 443, 554 and 928 s^{-1} respectively, particle motions are identical, and therefore size effects seem to be negligible. Indeed, in this moderate velocity gradient situation, all particles are expected to closely follow the decelerating flow. However, remarkable differences can be observed on Figure III.6. While micron-size Al_2O_3 (0.44-1.67 μm) and ZrO_2 (1.8 μm) particles give closely matching velocity profiles at any point in the flow, profiles obtained for the submicron Al_2O_3 (0.32-0.43 μm) and larger sizes (20-50 μm) significantly depart from the two first ones in the fast accelerating preheat zone. The results are however unexpected: compared to micron size particle velocities, the larger lag is observed for the smallest particles when larger ones seem to better catch the higher velocity gradient (2900 vs. 2400 s^{-1}). It was however clear that fairly large particle images were observed on DPIV images taken for the submicron size Al_2O_3 particles, suggesting the formation of strong agglomerates during the experiment. To remove the ambiguity, powder samples structures were determined by Scanning Electron Microscopy (SEM). Samples were acquired either directly from their original recipient or at the burner exit by adhesive tape. Figure III.7 to Figure III.10 gather SEM analysis. If the largest Al_2O_3 particles effectively have diameters in the order of few tens of microns (Figure III.7), their detailed structure suggests networks of submicron chains (Figure III.8). Thus, an increased drag force due to large particle diameters d_p and reduced inertial effects due to a low particle density ϱ_p might explain that these larger particles are better tracers than heavy agglomerates prone to gravity effects in the fast expanding region of the flame. Al_2O_3 and ZrO_2 micron size particles seem however to be the most adapted seeding materials for the present application. Their detailed structure can be seen Figure III.9 and Figure III.10. If primary particle sizes seem to be in accordance with manufacturer's specifications, shapes of particles are quite different. As sphericity is an assumption often made to apply force formulation mentioned earlier, rounded ZrO_2 particles (1.8 μm) were preferred to Al_2O_3 particles (0.44-1.67 μm) and have been used for experimental works reported herein.

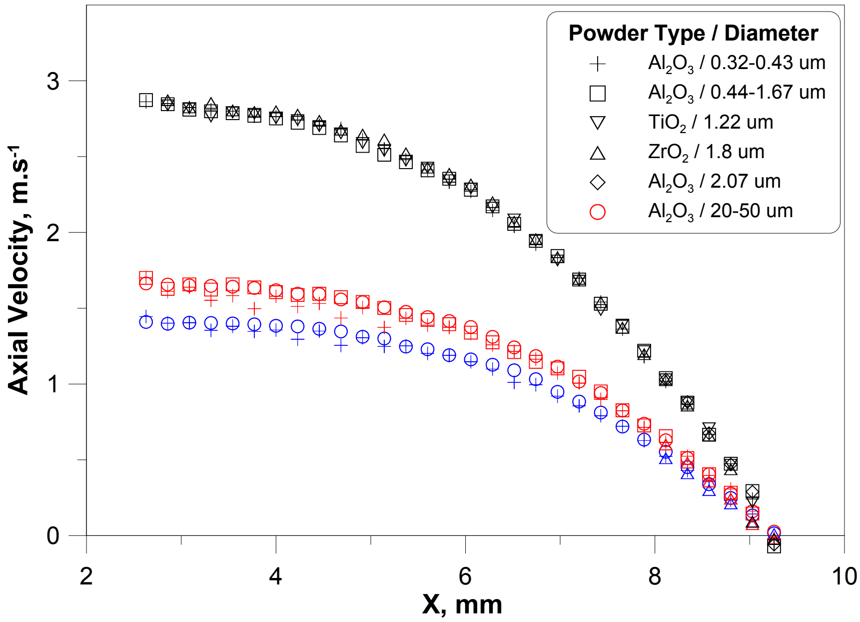

Figure III.5 Centerline velocity profiles of non-reacting nitrogen jets impacting on a stainless steel plate for different seeding materials and 3 different flow rates: 2.5 L/min-blue symbols, 3 L/min-red symbols, 5.5 L/min-black symbols (*BID*: 7 mm, *BC*: SP, L_{sp}: 7 mm, *CFR:* No).

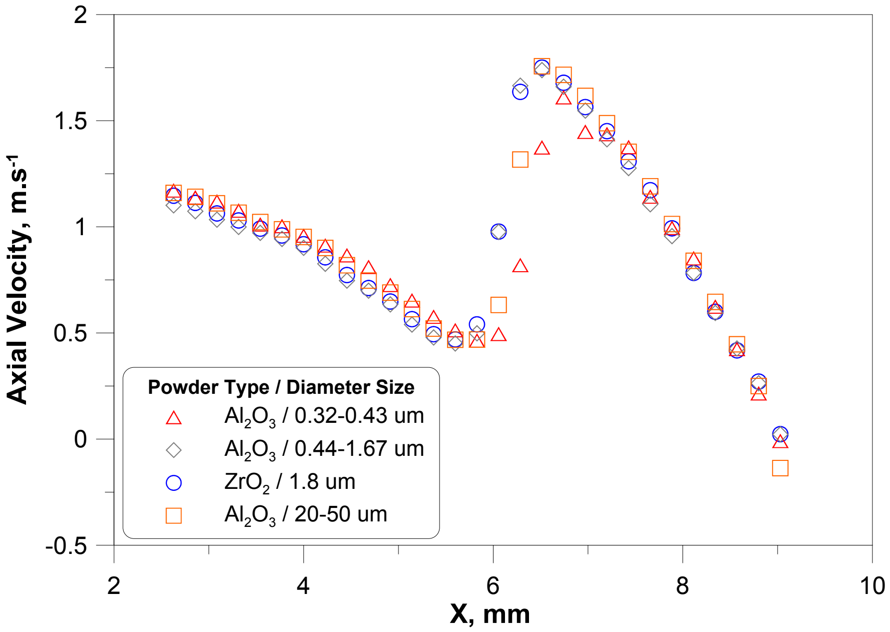

Figure III.6 Centerline velocity profiles of reacting jets impacting on a stainless steel plate for different seeding materials (*MB*: CH_4/Air, *ER*: 1.0, *BID*: 7 mm, *BC*: SP, L_{sp}: 7 mm, *MFR*: 2.144 L/min).

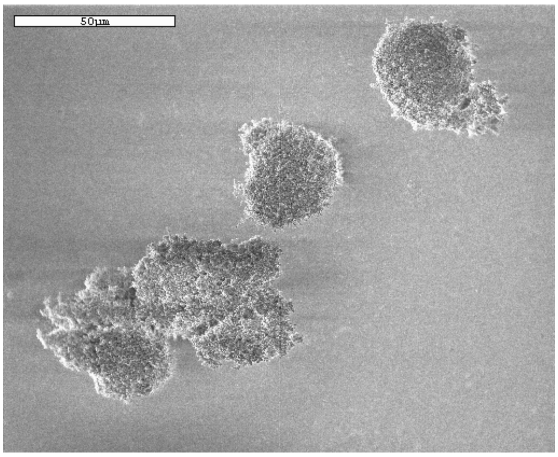

Figure III.7 Al_2O_3 particles (20-50 µm primary particle size) / Scale: 50 µm.

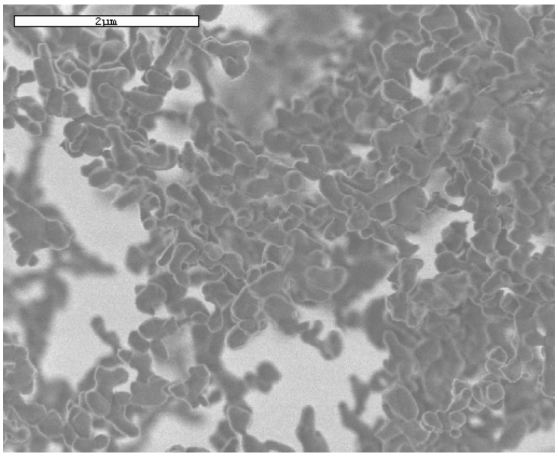

Figure III.8 Al_2O_3 particles (20-50 µm primary particle size) / Scale: 2 µm.

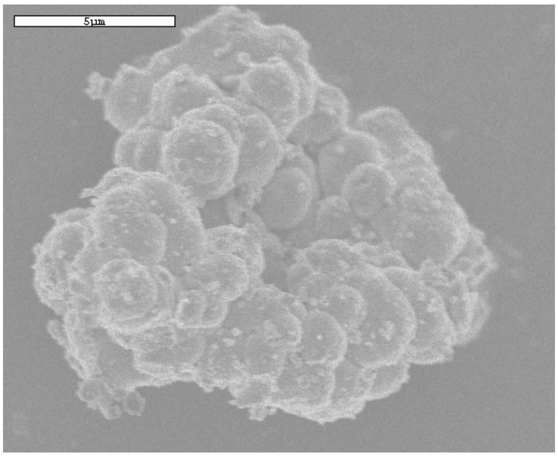

Figure III.9 Agglomerate of ZrO_2 particles (1.8 µm primary particle size) / Scale: 5 µm.

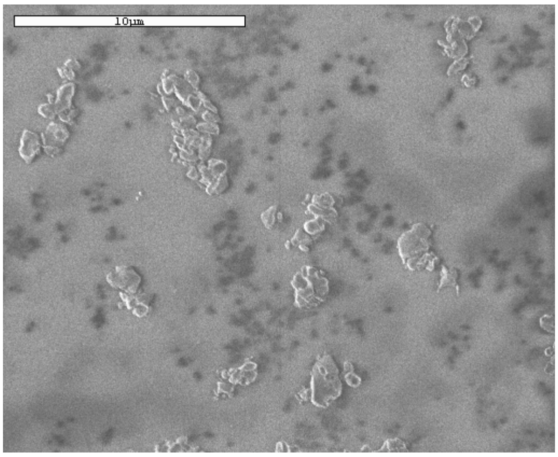

Figure III.10 Al_2O_3 particles (0.44-1.67 µm primary particle size) / Scale: 10 µm.

III.3.3 Particle Density Effects

Another concern in velocimetry experiment involving seeded flows is the relation between particle tracer density and quantity and quality of resulting measurements. For instance, increasing particle mass flow rate in the present experiment might improve or even render possible computations of area with lower particle densities (i.e. post-flame regions) but also decrease estimated displacement uncertainties by adding information to particle samples contained in interrogation spots. The underlying limit is of course when potential interactions with the studied medium occur. This is particularly true for combustion-related investigations were flames could be expected to have a thermal dependence on the particle density, although most experimental investigations readily assume zero interaction with the reactive medium. Only few studies reported on this matter. Andac and coworkers [151] numerically and experimentally investigated the effects of inert particles on the extinction of strained methane and propane laminar flames, both premixed and non-premixed, at normal and microgravity conditions in the counterflow configuration. Fairly large particle diameters were selected including 20 and 37 μm nickel-alloy and 25 and 60 μm aluminum oxide particles. Interestingly, it was shown that, for moderate strains, larger particles were more efficient at cooling the flame than smaller ones, even if, for an equivalent mass, the ratio of the exposed surface area to the total volume was less in this case. A second study by the same author [152] confirmed this trend but also showed that the reverse happened at higher strain rates. In addition, it was found that the flame cooling efficiency was not only governed by particle diameter but also equivalence ratio. This phenomenon was analyzed in the light of both particle dynamics and residence time within the flame reaction zone. A second numerical study of dusty reacting flows, already mentioned in the previous chapter, was reported by Egolfopoulos and Campbell [38] for laminar premixed hydrogen/air flames in the counterflow configuration. Small aluminum particles (0.3 μm) were found to closely follow the gas phase temperature in a counterflow H_2/air flame at equivalence ratio 0.57. Simulations were also carried out by varying the number of injected particle per cubic centimeter in the same flame. Concentrations spanning 10 to 24500 particles/cm^3 for 20 μm Al_2O_3 particles and 10 to 25258 particles/cm^3 for 50 μm Al_2O_3 particles were studied. It was shown that higher particle concentrations can significantly reduce the flame temperature and ultimately lead to flame extinction. These observations should be however put into perspective: flames studied above are in the very lean domain, seeded with large particles on the order of few tens of microns. Also, extinction phenomena observed in studies presented in reference [151-152] result in a progressive fuel decrease in the mixture rather than heavy seeding concentrations. For all these reasons direct comparison with experimental conditions involved herein might not be very meaningful.

Alternatively, it was decided to carry out a comparative study on seeding concentrations to approximately evaluate the average particle number per interrogation spots for all computed cases. A Matlab program, based on a particle intensity detection threshold level, was developed and applied to a trial case (300 DPIV image pairs) for which seeding concentration was decreasing in time. Results are presented Figure III.11 (a). The gray area is characterized by very heavy seeding concentrations (>20 particles/spot) and data points present in this region should be disregarded as the program fail to detect individual particles in this case. Particle concentrations are monitored in the core jet before the flame reaction zone and are visually displayed in the figures of the column (b). The column (c) gathers the corresponding velocity vector fields calculated in the flame region, encompassing both upstream unburned and downstream burned sides. It is clearly seen that even for very high particle concentrations (gray area), a certain number of vectors cannot be validated in the post flame region due to the important decrease of particle density. A drop of seeding concentration from 18 to 10 particles per interrogation spot slightly worsens the number of vectors that are resolved in the flame area. The vector loss is even more consequent with 5 particles per interrogation spot where important dark zones are observed. In the post flame region, particle concentrations were typically decreased by a factor of 7 or 8. From this test, it was evaluated that most runs done in the course of the present experimental study were recorded for a particle number per interrogation spot ranging from 10-12 to 16-18. The evolution of the total number of calculated vectors in percent versus the number of particle per interrogation spot is shown Figure III.12.

A turning point is observed for a concentration close to 5 particles per spot under which the total number of calculated vector is sharply decreasing. This is in accordance with numerical simulations of valid detection probabilities presented in ref. [42, 153]. In order to provide a comparison with particle concentrations involved in Egolfopoulos and Campbell numerical study [38], it was attempted to evaluate the equivalent particle concentrations per unit volume corresponding to the present experimental conditions, rescaled for particle sizes of ref. [38]. Based on an average 14 particles (2 μm spherical particles) per interrogation spot (32×32 pixels), a resolution of 14.27 μm/pixel and laser sheet thickness of 200 μm, the present concentration would correspond to 21 particles/cm^3 for 50 μm particle diameter and 336 particles/cm^3 for 20 μm particle diameter. These concentrations are somehow much lower than those observed to have thermal effects on the flame (see figures 5.12 and 5.14 of ref. [38]), which may suggest that no strong cooling effects have to be expected for the particle concentrations involved herein.

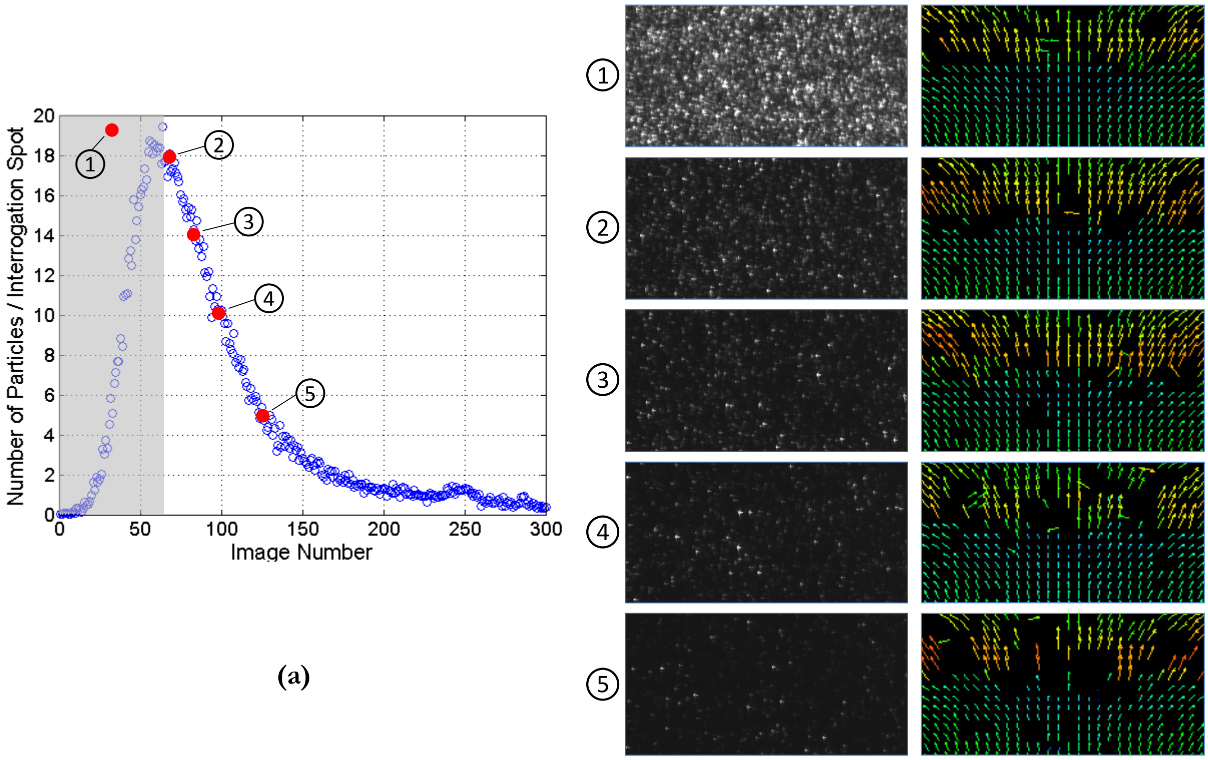

(a)

(b)

(c)

Figure III.11 Particle density effects: (a) Analysis of number of particles per interrogation spot for a continuously decreasing seeding concentration, (b) Seeding density in the center of the reactive jet (Upstream of the flame), (c) Corresponding velocity field at the flame location (*MB*: CH_4/Air, *ER*: 1.0, *BID*: 7 mm, *BC*: SP, L_{sp}: 7 mm, *MFR*: 2.576 L/min, *CFR*: 1.310 L/min).

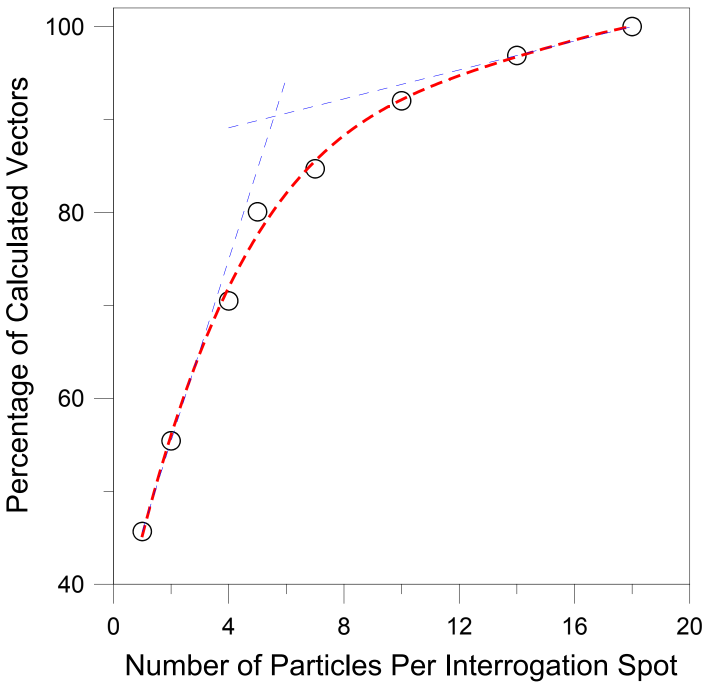

Figure III.12 Percentage of calculated vectors depending on the number of particles per interrogation spot. The number of vectors calculated (and validated) for the 18-particles/interrogation-spot case of Figure III.12 represent the 100% calculated vector case of the present figure.

III.3.4 Peak Locking Effects

During the analysis of certain velocity vector fields, an interesting issue arose. While plotting normal and tangential velocity gradients in the axial and radial direction respectively, ridges could be observed within the flow indicating periodical variations of measured velocity gradients (See Figure III.**13**).

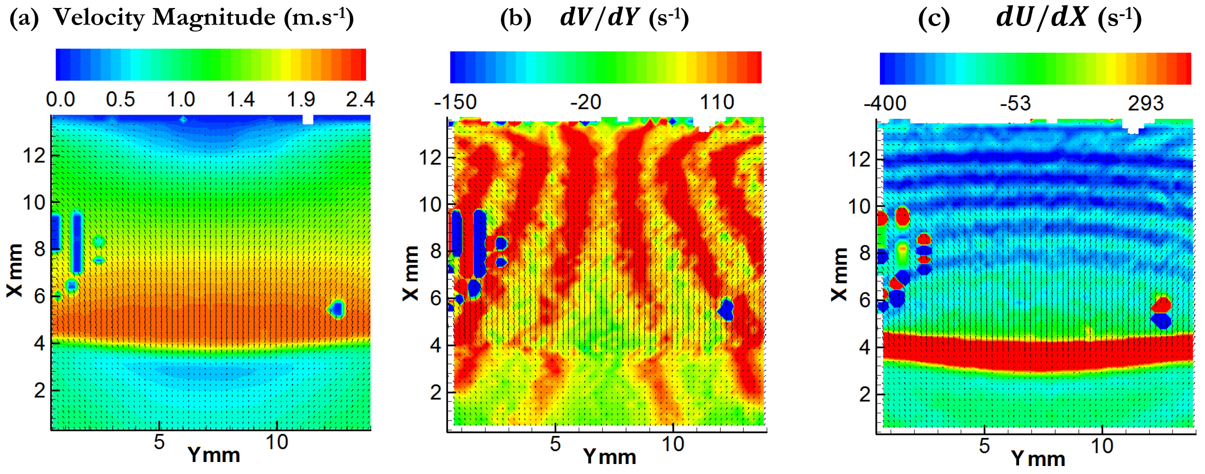
(a) Velocity Magnitude (m.s^{-1})

(b) dV/dY **(s^{-1})**

(c) dU/dX **(s^{-1})**

Figure III.13 Averaged vector velocity field characterizing a CH_4/air flame at an equivalence ratio of 1.0: (a) Velocity magnitude, (b) Tangential velocity gradient relative to location coordinate Y, (c) Normal velocity gradient relative to location coordinate X (*BID*: 15 mm, *BC*: SP, L_{sp}: 15 mm, *MFR*: 8.237 L/min, *CFR*: 8.301 L/min).

This curious pattern, however, could hardly be explained on physical grounds. Further investigations were performed and repartitions of normal and tangential displacements corresponding to velocity vectors of Figure III.13 were plotted Figure III.14 (a). It was found that the histogram of radial displacements was characterized by a distorted shape. This phenomenon is known as "peak locking" effect and tends to bias displacements towards integer pixel values. Several contributions to the peak locking effect are mentioned in the literature [42, 154]. They are including: sensor geometry effects (not enough spatial resolution to describe the particle), subpixel peak-fitting algorithm (bias in the location of the correlation peak maximum) and also truncation of particles at the border of interrogation spots (bias including systematic deviation towards zero displacement). Many attempts have been engaged to quantify peak locking bias on velocity measurements [155], alternatively minimize, correct or eliminate this effect [156-158].

Due to the extremely large number of parameters involved in the DPIV technique, a complete study of peak locking effects related to the present experiment was clearly impossible. Simple trial tests were however performed to evaluate the individual influence of the major PIV features including: the number/resolution of calculated vectors, the nature of the peak engines and the nature of the correlation engines. Results are presented in Figure III.14.

A first observation is that normal velocities are minimally affected by the peak locking phenomenon. As expected, a progressive increase of vector resolution from recursive large grids (64 to 64 pixel square spots) to small ones (32 to 16 pixels square spots) does not eliminate the aforementioned bias (Cases b → a → c). The respectively lower and higher peaks observed for the larger and smaller grids are only due to the total number of vectors that are considered, subsequently quadrupled in each step of the grid refining process. Surprisingly, the bias is smoothed when the bilinear peak detection is preferred to the Gaussian localization technique (case d vs. a). This somehow contradicts several observations usually recommending Gaussian fit to minimize peak locking effects [141]. This systematic bias is however not totally removed. Direct correlation, either by computing most significant pixels (Hart Correlator, case e) or all of them (Direct Correlator, case f) does not bring any particular improvement. In addition, it can be seen that compression of the information seems to significantly increase the histogram distortion (case e). A closer analysis of the cross correlation maps shows that the displacement peaks are generally clearly defined (see examples provided in Figure III.15), thus excluding any biasing effects due to improper shape of the displacement peaks.

DPIV Features	Axial Velocity Repartition	Radial Velocity Repartition
(a) 64 to 32 Recursive Algorithm • Maximum Displacement: **8 Pixels** • Grid Engine: **Recursive Nyquist** • Correlation Engine: **FFT Correlator** • Peak Engine: **Gaussian Peak**	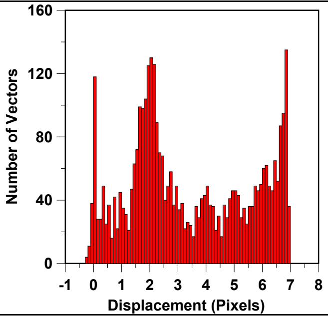	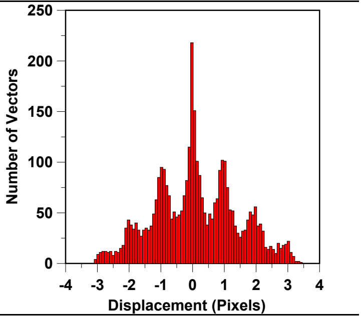
(b) 64 to 64 Recursive Algorithm • Maximum Displacement: 16 Pixels • Grid Engine: **Recursive Nyquist** • Correlation Engine: **FFT Correlator** • Peak Engine: **Gaussian Peak**	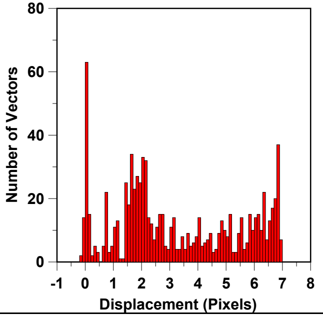	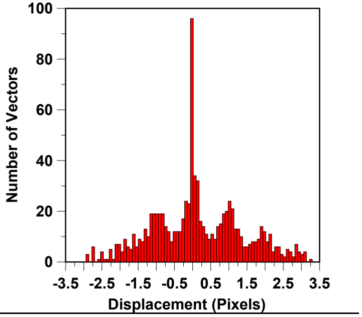
(c) 32 to 16 Recursive Algorithm • Maximum Displacement: **8 Pixels** • Grid Engine: **Recursive Nyquist** • Correlation Engine: **FFT Correlator** • Peak Engine: **Gaussian Peak**	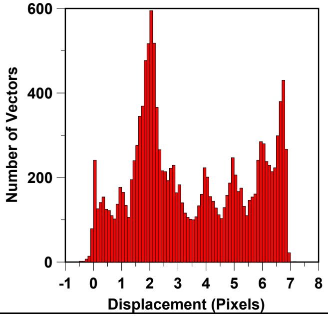	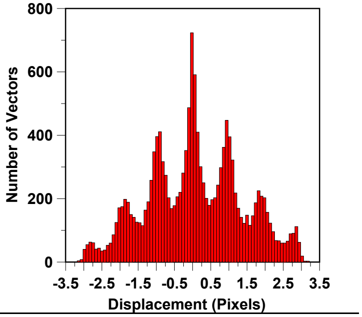
(d) 64 to 32 Recursive Algorithm • Maximum Displacement: **8 Pixels** • Grid Engine: **Recursive Nyquist** • Correlation Engine: **FFT Correlator** • Peak Engine: Bilinear Peak	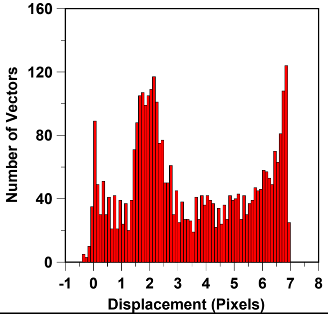	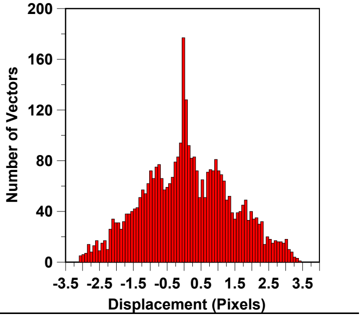
(e) 64 to 32 Recursive Algorithm • Maximum Displacement: **8 Pixels** • Grid Engine**: Recursive Nyquist** • Correlation Engine: Hart Correlator • Peak Engine: **Gaussian Peak**	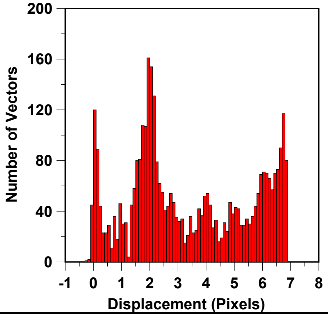	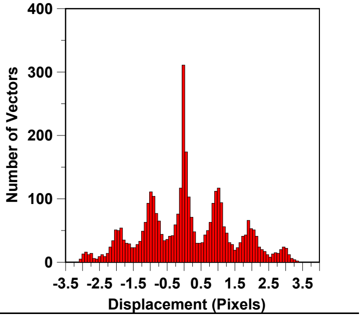
(f) 64 to 32 Recursive Algorithm • Maximum Displacement**: 8 Pixels** • Grid Engine**: Recursive Nyquist** • Correlation Engine: Direct Correlation • Peak Engine: **Gaussian Peak**	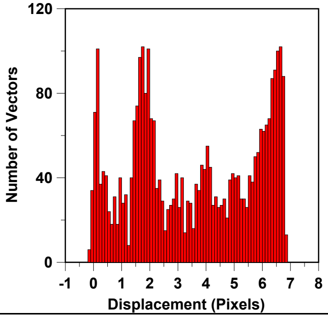	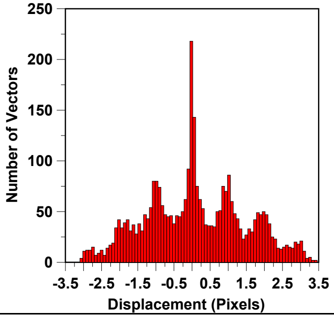

Figure III.14 Illustration of the peak locking phenomenon for different DPIV processing options.

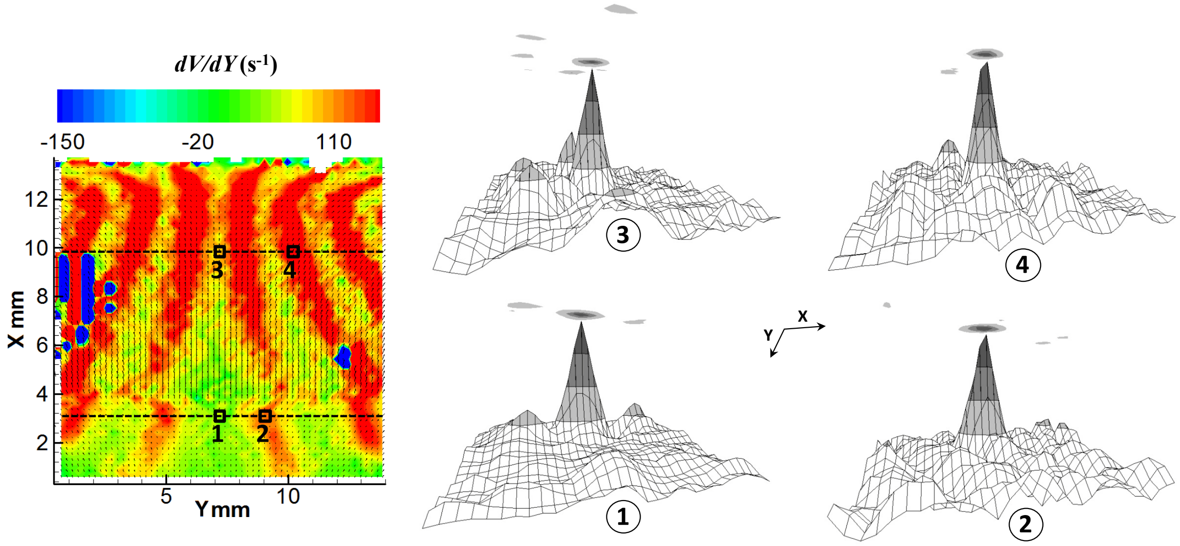

Figure III.15 Examples of correlation maps showing the main cross-correlation peaks for the case presented in Figure III.13. Corresponding processing options are listed in Figure III.14, case a.

Peak locking effects are further investigated Figure III.16 on normal velocity profiles taken at the centerline jet in the experimental conditions of Figure III.13. Velocity profiles computed with the different processing options of Figure III.14 confirm that peak locking has an insignificant effect on normal velocities. It can however be noticed that the velocity profile corresponding to the recursive 64 to 64 pixel spot grid substantially lays under other profiles at the beginning of the fast expanding preheat zone. The large window size is responsible for this discrepancy by giving an averaged displacement for interrogation spots in which strong velocity gradients are present, i.e. violating criterion III of Table III.1. By also poorly resolving the large velocity gradient close to the flame, such window sizes are clearly not adapted to the present experimental conditions. Looking at reference velocities $S_{u,ref}$ of Table III.5 extracted from the first local minima of velocity profiles of Figure III.16, determined values lay in a comprehensive 2 cm.s^{-1} range (64 to 64 grid algorithm excluded). Thus, if the choice of processing options is seen to have a minor influence on calculated velocities, it is reasonable to expect, at least, a ±1 cm.s^{-1} uncertainty on final unstrained flame velocities for flames with similar characteristics.

Tangential velocity profiles in the radial direction located at the first local velocity minimum are plotted Figure III.17. As discussed in the previous chapter, these profiles allow an unambiguous determination of flame strain rates. As predicted by velocity repartitions of Figure III.14, stronger peak locking effects are observed compared to normal velocities. The least distorted profile was obtained for the bilinear peak estimator (case d) while strongest velocity deviations were computed with the Hart Correlator engine (case e), up to 40 % lower on the positive velocity side. An intermediate less perturbed solution is obtained combining the FFT Correletor and Gaussian peak fitting (case a). All other cases, not plotted in Figure III.17, gave deviations similar to the latter case. An important implication of the present observations concerns linear fitting procedures that are used to extract strain rates from tangential velocity profiles. It is recommended to extend the linear fit on the largest possible number of data points as seen Figure III.18. While a fitting procedure performed on the entire data range (red curve) yields a strain rate of 153 s^{-1}, a local fit on two points on each side of the reference point (blue curve) reaches 85.7 s^{-1}, a value somehow much lower than expected. If not properly taken into account, it may result in serious misinterpretations of flame sensitivity to strain rate variations. Note that if a large data range is considered for linear interpolation, the strain rate determined from the least biased profile (i.e. case d) is 153.4 s^{-1}. As such, there is no particular merit in using specifically one of the two available 3-point estimators. As a large amount of data points was already processed following steps of Figure III.4, the Gaussian peak fitting procedure was kept for the remainder of DPIV series. Linear fits on tangential velocities were typically computed on more than 40 points.

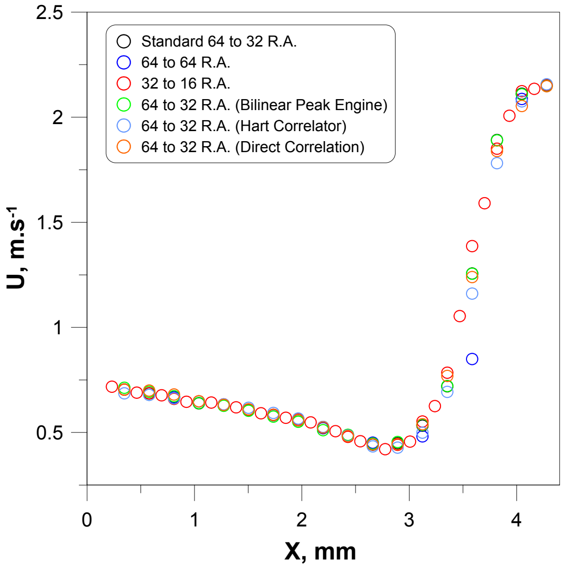

Figure III.16 Centerline velocity profiles of normal velocities calculated for the different processing options of Figure III.14 (R.A.: Recursive Algorithm).

Processing	Reference Velocity (cm.s^{-1})
Standard 64 to 32 R.A.	44.20
64 to 64 R.A.	45.15
32 to 16 R.A.	42.05
64 to 32 R.A. (Bilinear Peak Engine)	44.73
64 to 32 R.A. (Hart Correlator)	42.79
64 to 32 R.A. (Direct Correlation)	44.31

Table III.5 Reference velocities for the different processing options of Figure III.14. (R.A.: Recursive Algorithm).

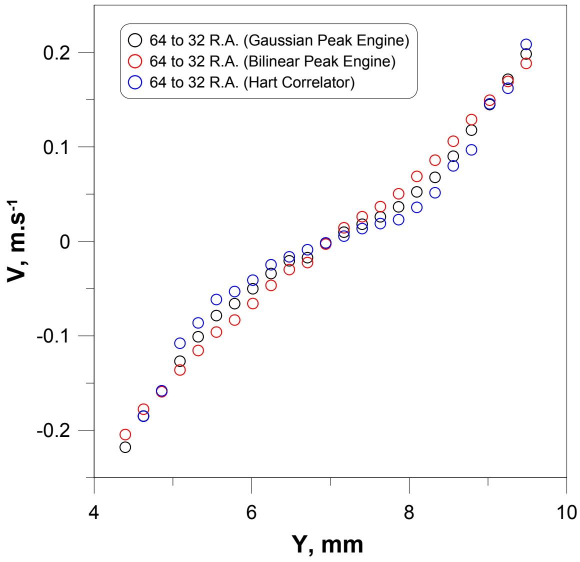

Figure III.17 Tangential velocity profiles in the radial direction at the minimum reference velocity location for different processing options (R.A.: Recursive Algorithm).

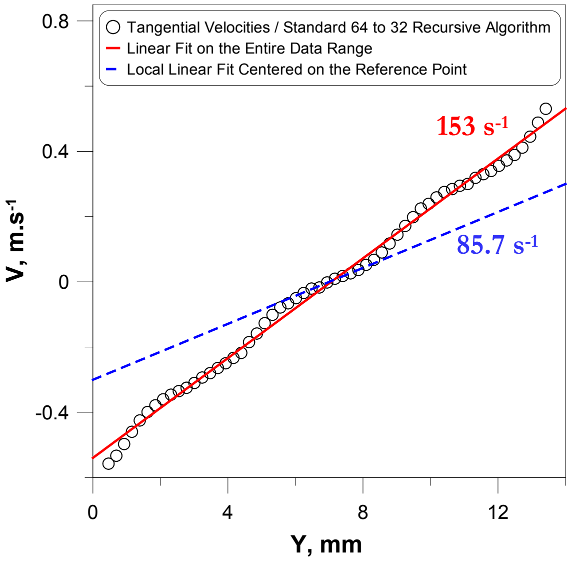

Figure III.18 Tangential velocity profile in the radial direction at the minimum velocity location and associated linear fits.

III.3.5 Laminar Flame Speed Extraction Procedures and Data Reduction

Large series of DPIV image pairs, typically 250-300, had to be recorded and processed in order to determine fundamental flame speeds. Therefore FORTRAN routines were developed to automatically extract useful information from computed instantaneous velocity profiles. These characteristic values appear on Figure III.19. They are: the first local minimum of the normal velocity on the centerline axis, referred before as the reference velocity $S_{u,ref}$ (a), the axial velocity gradient upstream of the point of reference, being the axially determined strain rate K (a), and the tangential velocity gradient taken in the radial direction at the point of reference, yielding the strain rate value K_r (b) when multiplied by 2.

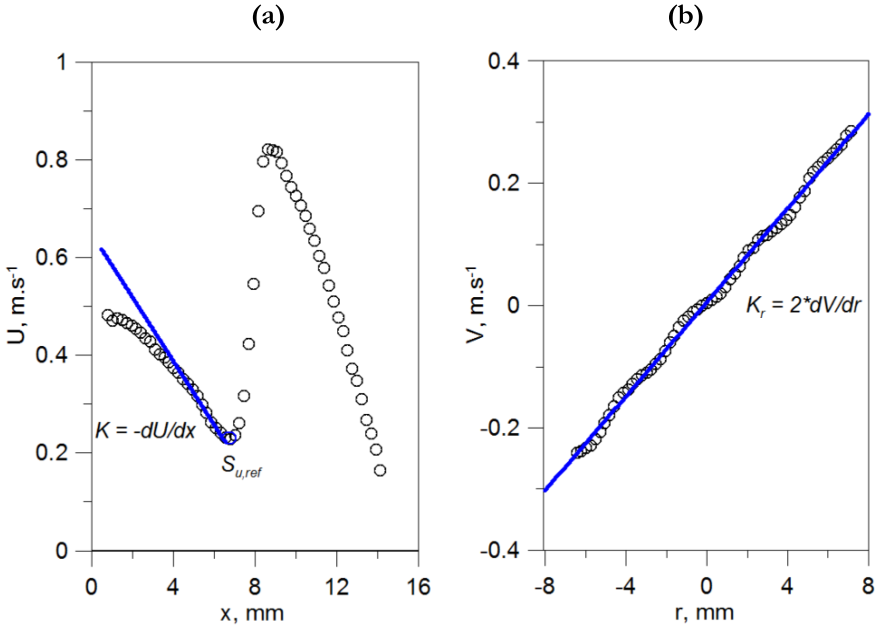

Figure III.19 Typical averaged velocity profiles measured in stagnation flames: (a) Normal velocity profile in the centerline of the reacting jet. The negative velocity gradient upstream of the reference point $S_{u,ref}$ is the axially-determined strain rate K, (b) Tangential velocity profile taken in the radial direction at the point of reference. The strain rate K_r determined in the radial direction is equal to twice the calculated gradient.

A non-negligible complication of this post-processing phase lays in the fact that instantaneous velocity fields have to be analyzed with a potential lack of data. Especially, the velocity at the point of reference should be clearly identified and linear fit computed on a sufficient number of data points. However, instantaneous fields rarely have high filling ratio mainly because seeding densities considerably vary across the flame. Also, heavy loads of particles are not recommended in the present application due to the possible perturbation of the flame front. The routine presented Figure III.20 is used to sort velocity fields and extract the useful data. Velocity vector fields are first read and a zone of interest is specified by the user to downsize the investigated region and decrease computation time. The jet centerline is then detected and local velocity minimum found through a gradient comparison method. Neighborhood points are then analyzed to make sure that the velocity minimum found is clearly defined, i.e. vectors upstream of this point are existing and belonging to the deceleration part of the velocity profile while downstream vectors, also defined, are indicating a velocity increase due intense preheating from the flame reaction sheet. Vector fields not complying with this "filling-condition" were discarded. For common seeding conditions and 250 image pairs, up to 150 were selected and the remainder removed. Strain rates associated to the extracted $S_{u,ref}$ were then calculated following the axial and radial definition indicated above, by linearly fitting velocity profiles on data ranges defined by the user.

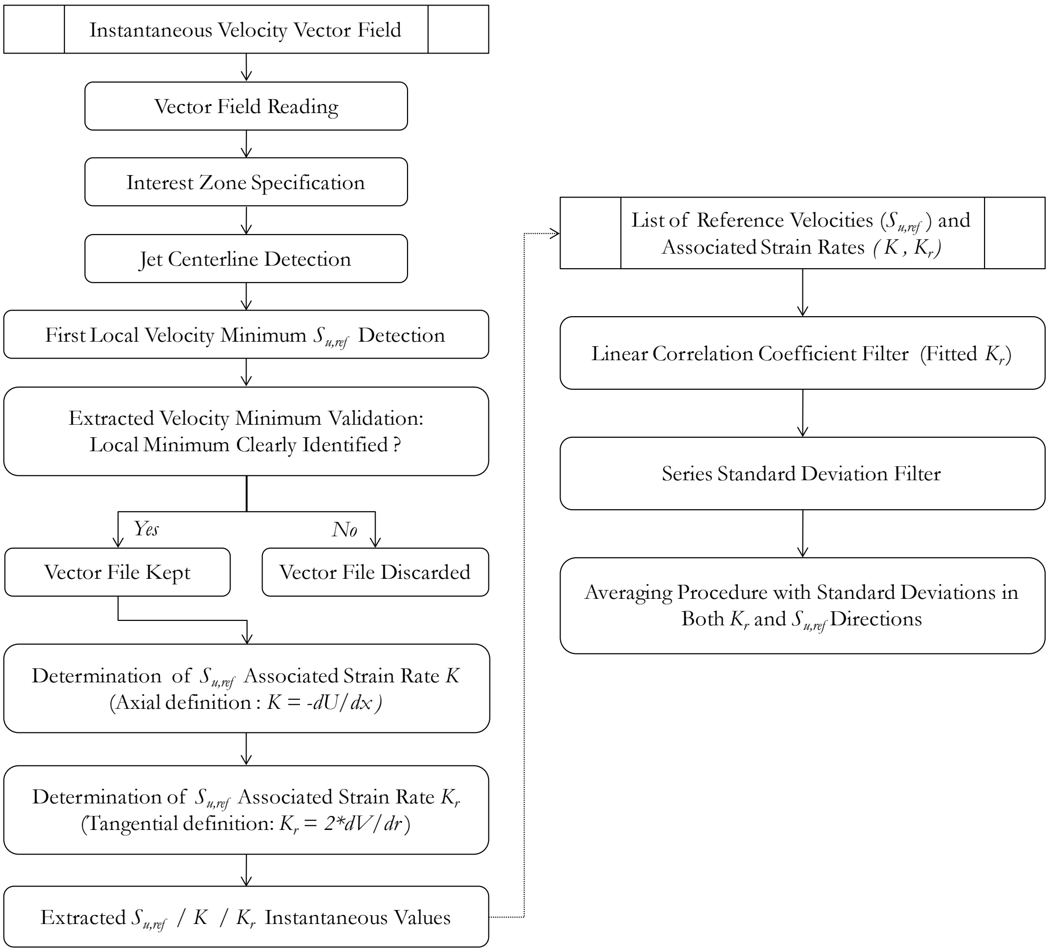

Figure III.20 Procedure for laminar flame speed (and related parameter) extraction from instantaneous velocity vector files and data reduction.

It is worth mentioning that the present methodology allows a dynamic tracking of the reference minimum and its associated strains along the centerline axis of the reactive jet. In other words, if the flame is prone to unsteadiness, the spatial localization of extracted velocity minimum is allowed to vary. This is a consequent improvement compared to post processing methodologies based on averaged observations (either PIV averaged fields or laser single point techniques such as LDV) "compressing" the experimental data in a single value for which the experimental uncertainty can be increased through the aforementioned positioning error.

The second step of the post processing phase, also visible on Figure III.20, consists of removing spurious data points by successively filtering poorly-fitted radial strain rates (Filtering according to linear correlation coefficient) and remote outliers (Filtering usually bypassing points outside the $\pm 3\ \sigma$ range). Not more than 5 points were usually discarded by this procedure. Averaging of small groups of data points (usually 10) were then performed among series of same experimental conditions and linear extraction was subsequently computed from these averages and their calculated standard deviations in both $S_{u,ref}$ and K_r directions (See next section). Note that the data reduction procedure applies on $(K_r , S_{u,ref})$ pairs. It can be seen Figure III.21 that determination of strain rates from the axial definition is prone to an important scatter. Indeed, for the present example, reference points are spread over a 150 s^{-1} range while strains calculated with the radial definition indicates that most values are in a range of 249 ±3.5 s^{-1}. The conventional fit performed on plug flow type profiles characterizing most of experimental counterflow works is clearly inferior for strain determination. The DPIV technique can remove this ambiguity by directly providing the radial information necessary to compute meaningful strain rates, without extensive and time consuming probe displacement as performed with single point measurement techniques. Thus, all results presented herein will be based on the radial determination of strain rates.

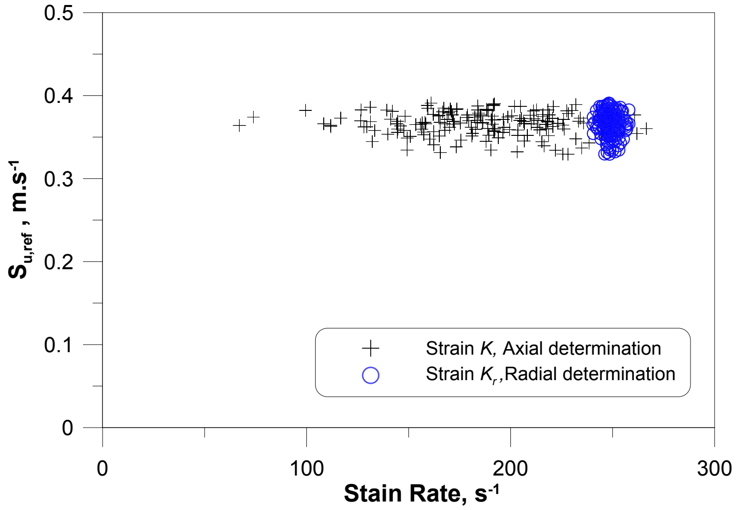

Figure III.21 Comparison of strain rates determined in the axial and radial direction with respect to the point of reference. (Axial strain: linear fit on the first 5 upstream points, radial strain: linear fit on 24 points on each side of the point of reference) – (*MB*: CH_4/Air, *ER*: 0.8, *BID*: 15 mm, *BC*: CT, *L*: 16.6 mm, *MFR*: 13.028 L/min, *CFR*: 12.818 L/min).

III.3.6 Uncertainty Analysis

A key parameter in DPIV experiments is the laser delay Δt between two consecutive pulses that determine, in accordance with the maximum ¼ rule displacement rule of thumb, the maximum velocity that can be calculated and therefore the dynamic spatial range. Figure III.22 shows different normal velocity profiles taken in the centerline jet of methane/air flame calculated for a varying pulse delay from 45 to 90 µs. While shortest delays (45 and 50 µs) still permit to capture the entire velocity profiles, an increase of the pulse Δt progressively truncates measurements and higher displacements cannot be resolved any more. If information is lost, however, smallest displacement are benefitting from an enhanced pixel resolution and therefore the uncertainty involved in the subpixel correlation peak localization will affect the final velocity value in a lesser extent.

Delta t (μs)	STANDARD DEVIATIONS IN %		UNCERTAINTY IN %	
	Minimum Velocity Tracking on Instantaneous PIV Files	Minimum Velocity Extraction from Averaged Series	0.1 Pixel Uncertainty for Correlation Peak Location Estimation	0.05 Pixel Uncertainty for Correlation Peak Location Estimation
45	5.7	10.1	7.7	3.9
50	8.5	9.9	6.3	3.1
60	3.3	3.5	5.3	2.6
70	1.7	4.5	4.8	2.4
90	2.7	18.9	3.5	1.7

Table III.6 Standard deviations for different velocity minima extraction methods and uncertainties in instantaneous determined velocities due to the correlation peak location estimation process.

This can be seen Table III.6 (Column 3 and 4) where uncertainties of 1/10 and 1/20 of a pixel will respectively lead to uncertainties of 7.7 to 3.5 % and 3.9 to 1.7 % on the calculated velocity for the different laser pulse delays of interest. One could, of course, be tempted to consequently increase the laser pulse delay to minimize the uncertainty related to the smallest observable length scale in the flow. This has been done in recent studies [90, 97] by imposing a maximum calculated velocity not exceeding 1.4 times the reference velocity. As seen Figure III.23, this criterion is extremely restrictive on the number of calculated vectors and a "clear" identification of the local minimum in the conditions describe in the previous sections seems to be compromised. Also, as detailed modeling was intended in the present study, it was necessary to obtain "entire" velocity profiles in order to provide enough information to validate results of computational approaches. This was done by reducing the pulse delay until entirely resolving the flow. Note however that the full scale accuracy of the present DPIV setup, as defined by Wernet in ref. [159], is equal to 1.25%, a value similar to those determined in ref. [90, 97].

As standard deviations in experimental series performed for the same experimental conditions (Table III.6, column 1) were seen to be in the range of the aforementioned uncertainty values (Table III.6, columns 3-4), and confronted to the difficulty of evaluating uncertainties related to subpixel localization procedures, it was decided to perform average of groups of instantaneous reference velocity values (typically 10) within experimental series. These points were further used in an extrapolation procedure [160], taking into account standard deviations in both K_r and $S_{u,ref}$ values to finally yield the unstrained fundamental flame velocity S_u^0. A such, scatter in both coordinates, mainly due to slight unsteadiness of the flow, were incorporated while undesired sensitivity of the linear extrapolation to outlying points was minimized.

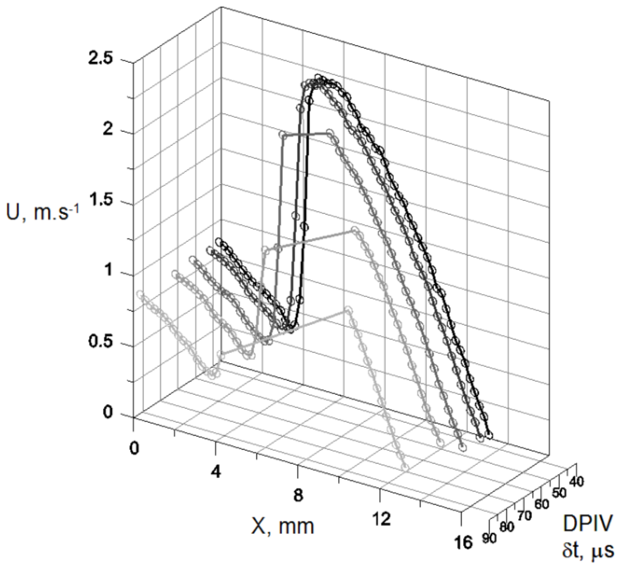

Figure III.22 Centerline normal velocity profiles for a CH_4/air flame at equivalence ratio 1.0 and different DPIV delays: from black to clear gray 45, 50, 60, 70, 90 μs respectively (*BID*: 15 mm, *BC*: SP, L_{sp}: 15 mm, *MFR*: 8.975 L/min, *CFR*: 7.081 L/min).

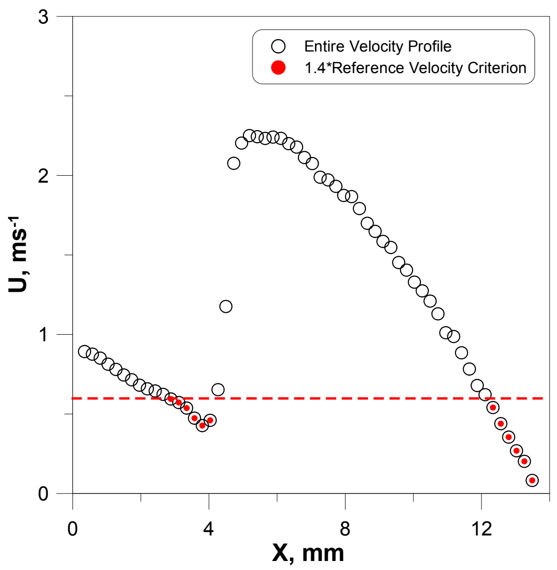

Figure III.23 Comparison of a fully-resolved centerline normal velocity profile and resolved profile applying the 1.4*(reference velocity) criterion (Same configuration and experimental conditions as Figure III.22).

An important remaining issue is to characterize the level of uncertainty related to the present extrapolation procedure as well as main parameters seen to influence this level. Such information is rarely mentioned in the literature although it can provide a practical insight into choices to be experimentally made for the extrapolation optimization. Based on experimental observations, 6 series of synthetic data points (see Figure III.24) were created by adding a random Gaussian noise to linearly-positioned data points ($y = 1.10^{-4}x + 0.4$). Each point, representing an average of instantaneous reference velocities, can be characterized by 4 degrees of uncertainty in both K_r and $S_{u,ref}$ directions including σ_{K_r} = 1, 5, 10, 15 s-1 and corresponding $\sigma_{S_{u,ref}}$= 0.005, 0.015, 0.025, 0.035 m.s-1. These different levels implicitly represent the flame "degrees of steadiness", the first and last one, respectively corresponding to very stable and perturbed flames, were hardly achieved in practice. The second and third levels were seen to be relevant for most flames studied herein. Linear extrapolations following the methodology proposed in ref. [160] were performed on the 6 artificially created series of data points by varying independently the three following parameters: i/the lowest strain rate achieved K_{low} , ii/the number of points per series N_{dp}, iii/ the strain rate range achieved ΔK_r. The baseline case assumes the following parameters: K_{low}= 200 s-1, N_{dp} = 10, ΔK_r = 200 s-1. It can be seen, Figure III.25, that the uncertainty in the extrapolated S_u^0 value follows a linear dependence with the lowest achieved strain rate. To yield uncertainties on the order of ±1 cm.s-1, the first lowest point should be located around 150 s-1 for an "intermediate" flame stability. This recommendation might be difficult to apply while studying very fast flames: for a fixed burner to stagnation plane distance, decreasing the strain rate might lead to stabilization of the flame on the burner rim or even flashback event. On the other hand, increasing the burner to stagnation plane distance will worsen flame stability. Clearly, a compromise has to be found. S_u^0 uncertainty, however, display a power law dependence with an increased N_{dp} (see Figure III.26). It is worth to mention that beyond 10-15 averaged points per series, the gain on the uncertainty is substantially reduced. Thus, there is no advantage in further increasing the number of data points per series. Therefore, based on 10 instantaneous points per average, 150 instantaneous velocity fields are seen to provide a reasonable amount of information for the extrapolation procedure, requiring in return a slightly higher number or recorded cases (typically 250), depending on seeding quality and post processing issues commented earlier. Finally, the influence of the strain rate range achieved is presented Figure III.27. Similarly to the previous case, S_u^0 uncertainty describe power law variations with the width of strain rate span, indicating that ΔK_r should at least cover a 150 s^{-1} range for the uncertainty to be kept on the order of ±2.5 $cm.s^{-1}$ for all flames. A wider strain rate interval does not provide a significant improvement on the extrapolated velocity value. It is important to emphasize that consequent deviations can occur if ΔK_r is not wide enough (Figure III.28). Under a 100 s^{-1} wide strain range, extrapolated values start to be biased towards lower values which can be explained by the enforced influence of outlier points. Note however, that the present example was developed for points with equal individual deviations which implies that all points were “equally considered” in the extrapolation computations. This is however not true for realistic cases were outliers are generally characterized by higher standard deviations. As such, the extrapolation methodology presented herein is weighting each individual point thanks to the given standard deviations, thus minimizing the impact of outlying points on the extrapolated values.

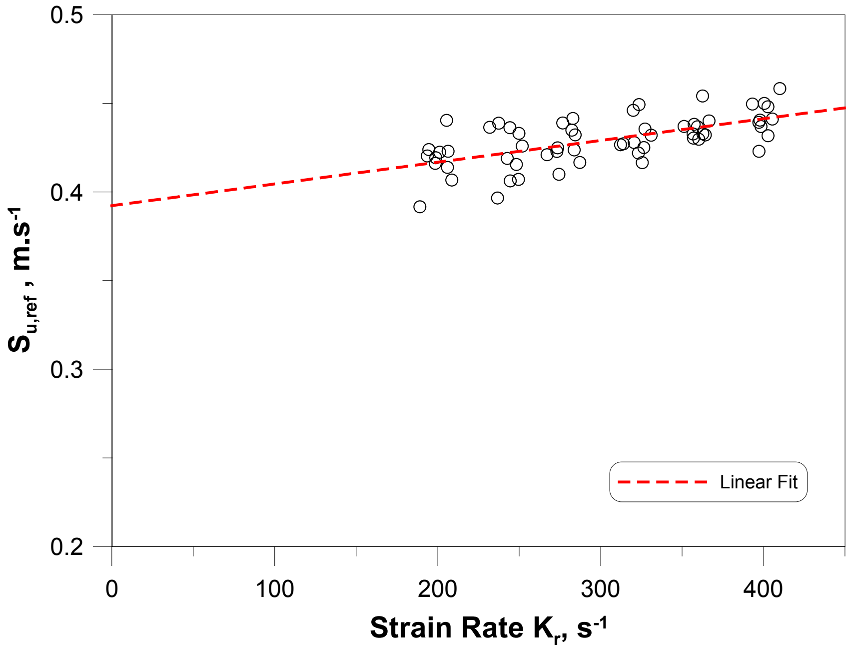

Figure III.24 Examples of randomly generated points for linear extrapolation evaluation (K_{low} : 200 s^{-1}, N_{dp} : 10 and ΔK_r : 200 s^{-1}).

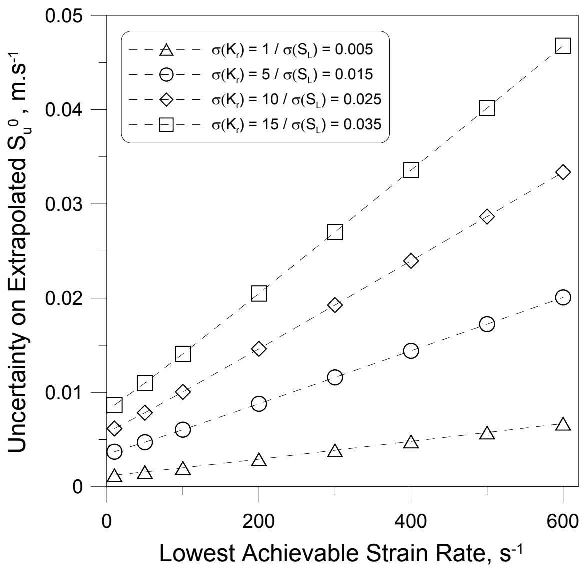

Figure III.25 Uncertainty on extrapolated S_u^0 value depending on the lowest achieved strain rate (N_{dp}: 10, ΔK_r: 200 s^{-1}).

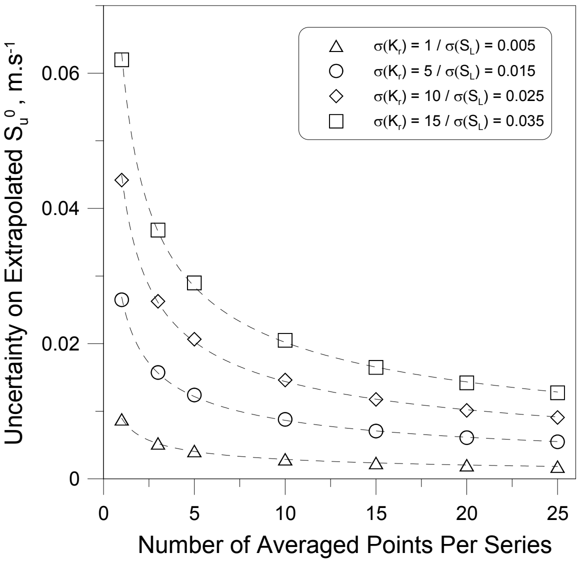

Figure III.26 Uncertainty on extrapolated S_u^0 value depending on the number of averaged fitted points (K_{low} : 200 s^{-1}, ΔK_r: 200 s^{-1}).

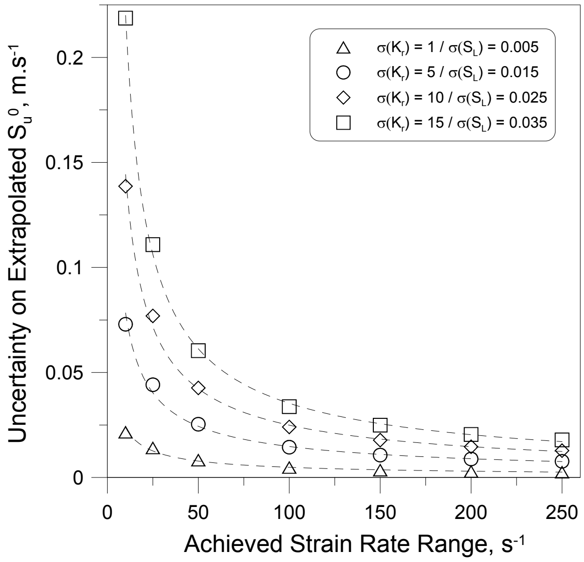

Figure III.27 Uncertainty on extrapolated S_u^0 value depending on the strain rate range achieved (K_{low} : 200 s^{-1}, N_{dp} : 10).

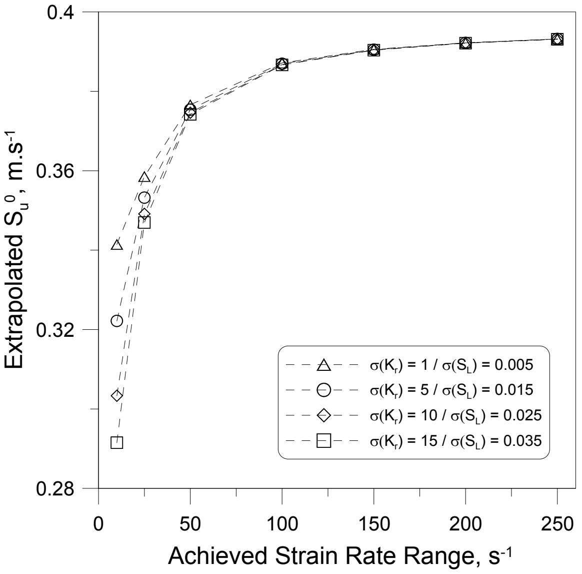

Figure III.28 Extrapolated S_u^0 value depending on the strain rate range achieved (K_{low} : 200 s^{-1}, N_{dp} : 10).

III.4 Summary

Principles of Digital Particle Image Velocimetry have been recalled. The diagnostics setup for flame speed determination, as well as DPIV specifications, have been presented. A spatial resolution on the order of 200 μm is typically achieved. The customized vector processing algorithm encompasses a recursive Nyquist grid (64×64 → 32×32), a FFT correlator engine and a Gaussian peak localization engine.

Tests have been performed on various flow tracers seeded in inert and reactive jets impacting on a stagnation plate. It has been observed that ZrO_2 particles with a primary particle size of 1.8 μm were the most appropriate for the present study among tested seeding materials. They were consequently selected for the flame speed measurements to be performed. A particle detection program has been developed to estimate the particle concentrations recorded on DPIV images. It was found that most of DPIV instantaneous series were characterized by 10-12 to 16-18 particles per interrogation spot. When compared to values of the literature, these estimated concentrations were found to be considerably lower than those shown to have thermal effects on flames.

An important finding of the present chapter is that peak locking effects may significantly bias the flame strain rates deduced from radial velocity profiles at the conventional point of minimum axial velocity. Indeed, it was shown that strain rates, calculated from a local evaluation of the radial velocity gradient, could be reduced by half. It is therefore recommended to perform the corresponding linear regression on the largest possible number of data points, and thus favour the use of large burner diameters when possible. Contrary to the literature recommendations, the bilinear peak engine seems to reduce the bias introduced by the peak locking phenomenon. Additional calculations were performed with a recently developed image deformation scheme, allowing deformations of the vector grid according to the flow velocity variations. It however did not provide any substantial improvement as compared to traditional processing schemes.

Instantaneous DPIV images were processed using a home-developed program. The latter allows for jet centerline detection, minimum velocity tracking, as well as associated strain rate calculations. It is shown that the radial strain rate determination is in practice significantly superior to the conventional approach using the axial velocity profile. The linear extrapolation necessary to yield the unstrained flame speed value is performed on averages of instantaneous data points, using a weighted procedure for both K_r and $S_{u,ref}$ coordinates. An uncertainty analysis has been carried out in order to assess the importance of three leading parameters that are: i/ the number of data points N_{dp} per DPIV series, ii/ the lowest strain rate achieved K_{low}, iii/ the strain rate range achieved ΔK_r. For a stable flame and $N_{dp} = 10$, $K_{low} = 200$ s^{-1} and ΔK_r=100 s^{-1}, the estimated uncertainty on the extrapolated unstrained flame speed is found to be 2.5 cm.s^{-1}.

IV. Laminar Strained Flames in CH_4/Air Mixtures in Stagnation Flow Configurations: Experimental and Numerical Studies

IV.1 Introduction and Objectives

This section is dedicated to the validation of the methodology presented in chapter III. In part I, laminar flame speeds of CH_4/air mixtures are investigated in both stagnation plate and counterflow flame configurations using the DPIV diagnostics. Impacts of the non-heated stagnation plate on strained flame speed measurements are analyzed. Results obtained for the counterflow configuration case are confronted to a large number of experimental datasets, encompassing stagnation flow, outwardly propagating and heat flux-stabilized flat flames. Present results are also compared with numerical predictions given by leading kinetic mechanisms. The second part is devoted to the numerical study of stagnation flames in both stagnation plate and counterflow configurations. The classical 1D approach is confronted to both 2D realistic simulations and experimental results obtained in part I for strongly burning flames. Important terms of the momentum equation are compared for both 1D and 2D models to account for observed discrepancies. Measurement errors due to the particle slip are evaluated for the stagnation plate flame case by simulating the particle motion including the Stokes drag, gravity and thermophoretic forces. The validity of the different strain rate definitions is discussed in the light of the 2D simulated counterflow case.

IV.2 PART I: Experimental Study Using DPIV

IV.2.1 Experimental Methodologies

Burner Apparatus

Nozzle Burner Design

The nozzle burner in counterflow related studies is of prime importance as only pure flow straining is supposed to affect studied flames, i.e. curvature effects have to be negligible. Conventional nozzle contour design relies on high degree polynomial curves optimized to deliver plateau velocity profiles at the nozzle exit. The present nozzle design is partly based on the empirical formulation proposed by Rolon [161], a design seen to be adapted for the counterflow study of laminar diffusion flames. Interestingly, it was found that the contour used in the present study could be closely approached by an analytical formulation of surfaces of constant stream function values described by Cohen and Ritchie [162]. The latter methodology, mainly based on series solutions of the Stokes-Beltrami equation, yields a convenient way to successfully design axisymmetric contractions. Comforted by this observation, cold flow tests were performed for the 7 mm and 15 mm nozzle burners used for the present experiment. Results are shown in Figure IV.1. Both contractions allow the formation of wide “plateau” velocity profiles. The maximum planar velocity widths were obtained at the highest tested flow rates and were found to represent 69% and 77% of the nozzle I.D. for the 7 and 15 mm burners respectively.

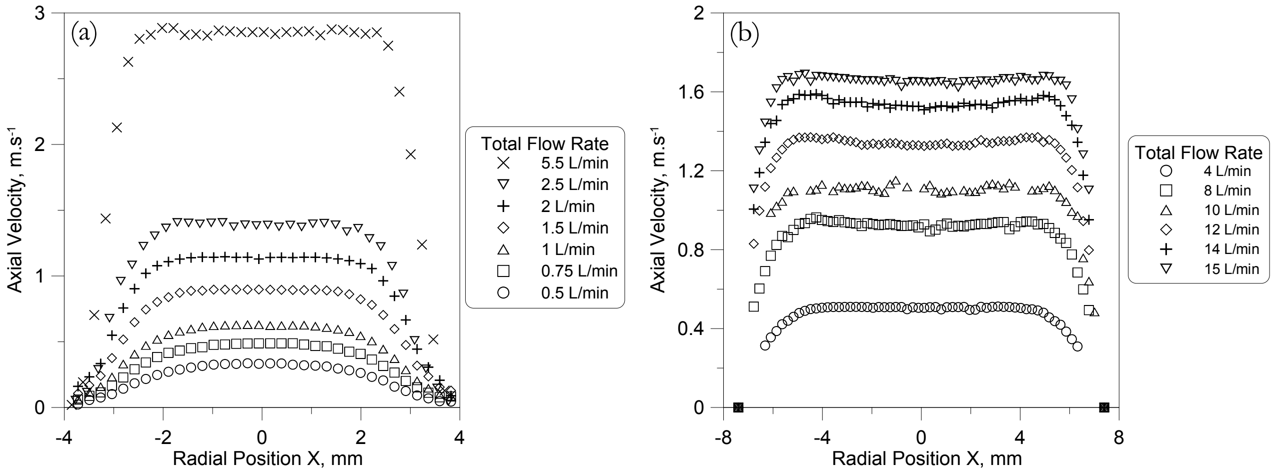

Figure IV.1 Cold flow (N_2) velocity profiles 1 mm above the burner exits for various flow rates: (a) 7 mm burner (*BC*: SP, L_{sp}: 7 mm), (b) 15 mm burner (*BC*: SP, L_{sp}: 14.8 mm).

The Stagnation Plate Flame Configuration

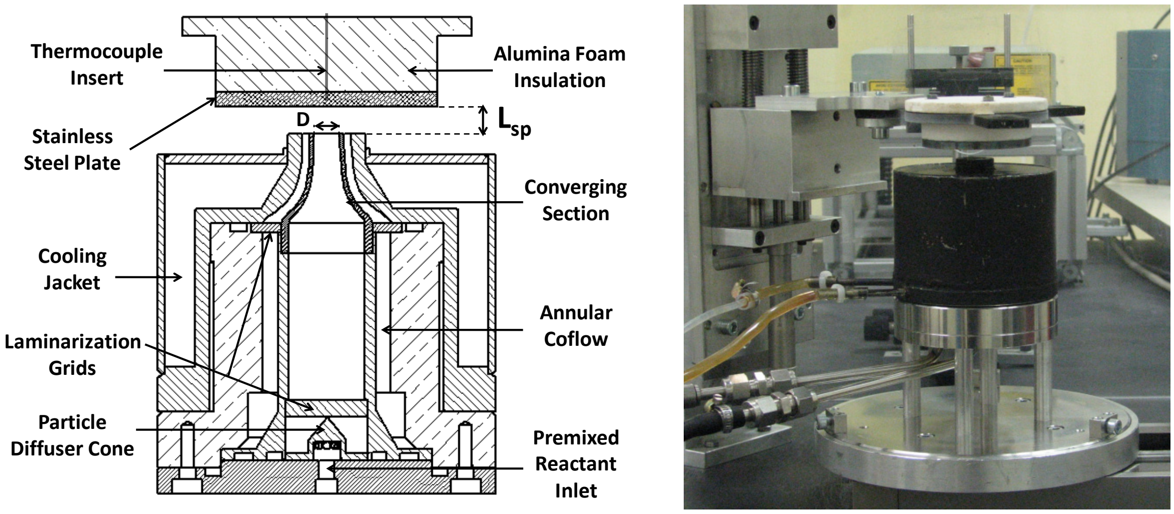

(a) **(b)**

Figure IV.2 The stagnation plate flame configuration: (a) Schematic view, (b) Photography of the experimental apparatus.

The stagnation plate flame configuration is detailed in Figure IV.2. The fuel and oxidizer are first introduced through the burner ground plate. A so-called "particle diffuser cone" is used to break the reactive jet and ensure a homogeneous seeding in the nozzle plenum. Absence of this part would result in strong concentrations of particles in the centerline of the reacting jet while a consequent depletion of seeding material would be observed in its outer part. The conical shape considerably reduces the accumulation of particles in the first stage of the burner, which is generally a crucial issue in experiments using solid particles. Nevertheless, periodic disassembling was needed to clean the burner. The reactive mixture is then introduced into the burner plenum through a 4 mm thick brass laminarization grid (≈ 170 holes, 1.3 mm I.D.). It is finally accelerated in the converging section with a 7 mm outflow diameter *(D)*, creating an upward-oriented jet, impacting on a 4-mm-thick stainless steel plate. The stagnation plate is attached to an alumina foam plug selected for its insulation properties. The burner-to-plate distance L_{sp} is adjustable and can be independently set to the desired value. The temperature of the stainless steel disc can be measured thanks to a Cr-Al thermocouple inserted in its center, 1 mm away from the impacted surface. In order to minimize heat transfers to the burner body, and therefore ensure the fresh mixture injection at room temperature, a cooling jacket is placed on the assembly. A coflowing nitrogen shroud is used which considerably improves the flame stability that could be prone to external perturbations, such as room drafts. The nitrogen flow rate was generally set so that the coflow exit velocity would closely match the one of the main flow.

Notice that several plate assemblies were tested in the course of this work. An original massive stainless plate fixed on three peripheral columns was first implemented. To avoid heat sink effects created by the metallic assembly, the stainless steel plate was replaced by an alumina foam plug. A parametric study showed that for small flame-to-plate separation distances, the flame would be stabilized against the plug, as seen in Figure IV.3. Ultimately, it was noticed that for rich methane/air mixtures, it was not possible to obtain a planar stagnation flame, the flame being either anchored to the plug or stabilized on the burner rim. It was also noticed that flames that could be stabilized at the beginning of the study could not be reproduced later on in the same experimental conditions. The following explanations can here be mentioned: i/ the plate, being characterized by poor conductivity, does not evacuate the heat through conduction. When the flame is in the vicinity of the plug, a hot spot is created and the flame preferentially anchors at this location. ii/ the poor repeatability of experimental conditions might be due to a progressive degradation of the plate surface, probably modified by incrustations of Zirconium seeding particles. To circumvent these difficulties, it was decided to add a stainless steel layer covering the exposed face of the foam plug, as presented in Figure IV.2.

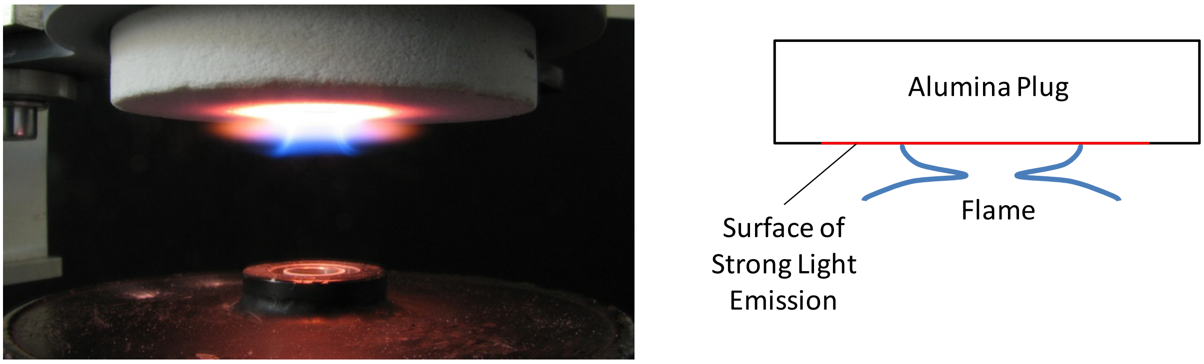

Figure IV.3 Methane/air flame stabilized against the alumina foam plug. On the left: photography, on the right: schematic view.

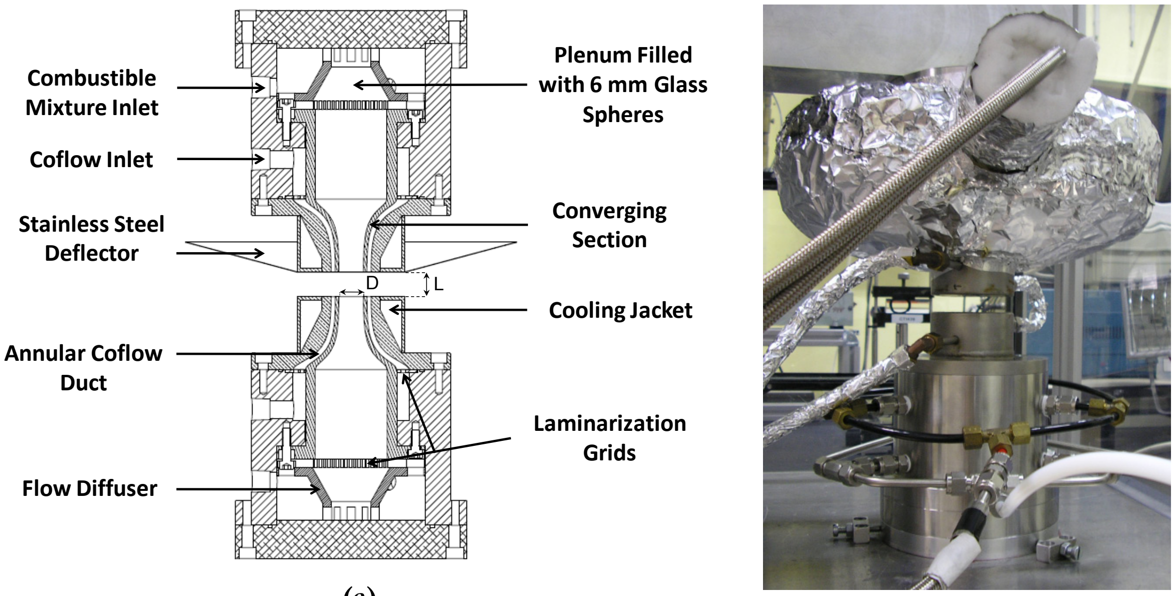

(a)

(b)

Figure IV.4 The counterflow twin flame configuration: (a) Schematic view, (b) Photography of the experimental apparatus (without deflector).

The counterflow twin flame configuration is shown in Figure IV.4. Two identical nozzle burners (*D*=15 mm) are facing each other to create a twin flame system. The reactive mixture is brought to the burners at three separated ports regularly spaced around the burner body. Similarly to the previous apparatus, flow diffusers are inserted ahead of 5 mm thick aluminum laminarization grids (1116 holes, 1 mm I.D.). The flow diffusers are filled with 6 mm glass spheres to ensure a homogeneous seeding concentration before feeding the converging sections. Annular coflowing inert is also provided to enhance flame stability. In addition to the protective cooling jacket, the upper burner is equipped with a stainless steel deflector diverting the hot combustion products on the side. As seen in Figure IV.4 (b), it is also heavily insulated with refractory materials to avoid overheating of the inlet gas manifolds. If not properly protected, they would deliver a reactant mixture whose temperature would be affected and therefore, a shift of the twin flame system in the upward direction would have to be expected. The upper burner was fixed on a translatable stage allowing users to achieve different burner separation distances (*L*).

Flow Control and Gas Delivery Systems

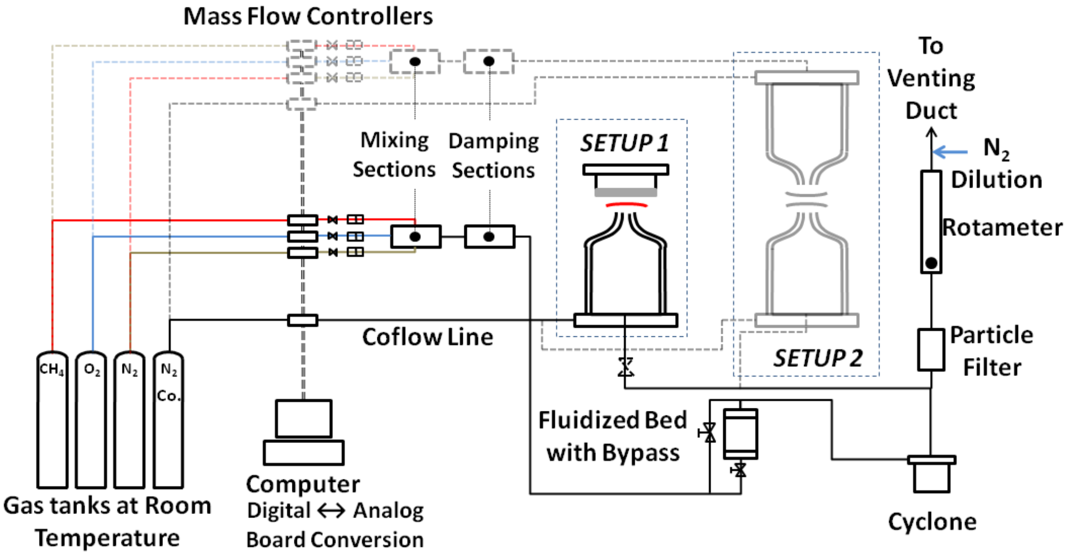

Figure IV.5 Schematic of the gas delivery system for the CH_4/air flame experiments.

Figure IV.5 displays a schematic of the gas delivery system used for the CH_4/air flame experiments. Reactants, including CH_4, O_2 and N_2 were provided by AIR LIQUIDE© and stored at room temperature in separated tanks. They were filtered through SWAGELOK© filters (2 μm mesh size) to remove any particulate impurity left in the gas tanks. Additional details on the industrial gases used in the present experiment are available in Table IV.1. Each individual flow rate was controlled by BROOKS© mass flow meters, including 5850S and 5850TR series. Although these mass flow controllers were generally factory-calibrated for the gas of interest, an in-house "re-calibration" was periodically performed using bubble meters or ACTARIS© wet meters (Measuring uncertainty 0.5%). All calibrated mass flow meters, without exception, showed excellent linearity with corresponding determination coefficients above 0.999. Systematic post-calibration verifications showed that experimental uncertainties in flow rates were within 1% passed the first 10 % of the full flow rate scale. Further information on the controllers used in the present study can be found in Table IV.2. The mass flow meters were piloted through a home-developed LABVIEW© interface allowing for an individual control of each flow rate as well as separate control of both lower and upper burners for the counterflow configuration case. To minimize flame perturbations due to remote modulation of individual flows while trying to achieve different flow rates at the same flame condition (i.e., achieving different strain rates), a common command was added to simplify burner operations. As such, reactants flow rates could be simultaneously controlled through a single proportional command, an operation that could have been cumbersome otherwise. Digital output from the computer was converted into analog signals (the only communication mode supported by both 5850 S and TR series) thanks to NATIONAL INSTRUMENTS© Digital/Analog conversion boards (NI-DAQ PCI 6703 and 6224). After being metered, individual reactants were mixed in a cylindrical section filled with 3 mm glass spheres. A damping section was added to smooth flow rate variations and therefore limit perturbations at the burner exits. A double stage seeding section, including a fluidized bed with a bypass and a cyclone was used to seed the flow. The combination of these two elements considerably reduced accumulations of particles in the burner while achieving proper seeding densities for the DPIV processing phase. As seeding problems were encountered for flame stabilizations requiring very small flow rates, an additional bypass branch was included in the system. Higher flow velocity could therefore be reached within the seeding section while keeping the burner outflow at the same level. The diverted part of the main flow was first filtered and then passed through a calibrated rotameter before being diluted and released in a venting duct. A precise flow rate measurement of the extracted flow was needed for accurate evaluation of the flow rate passing through the burner. For all methane counterflow flame experiments, fresh gases were injected at room temperature and atmospheric pressure, with all initial temperatures being within the 296 ±3.3 K interval.

GAS	DESIG.	MANUF.	MAXIMUM IMPURITIES (ppm-mol)							GLOBAL PURITY (%)
			H_2O	O_2	CO_2	H_2	N_2	C_2H_6	Other	
CH_4	N35	AIR LIQUIDE	5	10	10	20	200	200	C_nH_m: 50	99,95
O_2	ALPHA GAZ I	AIR LIQUIDE	3	×	×	×	×	×	C_nH_m: 0.5	99,995
N_2	ALPHA GAZ I	AIR LIQUIDE	3	2	×	×	×	×	C_nH_m: 0.5	99,999

Table IV.1 Gas impurity table (DESIG.: Designation, MANUF.: Manufacturer).

Mass Flow Meter Series	Communication	Flow Accuracy (At calibrated conditions)	Repeatability
5850S	Analog	±0.7 % of rate and 0.2 % full scale	±0.25 % of rate
5850TR	Analog	±1.0 % full scale	±0.2 % of full scale

Table IV.2 Mass flow meters communication modes, accuracy and repeatability.

Protocol for Data Acquisition

The protocol for data acquisition is as follows: flames are first stabilized at the desired equivalence ratio and flow rate that are recorded. After few minutes, particles are gradually introduced in the burner by diverting a part of the main flow to the fluidized bed. The seeding concentration is simultaneously checked by looking at DPIV images and performing live processing passes to ensure optimal vector filling ratios. The particle concentration being set, the laser pulse delay Δt is adjusted to properly resolve the entire flow field. This delay is optimized by closely matching the maximum authorized displacement to the largest motion scale in the flow field i.e. downstream of the flame. 250 image pairs are then acquired at a 14 Hz rate and the flame stability is carefully checked. If any perturbation arises during the acquisition phase, recorded data is discarded and a new dataset for the same experimental conditions is reinitiated. Various strain rate conditions of interest are then covered by varying the main flow rate. For the counterflow cases, the main and coflowing inert flow rates were set equally for both lower and upper burner. The strain rate ranges investigated herein depend on several parameters including:

- The ratio L/D for counterflow flames or the equivalent $2\,L_{sp}/D$ ratio for stagnation plate flames. These ratios were generally set to 1 in the counterflow case and to 2 for the stagnation plate flame case, unless otherwise stated. Large separation distances would generally lead to enhanced flame sensitivity to particles and therefore increased perturbations that could bias measurements. Single jet flames were generally found to be more stable than counterflow flames for large burner-to-stagnation plane distances.
- The minimum and maximum allowed flow rates, depending on the full scales of the chosen mass flow meters. For a fixed burner-to-stagnation-plane distance, the scale of the selected mass flow meters readily determines the lowest and highest achievable strain rates for a domain of reasonable accuracy. In other words, if a 0.2 L/min flow rate is to be reached and, as previously mentioned, if reasonable measurement accuracy is obtained past the 10 first percent of the mass flow device, a maximum full scale flow rate of 2 L/min is obtained. This example illustrates the fact that, for strongly stable flames, the maximum strains achieved can be far from the strain conditions of extinction. For the considered application, a good accuracy at low flow rates (i.e. low strain rates) is primordial because extrapolation methodologies, as discussed in the previous chapter, strongly rely on the lowest strain achieved.
- The flame propensity to flashback and extinction. By gradually decreasing flow rates while keeping the inert coflowing mixture, flat flames can be obtained until the curvature at their center becomes important. By further reducing the flow rate, flashback events eventually arise. Data acquisition is here limited to the state before apparition of the curved center of the flame. On the contrary, strain rate increase can also be limited by extinction event, predominant for the weakest methane/air flames studied herein (*E.R.* = 0.6). These experimental limitations are illustrated Figure IV.6.

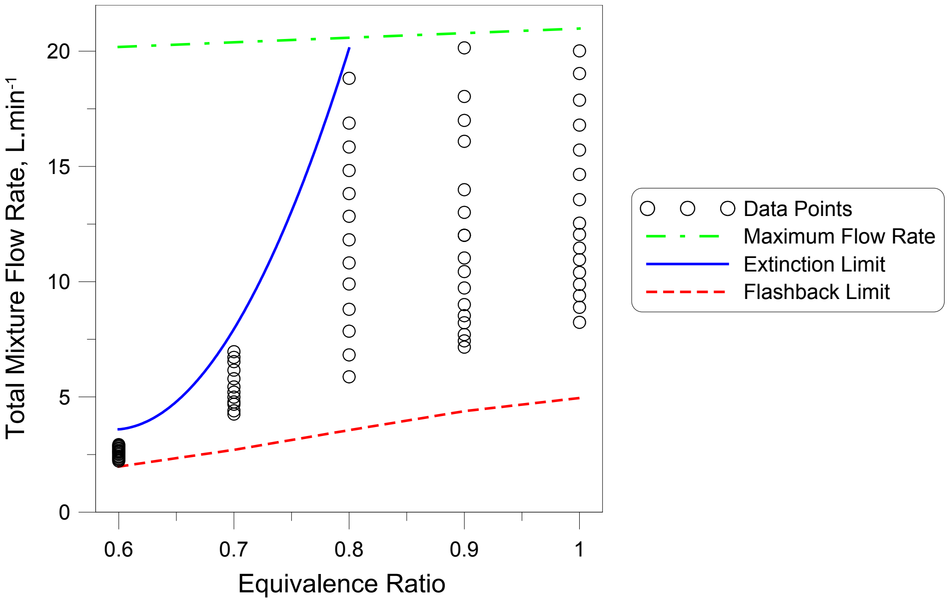

Figure IV.6 Example of probed domain for CH_4/air lean mixtures displaying technical and physical limitations for the strain rate ranges (*BID*: 15 mm, *BC*: SP, L_{sp}: 14.8 mm).

IV.2.2 Results and Discussions

On the Flame Transition Methodology for Laminar Flame Speed Determination

The original intention of the present experimental study was to perform the flame transition methodology developed by Vagelopoulos and Egolfopoulos [89] as described earlier. The main principle of the aforementioned technique is to measure flow velocities in the vicinity of the flame while it undergoes a non-assisted transition from a planar stagnation to a conical flame. A near zero strain state is observed and the corresponding minimum velocity is extracted and assumed to be the true laminar flame speed. This flame transitions have been performed on the stagnation flame setup presented in Figure IV.2 for three different burner-to-plate separation distances: 10.5, 12.5 and 14 mm (L_{sp}/D = 1.5, 1.75, 2). Flow rates corresponding to the transition states are potted in Figure IV.7 a, b, c. For L_{sp}/D = 1.5 (a), the transition state is observed for only one mixture with equivalence ratio 0.8. Leaner flames could not be stabilized and were systematically prone to instabilities close to the plate and rapidly extinguished. Richer flames (E.R.=0.9 and 1.0) could be ignited against the plate displaying an unstable annular flame pattern. However, by progressively reducing the burner inlet flow rate, a direct transition to a conical flame was initiated without any intermediate state. Further increasing the burner-to-plate distance (b) rendered possible 2 other transitions for mixture equivalence ratios of 0.7 and 0.9. A very lean flame at E.R.=0.6 could be sustained in the planar configuration and interestingly, while flow rate was decreased, did not transit towards a conical flame. This quasi-planar flame with edges oriented in the upward direction would progressively head upstream the flow to eventually enter the nozzle without any sign of stabilization on the burner rim. Such very weak flames have been observed in ref. [138] where an additional unsteady wavy motion of the entire flame disk was noticed. Stabilization of such flames is expected to be essentially governed by combined effects of flow acceleration, flame heat release and buoyancy forces. Thus, the transition methodology has to be reconsidered for very weakly burning flames. By further increasing the L_{sp}/D ratio (c), a flat flame could be stabilized for the stoichiometric case with a possible transition to the conical flame state. The leanest flame was however constantly blown off independently of the inlet flow rate. An important fact noticed during experimental runs is that, whatever the L_{sp}/D ratio and equivalence ratio, the flame state close to the transition is fairly unstable and the transition was not found to be steady or a well-behaved phenomenon. In some cases, curvature effects would perturb the flame before transition or the transition would display an asymmetric behavior with earlier departure towards the burner rim of some part of the flame edge. Such flame behaviors were also reported in the experimental works of Hsieh and Lin [163]. Addition of seeding particles close to the state of transition was seen to considerably complicate the experiment, especially by initiating non-desired flame transitions or creating important perturbations for these weakly strained flames. Repeatability of different runs at the same experimental conditions is clearly questionable, although the methodology relies on several experimental runs to extract the quasi-unstrained flame speed value. Aware of these important drawbacks, it was consequently decided to abandon the transition methodology and perform velocity measurements on stagnation strained flames. Such difficulties were also reported by Zhao in ref. [105] for which the more conventional planar strained flame configuration was preferred to the transition approach.

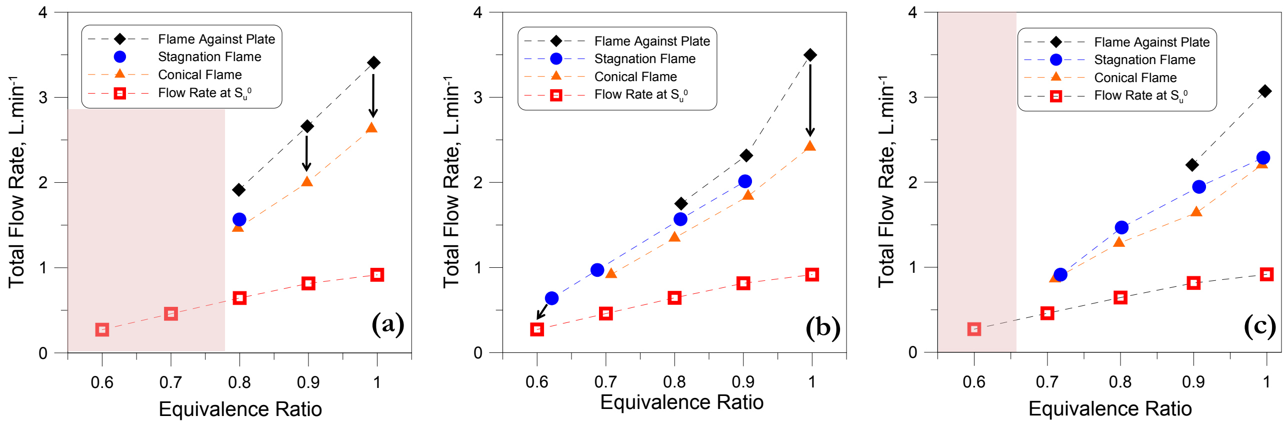

Figure IV.7 Transition from the stagnation to the conical flame for various burner-to-plate distances L_{sp}: (a) 10.5 mm, (b) 12.5 mm, (c) 14 mm (*MB*: CH_4/Air, *BID*: 7 mm, *BC*: SP). Dark arrows indicate direct transitions between the two marginal states without any intermediate state. Red areas correspond to conditions for which flames could not be stabilized.

The Stagnation Plate Flame Experiments

Initial tests on the stagnation plate configuration aimed at determining the optimal burner-to-plate distance that would be used for laminar flame speed determination. $S_{u,ref}$ evolutions with the strain were investigated for various burner-to-plate distances yielding L_{sp}/D ratios from 1 to 3.5. Results are presented Figure IV.8. It can be seen that the distance L_{sp} has no influence on the reference flame velocity variations with strain. This result is consistent with the findings of Chaos et al. [119]: a nozzle separation distance L above 14 mm (i.e. corresponding to L_{sp} above 7mm) closely yields the same experimental $S_{u,ref}$ trend for stoichiometric methane/air mixtures. This is also concordant with experimental results of Vagelopoulos et al. [71] for ultra-lean hydrogen/air mixtures for which "finite domain effects" are observed for lower nozzle burner separations (L = 7 mm). There is however no substantial range gain for lower strain rates by increasing the separation distance L_{sp}, as recommended in ref. [89]. The lowest strain achieved for L_{sp}/D = 3.5 is just 50 s^{-1} lower than for the L_{sp}/D = 1 case. It is also worth to mention that for large burner-to-plate distances, the flame is usually prone to various types of motion and becomes particularly sensitive to external perturbations and seeding particle injection, which renders experimental operations more delicate. The present experimental results, supported by a thorough literature review, seem to indicate that nozzle separation distances L in the range of 14 to 20 mm (i.e. L_{sp} of 7 to 10 mm) are a good compromise for most hydrocarbon/air flames with burning characteristics similar to those of methane/air mixtures.

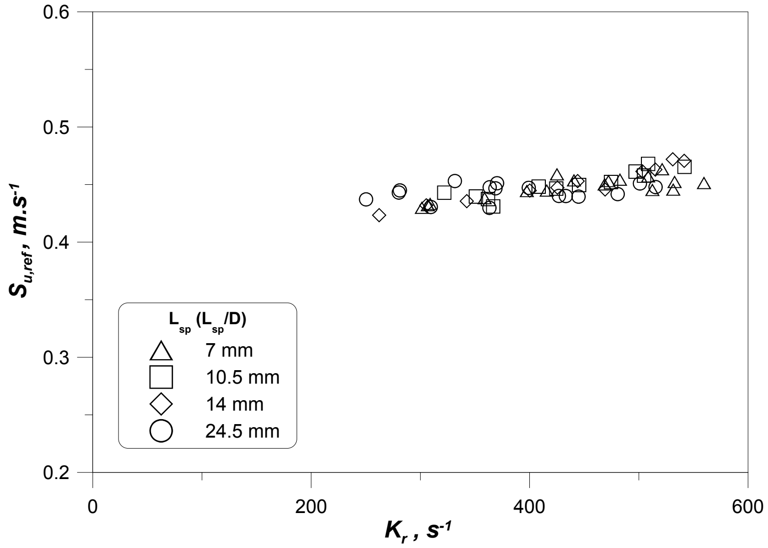

Figure IV.8 $S_{u,ref}$ variations with the strain rate for different nozzle-to-plate distance L_{sp} (*MB*: CH_4/air, E.R.=1.0, *BID*: 7 mm). A single point represents an average of 250 instantaneous image pairs.

To further validate the stagnation plate flame approach, it was decided to confront the strain sensitivities obtained for methane/air mixtures to results reported in the literature. Surprisingly, it was found that a very limited number of datasets for methane/air flame was available despite the common use of such mixtures. In this context, the reference velocity evolution obtained for a stoichiometric CH_4/air flame and a L_{sp} distance of 14 mm is confronted in Figure IV.9 to published datasets including results on opposed and single jet apparatuses. A very good agreement is found with earlier studies on counterflow flames of Law et al. [60], Yu et al. [58] and Chao et al. [119]. This indicates that our results are minimally affected by downstream heat losses in the range of investigated strain rates. Strain sensitivity indicated in Egolfopoulos' study [135] on single and opposed reactive jets is obviously departing from this overall trend: the corresponding slope is about 1.6 times higher than for the remaining datasets. This discrepancy might be explained by the determination of strain rates, seen to be prone to important scatter depending on the chosen evaluation methodology. The following observations support this hypothesis: i/ similarly to the other investigations, the reference velocity considered in ref. [135] is the first local minimum of the axial velocity profile, i.e. the observed discrepancy is not due to a different choice regarding the velocity reference plane; ii/ single and opposed jets experiments of ref. [135] give comprehensive trends for strain sensitivities, excluding any configuration-dependant bias; iii/ linear extrapolation performed on datasets of ref. [135] yield an unstrained flame speed of 39.3 cm.s^{-1} to be compared to 38 cm.s^{-1} for the ensemble of remaining datasets. This difference might be within the present extrapolation uncertainty. To summarize, the strain sensitivity found for stoichiometric methane/air mixtures for our stagnation plate configuration agrees well with earlier experimental studies of counterflow twin flames. Generally, care must be taken by directly comparing evolution of reference velocities with strain from different investigations, unless the strain rate calculation procedure associated to the extracted $S_{u,ref}$ values is clearly stated.

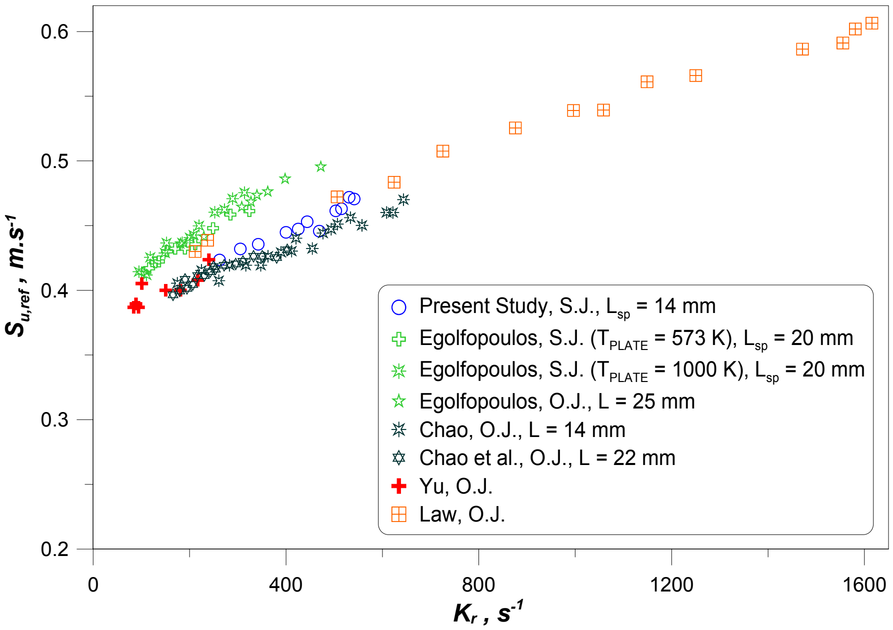

Figure IV.9 $S_{u,ref}$ variations with strain rate K_r : comparison with other experimental data sets (*MB*: CH_4/air, E.R.=1.0, S.J.: Single Jet, O.J.: Opposed Jets). Data sets are from Egolfopoulos [135], Chao [119], Yu [58] and Law [60].

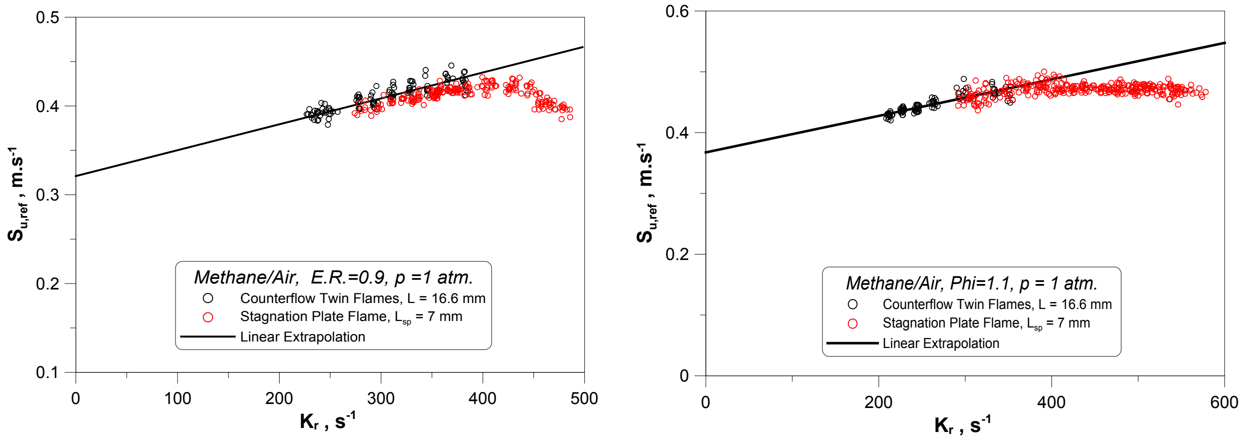

(a) **(b)**

Figure IV.10 $S_{u,ref}$ evolutions with strain rate for the stagnation plate and counterflow flame configurations for two methane/air mixtures: (a) E.R.=0.9, (b) E.R.=1.1.

Comforted by previous observations, laminar flame speed determination in the stagnation plate configuration was performed for L_{sp} distances of 7 mm and various mixture equivalence ratios. The experimental procedure and data analysis were identical to those described in chapters III and IV. Two difficulties arose in the course of the present study. The first is related to the influence of downstream heat losses on the flame. Figure IV.10 presents $S_{u,ref}$ evolutions with strain for two methane/air mixtures (E.R. =0.9 and 1.1). Corresponding datasets in the counterflow twin flame configuration for an equivalent burner-to-plate distance are added for comparison. It is clear that for higher strain rates downstream heat losses play an important role, providing an apparent “bending” in the evolution of the velocity with strain. The curve behavior seems however to be mixture-dependent, with a strong inflection for the E.R.=0.9 case followed by extinction and an almost linear response for the E.R.=1.1 case up to 600 s^{-1}. Clearly, these trends are opposite to interpretations that could be done if nonequidiffusion phenomena ($Le \neq 1$) were assumed to be important. In the latter case, the leaner flame (E.R.=0.9), characterized by $Le < 1$, would be expected to be more robust with increasing strain until getting very close to the wall and being influenced either by heat losses or a reduced residence time. On the opposite, the rich flame (E.R.=1.1) with $Le > 1$ would be readily affected by nonequidiffusion phenomena and ultimately extinguish far from the plate at a lower strain. Standoff distances from the plate and axial velocity profiles for strain rates of about 400 s^{-1} are presented in Figure IV.11 and Figure IV.12 for the two cases of interest. It can be seen that for the same range of strain rates, the lean flame stands systematically half a millimeter downstream compared to the rich one and will therefore experience first the effects of heat losses at the wall. The rich flame, characterized by a higher burning intensity and hence higher post-flame velocities, is pushed back slightly upstream and is, in a lesser extent, affected by the presence of the nonadiabatic plate. Thus flame behaviors observed in Figure IV.10 are expected to be governed by joint effects of flame heat release and heat losses at the stagnation plate. Such observations are in agreement with the results of Egolfopoulos et al. [135] on methane/air flame extinction characteristics that showed that for nonadiabatic wall, the burning intensity of the flame is an important parameter, while the coupling between strain and nonequidiffusion ($Le \neq 1$) is not as strong as the flame response to the downstream heat loss. To summarize, care must be taken by performing extrapolation procedure on such data. It should be noticed that the useful strain rate range is consequently reduced, for the present cases, by half and any inclusion of data points under the influence of heat losses will lead to an overestimation of the unstrained flame velocity.

Experimentally determined speeds of unstrained laminar flames are presented in Figure IV.13 for mixture equivalence ratios ranging from 0.8 to 1.2. A reasonable agreement is found for predictions with GRI Mech. 3.0, even though higher equivalence ratios might be subjected to biasing effects mentioned earlier.

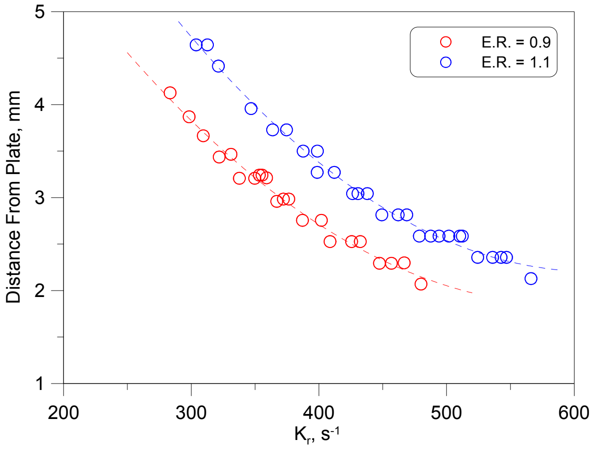

Figure IV.11 Flame standoff distance from the plate for methane/air mixtures at E.R.=0.9 and 1.1 (*BID*: 7 mm, L_{sp}: 7 mm).

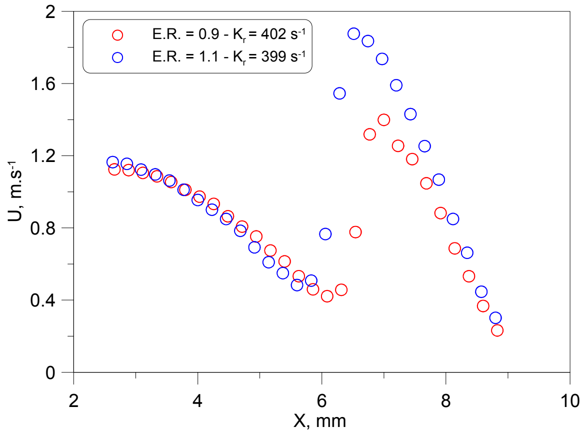

Figure IV.12 Axial velocity profiles for methane/air flames at E.R.=0.9 and 1.1 and $K_r \approx 400$ s^{-1} (*BID*: 7 mm, L_{sp}: 7 mm).

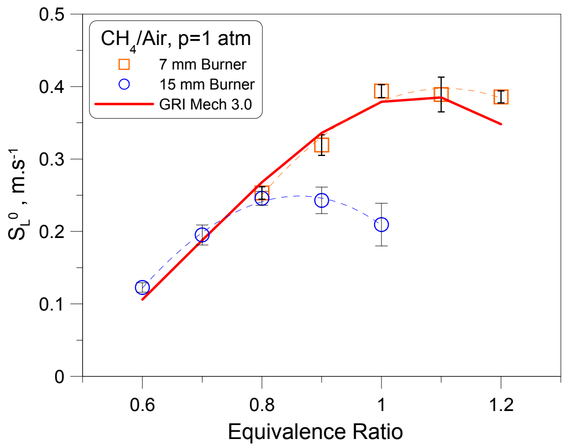

Figure IV.13 Comparison of laminar flame speeds of methane/air mixtures obtained on the 7 and 15 mm stagnation plate burners ($L_{sp}/D \approx 1$).

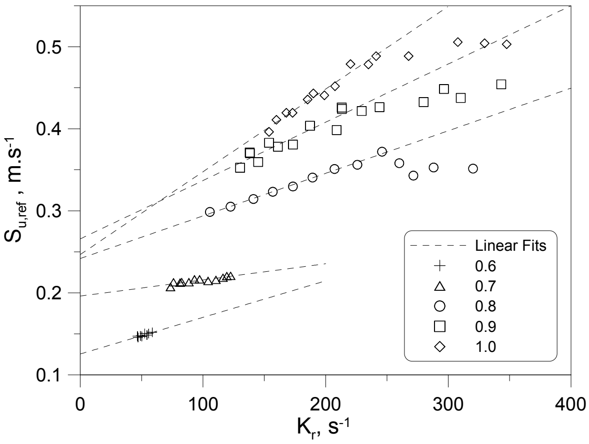

Figure IV.14 $S_{u,ref}$ evolutions with strain for methane/air mixtures on the 15 mm stagnation plate burner (L_{sp}=14.8 mm, averaged series).

Another difficulty encountered is that leaner mixtures, for instance at equivalence ratios 0.6 and 0.7, could not be properly stabilized on the 7 mm I.D. nozzle burner. Therefore, it was decided to perform measurements in the same configuration with the 15 mm burner I.D. presented earlier. The L_{sp}/D ratio was set close to 1. Laminar flame speed measurements are shown in Figure IV.13 along with the previous dataset. If flame speeds of leaner mixtures seem to be in a reasonable agreement with the GRI Mech. 3.0 predictions, significant discrepancies were observed for equivalence ratios of 0.9 and 1.0, yielding flame speeds respectively of 24.3 ±1.8 $cm.s^{-1}$ and 21 ±3 $cm.s^{-1}$ against 31.9 ±1.4 $cm.s^{-1}$ and 39.3 ±0.9 $cm.s^{-1}$ for measurements obtained on the 7mm I.D. burner. These lower values were essentially due to the "collapsing" trends of the corresponding $S_{u,ref}$ profiles in the lower strain rate range (See Figure IV.14). It is unknown why such a decreasing trend occurred, although several observations can be made: i/ this phenomenon was observed only for the most intensely burning flames (E.R. = 0.9 and 1.0), the close data overlap for the flame equivalence ratio 0.8 indicating that leaner mixture were not concerned, ii/ compared to the previous case, the stainless steel plate was submitted to intense heating due to the increase of the burner area, leading to apparent white heat conditions, iii/ the plate temperature followed $S_{u,ref}$ variations starting, for the E.R.=1.0 case, at 700 K for the lower strain and finishing at 850 K for the highest. For E.R. = 0.8-1.0, a slope change is observed around 240 s^{-1}, for a temperature of approximately 800 K, suggesting a change in the heat transfer mechanism, possibly due to a change in steel conductive and/or radiative properties at these higher temperatures.

Considering previous experimental observations, it is clear that the use of a non-heated stagnation wall in the present context was found to be very challenging. If the experimental setup and operation procedures are simplified as compared to the classical counterflow setup, the nonadiabatic boundary has a marked influence on strained flame velocity evolutions at moderate burner-to-plate distances ($L_{sp}/D \approx 1$), particularly for: i/flames with higher heat release; ii/flames stabilized at higher strain rates. The isolated plate setup, as described earlier, is compromised for large burner diameters and hence provides a limited flexibility for the remaining work. Also, if the plate setup is to be used, the impact of heat losses on the flame propagation has to be assessed in the light of flame heat release and distance to the plate, a property and a condition that might greatly vary depending on the considered mixture. It would also be necessary to define a criterion to isolate the unaffected part of the unstrained velocity profile, an operation that is left to the experimenter's own judgment. Notice that heating the stagnation plate at higher temperatures, as proposed in ref. [135], does not seem to yield an important gain in the data range useful for the extrapolation procedure. To remove any ambiguity in the determination of laminar flame speed inherent in the stagnation flame configuration, it was ultimately decided to perform DPIV measurements in the counterflow twin flame configuration.

The Counterflow Twin Flame Experiments

The opposed jet setup with 15 mm I.D. burner is used for the present experimental series. The main flow and coflowing inert mixtures were set identically on both sides. The nozzle separation distance is fixed at 16.6 mm, a distance seen to provide an enhanced stability for most flames studied herein. To simplify experimental operations, only the lower jet was seeded with particles. Results for this configuration are compared to the available literature data sets encompassing stagnation (Figure IV.15), spherically expanding (Figure IV.16) and heat flux stabilized (Figure IV.17) flames.

For stagnation flames, excellent agreement is found with data points of Dong and coworkers [94] performing DPIV measurements for stagnation plate flames stabilized close to the state of transition (see Vagelopoulos and Egolfopoulos [89]). A good agreement can also be noticed for counterflow measurements of Vagelopoulos et al. [71] with a large nozzle separation distance (22 mm). Most important discrepancies are observed for the measurements of Vagelopoulos and Egolfopoulos [89] for the stagnation-to-conical flame transition methodology: their measurements are systematically lower in the intermediate lean and rich ranges, yielding differences up to 6.4 cm.s^{-1} for a mixture equivalence ratio of 1.35. The higher rich branch found by Wu and Law [23] might be due to the so-called "finite domain effects" as early measurements were done for very small nozzle-to-plate separation distances (5-7 mm), which might affected extrapolated velocity values.

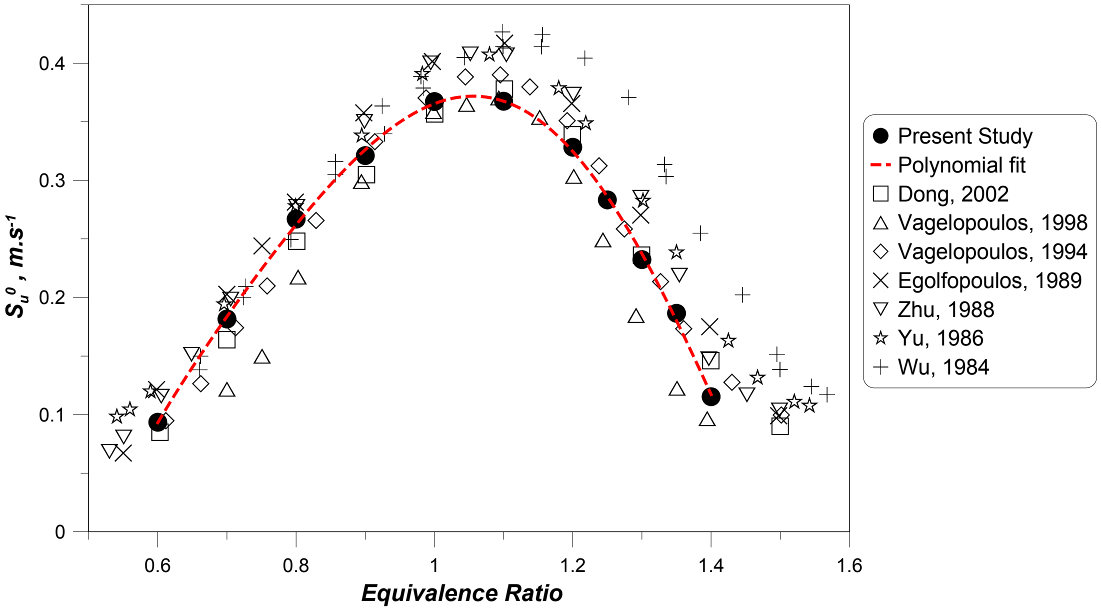

Figure IV.15 Laminar flame speed comparison for various data set obtained in the stagnation flame configuration for CH_4/air flames at atmospheric pressure and ambient temperature. Data sets are from Dong [94], Vagelopoulos [71, 89] for 1998 and 1994 respectively, Egolfopoulos [63], Zhu [62], Yu [58] and Wu [23].

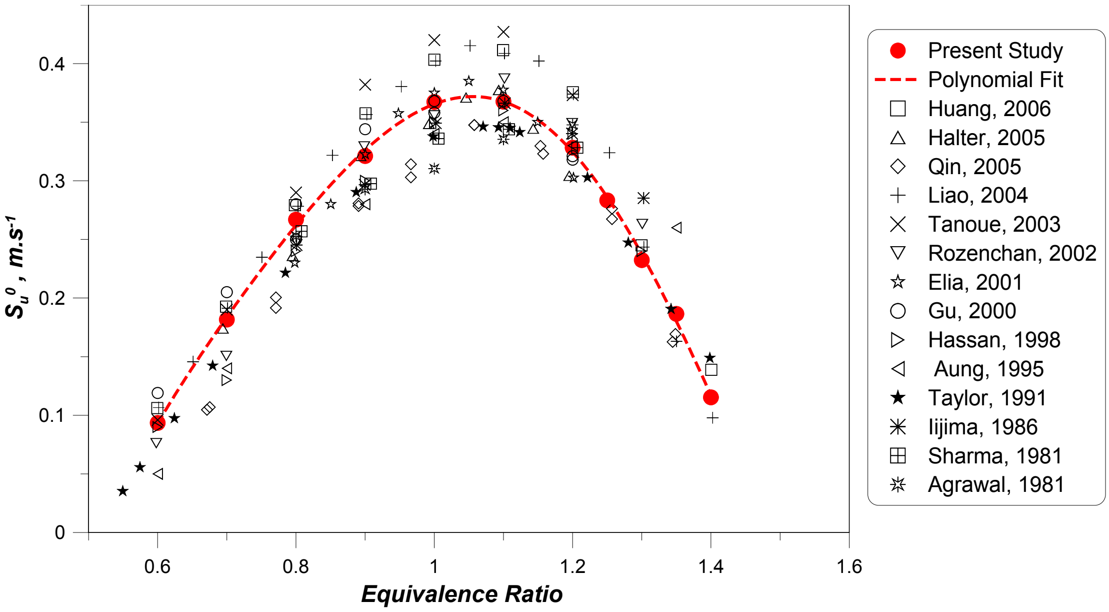

Figure IV.16 Laminar flame speed comparison of present results for CH_4/air mixtures with various data sets obtained for spherically expanding flames. Data sets are from Huang [164], Halter [165], Qin [166], Liao [167], Tanoue [168], Rozenchan [169], Elia [170], Gu [25], Hassan [171], Aung [172], Taylor [173], Iijima [174], Sharma [175] and Agrawal [176].

Comparison with spherically expanding flame datasets shows three different trends:

- Recent measurements from the works of Huang et al. [164], Liao et al. [167] and Tanoue et al. [168] are in accordance with the present experimental measurements for the leanest and richest cases.

Flame speeds are however found to be much higher for the central equivalence ratio range 0.8-1.25 with laminar flame speeds above 40 cm.s^{-1} at stoichiometric conditions.

- A globally good agreement is found with the results of Halter et al. [165], Rozenchan et al. [169], Elia et al. [170] and Gu et al. [25].
- Flame speeds from Qin and Ju [166], Hassan et al. [171], Aung et al. [172], Taylor and Smith [173] are lower than the present results with an almost constant offset up to the equivalence ratio 1.2. Above, these measurements are in very close agreement with the present ones.

A detailed discussion on disparities of experimental measurements for the outwardly propagating flame is clearly out of the scope of the present study. Few explanations can however be mentioned. For instance, recent investigations have shown that the effect of cylindrical confinement on the determination of laminar flame speed are non-negligible and can achieve a flame speed reduction on the order of 15 % [177]. As a result, it was concluded that flame radii less than 0.3 times the wall radius should be considered for data processing. Also, the recent regain of interest in non-linear extrapolation methodologies put an emphasis on the possible scatter commonly introduced by selecting an apparent linear portion of the highly non-linear flame speed evolution with stretch to make a linear extrapolation. Indeed, experimenters are usually left with the difficult task of evaluating ignition and chamber affected parts of the flame velocity evolution with stretch [121]. Another point of possible discrepancy of data from cited references is the evaluation of thermal expansion coefficient that is usually computed from “classical combustion” codes. As unstretched flame speeds are conventionally obtained by multiplying the spatial flame velocities by thermal expansion factors, final unstretched flame speed values have consequently an inherent strong dependence on these estimated factors. All aforementioned issues are expected to be relevant while trying to characterize the diverse trends observed in Figure IV.16. They however require additional information, for example on experimental device geometries, processing procedures as well as computation specifications that are not fully available in publications discussed herein.

The last comparison provided in Figure IV.17 displays datasets obtained using the heat flux method along with the present measurements. The overall agreement is good, especially on the rich side with the data points of Van Maaren and coworkers [20]. The present measurement yield velocity values slightly higher on the lean side compared to ref. [20, 178] (up to 4.4 cm.s^{-1} at E.R.=0.7), and lower on the rich side compared to ref. [178] (up to 5.5 cm.s^{-1} at E.R.=1.4).

The overall good agreement of the present results with datasets from the literature allows concluding on the reasonable accuracy and reliability of the developed approach.

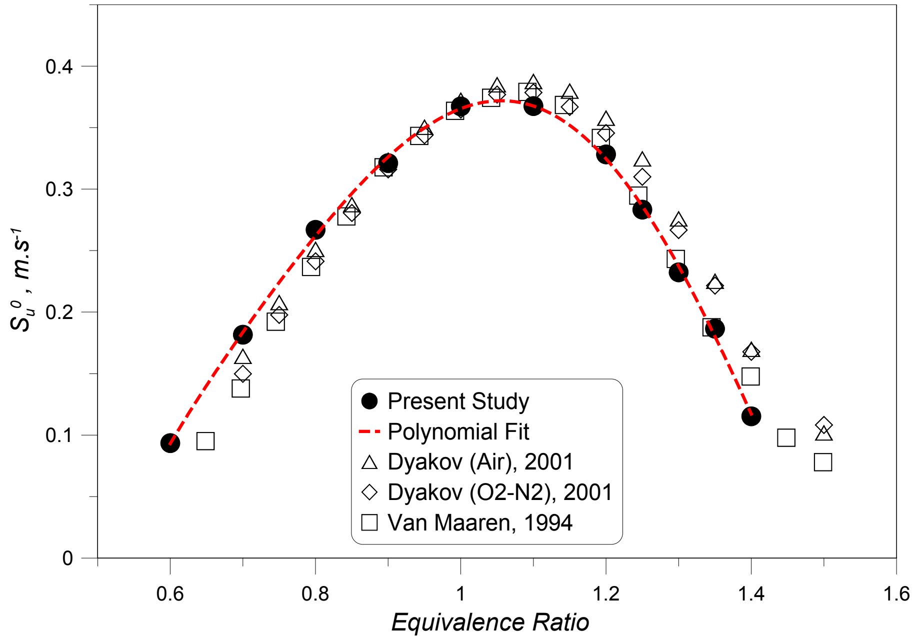

Figure IV.17 Laminar flame speed for CH_4/air mixtures. Comparison of present results with various data sets obtained for the heat flux method. Data sets are from Dyakov [178] and Van Maaren [20].

To quantify the possible influence of the non-linear dependence of flame velocity at lower strain rates, expressions (II-18) and (II-19) were used to perform constrained non-linear least square regressions to yield fundamental flame speed values for the studied methane/air mixtures. $S_{u,ref}$ evolutions with strain for lean and rich mixtures as well as linear and non-linear fits (Tien formulation (II-18) only) are shown in Figure IV.18 (a) and (b) respectively. Final extrapolated values for each extrapolation procedure are presented in Figure IV.19. As expected, methane/air mixtures all display a positive sensitivity to strain, a result in adequacy with early observations of Wu and Law [23] as well as analytical predictions of Tien and Matalon [68] related to the effective $S_{u,ref}$ evolution according to the chosen plane of reference. Velocity differences observed between the linear and non-linear extrapolations are somehow mitigated: the Tien and Matalon formulation yields flame speeds slightly lower than the linearly determined ones (up to 2.2 cm.s^{-1}, E.R.=0.8 and 1.4 excluded), a result in accordance with the general observations of the literature. The Kelley and Law formulation, however, provides significantly lower velocity values from 3 cm.s^{-1} up to 10.4 cm.s^{-1}. A closer look at the integral analysis yielding expression (II-19) (see for example ref. [179]) reveals that some simplifying assumption might prevent (II-19) to be directly applicable to the classical counterflow reference flame speed data, as suggested in ref. [120]. Indeed, this approach is assuming that the upstream unburned streamtube area A_u equalizes A_T, the streamtube area at the beginning of the thermal zone (location of our velocity minimum $S_{u,ref}$). Assuming constant unburned gas density, a mass conservation between both A_u and A_T, shown that the upstream velocity is constant, whatever location considered. This is however not true for practical counterflow flames, for which important velocity variations are observed on the unburned side. Therefore, the quantity S_u defined in (II-19) as the upstream flame speed is ambiguous since its value essentially depends on the reference location where it is evaluated. Expression (II-19) should probably be modified in that sense. Note however that (II-19) will perform better as strain is decreased since, in that case, $A_T \rightarrow A_u$.

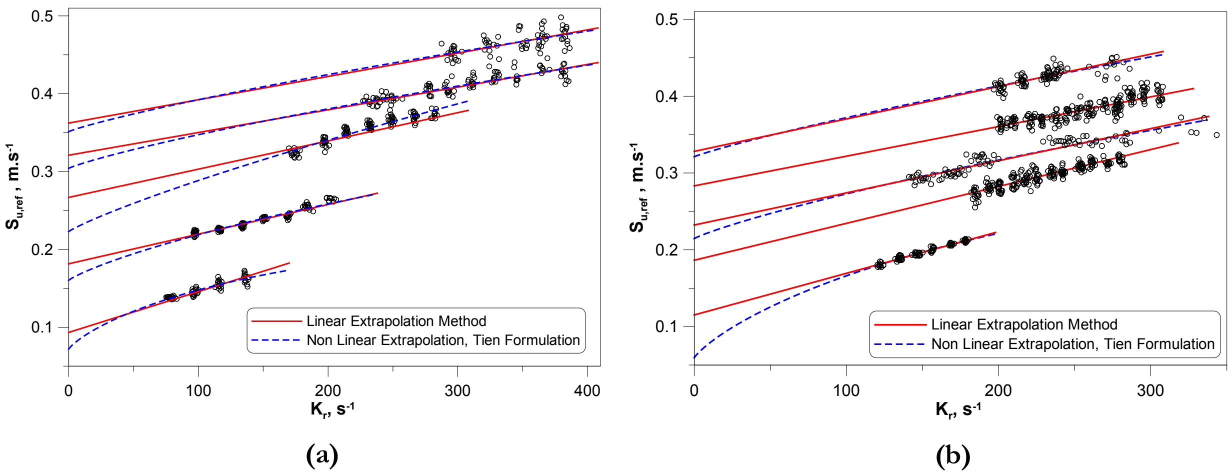

Figure IV.18 $S_{u,ref}$ evolutions with strain for various CH_4/air mixtures: (a) Lean mixtures including from top to bottom: E.R.= 1.0, 0.9, 0.8, 0.7 and 0.6; (b) Rich mixtures including from top to bottom: E.R.= 1.2, 1.25, 1.3, 1.35 and 1.4. Notice that each single point is an average of 10 instantaneous velocity values.

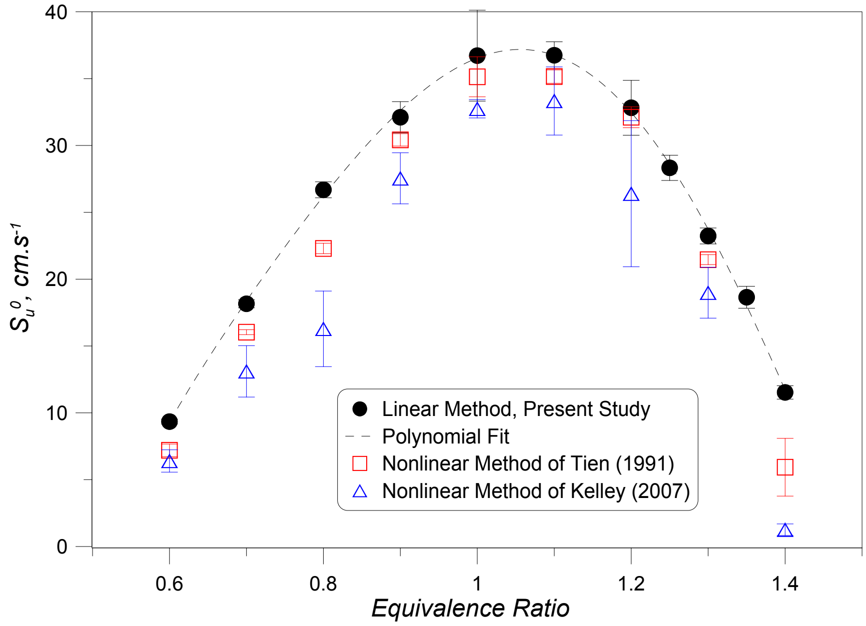

Figure IV.19 Laminar flame speeds of CH_4/air mixtures according to the linear and non-linear extraction methodologies. Non-linear formulations presented here are from Tien and Matalon [68] and Kelley and Law [120].

DPIV Results are compared to predictions obtained with various kinetic mechanisms including the GRI Mech. 3.0 [148], GDF Kin. 3.0 [180], Konnov [181] and Le Cong [182]. An overall excellent agreement is obtained on the lean side from E.R.=0.6 to 0.9 with measurements and predictions being gathered in a 1.5 cm.s^{-1} and 3.0 cm.s^{-1} interval respectively. On the rich side, however, different trends are observed. GDF Kin. 3.0 is over predicting measurements up to 7.3 cm.s^{-1} at E.R.=1.4 while Konnov [181] and Le Cong [182] yield an excellent agreement with DPIV datapoints. At stoichiometry, the best concordance is obtained with the predictions of Le Cong [182] with both experimental and computed values being 36.7 cm.s^{-1} and 36.2 cm.s^{-1} respectively. Note here that commenting on such level of agreement might be vain since it has been shown that magnitude of errors of rate parameters typically induce uncertainties on calculated predictions from 2 to 5 cm.s^{-1} for methane/air flames [183].

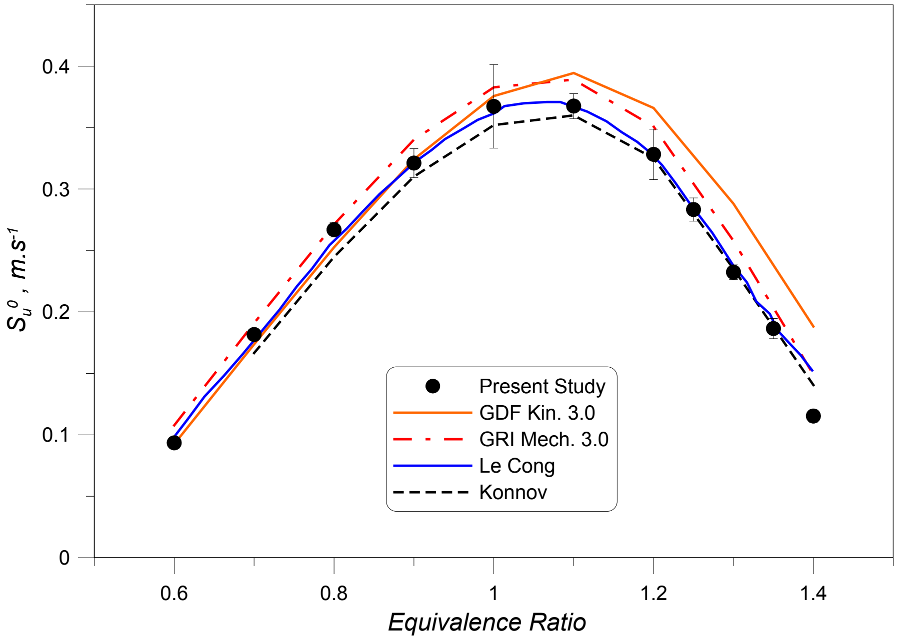

Figure IV.20 Comparison of experimental CH_4/air flame speed results along with predictions of various kinetic mechanisms: GRI Mech. 3.0 [148], GDF Kin. 3.0 [180], Konnov [181] and Le Cong [182].

IV.3 PART II: Numerical Study

A common practice is to use one-dimensional (1D) codes to validate thermochemical models against experimental results. This is rendered possible for stagnation flow flames by using dedicated programs, such as OPPDIF [28] or CANTERA [55], widely used in the combustion community. Such experimental and numerical confrontations have been performed, for example, in the works of Lim [184] with studies on temperature and species profiles for laminar diffusion flames in methane/air mixtures, in the works of Bergthorson [56] with comparisons of velocity and CH profiles for methane-ethane-ethylene/air flames or more recently in the investigation of Wu and coworkers [185] on the general impact of CO addition in laminar premixed methane/air flames. To a lesser extent, two-dimensional (2D) simulations have been made, mainly for steady laminar diffusion flames [186-188] and more complex unsteady or transient phenomena including extinction/flame vortex interactions [189-193] and transition from diffusion to edge flames [194-195]. It was generally observed that matching experimental and 1D numerical results is a hard task and that even detailed modeling including various forces contributions on the particle motion can still result in noticeable discrepancies [40, 56]. On the other hand, it has been found that the 1D approach might be inaccurate if the initial velocity profile is nonuniform [187]. To our knowledge, a systematic confrontation of 1D and 2D computational results with experimental measurements for steady premixed stagnation flames has not been performed before. It deserves a particular attention because, as stated earlier, 1D tools are commonly used to develop and assess the performances of kinetic mechanisms. Thus, a deficiency in the 1D modeling approach would have dramatic consequences, resulting in wrongly optimized kinetic models. The present section also gives the opportunity to assess the dynamics of seeding particles in the stagnation flow configuration. Although several studies did evaluate particle motions and the influence of main parameters, such as inlet velocities, particle diameter etc., mostly highly diluted [35] or weak flames [38] were concerned. They will be here characterized for the stronger burning CH_4/air flames studied in the first part of the present chapter.

IV.3.1 Simulated Cases

Two cases were considered for the detailed 1D and 2D simulations whose properties were based on experimental measurements presented in the previous sections. Cases specifications are shown in Table IV.**3**. Cases I and II correspond respectively to stagnation plate and counterflow twin flames for an intermediate strain of the experimentally determined strain rate range. Stoichiometric mixtures were chosen since the chemistry is expected to be well known. Also, important variations of velocity and higher temperature are expected for these strongly burning cases, providing therefore stringent conditions for the evaluation of the particle capacity to closely follow the flow.

Case Property	**Case I**	**Case II**
Burner configuration	Stagnation plate flame	Counterflow twin flames
Burner I.D., mm	7	15
L_{sp} or L, mm	7	16.6
Temperature	Ambient	Ambient
Pressure	Ambient	Ambient
Mixture	CH_4/air	CH_4/air
Equivalence ratio	1.0	1.0
Inlet mean velocity, $m.s^{-1}$	1.07	1.31
Flame strain rate, s^{-1}	359	296
Inlet flow rate, $L.min^{-1}$	2.024	15.810
Inert coflow flow rate, $L.min^{-1}$	2.419	15.934
$S_{u,ref}$ minimum, $cm.s^{-1}$	43.8 ±1.8	45.2 ±2.6

Table IV.3 Specifications for the 1D and 2D calculations.

IV.3.2 Numerical Methodologies

Two approaches are used for the numerical simulation of the laminar strained flames: the quasi-1D and 2D axisymmetric respectively using the OPPDIF [28] and Fluent® v6.3 codes. For both simulations, the flow is considered steady state and incompressible. The latter means that the gas density is a function of the temperature and gas composition and does not depend on the local pressure variation.

1D Simulation Specifications

OPPDIF Cases

According to the 1D formulation presented in Table I.4, the axisymmetric flow is simulated along the axis between: the burner exit and the stagnation plate (Case I) or both nozzle exits (Case II). At the burner exit(s), the imposed boundary conditions are: axial velocity and radial velocity gradients perpendicular to the main axis, temperature and fresh mixture composition. For case I, the wall boundary conditions are defined by zero velocity, a given wall temperature, and zero gradient of species fractions. The latter condition implies that the wall surface is chemically inert. For convenience, the momentum equation (I-27) is rewritten as:

$$2F\frac{d}{dx}\left(\frac{G}{\rho}\right) = H + \frac{G^2}{\rho} + \frac{d}{dx}\left[\mu\frac{d}{dx}\left(\frac{G}{\rho}\right)\right] \qquad \text{(IV-1)}$$

This equation is solved together with the species transport (I-29) and energy (I-30) equations.

2D Simulation Specifications

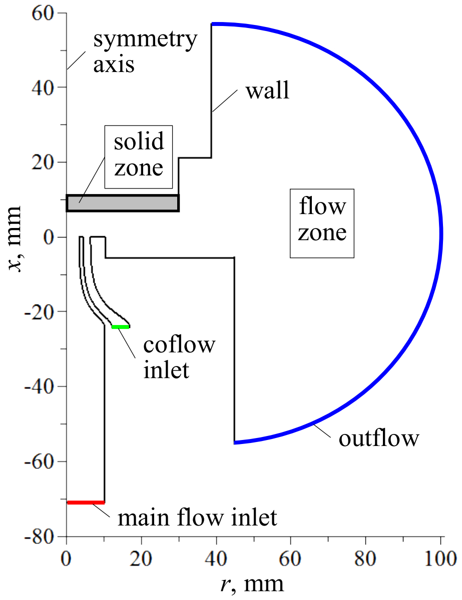

Figure IV.21 Schematic of the stagnation plate flame computational domain (*BID*: 7 mm, L_{sp}: 7 mm).

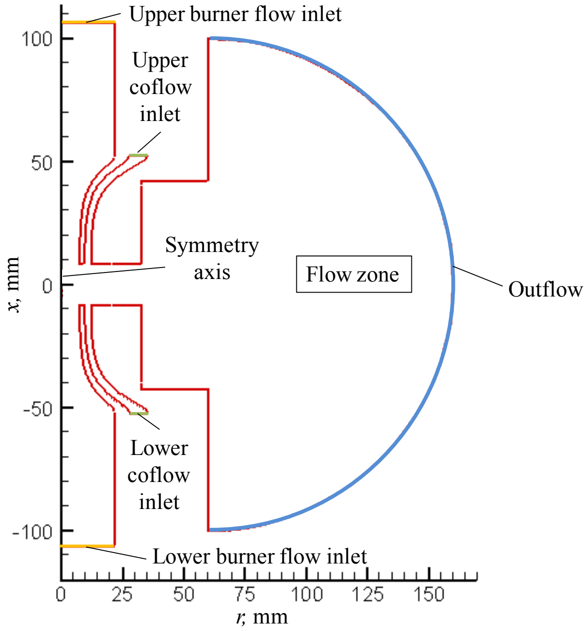

Figure IV.22 Schematic of the counterflow flames computational domain (*BID*: 15 mm, *L*: 16.6 mm).

The flow is simulated in a 2D domain that covers the burner internal ducts as well as regions around the burners. Schematic views of the computational domains are presented in Figure IV.21 and Figure IV.22. The domains consist of flow zones, for which the fluid transport equations are solved, limited by the inflow and outflow boundaries and by the solid walls. For case I, an additional solid zone representing the stainless steel disk is considered, for which the heat conduction equation is solved. The flow and solid zone solutions are coupled through the temperature distribution on the open wall of the disk. The back wall of the disk is assumed adiabatic.

The inflow boundaries of the computational domains are set in the sections where the laminarization grids are located. This is necessary to create physically correct conditions at the burner exit taking into account the boundary layers on the internal walls. Uniform profiles of velocity, temperature and species concentrations are imposed on the inflow boundaries. The outflow boundaries are set far from the flame zones in order to avoid perturbations that may be caused by the constant-pressure condition imposed on this boundary. The computational meshes are mixed including: i/ structured quadrilateral in the internal ducts and within the regions “burner-to-disk” (case I) and “burner-to-burner” (case II), ii/ unstructured triangle meshes for the rest of the flow zones and the entire solid zone. The finest spatial resolution in the flame zones is 50 μm on the base level. For case I, two subsequent mesh refinements are made within regions covering the flames in order to improve the solution quality and study the solution dependence on the spatial resolution. At each refinement, the mesh cells are split by 2 in each spatial direction. Based on the latter results (see incoming discussion on case I) only one level of mesh refinement is used for the counterflow case. Computations of case II are done in two distinct steps: 1/ calculations are performed on one half of the computational domain presented in Figure IV.22, considering an symmetry plane located at the center of the nozzle separation distance, 2/ the full domain is obtained by mirror symmetry and initialized from the converged solution of step 1 and the gravity force is added. The used numerical schemes provide, for both cases, a solution that is 2nd order accurate in space.

Thermochemical and Transport Models

The thermochemical and transport models employed in the simulations take a particularly important place. A specific attention has been paid to ensure that the thermochemical properties of the reacting mixture are determined in the same way for the 1D and 2D approaches.

The chemical kinetic mechanism developed by Smooke and Giovangigli [196] is taken due to its relative simplicity. Two modifications are introduced:

- The H_2O_2 species and related chemical reactions are eliminated as they are not important for the considered conditions;
- All the chemical reactions are considered reversible.

Finally, the mechanism consists of 15 species, including inert N_2, and 23 reactions. The species thermodynamic properties are taken from the Fluent thermodynamic data base, which is compatible with that used in the CHEMKIN-II library.

Transport properties of pure species (viscosity, thermal conductivity, and binary diffusion coefficients) are determined according to the molecular kinetic theory [197] based on the Stockmayer potential function. Parameters of the potential function can be found either in the Fluent data base or in the data base related to the CHEMKIN-II transport library. To ensure that the species transport properties are compatible in the 1D and 2D simulations, their temperature dependencies are approximated by polynomial functions and introduced in this form in the Fluent computational cases. For the mixture, a specific model is applied to each kind of transport property. Classical formulations used in the 1D and 2D codes were recalled in Table I.5. One can obviously notice that both models are originally not fully compatible. Therefore, the following choices and modifications are made:

- The mixture viscosity is determined from the Wilke formula (see expressions (I-38) and (I-39) of Table I.5).
- The default formulations for the mixture thermal conductivity λ being different for 1D and 2D approaches, the combination averaging formula (I-40) is chosen [32]. Fluent formulation (I-41) is replaced by a user function written according to (I-40).
- Notable differences can be found for diffusion mass fluxes and diffusion coefficients between the classical formalism [31] and the one adopted in Fluent. As it appears to be a tedious task to change Fluent diffusion model, Fluent formalism is adopted for the 1D simulations, i.e. (I-42) and (I-44) are respectively replaced by (I-43) and (I-45) in the 1D code.

Additional Considerations

The effect of the gravity force has been tested with the 2D approach for cases I and II. If it was found to have a negligible effect in the region between the burner and the disk, it had a notable influence on the counterflow twin flames. This effect will be commented in a later section.

For case I, the thermal radiation is taken into account only for the open wall of the disk. The radiative heat flux is expressed as follows:

$$q_{rad} = \sigma\varepsilon(T_\infty^4 - T_w^4) \tag{IV-2}$$

where σ is the Stefan-Boltzmann constant, $\varepsilon = 0.8$ is the effective emissivity whose value is found empirically, $T_\infty = 293$ K is the ambient temperature far of the plate, T_w is the disk wall temperature.

The wall temperature of the burners is taken equal to T_∞. Radiation absorption and emission in the gas are neglected.

Validation of the Chemical and Transport Models

Before presenting results for the strained flames, the chemical and transport models are validated in the case of freely propagating adiabatic flame using the PREMIX code [27] presented in chapter I. For atmospheric pressure and room temperature in the fresh mixture, the fundamental velocity of laminar flame in the stoichiometric CH_4/air mixture is assessed using different options discussed above. The results are summarized in Table IV.4. Numerical predictions are compared with an average of experimentally determined values included in Figure IV.15, Figure IV.16 and Figure IV.17. It can be seen that predicted values agree very well with the experimental one. The highest velocity is obtained for the original mechanism and the diffusion flux formulation (I-42). Also, results seem quite insensitive to the diffusion flux formulation with a difference of only 0.3 cm.s^{-1}.

Description	**Value, cm.s^{-1}**
Experiments	36.5 ±2.7
Original mechanism, diffusion flux formulation (I-42)	37.1
Modified mechanism, diffusion flux formulation (I-42)	35.9
Modified mechanism, diffusion flux formulation (I-43)	35.6

Table IV.4 Comparison of experimentally determined and calculated values of the laminar flame speed of the stoichiometric methane/air mixture. Different modeling options are considered.

IV.3.3 Results and Discussions

The Stagnation Plate Flame Case

The 2D approach

First 2D simulations correspond to the case of cold nitrogen jet impacting on the stagnation plate. In this case, nitrogen at room temperature is injected through the center nozzle without coflow. Radial profiles of the axial velocity component are plotted in Figure IV.23 for three cross sections, respectively at x = 1, 4 and 6 mm away from the burner exit. The radial coordinate is normalized by the center nozzle radius at the exit, ie. R_0 = 3.5 mm, and the velocity is normalized by the mean velocity at the exit, $U_0 = Q/A_0$, where Q is the volumetric flow rate and A_0 is the cross section area at the nozzle exit. The experimental profiles (points) are folded to demonstrate their symmetry with respect to the axis. The experimental and numerical results are in a good agreement. At x = 1 mm, the core flow velocity is 34 % higher than U_0 because of the boundary layer, which is formed near the wall inside the duct.

For the reactive case (case I), the computed temperature field in the vicinity of the flame is shown Figure IV.24. The black contours delimit the zones where the mesh has been refined. The superimposed white lines are contours of constant mass fraction of N_2, i.e. Y_{N2} =constant. As Y_{N2} = 0.725 in the fresh mixture, the contour Y_{N2} = 0.75 roughly represents the boundary of the main flow, which is not diluted with N_2 from the coflow. The flame front is flat in the core flow while its edge is bended in the wake because of lower velocity due to the finite nozzle burner thickness.

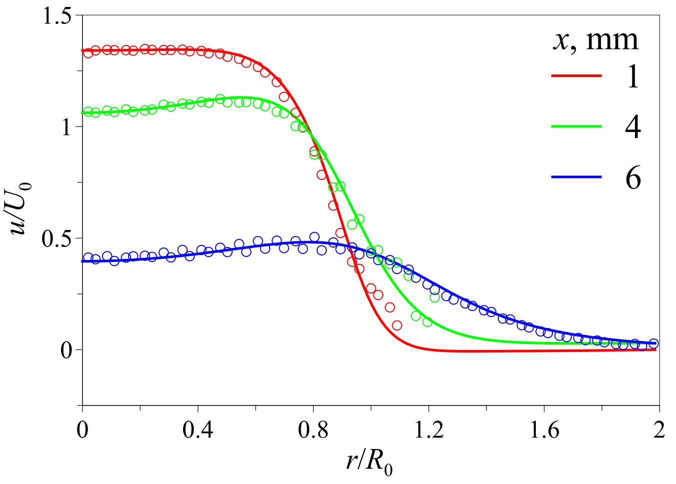

Figure IV.23 Normalized cold flow velocity profile at different distances from the burner. Lines: Fluent simulation, symbols: experiment.

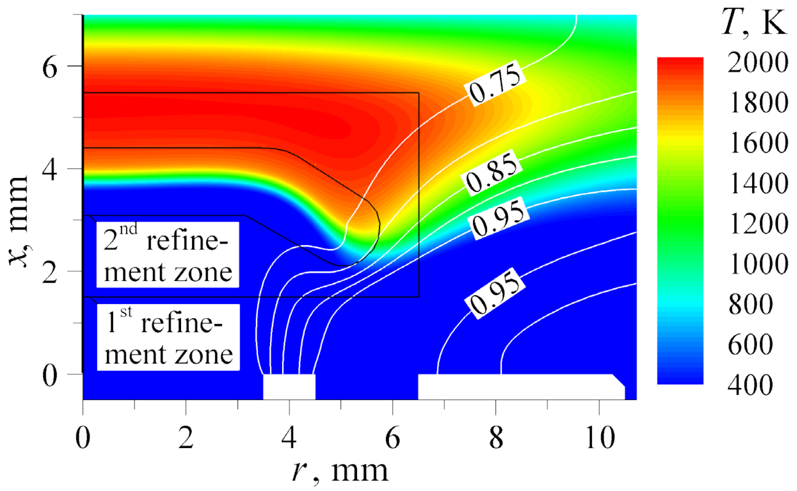

Figure IV.24 Temperature field, grid refinement zones and superimposed iso-contours of N_2 mass fraction.

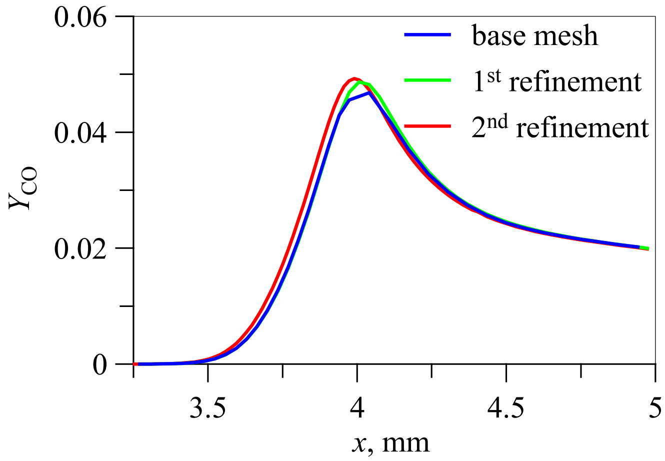

Figure IV.25 Axial distributions of CO mass fraction computed with different spatial resolutions.

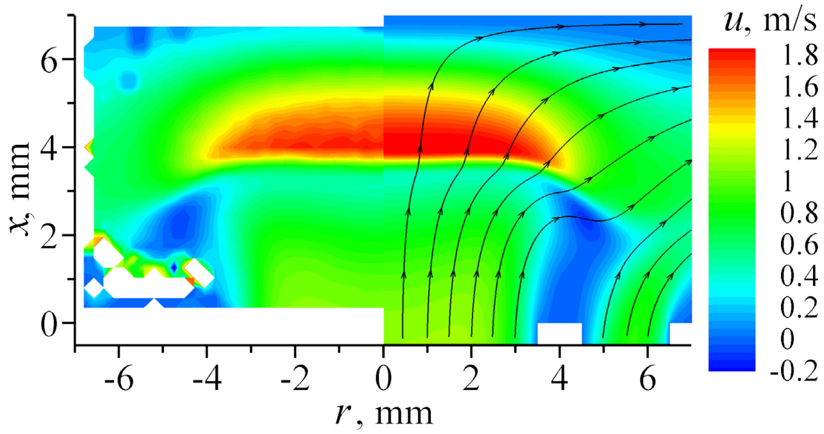

Figure IV.26 Comparison of the field of axial velocity component for DPIV measurements (left side) and 2D computations (right side). Streamlines are superimposed for the computed velocity field.

The predicted temperature on the axis of the metal disk is about 790-800 K, whereas the temperature measured by thermocouple is close to 750 K. Taking into account the simplicity of the heat radiation model (expression (IV-2)) as well as possible errors due to the heat losses in the thermocouple wires, the agreement is satisfactory. The numerical solution appears quite insensitive to the mesh refinement. From the solution comparison, notable differences are found only for intermediate species and radical whose mass fractions have maxima in the flame zone. As an example, axial distributions of CO mass fraction are plotted in Figure IV.25. These results clearly indicate that a single level of refinement is expected to yield sufficient accuracy for the data comparisons intended herein.

The measured and computed fields of axial velocity component are compared in Figure IV.26. Streamlines are traced for the computed velocity field. In the lower part, one can distinguish the main flow and the coflow divided by the wake from the center nozzle lip. In the upper part, the flame front is marked by a rapid flow acceleration, due to the gas heating, followed by a gradual velocity decrease toward the disk wall. As the flow accelerates in the direction normal to the flame front, the streamlines deflect while crossing the flame. The simulation provides an accurate prediction of the velocity field both in the core flow and in the wake.

1D versus 2D results

A 1D simulation has been performed for the boundary conditions specified for the case I (see Table IV.3), an initial radial velocity gradient of 55 s^{-1} and a disk wall temperature of 800 K. The imposed velocity and temperature are taken the same as in the 2D simulation. The velocity gradient is adjusted to have the same position of the flame front as in the 2D simulation. Velocity and temperature distributions along the axis are compared in Figure IV.27 and Figure IV.28. For the velocity distribution, experimental results are included along with numerical predictions of both approaches. It can be seen that all velocity distributions agree well in the hydrodynamic and fast expansion regions of the flame. However, the 1D simulation overestimates the maximum velocity by about 18 cm.s^{-1} whereas the 2D simulation is significantly more accurate compared to the experimental results. On the other hand, the compared temperature profiles are in close agreement. Hence the velocity deviation is due to different radial spillage of flow in the 1D and 2D simulations. To check the validity of the 1D approach, two principal terms of the momentum equation (IV-1), H and G^2/ρ, are evaluated from the 2D simulation. Distributions obtained in the vicinity of the burner axis are put together in Figure IV.29 and Figure IV.30. Both terms are of the same order of magnitude. An important finding is that H strongly varies through the flame front for the 2D simulation, whereas H = constant = -3.89×10^4 Pa.m^{-2} in the 1D simulation. Thus in the present case, the velocity overshoot in the 1D simulation is due to the simplifying assumption H = constant. Frouzakis et al. [187] also found important variations of the H term in the case of laminar hydrogen-air diffusion flames in the counterflow configuration (L=10 mm). In our case, however, the variation of H is much stronger while crossing the flame front.

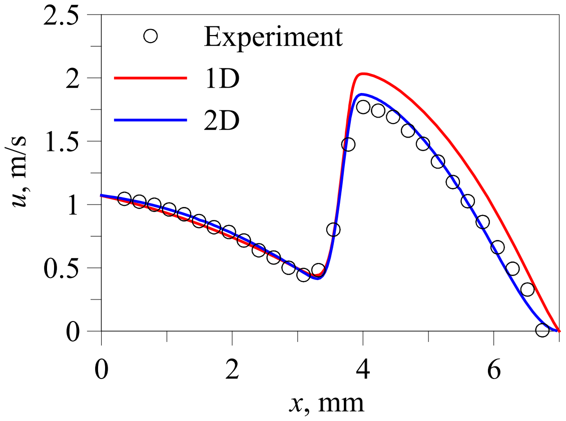

Figure IV.27 Comparison of axial velocity profiles for measurements, 1D and 2D simulations.

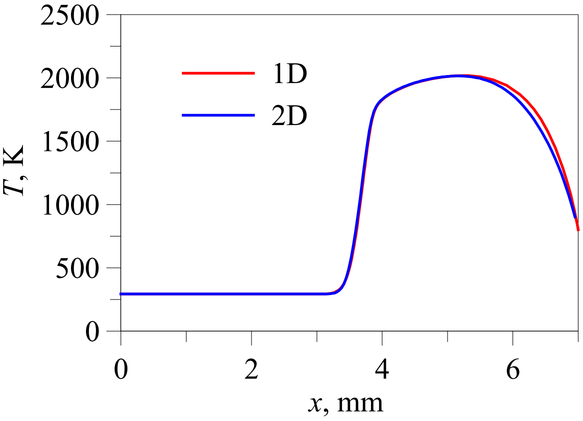

Figure IV.28 Temperature profiles along the axis for the 1D and 2D simulations.

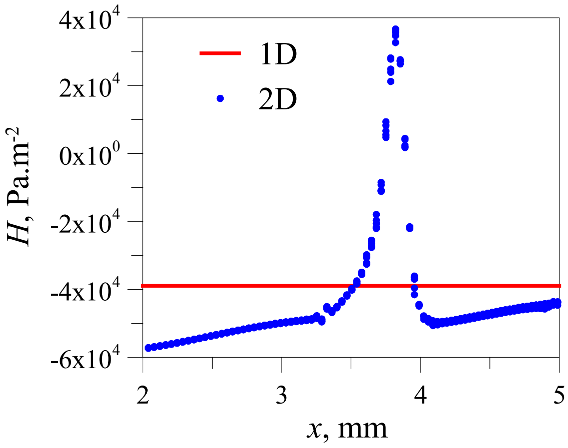

Figure IV.29 Evolution along the axis of the H term of the momentum equation for the 1D and 2D computations.

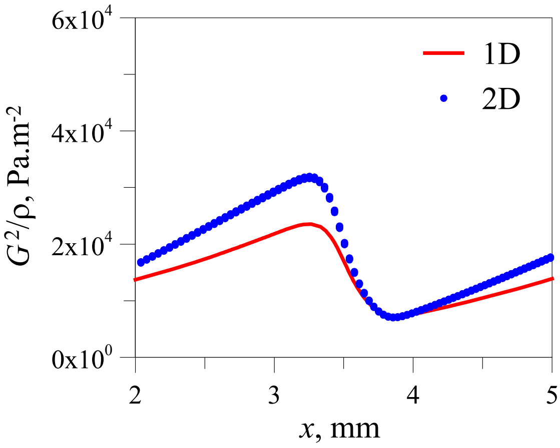

Figure IV.30 Evolution along the axis of the G^2/ρ term of the momentum equation for the 1D and 2D computations.

Estimation of flow tracking errors

Provided by the PIV technique, the experimentally measured velocity corresponds to the mean velocity of seeding particles within an interrogation cell. The accuracy of such measurements, as emphasized earlier, relies on the hypothesis that seeded materials closely follow the flow. It is therefore of a particular interest to evaluate the particle slip with respect to the gas flow for the present case. The slip error can be estimated based on the 2D simulation results. The following analysis is made considering the motion of a single solid particle along the flow axis. The particle motion equations are:

$$\frac{dx_p}{dt} = u_p \tag{IV-3}$$

$$\frac{du_p}{dt} = -F_D(u_p - u_f) + g_x\left(\frac{\rho_p - \rho_f}{\rho_p}\right) + a_{th} \tag{IV-4}$$

Where the “p” and “f” subscripts refer to the particle and fluid properties respectively, u is the axial velocity component, F_D is the aerodynamic drag coefficient; g_x is the gravity acceleration; a_{th} is the particle acceleration due to the thermophoretic force. Other acceleration factors like the Brownian force or Saffman’s lift force are neglected. The aerodynamic drag coefficient is obtained from the drag coefficient of expression (II-6) divided by the particle mass $m_p = \varrho_p \pi d_p^3/6$:

$$F_D = 18\mu\left(d_p^2\rho_p C\right)^{-1} \tag{IV-5}$$

where C is the Cunningham correction factor defined in (II-7). The thermophoretic acceleration is determined according to the following formula:

$$a_{th} = -\frac{C_{th}}{m_p T_0}\frac{dT}{dx} \tag{IV-6}$$

where C_{th} is the thermophoretic coefficient whose definition can be deduced from expression (II-16):

$$C_{th} = \frac{6\pi\mu\eta d_p C_s\left(\frac{k_f}{k_p} + C_t Kn\right)}{(1 + 3C_m Kn)\left(1 + 2\frac{k_f}{k_p} + 2C_t Kn\right)} \tag{IV-7}$$

Parameters involved in the latter expression are defined in chapter II.

The particle chosen for the present simulation has the following constant properties: diameter $d_p = 1.8$ µm, density $\varrho_p = 5890$ kg/m^3, thermal conductivity $k_p = 2.2$ W.m^{-1}.K^{-1}. Its motion is simulated from the main flow inlet ($x = -70$ mm) to the disk wall ($x = 7$ mm).

First of all, it can be seen, in Figure IV.31 and Figure IV.32, that the particle temperature closely follows the flow temperature with a maximum difference of approximately 45 K within the flame region. This result is in accordance with the numerical study of Egolfopoulos and Campbell [38] for which it was stated that small particles heat up very quickly and hence usually closely follow the gas phase temperature.

The distribution of the particle slip, defined as $u_p - u_f$, is plotted in Figure IV.33 for three different cases. Case 1: Gravity and thermophoretic accelerations are neglected ($g_x = 0$ and $a_{th} = 0$). Case 2: Thermophoretic acceleration is neglected ($a_{th} = 0$). Case 3: All accelerations are taken into account. This comparison shows that the particle slip is affected by the drag and thermophoretic forces whereas the gravity force is practically unimportant. The thermophoretic force is a strong factor that slows down the particle in the flame front and accelerates it close to the disk wall. The estimated slip error globally varies from –0.43 m.s^{-1} to 0.1 m.s^{-1}. Note however that the minimum velocity $S_{u,ref}$ used in the present methodology stays unaffected since induced thermophoretic and drag slips are important only in the fast expansion zone of the flame. In Figure IV.34, the distribution of particle velocity is compared with the experimental results and the flow velocity from the 2D simulation. With respect to the flow velocity distribution, the observed deviations of the particle velocity are coherent with the deviations of the experimental data: slower velocity increase in the flame front, lower velocity maximum, and higher velocity in the thermal layer near the disk wall. Similar results were obtained for diluted counterflow premixed methane/air flames by Sung and coworkers [35, 40] for smaller Al_2O_3 particles (0.3 μm) and also Bergthorson and Dimotakis [41] in the stagnation plate configuration using 3 μm ceramic microspheres. In the latter case, their 1D model, incorporating both particle drag and thermophoretic forces, still largely overestimates their experimental measurements. An attempt to match both approaches is proposed in ref. [41] by tuning the pre-exponential factor of the main chain branching reaction $H+O_2 \leftrightarrow OH+O$ until obtaining matching experimental and computed velocity profiles. In the light of the present analysis and aware of the limitations of the 1D approach demonstrated in the previous section as compared to the 2D modeling, it appears reasonable to assume that discrepancies observed in ref. [41] might not only arise from chemical kinetics but also from the inadequacy of the 1D model employed. Therefore, a direct evaluation of kinetic mechanisms with respect to stagnation flow velocimetry data using classical 1D approaches should be used very cautiously.

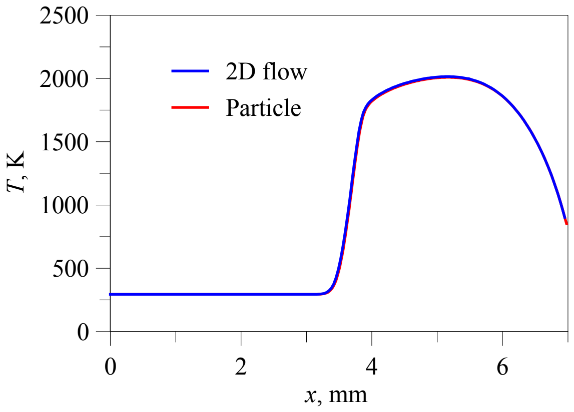

Figure IV.31 Gas and particle temperature distributions along the axis.

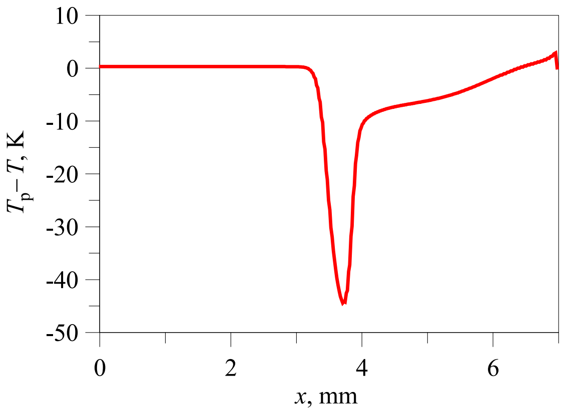

Figure IV.32 Temperature difference between the particle and gas.

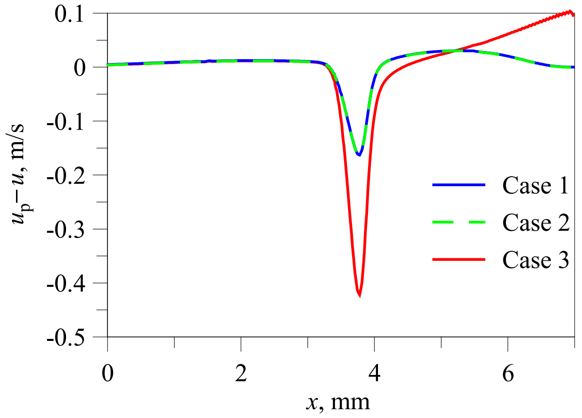

Figure IV.33 Predicted particle slip velocity along the flow axis for various cases. Case 1: gravity and thermophoretic accelerations neglected; case 2: gravity acceleration included; case 3: gravity and thermophoretic accelerations included.

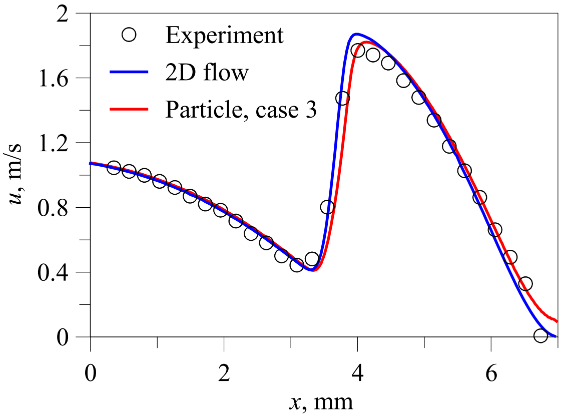

Figure IV.34 Comparison of axial velocities given by DPIV measurements, 2D flow and particle motion simulations.

The Counterflow Twin Flame Case

The 2D approach

As discussed earlier, case II was performed in two distinct steps. The first calculations were done for the lower half of the full counterflow geometry assuming a symmetry plane perpendicular to the burner main axis. Gravity effects were neglected. The second set of calculations was done for the full realistic counterflow geometry described in Figure IV.4. This time, the gravity force contribution was included. Comparison of both axial velocity and temperature profiles are shown in Figure IV.35. Results for the symmetry case (half domain) are duplicated in the other half of the full domain for the ease of comparison. A slight displacement of 0.25 mm in the upward direction is observed for the twin flame system due to the gravity effect. To analyze the influence of this effect on the flame structure, velocity and temperature profiles of the full counterflow case were shifted downward by this displacement. It can be seen that both profiles are perfectly superimposed attesting in return that the gravity force does not affect the flame structure for the present case. Indeed, minimum reference velocities $S_{u,ref}$ are respectively 41.2 and 41.4 cm.s^{-1} for the lower and upper twin flames against 41.2 cm.s^{-1} for the single flame of the symmetry case. This result yields an interesting implication by suggesting that only half of the full counterflow domain can be considered, which considerably reduces the computation times involved.

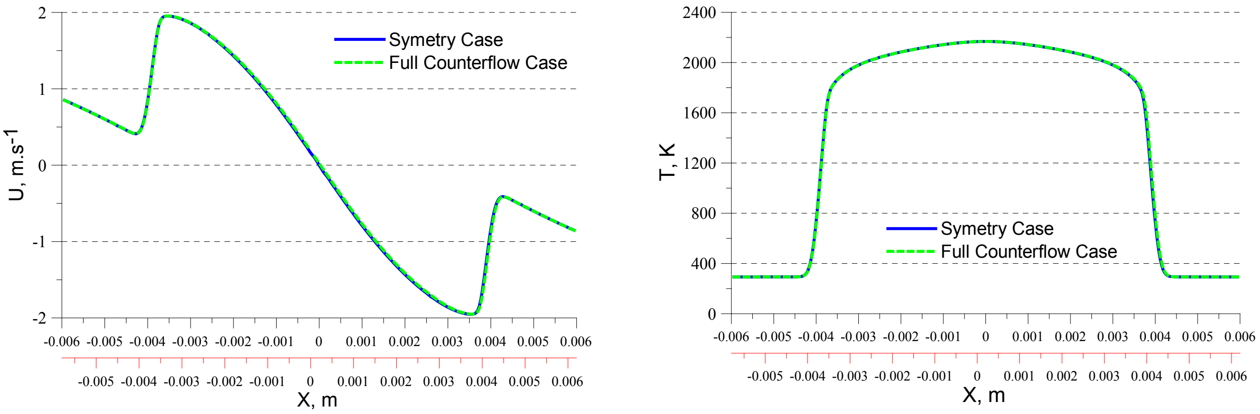

Figure IV.35 Axial velocity profiles (left) and temperature profiles (right) for the symmetry and full counterflow case computations. The latter includes the gravity force. Upper and lower abscissa scales respectively correspond to the symmetry and full counterflow cases.

For the full counterflow case, the temperature field in the vicinity of the twin flames is shown in Figure IV.36. The black boxes indicate the localization of the mesh refinement zones. The twin flame system is roughly located in the center of the nozzle separation distance. It can be seen that hot products, characterized by a lower density, are convected upwards and progressively wrap the upper burner head and the body. This particularly underlines the importance of providing sufficient insulation for the upper burner, as shown in Figure IV.4, a rather cumbersome task that usually alters the system flexibility. An interesting point seen in the temperature field is that the angular shape of the burner water-cooled head gives rise to a recirculation zone whose temperature is much lower than in hot products due to the dilution and wall heat exchange effects. Thus, if the upper burner is not properly protected, heat transfers are expected to be enhanced along the burner body where combustion products are still above 1000 K.

Axial and radial velocity components for the 2D counterflow simulated case are provided in Figure IV.37. Corresponding experimental velocity fields are superimposed in the central black boxes. Color scales of velocity fields are the same for both simulation and experiment. A very good agreement is found for both velocity fields. For the axial component of the velocity, the thickness of the flame zone, characterized by higher velocities, closely coincides for both experimental and numerical approaches. Also, the same can be affirmed for the range of unaffected core flow parts by straining at the beginning and end of the measurement zone. An interesting point, brought by the simulation results, is that radial spillage already starts inside the burner nozzle which indicates that the jet of fresh reactants is already strained at the burner exit. This was also the case for the precedent stagnation plate flame configuration. It deserves a particular attention since many numerical investigations are performed assuming pure plug flow conditions i.e. $a = 0$ s^{-1} at the burner exit, whereas practical systems are always characterized by an initial radial strain.

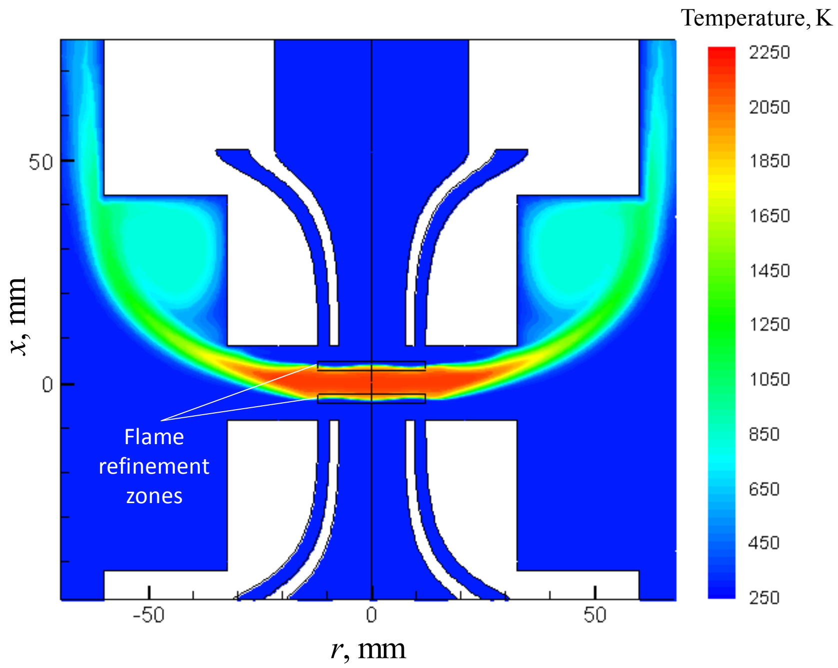

Figure IV.36 Temperature field and grid refinement zones for the counterflow flame case.

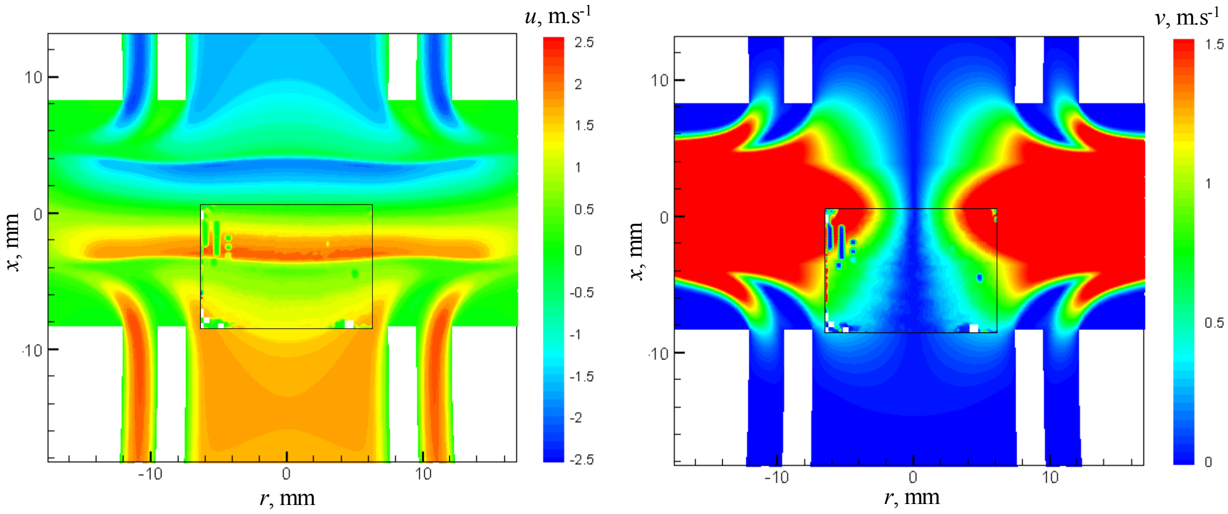

Figure IV.37 Axial (left) and radial (right) velocity components for the 2D simulated case with superimposition of DPIV measurements in the zone of interest (central rectangular box).

1D versus 2D results

For the sake of clarity, the OPPDIF version with the modified diffusion formalism as well as the Smooke modified mechanism will be identified by the "*" symbol following their names in the remainder of the present section. Absence of this symbol designates the classical non-modified formulation of the diffusion model as well as non-modified version of the Smooke and Giovangigli [196] mechanism.

1D simulations have been performed for the boundary conditions specified for case II (see Table IV.3) and an initial radial velocity gradient of 81.6 s^{-1} estimated from experimental measurements.

The velocity and temperature profiles are compared in Figure IV.38 and Figure IV.39. Results from 1D computations with the GRI Mech. 3.0 are added for comparison. The extent of deviation between the 1D and 2D results is not as obvious as in the precedent case. If both approaches still display perfectly superimposed temperature profiles, the discrepancy between 1D and 2D model is only noticeable for the maximum velocity achieved in the flame region that is still higher for the 1D simulation with respect to the 2D one. Both seem to slightly underestimate experimental results in the flame zone. The use of a different kinetic mechanism for the 1D computation does not bring any fundamental difference, the slight temperature increase observed in Figure IV.39 being responsible for the superior trend observed in the velocity profile of Figure IV.38.

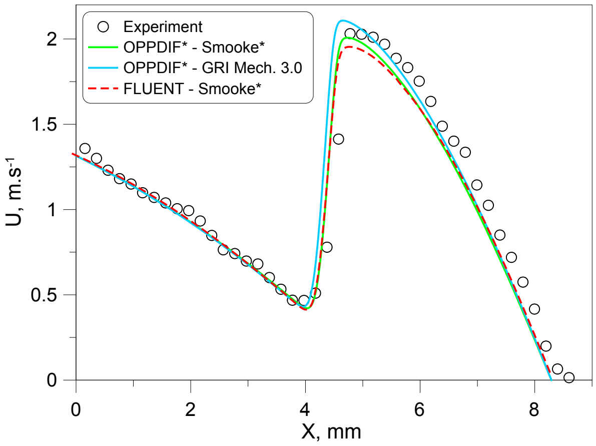

Figure IV.38 Axial velocity profiles comparison for 1D (Smooke* and GRI Mech. 3.0 mechanisms), 2D and experimental results.

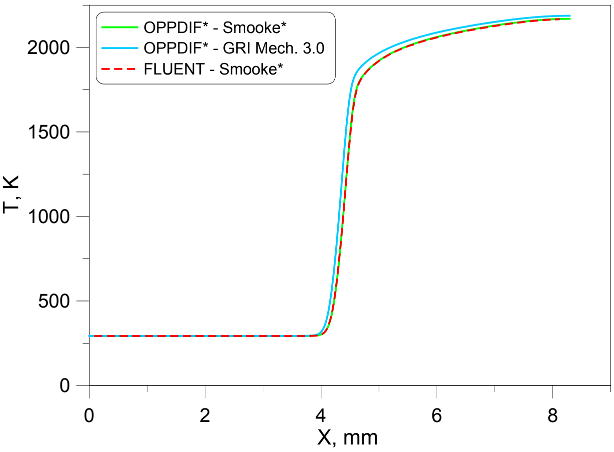

Figure IV.39 Centerline temperature profiles for 1D (Smooke* and GRI Mech. 3.0 mechanisms) and 2D models.

The main terms H and G^2/ρ of the momentum equation are plotted in Figure IV.40 for the 1D and 2D models. The pressure derivative term is still considerably different from the constant values imposed by the 1D formulation in the flame region. A considerably improved agreement is however found for both terms in the rest of the entire domain, which may explain in return the better adequacy between the 1D and 2D approaches observed in Figure IV.38.

An interesting confrontation that has not been done yet is the comparison of radial strains for experiments and computations at different characteristic locations within the flow. This is of particular interest since: i/ the 1D model requires an inlet radial velocity gradient a if plug flow conditions are to be used, ii/ the DPIV methodology developed herein is based on the strain rate determination from the profiles of radial velocity component at the local velocity minimum $S_{u,ref}$.

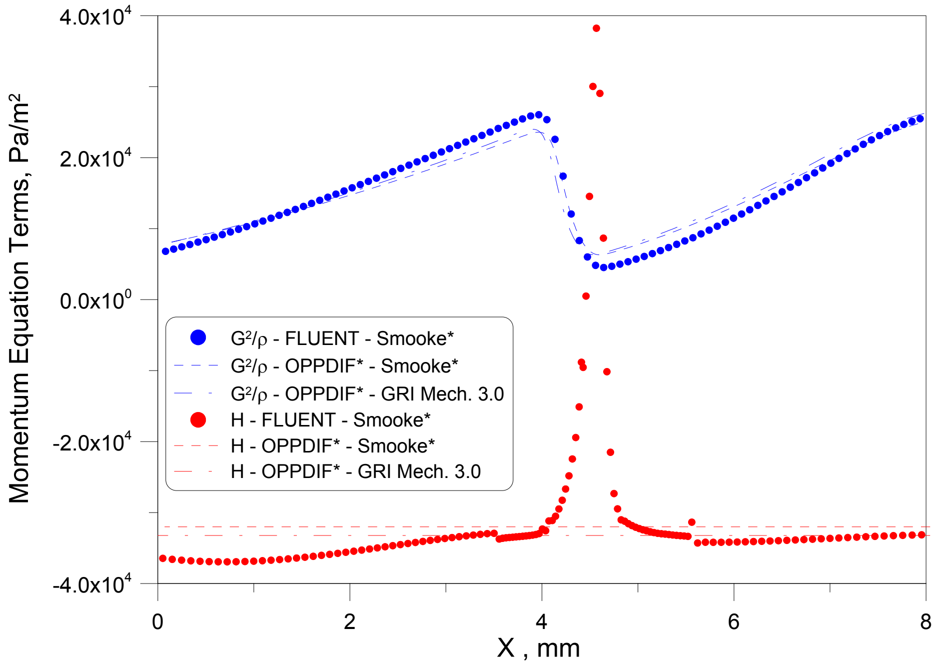

Figure IV.40 Evolutions along the axis of the H and G^2/ρ terms of the momentum equation for the 1D (Smooke* and GRI 3.0 mechanisms) and 2D computations.

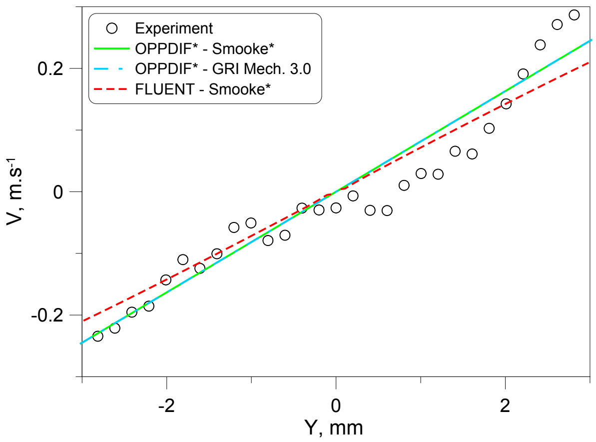

Figure IV.41 Radial component of the velocity plotted in the radial direction at the burner nozzle exit for the 1D (Smooke* and GRI 3.0 mechanisms), 2D and experiments.

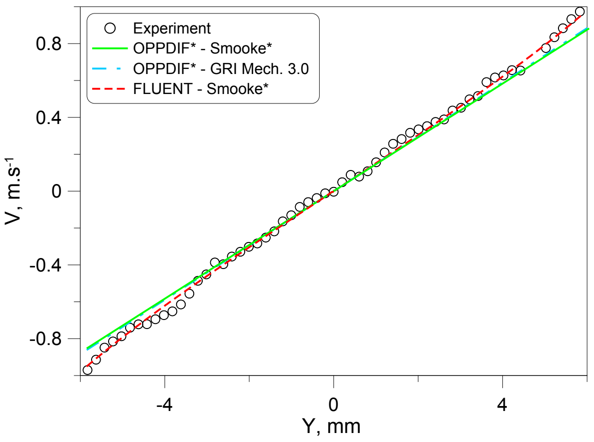

Figure IV.42 Radial component of the velocity plotted in the radial direction at the position of minimum velocity, $S_{u,ref}$, for the 1D (Smooke* and GRI 3.0 mechanisms), 2D and experiments.

Figure IV.41 and Figure IV.42 show comparisons of measured and computed profiles of radial velocity in the radial direction at the burner nozzle exit and at the local minimum velocity ($S_{u,ref}$) location respectively. In Figure IV.41, it can be noticed that the experimental profile is slightly wavy. This behavior is mainly due to the biasing effect of the laser reflections on the burner lip that perturbs DPIV processed velocities in this specific zone. However, a rough estimation of the inlet radial velocity gradient from experimental data is necessary as a 1D input parameter since it can remove the need of fitting experimental velocity profile by scanning all possible inlet conditions from pure plug flow to potential flow until computed and measured profiles match [40]. Here, a satisfactory agreement is obtained between the 1D and 2D models providing radial velocity gradients equal to 81.6 and 70.6 s^{-1} respectively. An excellent agreement is found however at the location of the minimum velocity (see Figure IV.42) with 145.9 and 147.3 s^{-1} for 1D computations (Smooke* and GRI mechanisms), 151.6 s^{-1} for 2D computation and 152.5 s^{-1} for experiment. Interestingly, $S_{u,ref}$ values calculated for the Smooke* mechanism for both 1D and 2D approach differ of about 1 cm.s^{-1}, a value somehow important since applied strain rates are similar and also given that methane/air flames are known to display poor sensitivity to strain. Figure IV.43 shows the evolution of the radial velocity gradient along the burner axis from the computations and experiment. An excellent agreement is found between the 2D computation and experiment on the entire domain. 1D computations, however, significantly overestimate the radial velocity gradient after the velocity minimum located approximately at x = 4mm, suggesting in this case a higher aerodynamic strain felt by the 1D computed flame. This is coherent with preceding observations for which the reference flame speed was higher for the 1D computed case as compared to the 2D value. The additional straining arising from density variations throughout the flame front are expected to be of the same order since the density profile for both 1D and 2D is the same.

Since the 2D model presented herein seems to accurately describe the stagnation flame of case II, it was decided, in the light of the present example, to assess several strain rate definitions used in experimental and numerical studies. Three expressions for the strain rate are considered: i/ the conventionally used derivative of the axial velocity component $K=-du/dx$, ii/ the radial velocity gradient-based expression $K_r = 2a$, iii/ the general formulation of the strain rate for variable density stagnation point flows (see expression (I-32)), denoted here as K_g:

$$K_g = -\left(\frac{1}{\rho}\right)\frac{d\rho u}{dx} \tag{IV-8}$$

The first two expressions cease of course to be accurate when flow density variations take place, as recalled in chapter I. Spatial variations of these quantities are plotted along the burner axis in Figure IV.44. The conventional plane or reference corresponding to the local minimum velocity, $S_{u,ref}$, is indicated by a black dashed line. It can be seen that the radial strain definition, K_r , agrees particularly well with the general definition, K_g , and that deviations introduced by the variable density of the flow are felt only further downstream of the chosen reference plane. On the other hand, the axial definition of strain, prone to important variations in the vicinity of the reference plane, needs to be evaluated further upstream, a procedure widely applied in experimental works. Usually few points are selected and a linear regression is performed to determine the associated strain rate. In the present case, a similar procedure performed on 6-7 data points centered at x = 3.17 mm (i.e. first experimental point of Figure IV.44) yields a strain rate value K = 269.8 s^{-1}, to be compared to K_r = 304.9 s^{-1} and K_g = 293.3 s^{-1}. This clearly indicates that the conventional flame strain rate evaluation will tend to give a lower value than the actual strain rate at the reference plane. This conclusion is concordant with the experimental trends observed in Figure III.21 and underlines the advantage of using the strain rate definition K_r to yield coherent flame answers to straining.

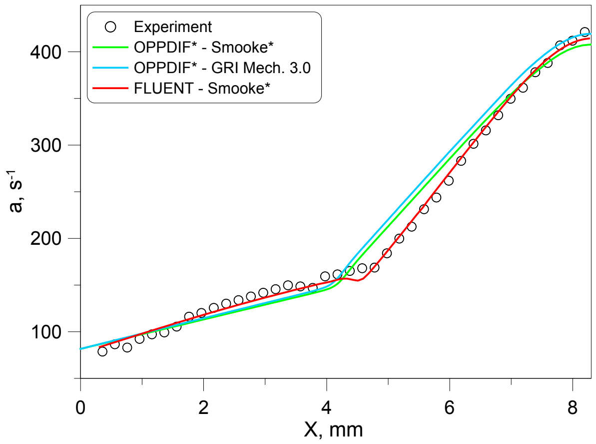

Figure IV.43 Radial velocity gradient evolution along the burner axis for 1D (Smooke* and GRI Mech. 3.0 mechanisms), 2D and experimental approaches.

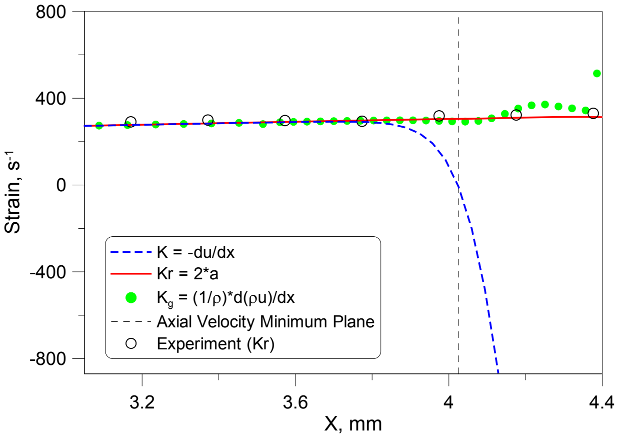

Figure IV.44 Comparison of various strain rate definitions along the burner axis for the 2D simulated case (II). The experimentally determined radial strain rate K_r is superimposed for comparison.

Additional Considerations

If an overall reasonable agreement between 1D and experimental results was found in the previous section, attention should be paid to lower equivalence ratio cases for which important discrepancies appear. Figure IV.45 displays a comparison between experimental and simulated axial velocity profiles for a methane/air flame (E.R.=0.6) stabilized at an intermediate strain rate (K_r = 79 s^{-1}) in the counterflow configuration of case II. All 1D calculations are seen to largely overestimate the experimental trend. Particularly, the use of different kinetic mechanisms (Smooke and Giovangigli [196], its modified version Smooke* and the GRI Mech. 3.0 [148]) as well as different versions of the OPPDIF program discussed above (see modifications brought to the original code for transport options) do not bring any substantial improvement. Also, variations of the inlet radial velocity gradient were tested for two extra cases with a = 0 s^{-1} (pure plug flow case) and a = 30 s^{-1}. Additional discrepancies were obtained in the hydrodynamic zones showing a posteriori the adequacy of the experimentally-evaluated inlet radial velocity gradient (a = 14.3 s^{-1}). Such trends were observed for weakly burning flames, either in the rich or lean domains, see for instance ref. [41] and [56] for additional cases. They might be due to the inadequacy of the classical one-dimensional approach as pointed out for the case I discussed in an earlier part of the present chapter.

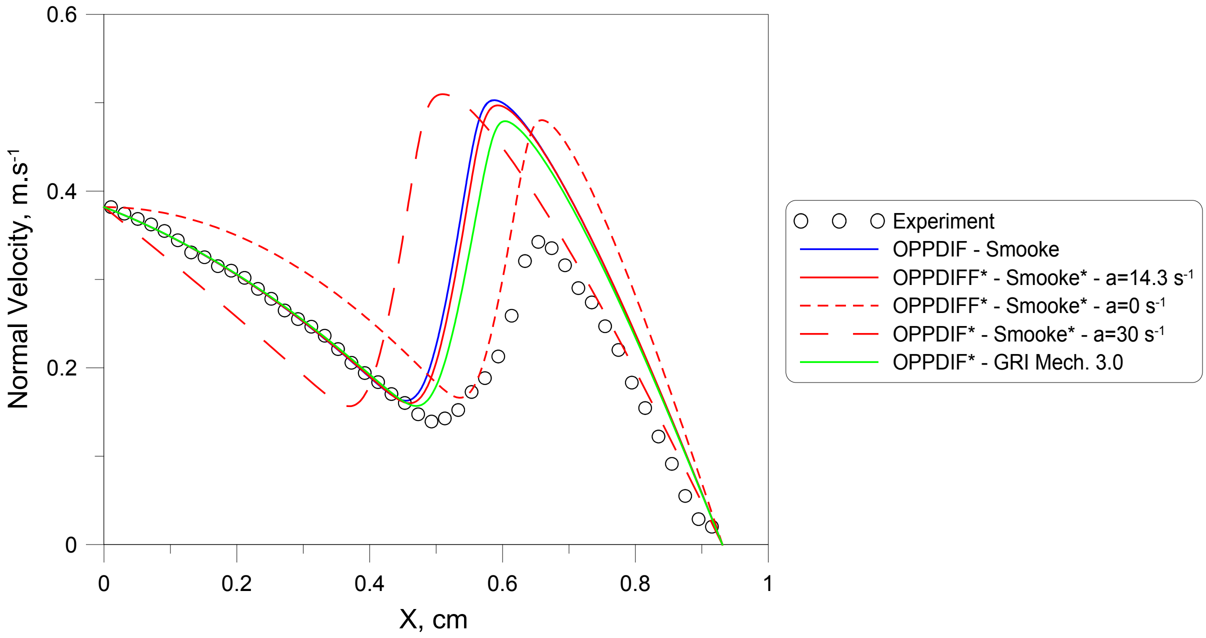

Figure IV.45 Spatial variations of the velocity along the burner axis for a methane/air mixture at equivalence ratio 0.6 in the counterflow configuration. Symbols: experiments, lines: 1D computations.

IV.4 Summary

Nozzle burner assemblies designed and fabricated for the present study have been presented; the experimental configurations used in the present study include: i/a stagnation flame plate setup (7 mm nozzle burner I.D.), ii/ a counterflow twin flame setup (15 mm nozzle burner I.D.). The dedicated gas supply and home-developed flow control systems have been detailed.

Experimental efforts were first oriented towards flame speed determination using the flame transition methodology proposed by Vagelopoulos and Egolfopoulos [89]. Consequent difficulties were encountered while trying to perform the planar to conical flame transition with, for instance, unstable flames that were highly sensitive to seeding conditions. In this context, this methodology was deemed unreliable for flame speed measurements and the planar strained flame configuration was chosen.

Tests performed with the stagnation plate apparatus for various methane/air mixtures have demonstrated that heat losses to the plate affect the flame propagation at higher strain rates. Resulting evolutions of reference velocities are characterized by a gradual bending that might bias extrapolation procedures needed to yield unstrained flame speeds. To remove any ambiguity, the DPIV approach developed in the previous chapter has been applied to planar flames stabilized in the counterflow configuration. Laminar flame speeds of methane/air mixtures have been determined for equivalence ratios from 0.6 to 1.4 at atmospheric conditions. Results were compared to various datasets of the literature as well as 1D-computed velocities. An overall good agreement was found which confirmed that the methodology developed in chapter III is reliable and yields a reasonable accuracy for laminar flame speed determination purposes.

The stagnation plate and counterflow flame configurations were simulated for stoichiometric methane/air mixtures using both classical 1D and 2D-realistic approaches. For the stagnation plate flame configuration, the 1D model failed to accurately predict axial velocity variations in the post-flame region. The 2D approach, however, demonstrated excellent agreement with the experiment. It was shown, by evaluating important terms of the momentum equation, that the simplifying assumption "$(1/r)\times(dp/dr)$ =constant" is responsible for the post-flame velocity overshoot in the 1D simulation. An estimation of flow tracking errors was performed. The estimated particle slip error was on the order of -0.43 $m.s^{-1}$ in the fast expansion region of the flame, emphasizing the importance of the thermophoretic force in such experiments. However, the minimum velocity $S_{u,ref}$ used in the present methodology was found to be unaffected, confirming in return the reliability of DPIV measurements performed at the upstream edge of the flame.

The 2D simulation for the counterflow case revealed that, although a small displacement of the flames in the upward direction is observed while gravity is considered, the flame structures are not altered by gravity effects. An overall better agreement is found between 1D, 2D simulations and experimental results as compared to the stagnation plate flame case. A detailed comparison of spatial variations of strain rates following different definitions has been performed. It is shown that the conventional strain rate evaluated from the axial velocity profile will systematically yield a lower value than the actual strain "felt" at the reference plane. It is therefore recommended to evaluate strain rates from radial velocity profiles.

Important discrepancies were found between experiment and 1D simulation for the weakly burning E.R.=0.6 flame case. This trend has been observed in the literature for very lean/rich mixtures. As demonstrated earlier, if the adequacy of the classical one-dimensional approach is clearly questioned, additional investigations are now required to analyze in detail the influence of buoyancy effects that might become predominant for these weakly burning flames.

V. Laminar Flame Speeds of Syngas/Air Mixtures in the Counterflow Twin Flame Configuration

V.1 Introduction and Objectives

Laminar flame speeds of various syngas mixtures are investigated in the counterflow flame configuration using the DPIV diagnostics and the methodology developed and validated in the precedent chapters. Modifications of the burner setup as well as newly implemented gas delivery and flow control systems are presented. Specific efforts were oriented towards the formation minimization and capture of carbonyl compounds. DPIV results are confronted to a large number of literature datasets obtained for various flame configurations and mixture compositions. Predictions of two leading mechanisms for syngas combustion are compared and discussed in the light of available experimental results.

V.2 Syngas Flame Speeds in the Literature

A detailed listing of laminar flame speed studies involving syngas mixtures is provided Table V.1. Diverse experimental setups were considered including flat, conical, spherical and counterflowing flames. Most investigations are restrained to the lean domain presumably because syngas is mainly intended as an alternative fuel for dry low-NO_x gas turbines, but also because serious safety issues arise when large quantities of H_2 and CO have to be handled. Although it might be important for kinetic mechanism developments to carry out studies on the entire range of possible equivalence ratios, a very limited number of investigations have studied entire bell-shaped curves from the very lean side (E.R.=0.6) up to the very rich side (E.R.=5.0-6.0). To date, only experimental works on spherically expanding flames [177, 198-200] report this type of measurements for which a considerable scatter can be noticed, especially at rich conditions [201]. At higher pressure (>5 atm), syngas flames are prone to cellular instabilities and nitrogen is usually replace by helium to prevent the development of unstable flames [177, 200, 202]. Studies involving preheating of fresh reactants are fairly scarce and only available for the conical flame configuration [85, 202-203].

Authors	Set-up	Diagnostics	Composition (by Volume)			E.R.	P [bar]	T [K]	Figure/Page in Ref.	Ref.
			H_2	CO	Diluent					
Badami & Egerton, 1955	FF	×	5.30 → 18.05	94.70 → 81.95	+ 0.12 % H_2O of total volume	0.33 → 0.36	1	Amb.	F12/309	[204]
Scholte & Vaags 1959	CF	Schlieren (CA)	0.58 → 6.69	99.42 → 93.31	×	1.95	1	Amb.	F1/505	[205]
			0 → 24.42	100 → 75.58	×	2.38	1	Amb.	F2/506	
			0/0.55/3/10.5/24.1/43.3/69.7/100	100/99.45/97/89.5/75.9/56.7/30.3/0	×	Rich side, ≈ 1→ 4.5	1	Amb.	F1/512, T1-F2/513, F3/514	[206]
Yumlu, 1967	HF	×	0/10/25/40/ 60/90/100	100/90/75/60/40/10/0	×	0.6	1	Amb.	F3/192, F5-F6-F7/193, F8/194	[207]
Günther & Janisch, 1971	CF	Schlieren (CA)	0/10/20/40/60/80/100	100/90/80/60/40/20/0	×	1.0	1	Amb.	F8/977	[208]
McLean et al. 1994	OPF	Schlieren	5/50	95/50	×	0.5 → 6.0	1	Amb.	F3-F4/753	[199]
Vagelopoulos & Egolfopoulos 1994	CTF	LDV	12.19 → 29.86	87.81 → 70.14	×	0.39	1	Amb.	F1/1319	[70]
			1.41 → 28.92	98.69 → 71.08	×	0.49				
			1.07 → 28.84	98.93 → 71.16	×	0.6				
Brown et al. 1996	OPF	Schlieren	5/50/100	95/50/0	×	0.5 → 2.4	1	Amb.	No flame speeds/Markstein length results only.	[209]
Hassan et al. 1997	OPF	Shadow	3/5/10/25/50	97/95/90/75/50	×	0.6 → 5.0	1	Amb.	F5/244	[198]
			5	95	×	0.6 → 5.0	0.5, 1.0, 2.0, 4.0	Amb.	F6/244	
Huang et al. 2004	CTF	PIV	28	25	47 % N_2	0.7-1.4	1	Amb.	F13-14/248, F17/250	[97]
Bukunte & Moss 2007	CF	Schlieren (FSA)	33	67	×	Limited-Lean side	1, 3.5, 5	Amb., 292 → 603	F7-F8/5 F10/6	[203]
			28.5	1.5	70	Limited	1, 3, 4, 5	Amb.	F9/5	
Serrano et al. 2007	OPF	Schlieren	21	24	55	0.8 → 1.8	1, 2.5, 5	Amb.	T1/6, F5-F6/8, F7/9	[210]

Sun et al. 2007	OPF	Schlieren	1/5/25/50	99/95/75/50	×	0.6 → 4.5	1	Amb.	F1/442	[200]
			5/25/50	95/75/50	×	0.6 → 4.5	2	Amb.		
			50 25 5	50 75 95	N_2 of air is replaced with He	0.5 → 3.5/4.0	5, 10 5, 10, 20 5, 10, 20, 40	Amb.	F2/443	
Natarajan et al. 2007	CF & SPF	Chemi. (FSA) & LDV	5/50	95/50	×	0.6 → 1.05	1	Amb.	F3/6	[85, 87-88, 211]
			5/50/95	95/50/5	0/20, 0/10, 0/20 % CO_2	0.6 → 1.05	1	Amb.	F5/8, F7-F8/10	
			5/50/95	5/50/955	×	0.6 → 1.05	1	300 → 700	F9/11, F12/13, F13/14	
Prathap et al. 2008	OPF	Shadow	50/40/30/20	50/40/30/20	×/20/40/60	0.6 → 1.8/3.5	1	Amb.	T1 /6, F5/9, T2/6, T3/6, T4/7, F10/12, F12-F13/14	[212]
Burke et al. 2009	OPF	Schlieren	50	50	×	0.6 → 4.0	1	Amb.	F11/8 (Ref. [177])	[177, 213]
			25	75	He (Oxidizer: O_2:He 1:7)	0.8 → 3.5	10, 20	Amb.		
Dong et al. 2009	CF	Direct visualization (FSA)	0/10/20/30/40/50/60/70/80/90/100	100/90/80/70/60/50/40/30/20/10/0	×	0.4/0.6 → 2.2	1	Amb.	F5/1860, F6-F7-F8/1861, F9-F10F11/1862	[214]
Natarajan et al. 2009	CF	Chemi. (FSA)	50	50	×	0.6 → 1.0	1	300 → 700	F3 /1264	[202, 215]
			50	50	He (Oxidizer O2:He 1:7)	0.6 → 1.2	10	Amb.	F2 /1263	
			20 → 80 30 → 80	80 → 20 70 → 20	He (Oxidizer O_2:He 1:9)	0.6 0.8	15	600 300	F4 /1264 F5/1265	
			50 → 90	50 → 10	He (Oxidizer O_2:He 1:9) + 40 % CO_2 dilution	0.75	15	600	F8/1267	

Table V.1 Summary of H_2/CO blends and conditions, for which laminar flame speeds are available in the literature (in “Setup”: *FF* - Flat Flame, *CF* - Conical Flame, *HF* - Heat Flux, *OPF* - Outwardly Propagating Flame, *CTF* - Counterflow Flames, *SPF* - Stagnation Plate Flame; in “Diagnostics”: *CA* - Cone Angle, *FSA* - Flame Surface Area, Chemi.: Chemiluminescence; *E.R.* = Equivalence Ratio).

V.3 Experimental Methodology

V.3.1 Burner Apparatus Modifications

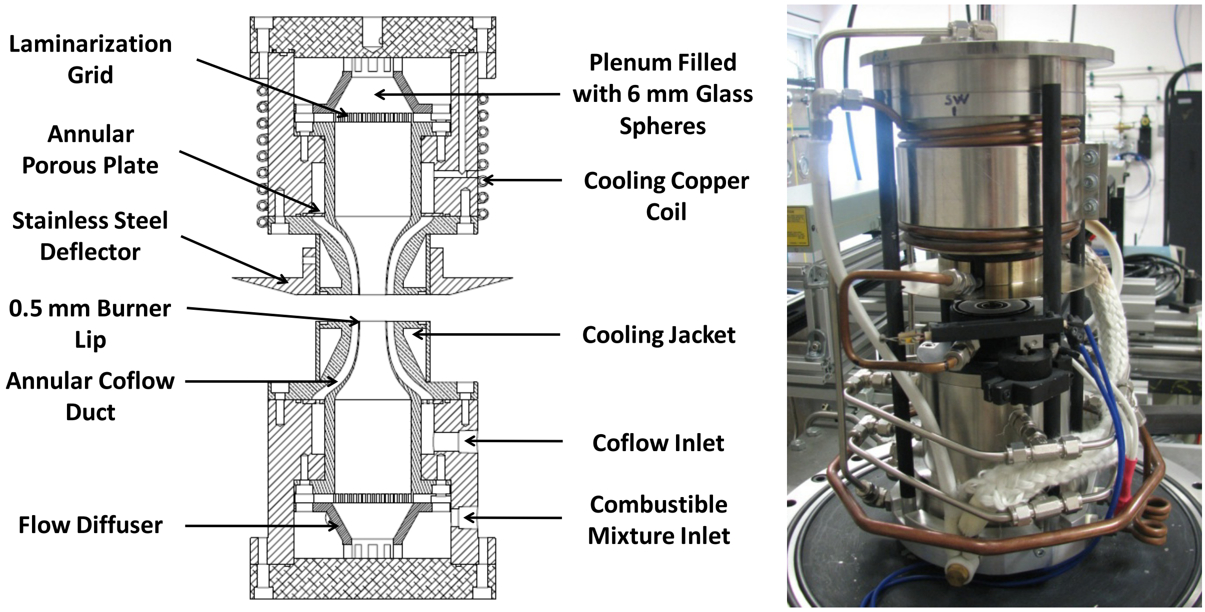

(a) (b)

Figure V.1 Counterflow flame burner apparatus for the syngas premixed flame experiments: (a) Schematic of the counterflow burner, (b) Photography of the experimental apparatus.

The counterflow burner apparatus was modified as compared to the previous assembly presented in Figure IV.4. Major improvements were needed, since it was decided to enclose the entire apparatus in a ventilated chamber, to: i/ enable studies of very rich flames without perturbations induced by diffusion flames on the hot product side, ii/ ensure safer working conditions with continuous dilution of highly inflammable (H_2) or toxic (CO) gases. As seen in Figure V.1, the lower stainless steel burner is kept unchanged, while the upper one has been replaced by a more compact aluminum burner, with two individual gas inlets (reactive and inert flows) located at its back. The upper burner is supported by four columns allowing a fixed nozzle burner separation distance of 15 mm. A massive stainless steel deflector is mounted on its water-cooled head to divert hot combustion products far from the upper burner body. The latter is protected by an additional cooling copper coil closely wrapped around its external surface. High cooling water flow rates were set during experiments in order to provide an intense heat extraction. Thanks to this arrangement, the upper burner could be easily handled and did not show any sign of overheating, even after prolongated runs. Flame ignition inside the chamber was remotely controlled thanks to an automated arm ensuring the circular motion of a Kanthal hot wire towards the center of the opposed jets. Flames were directly ignited in the counterflow configuration and the ignition device was subsequently moved back far from the zone of interest. As seen in Figure V.1 (b), all elements impinged by the laser sheet (burner heads, deflector…) or that could potentially cause strong laser light reflection (columns) were painted with a matte black thermo paint. This considerably increased the quality of DPIV images recorded in the course of the present study.

Concerning the burner internal structure, two important modifications were done. First of all, new converging nozzles were designed and fabricated. If the same exit I.D. diameters (15 mm) and contraction profiles were kept, the burner lip thickness was consequently reduced from 2 to 0.5 mm. The necessity of reducing the burner lip thickness has not been yet addressed and will be therefore detailed in the next section. The second modification concerns the laminarization grids of the coflowing gas. Since an evidence of slight turbulence was observed at high flow rates with notable ridges located at the flame edges, these grids were replaced by annular porous brass plates, as indicated in Figure V.1 (a), which was found to suppress this irregular pattern.

The entire burner assembly is mounted in a water-cooled stainless steel chamber (300 mm I.D., 1200 mm height) equipped with four optical accesses. An external ring surrounding the lower burner provides a constantly flowing nitrogen shroud sweeping the entire chamber. This nitrogen curtain was found to be primordial in order to suppress the occurrence of diffusion flames for the richest cases. A second dilution of exhaust gases was provided at the chamber exit by injecting a cold air jet. Hence, the temperature of diluted combustion products does not exceed 30-40 °C while leaving the chamber.

V.3.2 On the Influence of the Nozzle Burner Thickness on Flame Stabilization

An important issue related to the present burner setup is the interaction between the annular inert and main flows in the wake of the nozzle burner lip having a finite thickness. It deserves a particular interest since any important motion in this zone may affect the flame edge position and therefore the flame stability. To illustrate these effects, methane/air flames with seeded both inert coflow shroud and main flow are presented in Figure V.2, Figure V.3 and Figure V.4. Tests have been performed on the burner setup described in Figure IV.4 for which the nozzle burner exit area equals the coflow exit area. The burner lips (in green on the figures) are 2 mm thick for this configuration. Three cases are here considered: i/ the annular inert flow rate is lower than the main flow one (Figure V.2); ii/ the annular inert and main flow rates are set closer to each other (Figure V.3); iii/ the annular inert flow rate is increased above the main jet flow rate (Figure V.4). In the first case, the coflowing annular jet is divided at the flame edge into a faster external jet (yellow arrow in Figure V.2, b) and a slow inert recirculation branch located close to the main reactive jet (blue arrows in Figure V.2, b). In the second case, the flame seats on the coflowing shroud with an unseeded annular “dead” zone in the nozzle lip wake. In the third case, there is an unsteady motion of the flame edge with an external vortex characterized by higher velocities (yellow arrows) and an inner slow recirculation zone (blue arrows). Both structures are apparently “fed” with unreacted mixture brought when the flame edge is oriented downwards (Figure V.4, a) and “purged” while flame edge is pushed upwards (Figure V.4, b). All aforementioned cases provide stable flames, including the third case with higher inert coflow velocity, although it might be recommended to set the flow rate of the inert shroud at a lower or equal level with respect to the main flow rate to avoid any shear stress effects.

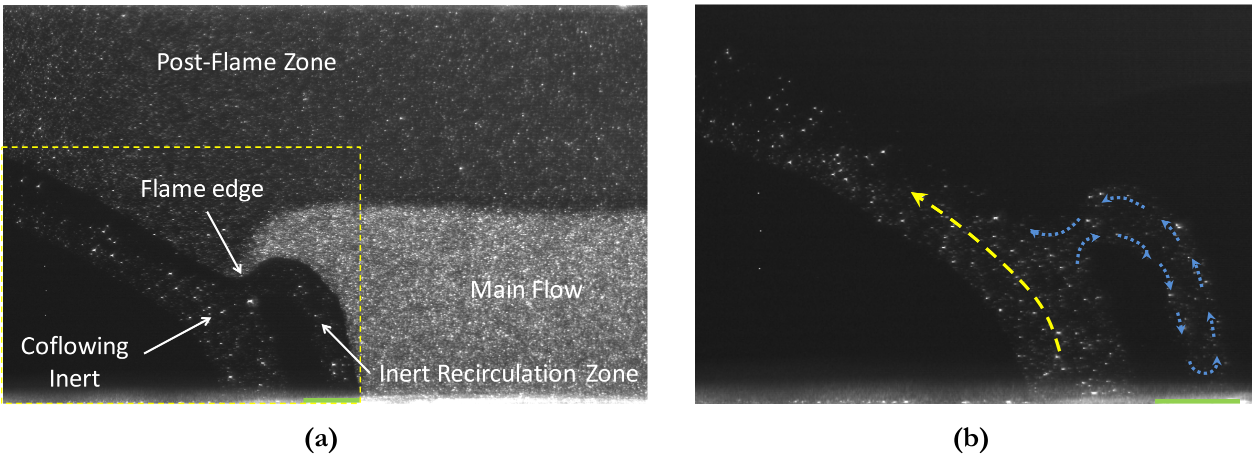

Figure V.2 Stable methane/air flame: (a) Annular and main flows both seeded, (b) Annular coflow seeded only (*ER*: 1.0, *BID*: 15 mm, *BC*: SP, L_{sp}: 14.8 mm, *MFR*: 11.126 L/min, *CFR*: 6.831 L/min).

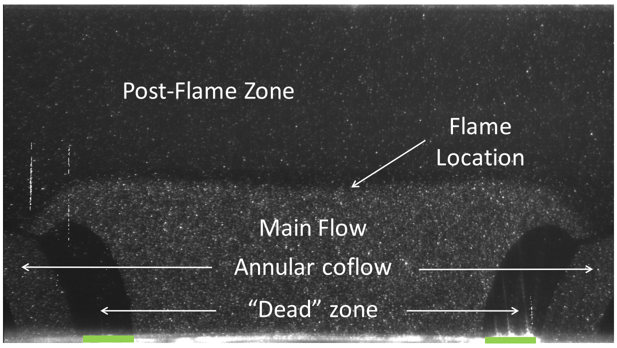

Figure V.3 Stable methane/air flame, both annular and main flows are seeded (*ER*: 1.0, *BID*: 15 mm, *BC*: SP, L_{sp}: 14.8 mm, *MFR*: 10.610 L/min, *CFR*: 8.682 L/min).

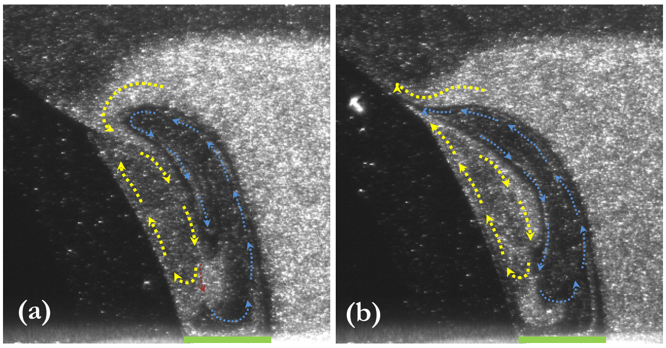

Figure V.4 Stable methane/air flame with unsteady motion of its edge: (a) edge oriented downwards, (b) edge oriented upwards (*ER*: 1.0, *BID*: 15 mm, *BC*: SP, L_{sp}: 14.8 mm, *MFR*: 10.126 L/min, *CFR*: 14.190 L/min).

Most flames considered in chapter IV were perfectly stable. However, for certain combinations of experimental parameters including mixture equivalence ratio, L_{sp} distance, main flow and inert shroud flow rates, apparent instabilities would perturb the flames giving rise to strongly flapping flame edges and ultimately coupled with noise. The flapping edge pattern has been previously observed for stagnation flames in ref. [56, 86] but not characterized. In this study, two types of instabilities are identified for flames stabilized at higher strains and illustrated in Figure V.5. Each time, three different images are shown (case I, II and III) chosen among the DPIV series performed for each instability type. The DPIV maximum acquisition rate did not allow a time-resolved characterization of the observed phenomena. It can be seen, however, that both types of instabilities are characterized by vortex roll-up structures moving from the burner rim towards the flame edge, therefore explaining the flapping pattern. The vortex propagation mechanism differs however depending on the instability type considered. For type I, vortices on each side of the jet are located at different heights suggesting the formation of a spiral structure.

Concerning type II, an annular structure is observed and intense noise can be heard. Although the vortex propagation seems to minimally affect the axial velocity profiles on the jet axis as well as tangential velocities in the radial direction at the point of reference (see Figure V.6 and Figure V.7), the structure of the reactive jet is considerably modified as seen on transverse profiles of axial velocity at the point of reference (Figure V.8). A variation of velocity profile curvature can be noticed for the type II instability depending on the vortices location.

Since higher flow rates were involved for syngas mixtures with higher hydrogen content, due to faster fundamental flame velocities, efforts were made to suppress these instabilities. It was thought that suppression of the low velocity regions created in the wake of the burner lips by closely matching the annular shroud to the central jet would prevent the onset of instability. Thus, as mentioned earlier, new nozzle burners were fabricated with 0.5 mm lips and tested for various syngas mixture compositions. Fairly large flame stability ranges could be achieved but instabilities of type I would still occur at higher flow rates, even with a lower shroud flow rate. In a lesser extent, instabilities of type II would arise. A possible explanation for these phenomena is that the burner possibly behaves like a Helmholtz resonator, enhancing the formation of vortex structures at the burner rim. Such self-induced instabilities have been observed by Durox at al. [216] for premixed jet flames, anchored at the rim of a nozzle burner, impinging on a flat plate. These induced bulk oscillations are characterized by a resonant frequency depending on sound speed and geometric parameters of the cavity, including the chamber plenum volume, the nozzle exhaust section as well as the effective length related to the converging throat shape. In our case, it is however not clear why two types of instabilities are observed and what causes the transition from one type to another. Interestingly, instabilities were found to vanish in most cases if nitrogen of the coflowing jet was replaced by helium, suggesting that the coflowing shroud and central jet interactions is a key parameter in the formation of such instabilities.

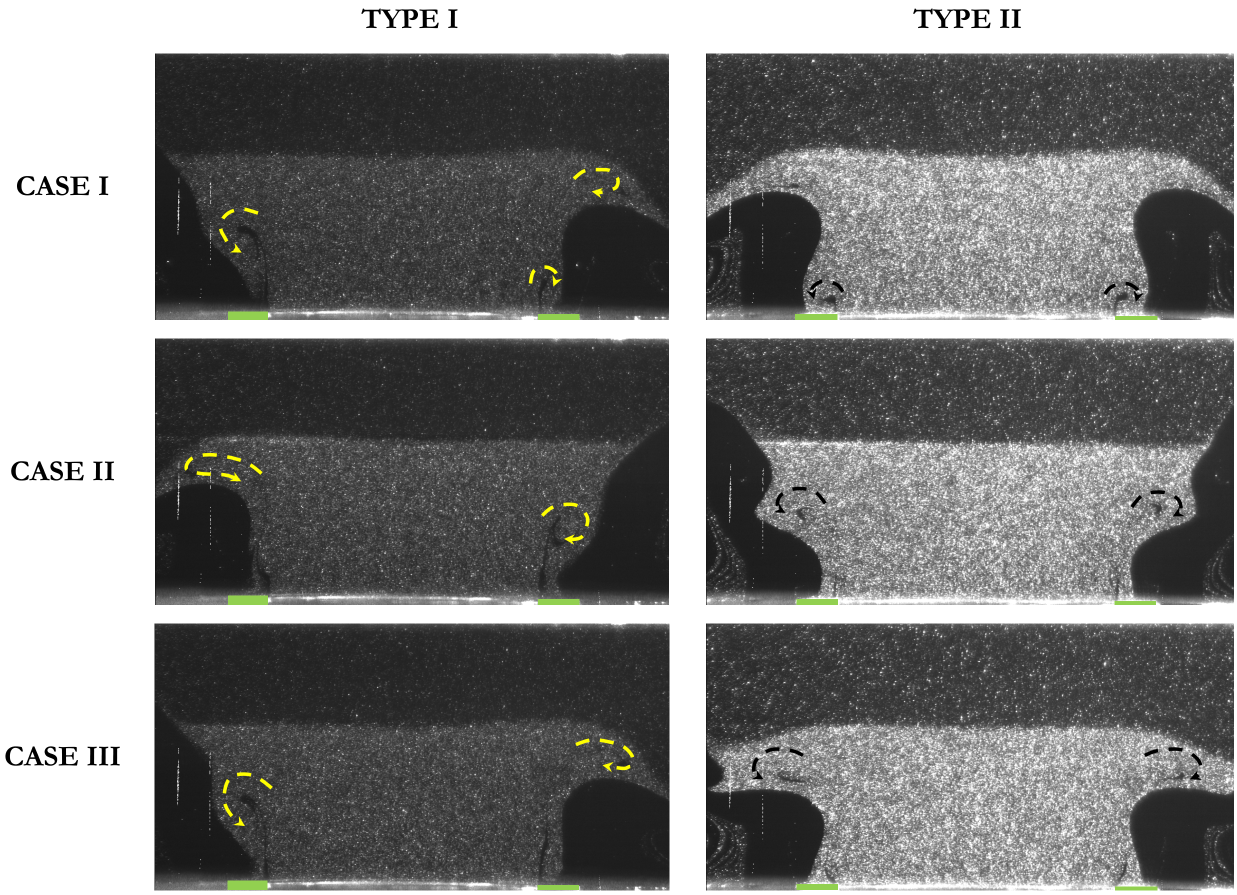

Figure V.5 Identification of two types of instabilities for stagnation flow flames (yellow and black arrows indicate the senses of rotation of vortices, green rectangles the location of the burner lips). (*MB*: CH_4/Air, *ER*: 1.0, *BID*: 15 mm, *BC*: SP, L_{sp}: 14.8 mm, *MFR*: 15.933 L/min (TYPE I); 16.818 L/min (TYPE II), *CFR*: 13.038 L/min (TYPE I); 13.762 L/min (TYPE II)).

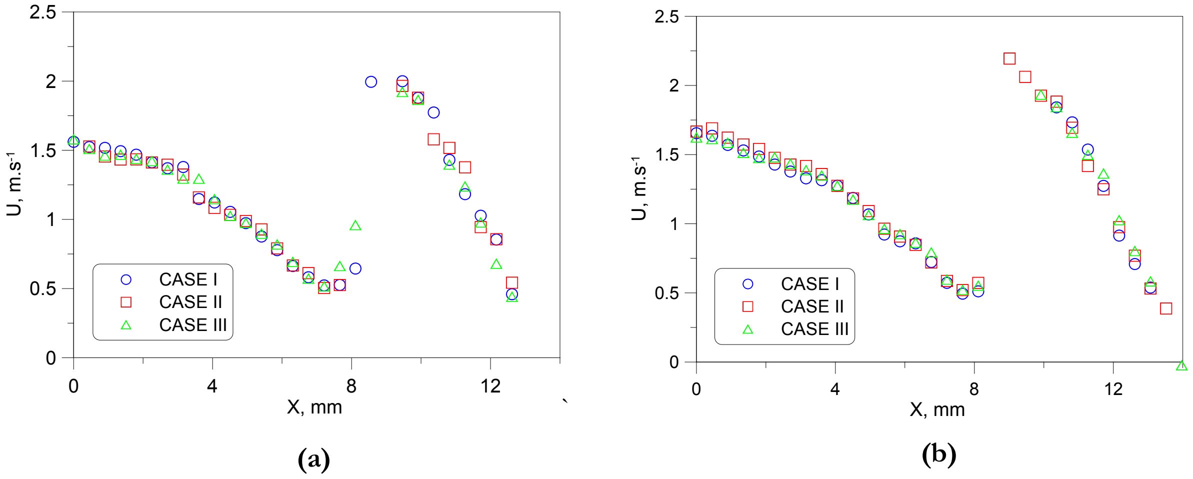

(a) **(b)**

Figure V.6 Profiles of axial velocity on the jet axis: (a) Type I instability, (b) Type II instability (Experimental conditions specified in the caption of Figure V.5).

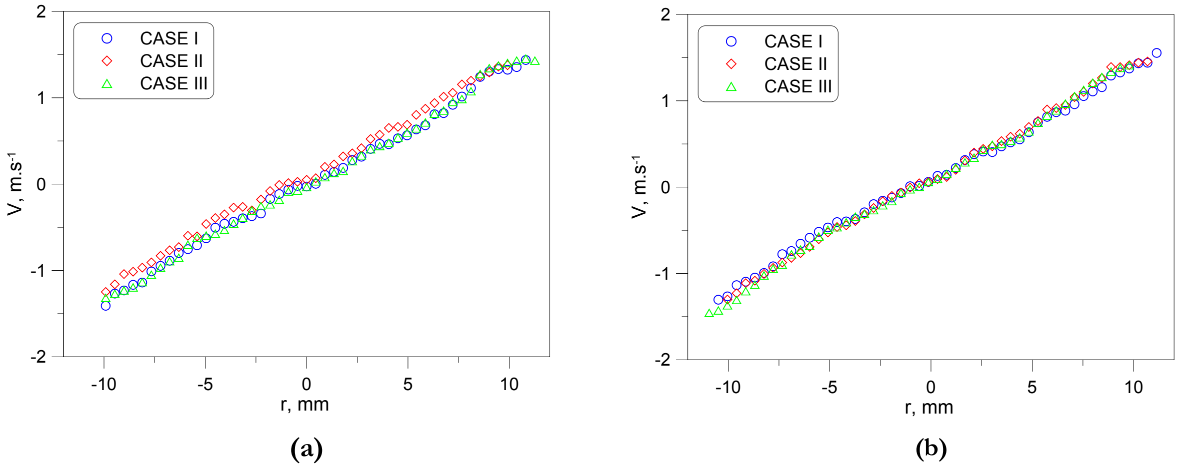

Figure V.7 Profiles of tangential velocity in the radial direction at the reference point: (a) Type I instability, (b) Type II instability (Experimental conditions specified in the caption of Figure V.5).

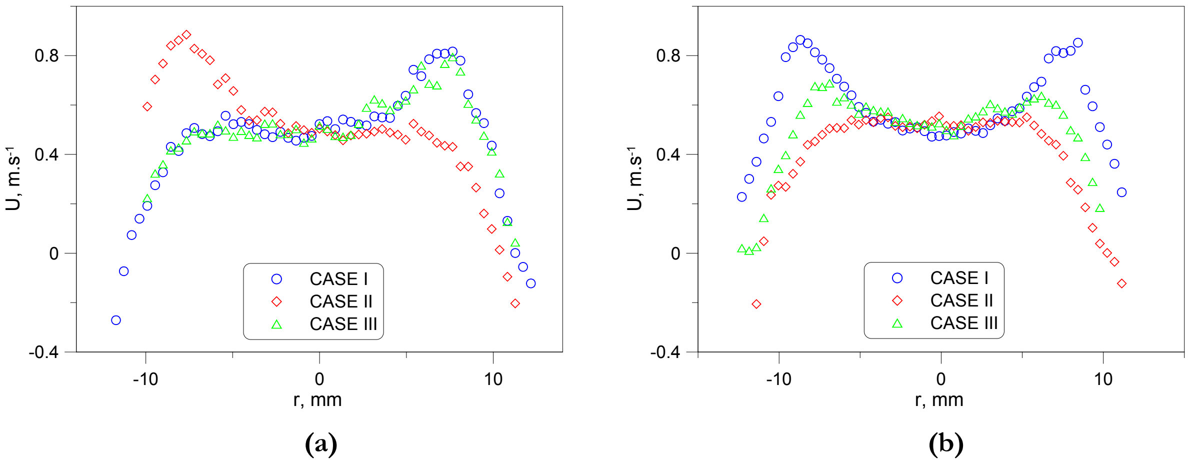

Figure V.8 Profiles of axial velocity in the radial direction at the reference point: (a) Type I instability, (b) Type II instability (Experimental conditions specified in the caption of Figure V.5).

V.3.3 Flow Control and Gas Delivery Systems

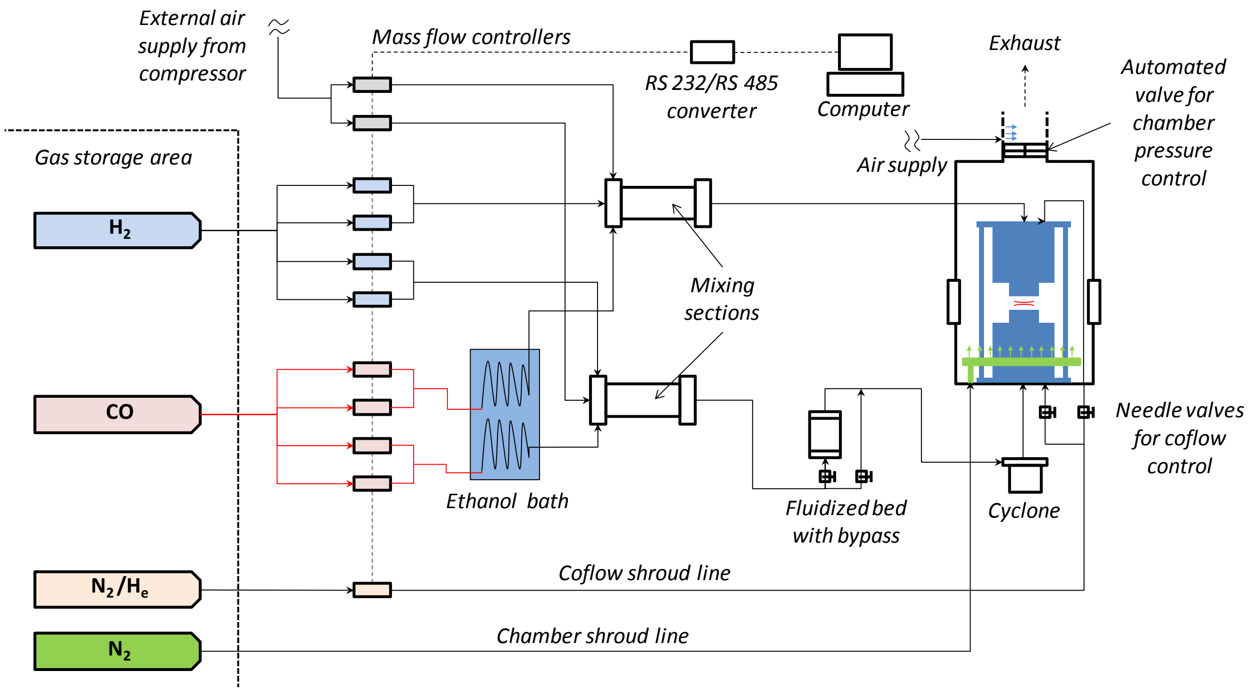

Figure V.9 Simplified schematic of the gas delivery system for the syngas/air flame experiments.

Figure V.9 displays a simplified schematic of the gas delivery system used for the syngas/air flame experiments. Gases, including H_2, CO, N_2 and He were provided by AIR LIQUIDE© and stored in separate tanks in a remote gas storage area. Additional details on gases are provided in Table V.2.

GAS	DESIG.	MAXIMUM IMPURITIES (ppm-mol)							GLOBAL PURITY (%)
		H_2O	O_2	CO_2	H_2	N_2	C_nH_m	Other	
H_2	ALPHA GAZ I	3	2	×	×	×	0.5	×	99,999
CO	N47	3	5	1	1	10	2	Ar: 7	99,997
N_2	ALPHA GAZ I	3	2	×	×	×	0.5	×	99,999
He	ALPHA GAZ I	3	2	×	×	×	0.5	×	99,999

Table V.2 Gas specification table (DESIG.: Designation). Manufacturer: Air Liquide.

A high carbon monoxide grade was chosen to match purity levels of other reactants. Due to larger flow rates required for syngas flames stabilization, atmospheric air was provided by a KAESER 26 compressor with a maximum allowed flow rate of 100 m^3/h at 13 bar. Particles down to 0.01 μm and potential oil residuals are successively removed by submicron size filters (Atlas Copco PD 17 and QD 17 respectively).

Apart from the nitrogen chamber shroud, all flow rates are controlled thanks to BROOKS 5850S and 5851S series mass flow controllers. Although these devices were factory calibrated for the gases of interest, additional in situ calibrations were periodically performed using, depending on the flow rates involved, classical bubble meters, ACTARIS© wet meters (Measuring uncertainty 0.5%) or AGILENT© Optiflow digital flow meters. All calibrated mass flow meters, without exception, showed excellent linearity with corresponding determination coefficients above 0.999. Post-calibration verifications were systematically performed showing that experimental uncertainties on flow rates were within 1% passed the first 10 % of the full flow rate scale. For H_2 and CO flows, a combination of two mass flow meters, mounted in parallel with different flow ranges, is used. Each one can be independently connected to the gas network using quarter-turn plug valves upon required flow rate. This allows working at a reasonable accuracy for both weakly and strongly strained flames (i.e. at lower/higher flow rates). Additional details on the mass flow meters, including lower and upper ranges for each line, accuracy and repeatability are provided in Table V.3. A new LABVIEW© interface has been developed in order to digitally control all devices. Data exchange with the mass flow controllers is rendered possible thanks to the BROOKS SmartDDE32 translation driver allowing Windows-based applications, such as LABVIEW©, to bi-directionally communicate with controller devices following the Dynamic Data Exchange (DDE) protocol. An additional GANTNER ISK 200 conversion board is used to convert encoded data from the RS 232 to RS 485 standard and vice versa. A home-developed LABVIEW program allows piloting all 11 devices simultaneously. Similarly to the first version dedicated to methane/flames, components of the reactive jet can be proportionally controlled to vary the strain rate without equivalence ratio modulation. Ultimately, flow rates of the entire counterflow apparatus including the lower and upper burner can be set through a single command, significantly simplifying burner operations. This is particularly important for syngas mixtures for which any flow rate deviation of a single component can rapidly lead to flashback or blowoff events and therefore considerably increase experimental breakdown times. Note that in the present case, the coflowing inert shroud, being either nitrogen or helium, is controlled through a single mass flow meter and equilibrated between the lower and upper burners thanks to two manual needle valves. For all counterflow syngas flame experiments, fresh gases were injected at room temperature and atmospheric pressure, with all initial temperatures being within the 296.2 ±2.0 K interval.

	Ranges, $L.min^{-1}$	**Series**	**Accuracy at Calibrated Conditions**	**Repeatability**	**Communication Mode**
H_2	0.5 (×2)	5850S	±0.7 % of rate and 0.2 % full scale	±0.25 % of rate	Digital
	5 (×2)	5850S			
CO	2 (×2)	5850S			
	20 (×2)	5850S			
Air	20 (×2)	5851S	±0.7 % of rate and 0.2 % full scale	±0.25 % of rate	Digital
N_2/He	100 (×1)	5851S			

Table V.3 Mass flow meter specifications for the syngas/air stagnation flame experiments.

A particular attention was devoted to all elements in direct contact with carbon monoxide. As discussed earlier, CO may react with the iron and nickel contained in stainless steel and form iron pentacarbonyl and nickel tetracarbonyl respectively [217]. These metallic compounds are known to have an inhibiting effect on flame propagation [218] and evidences of their decomposition in combustion related-experiments can be indicated by either noticeable changes in flame colors [185, 219] or oxide deposits on walls [220-221]. To minimize a possible carbonyl compound formation, new CO-delivery lines were built using 6 and 10 mm I.D. copper tubes. These lines are running from the CO gas tank (itself in aluminum) to the entrance of the spiral carbonyl traps (red lines in Figure V.9). The conventional manometer used for combustible gases is replaced by a SWAGELOK KCY two-stage regulator especially customized for CO compatibility (Body material: brass CW721R, seat/seal material: PCTFE). As such, almost all parts located in the initial high pressure branch (15 bar) of the CO-delivery network are free from metallic elements likely to promote carbonyl formation, including Fe and Ni. As recalled by Williams and Shaddix [220], carbonyl compounds can also be generated during the carbon monoxide production process and therefore be already present in industrial gas tanks, even for higher purity grades. Thus additional cold trap sections were implemented downstream of the CO mass flow controllers by immersing one-meter condensation coils in a -50 °C alcohol bath. A simplified analysis of heat transfer involved showed that, for the highest CO flow rates achieved (15 L/min), the calculated CO output stream temperature is approximately -27 °C, a value somehow close to the melting point of both iron pentacarbonyl (-20 °C) and nickel tetracarbonyl (-19 °C) as well as significantly lower than their boiling point at atmospheric conditions (103 °C and 43 °C respectively). The condensation/solidification of carbonyl compounds is a technique particularly suitable for laboratory scale carbon monoxide purification with a good removal efficiency [218], avoiding complex chemical washes or prohibitive costs of ultra-pure CO semi-conductor grades. Although no quantitative measurements of potential carbonyl content were performed in the framework of the present investigation, we did not observe any wall oxide deposits such as those mentioned in the literature [220-221]. Neither were obtained flames with strong post-flame colorations bringing to evidence the carbonyl decomposition process, such as in the work of Wu et al. [185] (See Figure V.10).

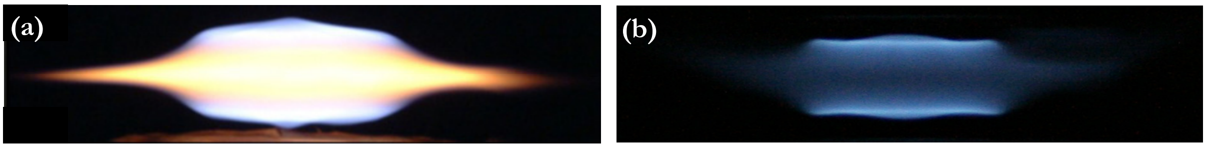

Figure V.10 Photography comparison of stoichiometric carbon monoxide-containing counterflow flames: (a) 10/90 % CH_4/CO flame of Wu et al. [185]. According to the authors, the orange and silver-bright colors in the post-flame region are due to decomposition of metal carbonyls, (b) Present work, 10/90 % H_2/CO flame.

Flame reactants, including H_2, CO and air are mixed in cylindrical vessels filled with glass spheres for both lower and upper burner delivery lines. Before being injected into the lower burner, the reactive mixture successively passes through a two-stage seeding section including a fluidized bed and a cyclone identical to those used for the methane/air flame experiments. Since a large amount of gases is released in the chamber, an automated KAMMER DS37 control valve is used to maintain the desired operating pressure set by a EUROTHERM 2408 PID controller.

V.3.4 DPIV Specifications and Setup

DPIV specifications have been detailed in chapter III and are globally unchanged. The entire optical layout is presented in Figure V.11. The laser beam is focused by a spherical lens (*f* = 592 mm) and expanded by a plano-cylindrical lens (*f* = -25.4 mm) before being redirected by a 45°-angled mirror in the symmetry plane of the counterflow burner. The laser sheet passes successively through a 27 mm-thick porthole (BK 7 glass or HQ310 quartz) and a 21 mm wide/81 mm high light slit before crossing the entire chamber. It is ultimately trapped in a cylindrical volume equipped with a light diffusion cone at its back. Laser light reflections in the chamber are significantly minimized with a substantial gain in the DPIV image quality. To further improve the diagnostic performances, inner chamber walls have been coated with matte black high-temperature paint.

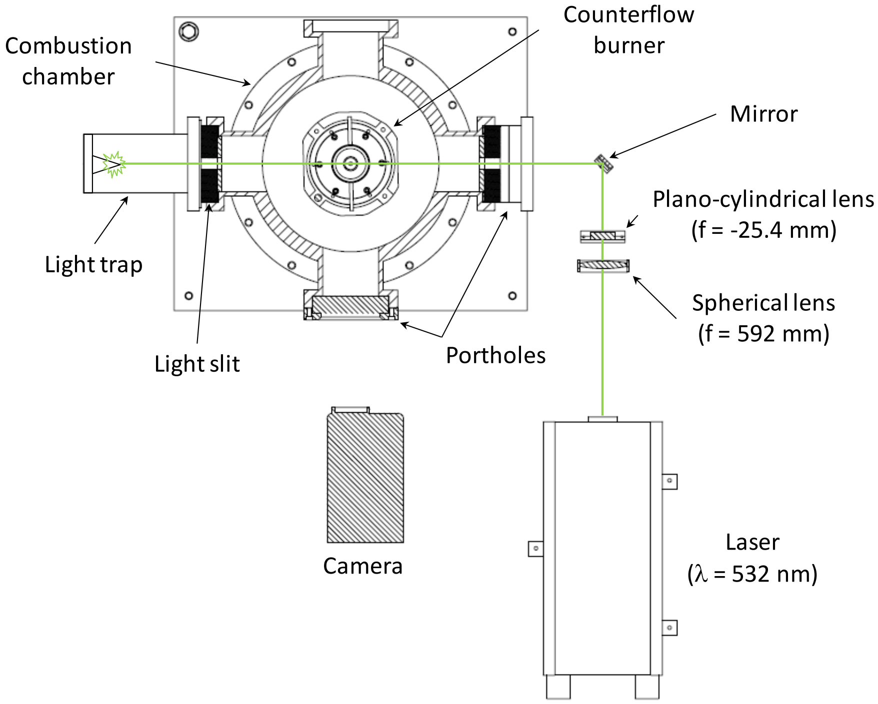

Figure V.11 Schematic of the DPIV setup for syngas/air flame experiments.

Two difficulties arose in the course of the present experiments. Strongly defocused DPIV images were generally obtained for flames with higher temperatures (See Figure V.12, a). This resulted in poor performance of the PIV correlation process with significantly lower vector filling ratios, especially close to the preheat zone of the studied flames. An increase of the nitrogen shroud did not improve the image quality. These defocusing effects were apparently due to important variations of the refractive index of gases present in front of the reactive jet. It is believed that the shear stress between the cold nitrogen shroud at higher density and hot combustion products at lower density could be the source of hydrodynamic perturbations close to the flame edge with potential recirculation of hot nitrogen+combustion products gas bulks. This problem was solved for almost all cases by replacing nitrogen by helium, hence providing a better density match with hot combustion products. The second difficulty was the occurrence of strong flame light emissions visible on the second frames of DPIV image pairs (See Figure V.12, b). These bright emissions were found to considerably worsen the PIV correlation process since the majority of pixels with lower intensity were irreversibly offset. In addition to the original 10 nm Half Band Width (HBW) interference filter (λ = 532 nm), a narrower filter (HBW=3nm) centered on the same wavelength was added in front of the camera lens. As such, bright emissions were removed suggesting a location of the perturbing emissions in the wavelength ranges of 527-530.5 nm and/or 533.5-537 nm. Heads of maxima of the narrow bands of CO_2 in carbon monoxide flames ($^1B_2 - X^1\Sigma^+$ system) revealed that a single band at 527.6 nm is present in the aforementioned ranges [222], which might explain bright emissions observed initially.

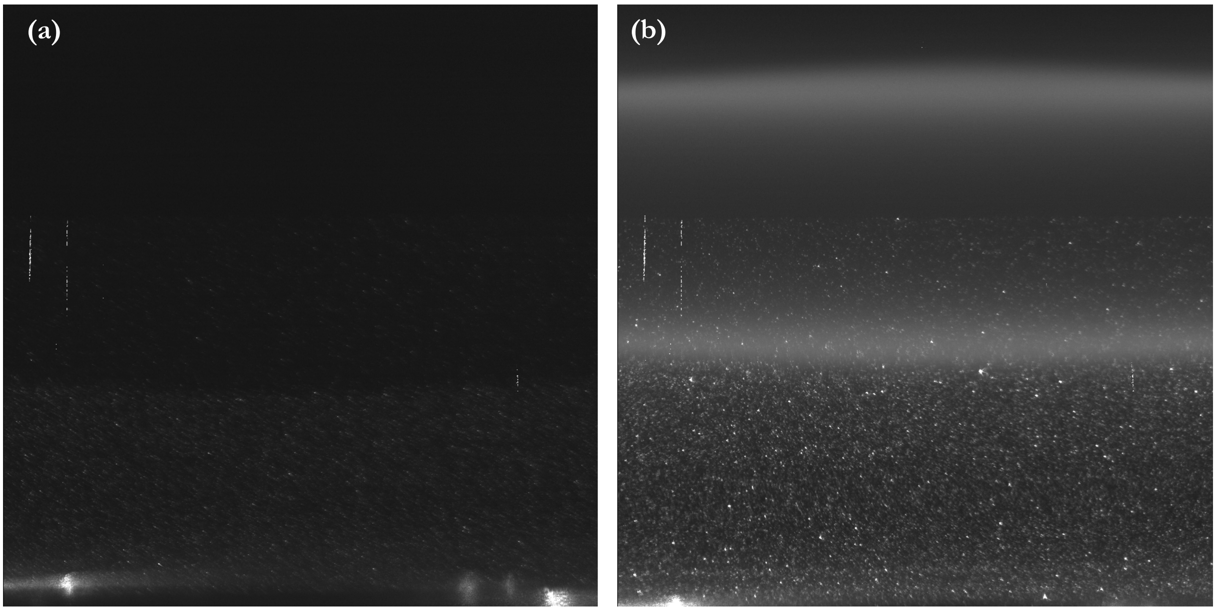

Figure V.12 Sample images of syngas counterflow flames: (a) Strongly defocused image for a 27/75% H_2/CO flame at equivalence ratio 0.8; (b) PIV image (2nd frame of an image pair) with strong flame emissions for a 5/95 % H_2/CO flame at equivalence ratio 1.5.

V.3.5 Data Acquisition, Processing and Uncertainty Analysis

The acquisition protocol and processing methodologies are identical to those presented earlier for the methane/air flame cases. Flame speed uncertainties are calculated during the data fitting procedure following calculations developed in ref. [160].

V.4 Computational Approach

Present DPIV measurements are commented in the remaining section in the light of numerical predictions (PREMIX) using two leading mechanisms relevant to syngas combustion. These are the C1 kinetic mechanisms of Li et al. [223] and Sun et al. [200], further detailed in Table V.4.

Mech.	Spec./ Reac.	Laminar Flame Speeds Datasets Used for Mechanism Validation (At atmospheric pressure, ambient temperature)			Ref.
		Source	**Mixture**	**E.R.**	
Li et al.	21/84	McLean et al.[199], OPF	5/95 % and 50/50 % H_2/CO +air	0.5-6.0	[223]
		Huang et al. [97], CTF	28/25/47 % H_2/CO/N_2 +air	0.7-1.4	
Sun et al.	16/33	Sun et al. [200], OPF	50/50, 25/75, 5/95, 1/99 % H_2/CO +air	0.6-4.5	[200]
		McLean et al.[199], OPF	50/50, 5/95 % H_2/CO +air		
		Hassan et al.[198], OPF	50/50 % H_2/CO +air		

Table V.4 Details on selected mechanisms relevant to syngas combustion (Mech.: Mechanisms, Spec.: Number of species, Reac.: Number of reactions, OPF: Outwardly Propagating Flame, CTF: Counterflow Flame).

V.5 Results and Discussion

A summary of laminar flame speed results for syngas/air mixtures is presented Table V.5. Six different compositions have been investigated including 5/95, 10/90, 15/85, 20/80, 25/75 and 50/50 % H_2/CO blends. Along with the fundamental flame speeds S_u^0 and the corresponding measurement uncertainties $\sigma_{S_u^0}$, spanned Karlovitz numbers (see *Ka* range), as well as corresponding mixture Lewis numbers, are added in the last four columns. The Karlovitz number is calculated thanks to the computed mixture thermal diffusivity (PREMIX Code with multicomponent transport properties) and fundamental flame speed (experiment), following the formulation: $Ka = D_T/(S_u^0)^2 K_r$ [224], where D_T is the mixture thermal diffusivity under standard conditions. For the Lewis numbers of lean and stoichiometric mixtures, the formulation of Law and coworkers proposed in ref. [225] is adopted. Contrary to the conventional approach, for which a single *Le* number is calculated (a single fuel is considered), the expression proposed in ref. [225] incorporates effects of the two distinct fuels present in the mixture in small quantities relative to the abundant inert. The effective Lewis number Le_{eff} can be expressed as:

$$Le_{eff} = 1 + q^{-1}\left[q_{H_2}\left(Le_{H_2} - 1\right) + q_{CO}\left(Le_{CO} - 1\right)\right] \quad \text{(V-1)}$$

where Le_{H_2} and Le_{CO} are Lewis numbers for both hydrogen and carbon monoxide based on the respective mixture thermal diffusivities and binary diffusion coefficients relative to the abundant inert (nitrogen). q_{H_2} and q_{CO} are the nondimensionnal heat release parameters defined as:

$$q_{H_2} = \frac{QY_{H_2}}{c_p\,T_u} \qquad \text{(V-2)} \qquad\qquad q_{CO} = \frac{QY_{CO}}{c_p\,T_u} \qquad \text{(V-3)}$$

with Q, the heat of reaction, Y_{H_2} and Y_{CO}, mass fractions of both H_2 and CO in the fuel ($Y_{H_2} + Y_{CO} = 1$), c_p, the mixture specific heat, and T_u, the unburned gas temperature. The total heat release q is defined as:

$$q = q_{H_2} + q_{CO} \qquad \text{(V-4)}$$

with q being related to the thermal expansion ratio σ ($=\rho_u/\rho_b$) through the simple relation:

$$\sigma = 1 + q \qquad \text{(V-5)}$$

Note here that expression (V-1) has been corrected as compared to the original equation proposed in ref. [225] (see equation 3) to account for a missing summation sign between both species Lewis number contributions. As such, it is indeed verified that: i/ if $q_1 = q_2$, the effective Lewis number reduces to the simple average of the Lewis numbers of the two fuels; ii/ if the supply value of one of the two fuels is equal to zero, the effective Lewis number reduces to the Lewis number of the other fuel. Combining (V-1), (V-2), (V-3), and (V-4) yields the following simplified weighted average for the effective Lewis number:

$$Le_{eff} = 1 + Y_{H_2}\left(Le_{H_2} - 1\right) + Y_{CO}\left(Le_{CO} - 1\right) \qquad \text{(V-6)}$$

In the present approach, it is supposed that the two fuels do not react with one another and that they are completely consumed by the available oxidant. Here, expression (V-6) is also used to characterize stoichiometric mixtures, although more appropriate schemes taking into account the Lewis numbers of both fuel and oxidant should be introduced to avoid a jump between the lean and rich conditions [226-227]. For rich mixtures, the mixture Le is calculated considering the mixture deficient species O_2.

Results of Table V.5 show that all calculated effective Lewis numbers based on expression (V-6) are greater than 1.0. The L_{eff} number of lean mixtures stays unaffected even for the highest H_2 contents (1.07 vs. 1.03 for the 5/95 and 50/50 % H_2/CO blends respectively). This is quite surprising since results provided by Hassan and coworkers [198] indicated negative Markstein numbers for lean H_2/CO mixtures with higher H_2 contents, thus suggesting $L_{eff} < 1.0$. The evolution of the predicted effective Lewis number for a mixture at E.R.=0.4 is plotted in Figure V.13. It is seen (round symbols, label: "Y_i weighted") that definition (V-1) predicts a slow Le_{eff} decrease up to 80 % of H_2 ($Le_{eff} \approx 0.95$) followed by a sharp decrease in the last 20 % of hydrogen addition. This questionable trend, in apparent contradiction with results of ref. [198], will be re-discussed in the next chapter in the light of Markstein lengths extracted from spherically expanding syngas flame results. For almost all syngas flames, an increase of the reference velocity with strain is observed. Slope inversions expected for mixtures with $Le \gg 1.0$ are only found for two marginal cases, i.e. the 20/80 % and 25/75 % H_2/CO mixtures at E.R.=5.0 with Le_{eff} =1.49 and 1.61 respectively. Corresponding $S_{u,ref}$ velocities versus strain rate are plotted in Figure V.14. These observations are concordant with Tien's and Matalon's [68] analytical developments as well as Wu's and Law's [23] experimental investigation of butane/air and butane/He/N_2. These investigations indeed suggested that only mixtures with *Le* numbers significantly greater than 1.0 would display a velocity decrease with strain, for a reference plane located at the upstream flame edge. Present results confirm this point. *Ka* ranges presented in Table V.5 show that the majority of Karlovitz numbers are lower than 0.1 apart from very lean mixtures with increased flame thicknesses δ ($=D_T/S_u^0$) and small S_u^0 values. These Karlovitz numbers are smaller than those obtained in the experimental works of Hassan and coworkers [198], suggesting that investigated strain rates are far enough from the extinction conditions.

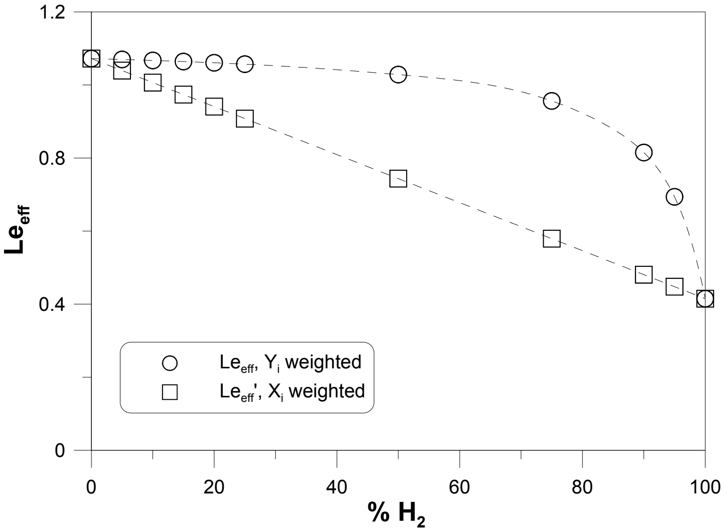

Figure V.13 Effective Lewis number evolutions with the mixture H_2 content for a mixture equivalence ratio of 0.4 (Y_i and X_i refers respectively to the mass fraction and mole fraction of the fuels). Le_{eff}' is the X_i-weighted effective Lewis number defined later by equation (VI-15).

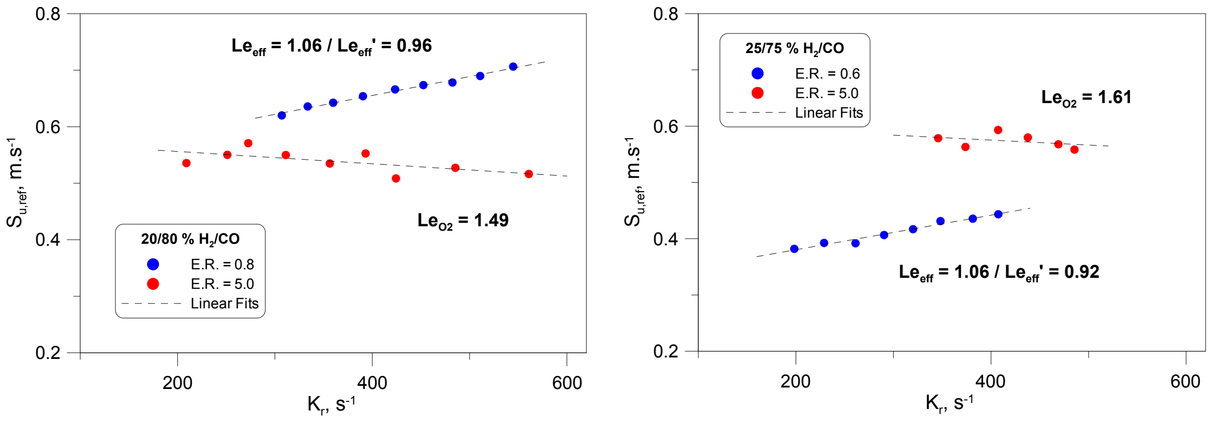

(a) **(b)**

Figure V.14 Evolutions of $S_{u,ref}$ velocities for two syngas/air mixtures and two opposite Lewis numbers: (a) 20/80 % H_2/CO at E.R.= 0.8 (Le_{eff} = 1.06) and E.R. = 5.0 (*Le* = 1.49); (b) 25/75 % H_2/CO at E.R.= 0.6 (Le_{eff} = 1.06) and E.R. = 5.0 (*Le* = 1.61).

Mixture Composition H_2/CO %	*E.R.*	S_u^0 (cm.s^{-1})	$\sigma_{S_u^0}$ (cm.s^{-1})	*Ka* range	Le_{H2}	Le_{CO}	Le_{eff} / Le_{O2}	$Le_{eff'}$
5/95	0.4	8.7	0.2	0.139 - 0.327	0.41	1.07	1.07	1.04
	0.6	18.3	0.7	0.082 - 0.128	0.47	1.07	1.07	1.04
	0.8	27.0	1.3	0.062 - 0.087	0.52	1.07	1.07	1.04
	1.0	41.3	1.2	0.031 - 0.061	0.57	1.07	(1.06)	(1.04)
		41.8	1.3	0.030 - 0.053	0.57	1.07	(1.06)	(1.04)
	1.5	57.2	0.8	0.028 - 0.040	×	×	1.13	×
	2.0	62.1	1.9	0.022 - 0.037	×	×	1.13	×
	2.5	68.6	2.5	0.019 - 0.029	×	×	1.14	×
	3.0	66.3	2.3	0.020 - 0.028	×	×	1.15	×
	4.0	51.2	1.4	0.028 - 0.046	×	×	1.15	×
	5.0	32.4	3.7	0.045 - 0.076	×	×	1.16	×
10/90	0.4	8.8	0.4	0.142 - 0.267	0.41	1.07	1.07	1.01
	0.6	21.9	0.7	0.066 - 0.099	0.47	1.07	1.07	1.01
	0.8	33.7	5.0	0.046 - 0.085	0.52	1.07	1.06	1.01
	1.0	49.2	4.0	0.029 - 0.043	0.57	1.07	(1.06)	(1.02)
	1.5	66.4	6.2	0.024 - 0.032	×	×	1.19	×
	2.0	78.0	14.2	0.022 - 0.026	×	×	1.21	×
	3.0	79.4	13.3	0.022 - 0.028	×	×	1.23	×
	4.0	64.4	1.7	0.024 - 0.041	×	×	1.25	×
	5.0	43.8	2.6	0.030 - 0.051	×	×	1.26	×
15/85	0.4	11.0	0.6	0.103 - 0.171	0.41	1.07	1.06	0.97
	0.6	33.7	0.7	0.052 - 0.087	0.47	1.07	1.06	0.98
	0.8	49.4	3.6	0.035 - 0.046	0.52	1.07	1.06	0.99
	1.0	72.0	2.3	0.017 - 0.027	0.57	1.07	(1.06)	(0.99)
	5.0	50.4	2.3	0.026 - 0.067	×	×	1.37	×
20/80	0.4	12.9	1.8	0.103 - 0.163	0.41	1.07	1.06	0.94
	0.6	31.2	5.3	0.048 - 0.090	0.47	1.07	1.06	0.95
	0.8	52.4	1.0	0.028 - 0.050	0.52	1.07	1.06	0.96
		56.6	2.0	0.022 - 0.036	0.52	1.07	1.06	0.96
	4.0	95.5	8.3	0.018 - 0.023	×	×	1.45	×
	5.0	58.5	2.4	0.019 - 0.052	×	×	1.49	×
25/75	0.4	12.8	0.3	0.112 - 0.252	0.41	1.07	1.06	0.91
	0.6	32.0	0.8	0.049 - 0.100	0.47	1.07	1.06	0.92
	0.8	43.1	4.2	0.051 - 0.071	0.52	1.07	1.06	0.93
	4.0	94.4	9.6	0.017 - 0.021	×	×	1.56	×
	5.0	64.2	4.9	0.029 - 0.040	×	×	1.61	×
50/50	0.4	16.0	0.7	0.103 - 0.177	0.41	1.07	1.03	0.74
	0.6	52.0	2.3	0.027 - 0.038	0.47	1.07	1.03	0.77
	0.8	102.4	17.0	0.015 - 0.017	0.52	1.07	1.03	0.80

Table V.5 Summary of experimental conditions for syngas/air flames at atmospheric pressure and ambient temperature (*E.R.*: Equivalence Ratio, *Ka*: Karlovitz number, *Le*: Lewis number). When E.R.=1.0, corresponding Le_{eff} numbers are between parenthesis since expression (V-1) should be evaluated for off-stoichiometric conditions. Le_{eff}' is the X_i-weighted Lewis number defined later by equation (VI-15).

Results for the 5/95 % H_2/CO mixture are presented in Figure V.15 and Figure V.16 along with experimental datasets from the literature and numerical predictions using the PREMIX code. An overall good agreement is found, although present measurements indicate slightly higher velocities in the equivalence ratio range 1-2.5. For very rich cases, i.e. E.R.= 4.0 and 5.0, our DPIV results show excellent agreement with outwardly propagating flame experiments by Sun et al. [200], Hassan et al. [198] and Mclean et al. [199]. In this case, predictions with the mechanism of Sun and coworkers [200] are found to be the most accurate, while Li et al. mechanism [223] provides higher velocities, up to 3.2 $cm.s^{-1}$ at E.R.=4.0. On the lean side (see Figure V.16), our measurements are in close agreement with PREMIX predictions for the E.R. range 0.4-0.8, with a higher determined flame speed at the stoichiometry (+3.6 $cm.s^{-1}$). They also show very good agreement with the measurements of Natarajan and coworkers [85] in the conical flame configuration. If outwardly propagating flame results (McLean [199]) are close to DPIV data points and computed velocity values for lean mixtures (E.R≤0.8) , they depart from both as the equivalence ratio increases, yielding a maximum discrepancy with counterflow/conical flame data of about 7 $cm.s^{-1}$ at E.R. =1.0. Close flame speed values at E.R.=0.6 for both counterflow configurations are obtained (Present work: 18.3 ± 0.7 $cm.s^{-1}$ and Vagelopoulos [70]: 16.9 $cm.s^{-1}$), thus showing the reliability of the counterflow approach. Note that the present measurements extend the available data down to E.R.=0.4 with a measured flame speed of 8.7 $cm.s^{-1}$. Such weak flames are usually difficult to study in the outwardly propagating and conical configurations, for which buoyancy effects and heat losses at the burner rim become prominent.

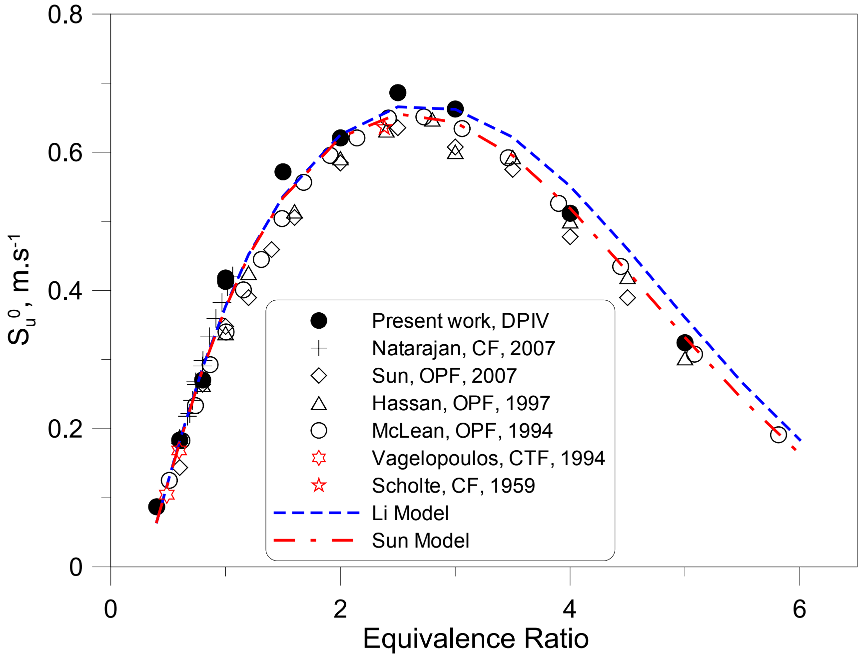

Figure V.15 Comparison of syngas laminar flames speeds for the 5/95 % H_2/CO blend with available data from the literature: Natarajan et al. [85] , Sun et al. [200], Hassan et al. [198], Mclean et al. [199], and single data points of Vagelopoulos [70] and Scholte and Vaags [205]. Models (PREMIX): Li et al. [223] and Sun et al. [200] (CF: Conical Flames, OPF: Outwardly Propagating Flames, CTF: Counterflow Flames).

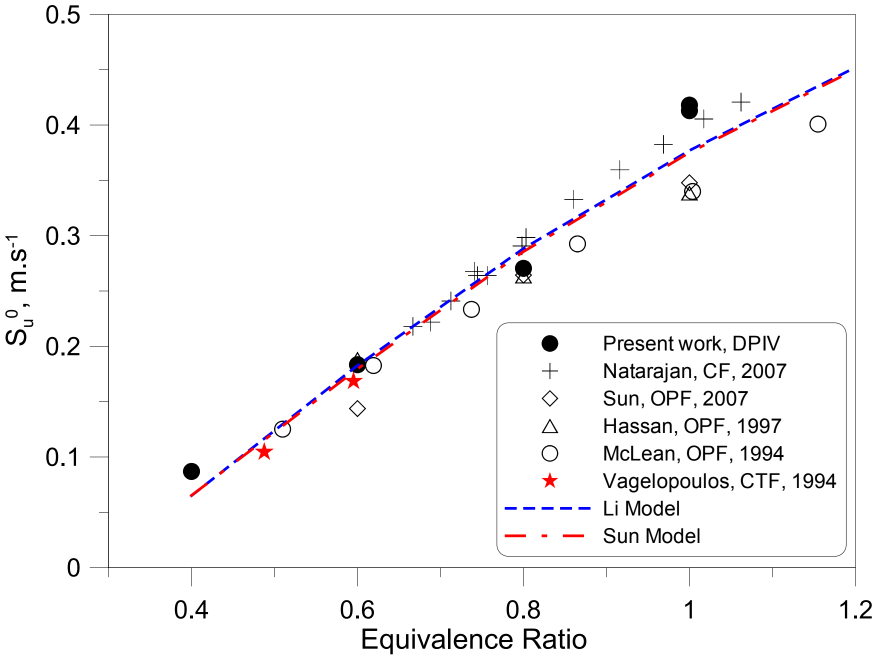

Figure V.16 Lean side of the diagram in Figure V.15.

Results for the 10/90 % H_2/CO mixture are shown in Figure V.17 and Figure V.18. A very good agreement is found with numerical predictions on the lean side (E.R.=0.4-1.0). Above E.R.=1.0, both mechanisms start to overpredict all available data points up to E.R.=3.0 included. Present DPIV measurements are in excellent agreement with outwardly propagating flame results for 0.6 < E.R. < 3.0, especially with those of Hassan and coworkers [198], for which differences between both datasets do not exceed 2.9 cm.s^{-1} for each single point. If an excellent agreement is also found at E.R=0.6 with data points of Vagelopoulos [70] for the counterflow configuration and Yumlu [207] for the heat flux methodology, conical flame results of Günther and Janisch [208] and Dong et al. [214] significantly depart from the numerical predictions as well as the other experimental trends. Different choices of diagnostics and methodologies (Schlieren with cone angle method for ref. [208] and luminous cone with flame surface area for ref. [214]) might explain the important scatter observed at E.R.=1.0 (28.8 cm.s^{-1}). For equivalence ratio above 3.0, important discrepancies are observed: our data points lay significantly higher than both conical (Scholte and Vaags [206]) and outwardly propagating (Hassan et al. [198]) flames, with a maximum difference of 11 cm.s^{-1} at E.R.=5.0. The numerical predictions seem to support these higher values. Given the excellent agreement of DPIV measurements with other experimental investigations at lower equivalence ratios, discrepancies observed for the rich side are quite surprising. Recently, important scatter in measured laminar flame speeds have also been reported in the literature for 50/50% H_2/CO mixtures at atmospheric conditions [201]. If the aforementioned scatter could be induced by differences in data processing methodologies, it was suggested in ref. [201], that metal carbonyls such as iron pentacarbonyl ($Fe(CO)_5$) or nickel tetracarbonyl ($Ni(CO)_4$), known to have noticeable flame inhibition effects, could be responsible for the observed discrepancies. The influence of iron pentacarbonyl on syngas flames is relevant since evidences of iron oxide deposits in laboratory syngas combustion experiments have been reported, as recalled earlier [220]. Recent investigations on iron pentacarbonyl effects on flames include the development of a dedicated mechanism by Rumminger et al. [228] for $CH_4/O_2/N_2$ diffusion and premixed flames (E.R.=0.9, 1.0 and 1.1). Further validations of the kinetic scheme were done by Rumminger and Linteris for premixed $CO/H_2/O_2/N_2$ flames [218]. These investigations underlined the importance of O-atoms and H-atoms scavenging cycles responsible for $Fe(CO)_5$ inhibiting effects as well as saturation of these catalytic cycles for concentration generally higher than 100 ppm. Since every possible effort was made to avoid contamination by metal carbonyls in our experiment and noticing that no specific measures were reported in other syngas flame speed investigations, it is reasonable to assume that datasets proposed in ref. [198] and [206] could suffer from $Fe(CO)_5$ contamination.

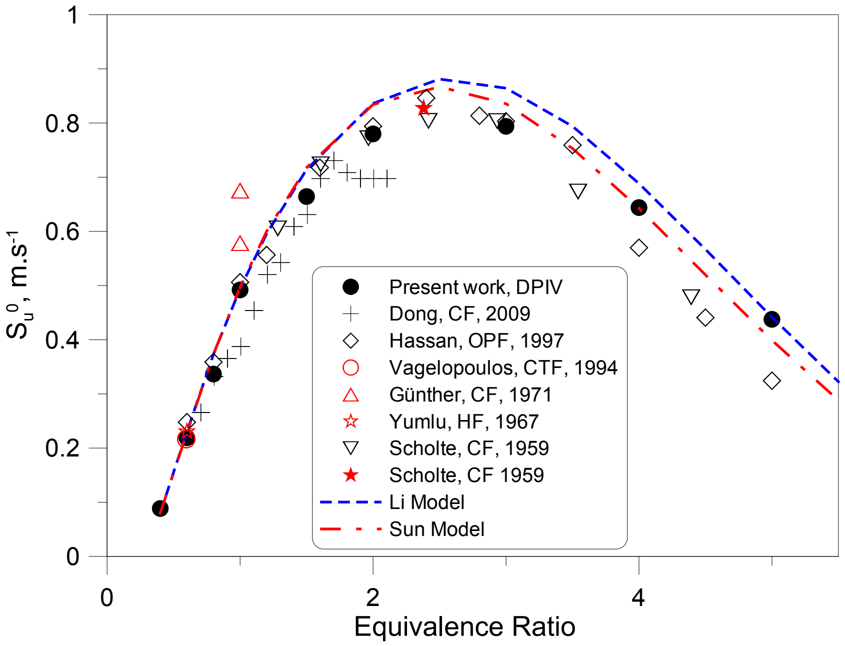

Figure V.17 Comparison of syngas laminar flames speeds for the 10/90 % H_2/CO blend with available data from the literature: Dong et al. [214], Hassan et al. [198], Vagelopoulos [70], Günther and Janisch [208] and Scholte and Vaags [206] (10.5/89.5 % H_2/CO). Single data points from Yumlu [207] and Scholte and Vaags [205] (10.36/89.64 5 % H_2/CO). Models (PREMIX): Li et al. [223] and Sun et al. [200] (CF: Conical Flames, OPF: Outwardly Propagating Flames, CTF: Counterflow Flames, HF: Heat Flux).

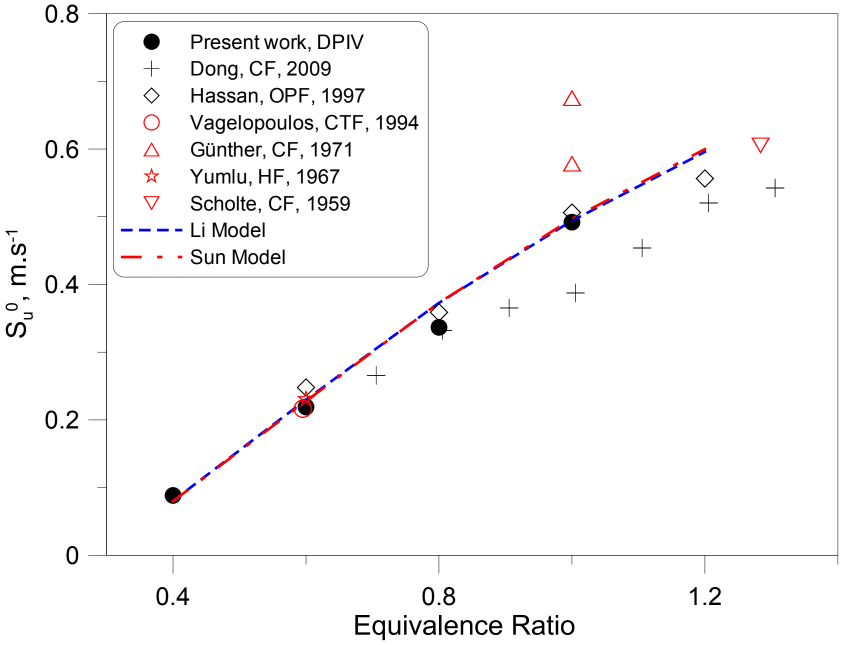

Figure V.18 Lean side of the diagram in Figure V.17

Following the approach adopted in ref. [201], we decided to implement the kinetic sub-mechanism of iron pentacarbonyl developed and validated in ref. [218, 228] in the mechanism of Li et al. [223] to quantify the potential impact of carbonyls on laminar flame velocities on the rich branch of the 10/90 % H_2/CO mixture. Corresponding transport and thermodynamic data for the Fe-containing species chemistry were also included. Levels of 50 and 100 ppm of $Fe(CO)_5$ were assumed to be present in the CO. These levels are well within the maximum 200 ppm $Fe(CO)_5$ content observed in carbon steel gas tanks after a nine month storage period [229]. They respectively represent between 6.5 to 31.4 ppm and 13 to 61 ppm of the total mixture depending on chosen equivalence ratio. Consideration of $Fe(CO)_5$ levels higher than 100 ppm should be excluded since the mechanism predictions consequently worsen at higher contents (see ref. [218]). Results are shown in Figure V.19. If a negligible effect is observed at lower equivalence ratios, the influence of $Fe(CO)_5$ is gradually felt as E.R. increases. At E.R.=5.0, the discrepancy of about 11 cm.s^{-1} observed between the present measurements and those of Hassan and coworkers [198] agrees well with the 9 c.ms^{-1} predicted decay due to the 31.4 ppm $Fe(CO)_5$ addition. The computed flame velocity reductions encompass the experimentally determined flame speeds, confirming that iron pentacarbonyl can possibly play an important role in the chemistry of rich syngas flames. Additional investigations are required to better quantify these inhibition effects, which are commonly overlooked in syngas flame speed studies, by for instance implementing systematic detection of Fe or Ni compounds in the studied flames.

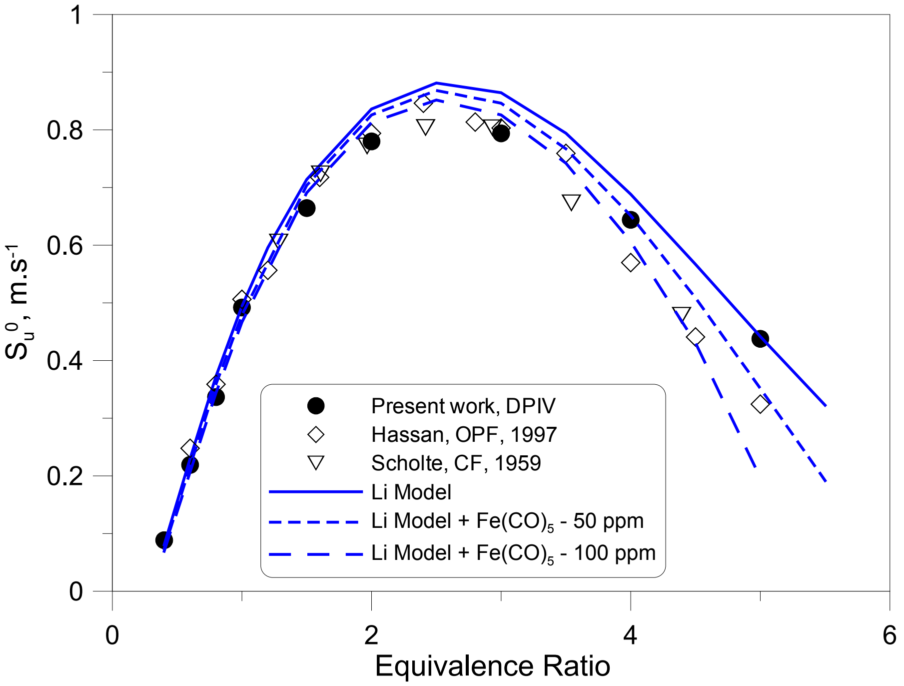

Figure V.19 Laminar flame speeds for the 10/90 % H_2/CO blend compared with model predictions incorporating 3 levels of iron pentacarbonyl contamination: 0, 50 and 100 ppm. Experimental datasets are from Hassan et al. [198] and Scholte and Vaags [206]. Models (PREMIX) from Li [230] and Li [230] modified with the iron pentacarbonyl submechanism used in the works of Rumminger and Linteris [218] (OPF: Outwardly Propagating Flame, CF: Conical Flame).

The remaining results considered in the present section are presented in Figure V.20 versus hydrogen mole fraction in fuel. The overall agreement of DPIV measurements with computed values is satisfactory for the E.R. range 0.4-1.0 (Figs. a, b, c, d), apart from measurements for 50% H_2 addition that are systematically above the numerical predictions. Very weak flames (E.R.=0.4, Fig. a) were found to be 2 to 4 cm.s^{-1} faster than those determined by Hassan and coworkers [198]. At E.R.=0.6 (Fig. b), our 50% H_2 measurements are further supported by higher velocities obtained in recent investigations using outwardly propagating flames (Prathap et al. [212], Burke et al. [213]). Agreement between the experiments and computations seriously shades off at higher equivalence ratios and H_2 additions. In Figures e and f, DPIV data for 25 % H_2 are respectively 24 cm.s^{-1} and 28.5 cm.s^{-1} higher as compared with Hassan's et al. [198] measurements. A discrepancy of about 36 cm.s^{-1} is found between the results of Hassan et al. [198] and Burke et al. [213] for the 50 % H_2 case. Interestingly, mechanism predictions also differ from each other for very rich mixtures with lower flame speeds given by the model of Sun et al. [200] (up to 17 cm.s^{-1} at E.R.=4.0, 50% H_2 and 7.5 cm.s^{-1} at E.R.=5.0, 25% H_2).

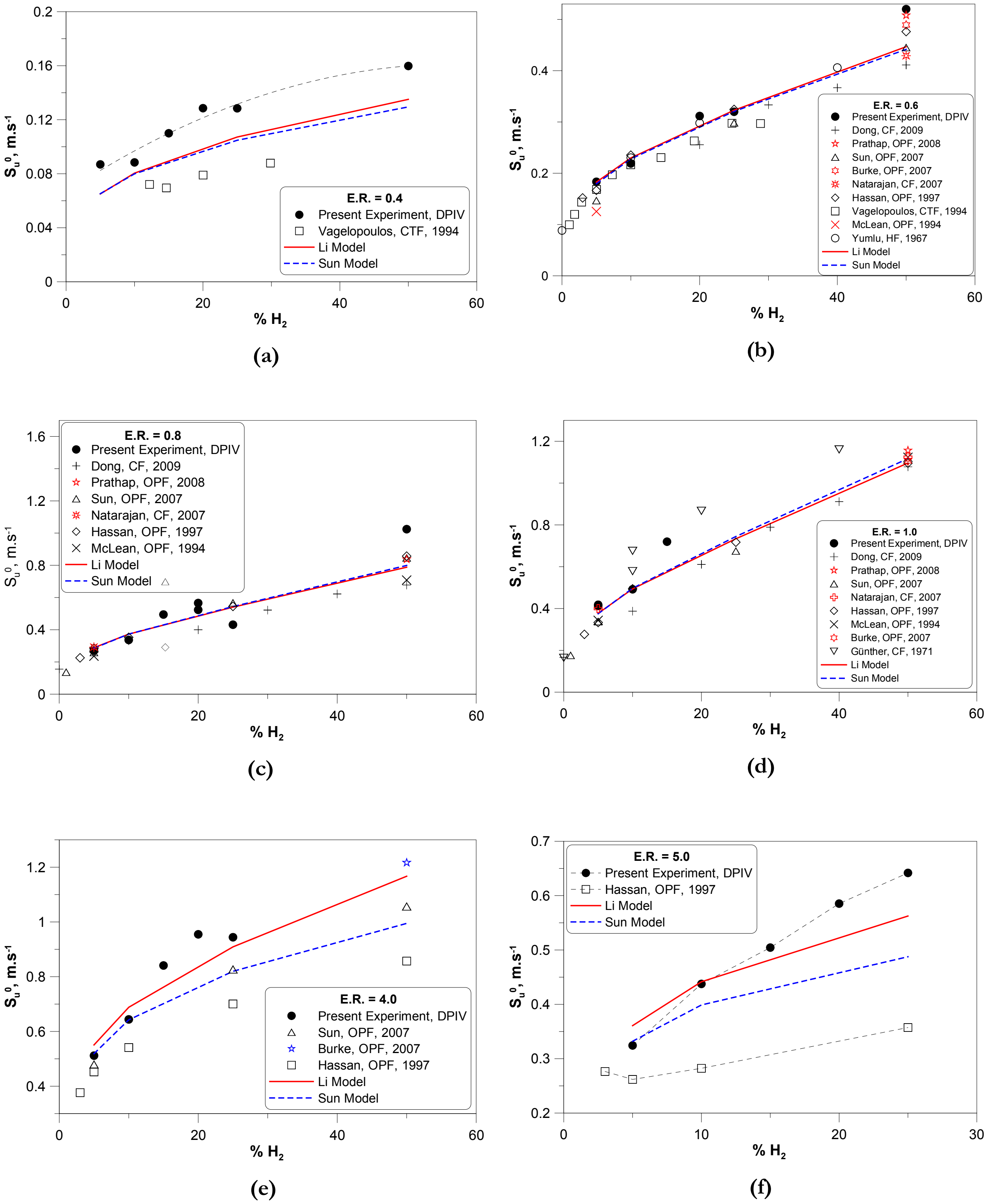
(a) (b) (c) (d) (e) (f)

Figure V.20 Influence of H_2 addition to CO for various equivalence ratios: (a) E.R.=0.4, (b) E.R.=0.6, (c) E.R.=0.8, (d) E.R.=1.0, (e) E.R.=4.0, (f) E.R.=5.0. Datasets and single points are from Vagelopoulos et al. [70], Dong et al. [214], Prathap et al. [212], Sun et al. [200], Burke et al. [213], Natarajan et al. [85], Hassan et al. [198], McLean et al. [199], Yumlu [207] and Günther and Janisch [208]. Models (PREMIX) are from Li et al. [230] and Sun et al. [200] (CTF: Counterflow Twin Flames, OPF: Outwardly Propagating Flames, CF: Conical Flames, HF: Heat Flux).

Sensitivity analysis performed with the mechanisms of Li et al. [230] and Sun et al. [200] for a 50/50% H_2/CO mixture (E.R. 4.0 and 5.0) revealed that the flame speed is mainly sensitive to the chain branching reaction $H+O_2=O+OH$ as well as the reaction $HO_2+H=OH+OH$. Comparisons of the chosen rate constants for both mechanisms and both reactions are provided in Figure V.21. Disparities observed for the rich cases of Figure V.20 are clearly due to the choice of different rate constant parameters, with Li and coworkers [223] providing the highest estimates for both reactions. Note that for the case f (E.R.=5.0), DPIV measurements are gradually underestimated by both mechanisms at higher hydrogen additions. A maximum discrepancy of 9.2 cm.s^{-1} is observed with the Li et al. [230] calculation at 25 % H_2 addition.

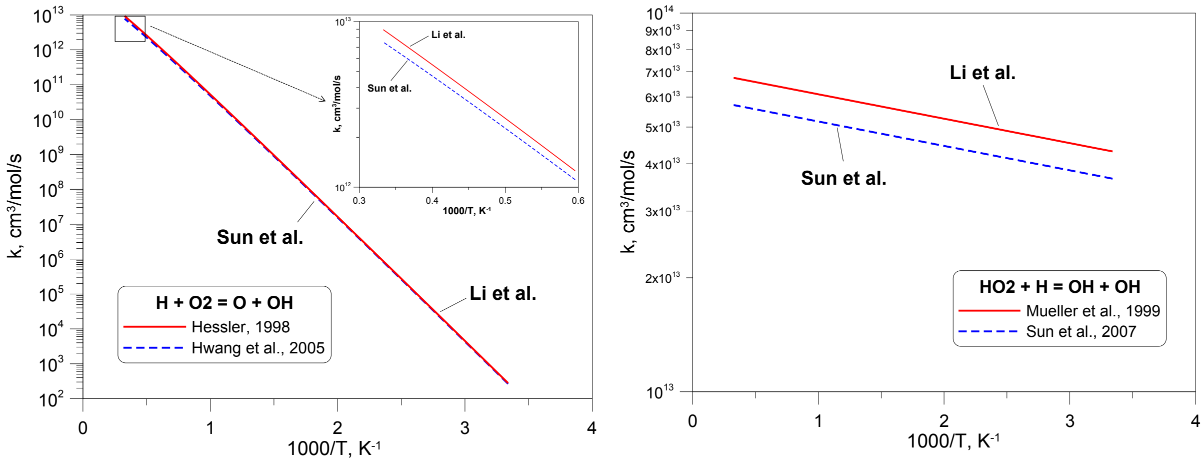

(a) (b)

Figure V.21 Comparisons of rate constants used in the Li et al. [223] and Sun et al. [200] mechanisms for: (a) $H + O_2 = O + OH$ reaction with rate constants from Hessler [231] and Hwang et al. [232]; (b) $HO_2 + H = OH + OH$ reaction with rate constants from Mueller al. [233] and adapted value of Sun et al. [200].

V.6 Summary

Laminar flame speeds of various H_2/CO blends have been studied using the counterflow flame approach along with the DPIV diagnostics. This study required modifications of the previous burner assembly in order to house the entire apparatus in a ventilated chamber to allow for investigations at flame-rich conditions. Since it was found that the nozzle burners could possibly behave like Helmholtz resonators promoting the formation of roll-up vortices leading to unstable flame conditions, new converging nozzles with 0.5 mm thick lips were designed to prevent the onset of instability. While the latter still arose at higher flow rates, significant improvements were found by replacing the coflowing nitrogen by helium. The entire gas delivery system was modified to minimize online formation of metal carbonyls by replacing stainless steel lines by copper lines and ultimately providing cold traps for carbonyl compounds condensation. A new flow control system was implemented to simplify burner operations for hydrogenated fuels usually prone to flashback and blowoff when mixture components are successively adjusted.

It was shown that evolutions of the velocity at the point of reference almost always display a positive slope with increasing strain even for mixture Lewis number above unity. A slope inversion is observed only for higher mixture Lewis numbers (*Le* ≈ 1.6-1.7) characterizing rich H_2/CO flames with higher H_2 contents. These trends are coherent with earlier analytical and experimental observations, suggesting that analyzing the flame sensitivity to strain from reference velocities taken at the upstream edge of the flame would yield ambiguous interpretations.

Flame speeds of various syngas mixtures (from 5/95 % to 50/50% H_2/CO) have been investigated and confronted to the literature data as well as numerical predictions of two leading mechanisms developed for syngas combustion. If an overall good agreement is found for the 5/95 % H_2/CO case, important disparities are observed among available flame speeds measurements of rich 10/90 % H_2/CO mixtures. It has been shown that flame inhibition effects of small amounts of iron pentacarbonyl (up to 61 ppm in the total mixture) could provide an effective flame speed reduction on the order of observed discrepancies. This significant scatter has also been noticed in the literature for measurements performed on spherical flames with higher H_2 contents (50/50 % H_2/CO). It is reasonable to expect that some part of observed discrepancies is possibly introduced by the processing methodologies. This should be taken into account before allowing any conclusion to be drawn.

An increasing disagreement was found between predictions of both Li et al. [230] and Sun et al. [200] mechanisms at higher equivalence ratio and H_2 contents. It has been shown that discrepancies among the two models are resulting from a selection of different rate constant parameters for both $H+O_2=O+OH$ and $HO_2+H=OH+OH$ reactions. Both mechanisms under predict DPIV measurements at higher H_2 contents.

VI. Laminar Flame Speeds of Syngas/Air Mixtures: the Bunsen and Outwardly Propagating Flame Approaches

VI.1 Introduction and Objectives

The present chapter is devoted to the study of laminar flame speed of syngas/air flames with two widely used techniques: the outwardly propagating and the conical flame. The chosen Bunsen flame approach is detailed in PART I and measurements performed for a wide range of syngas composition form 1/99 % H_2/CO to 100% H_2. Both classical flame surface area and flame cone angle techniques are compared. The influence of curvature effects for nonequidiffusive mixtures is illustrated through the flame tip opening phenomenon. The outwardly propagating flame approach is presented in PART II and used to determined laminar flame speed of four syngas mixture compositions including 5/95, 10/90, 25/75 and 50/50 % H_2/CO blends. Sate of art processing methodologies, including linear and non-linear extrapolation methods, have been used to extract both laminar flame speeds and corresponding Markstein lengths. Differences among processing methodologies are discussed in the light of the 50/50 % H_2/CO flame results. Confrontation of results obtained for the three investigated methodologies including the counterflow, conical and outwardly flame approaches is provided in PART III.

VI.2 PART I: The Bunsen Flame Approach

VI.2.1 Methodologies

The syngas laminar flame speed measurements were performed using two classical approaches for rim stabilized conical flames. First, the averaging methodology of the flame surface area has been used to determine the laminar flame speed S_u (Note that the notation "S_u^0" is not used since stretch effects are not subtracted as compared to the counterflow and spherical flame approaches). Assuming that the burning velocity is the same over the entire surface area of the flame *A*, the flame speed can be calculated applying the following mass conservation:

$$\rho_u S_u A = \rho_u \dot{Q} \quad \rightarrow \quad S_u = \frac{\dot{Q}}{A} \tag{VI-1}$$

with ϱ_u, the unburned gas density and $\dot{Q}$, the total volumetric flow rate of the unburned mixture. This method requires the knowledge of the total area of the flame surface *A*, deduced in the present investigation by analyzing OH* chemiluminescence images of the flames. As shown in Figure VI.1, a FORTRAN program has been developed to perform a three-point Abel inversion [234] of the recorded images to provide the 2-D boundaries of the flames, based on the maximum emission of OH*. Assuming axisymmetric conditions, two distinct flame surface areas are computed from each half of the recorded images and corresponding flame speeds are calculated using the measured burner inlet flow rate. The retained flame speed is an average of velocity values determined from both left and right sides.

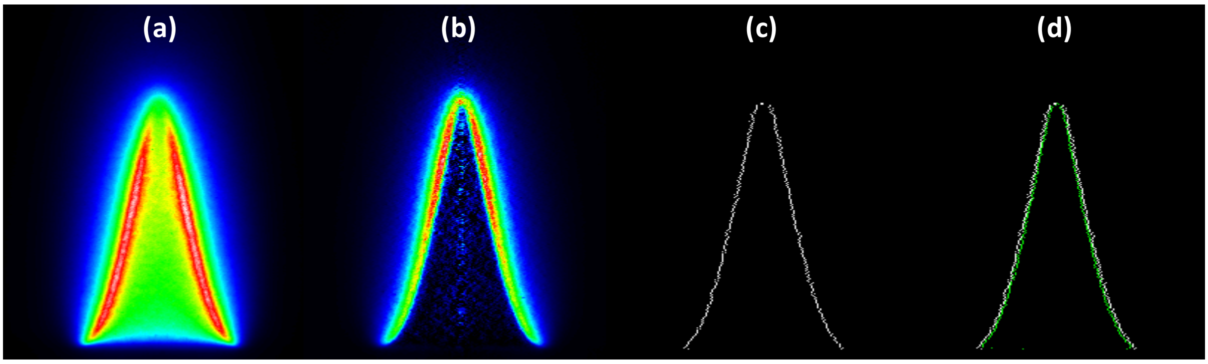

Figure VI.1 OH* chemiluminescence image processing: (a) OH* chemiluminescence original image, (b) Abel-inverted image, (c) Maximum intensity trace after inversion, (d) Superimposed traces of images with/without inversion (in white: maximum intensity trace of the Abel-inverted image, in yellow: maximum intensity of the recorded image without inversion).

The second measurement approach adopted herein is the flame cone angle methodology applied to Schlieren images of studied flames (see Figure VI.2). The latter approach is particularly adapted for flames displaying straight-sided cones and requires therefore the use of aerodynamically contoured nozzles. In this case, the velocity U_0 of the unburned mixture at the nozzle exit can be considered as uniform and the expression of the laminar flame speed S_u can be calculated (see Figure VI.3):

$$cos\left(\frac{\pi}{2}-\alpha\right)=\frac{S_u}{U_0} \quad \rightarrow \quad S_u = U_0\, sin(\alpha) \tag{VI-2}$$

with U_0, the bulk velocity of fresh reactants and α, the half cone angle of the flame. A FORTRAN program has been developed to perform edge detection on acquired Schlieren images in order to extract the flame cone angle α. U_0 is evaluated from the burner input flow rate and burner exit section, assuming a uniform velocity repartition at the burner exit.

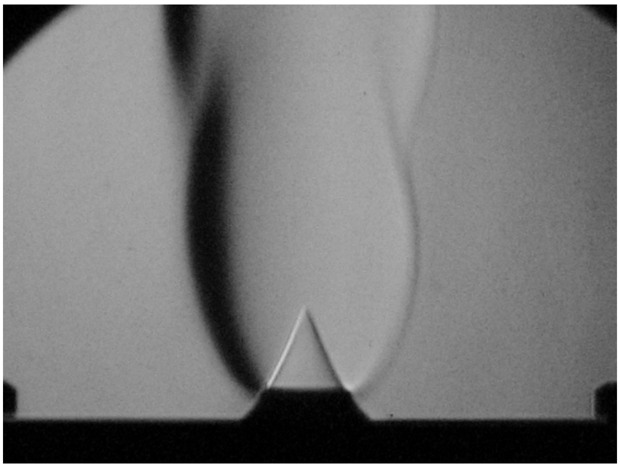

Figure VI.2 Example of a Schlieren image (8 mm nozzle burner, 40/60 % H_2/CO).

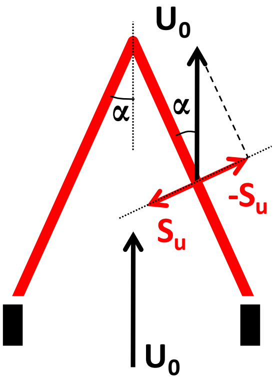

Figure VI.3 Illustration of the cone angle methodology (U_0 : bulk velocity of fresh reactants, α: half cone angle of the flame).

The simplicity of expressions (VI-1) and (VI-2) is however counterbalanced by several difficulties inherent to the flame configuration and the nature of chosen diagnostics. For instance, the choice of the surface area is clearly conditioned by the optical method that is used. Indeed, Expression (VI-1) would require the evaluation of the cold gas surface area (before increase of the gas density) while optical diagnostics generally allow the extraction of either the schlieren, shadow or luminous surfaces, already located in preheat zone of the flame, leading to an underestimation of the burning velocities [17]. The cone angle method should also be carefully considered; even with contoured nozzles, flames are rarely perfectly straight-sided since the burner exit velocity cannot be uniform over the entire burner diameter due to boundary layer effects. Thus, the conventional 1D calculations of U_0 by directly dividing the volumetric flow rate of fresh reactants by the burner area could potentially reach an inaccurate value. Although laminar flame speed measurements using conical flames seem to raise much controversy among experimental investigations found in the literature (see for instance the discussion of Andrews and Bradley in ref. [17]), this configuration is still widely used since burner implementations and operations are considerably simplified as compared with the spherical or counterflow flames. The last important point to be underlined is that the burning velocity is not constant over the entire flame surface, as reported originally by Lewis and Von Elbe in ref. [235] (p. 283) and further confirmed by Echekki and Mungal [236]. Indeed, heat losses at the burner rim contribute to the burning rate decrease at the flame base while curvature of the flame cone apex can considerably modify the burning velocity, depending on the importance of nonequidiffusion phenomena [179]. This will be illustrated in the incoming sections.

VI.2.2 Burner Apparatus

A series of six stainless steel burners have been designed and fabricated. Tested burners diameters are 3, 4, 6, 8, 12, and 16 mm. A nominal burner length of 900 mm was chosen based on the 50 x diameter criteria, therefore ensuring a fully developed laminar flow at the burner rim. Particular care was taken to fabricate sharp-edged burner rims so as to avoid any irregularity that could affect the flame stabilization. The apparatus also integrates a pilot flame ring with a premixed mixture of methane and air as reactants. Tests were conducted to determine if the pilot flame could enhance the syngas flame stability at lower equivalence ratios. As flames obtained on the 3 mm diameter displayed ridges characteristic of cellular instabilities and the use of the 16 mm tube was severely restricted by the available flow rates, results presented in this study were exclusively obtained for the 4, 6, 8 and 12 mm diameter tubes. Pictures of the burner tubes are provided in Figure VI.4.

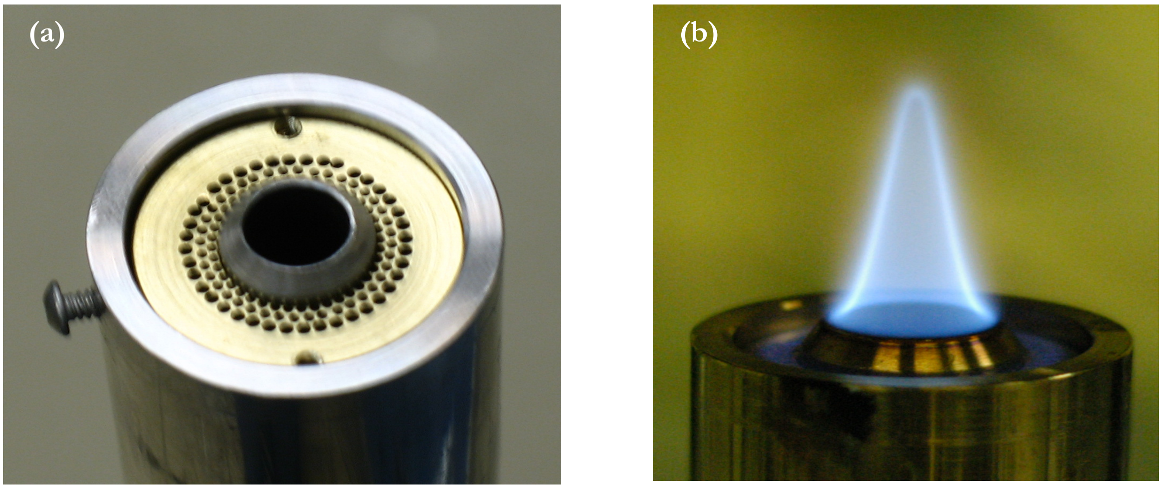

Figure VI.4 Details of the straight burner setup: (a) Burner exit with sharp edge and perforated plate for the pilot flame tests, (b) Syngas conical flame stabilized with a CH_4/air pilot flame on the burner rim.

Two additional nozzle burners (4 and 8 mm I.D.) were designed (see Cohen and Ritchie [162]) and fabricated to perform flame speed measurements using the cone angle methodology applied to Schlieren flame images. Examples of transverse velocity profiles measured using hot wire anemometry are provided Figure VI.5 for the straight and nozzle burners. Both 4 and 8 mm nozzles provide plateau velocity profiles, flat over approximately 63 and 71 % of their respective diameter. The theoretical 1D velocity profiles assuming uniform exit velocity (see dashed lines) are added for comparison.

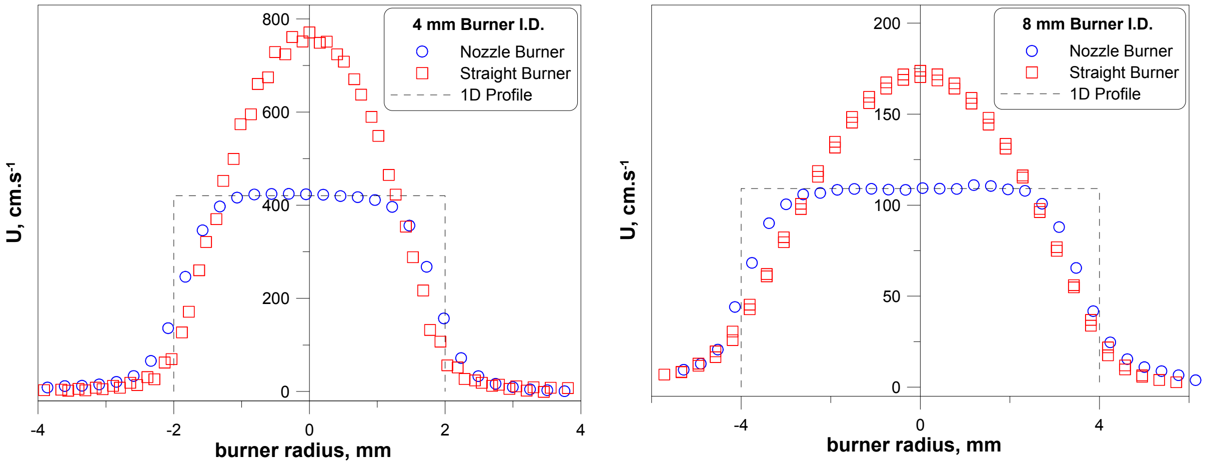

(a) (b)

Figure VI.5 Cold flow (Air) velocity profiles 3 mm above the burner exits for the nozzle and straight tube burners: (a) 4 mm I.D. burners (Flow rate straight burner: 3.18 L/min, flow rate nozzle burner: 3.17 L/min) and (b) 8 mm I.D. burners (Flow rate straight burner: 3.29 L/min, flow rate nozzle burner: 3.29 L/min).

VI.2.3 Flow Control and Gas Delivery System

A schematic of the experimental apparatus used is shown Figure VI.6. Each gas of the H_2/CO/Air mixture is initially stored in separated tanks. Degrees of purity are respectively 99.95% for the hydrogen and 99.995% for the carbon monoxide. Air used is of breathing quality (99.95%). Each gas flow rate is carefully controlled by calibrated mass flow meter with an accuracy of ±1% full scale. A mixing section allows a rapid mixing of the reactants prior to injection into the burner.

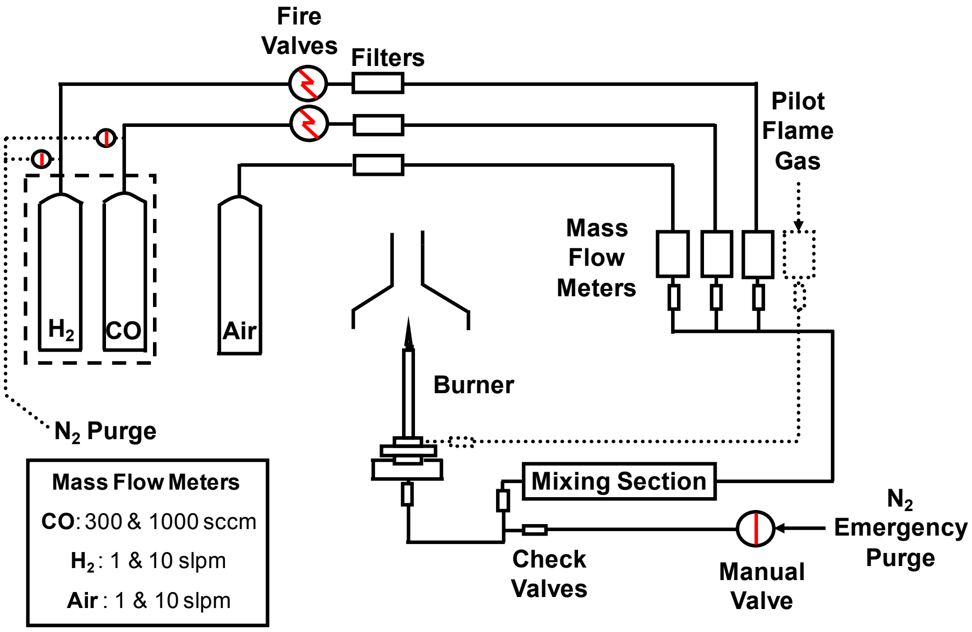

Figure VI.6 Schematic of the experimental gas delivery system.

VI.2.4 Chemiluminescence and Schlieren Diagnostics

Details on the experimental layout of the present study are presented Figure VI.7. OH* chemiluminescence images were recorded with an intensified CCD (ICCD) camera (PIMAX: 512´512 pixels) equipped with an UV lens (*f* #/4.5) and filters (long pass WG305 + band pass UG11). OH* chemiluminescence images were captured by accumulation, for each case, of 50 instantaneous images. During the experiment, the ICCD camera was moved to achieve the best resolution possible for each series of measurements. A horizontal knife edge was used to reduce the intensity from the base of the flame and make its tip more visible. This method substantially improves the trace of the flame reaction zone boundaries and thus the laminar flame speed computations.

The Z-type two-mirror schlieren system is arranged as follows: the light beam emitted by a tungsten lamp (30W) goes first through a condenser lens. The diverging beam issued from an aperture located at the focal point of the condenser lens is used as a point source for the first spherical mirror (*f*=1m). The top of the burner is placed in the middle of the test region defined by the parallel beam formed between two spherical mirrors. The resulting image is formed on a digital camera with

5 Mega pixels. A vertical knife edge located at the focal point of the second mirror is used to block the white beam and therefore to form the schlieren images. Schlieren and OH* chemiluminescence images were simultaneously taken for every flame studied. Typical resolutions achieved for the chemiluminescence diagnostics were ranging from 31 to 87 µm/pixel.

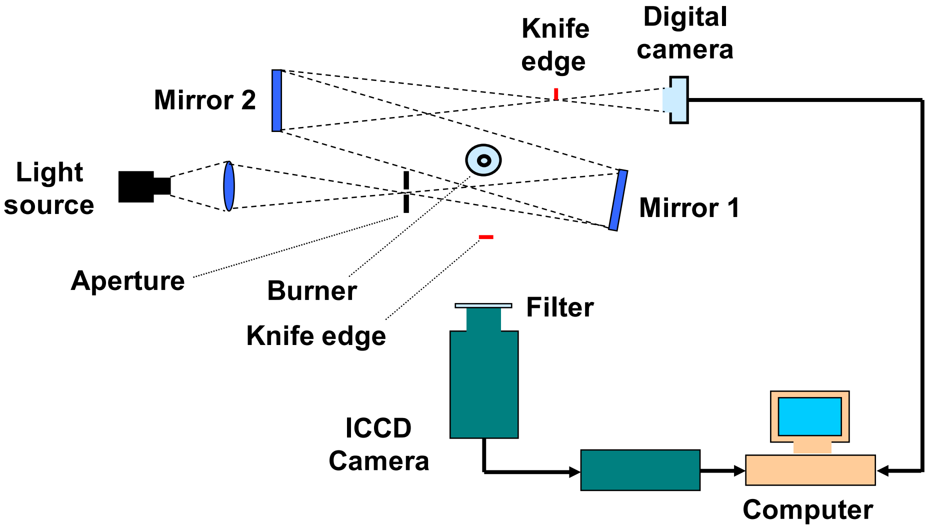

Figure VI.7 Schematic of the implementation of the chemiluminescence and schlieren diagnostics

VI.2.5 Results and Discussion

Since it was generally observed that straight-sided flame cones were difficult to obtain with contoured nozzle for the entire syngas mixture compositions and flow rates considered herein, the majority of results presented in this section were established using the OH* chemiluminescence methodology along with expression (VI-1). A limited number of tests were performed with contoured nozzles and the schlieren diagnostics. They will be discussed at the end of the present section.

Test matrices for the chemiluminescence experiments are provided Figure VI.8. Since the burner assembly was not housed in a closed vessel, performed measurements were restricted, for safety considerations, to the lean and moderately rich mixtures (E.R.=0.3 → 1.3). Mixture compositions from 1/99 % H_2/CO to 100% H_2 were studied.

It can be seen in Figure VI.8 that flame stability ranges are limited by: i/ the maximum allowed flow rate (FRL), fixed by the mass flow meter full scales. The upper E.R. ranges are progressively reduced with hydrogen addition due to the fast increase of the corresponding flame speeds; ii/ the mixture quenching diameters. It was for instance found that the slower flames (small hydrogen contents) could not be stabilized on the smaller burner tubes (mainly the 4 and 6 mm I.D. burners); iii/ flame propensity to flashback. An increase of the burner diameter is progressively restricting the study to the H_2/CO mixtures with lower H_2 contents; iiii/ flame propensity to blowoff. Flame blowoff mainly occurs while trying to stabilize very lean mixtures. This limit is usually reached for E.R.=0.55-0.6 but the E.R. ranges have been further extended down to E.R.=0.3 using the methane/air pilot flame (triangles on the stability maps, see for example Fig. b).

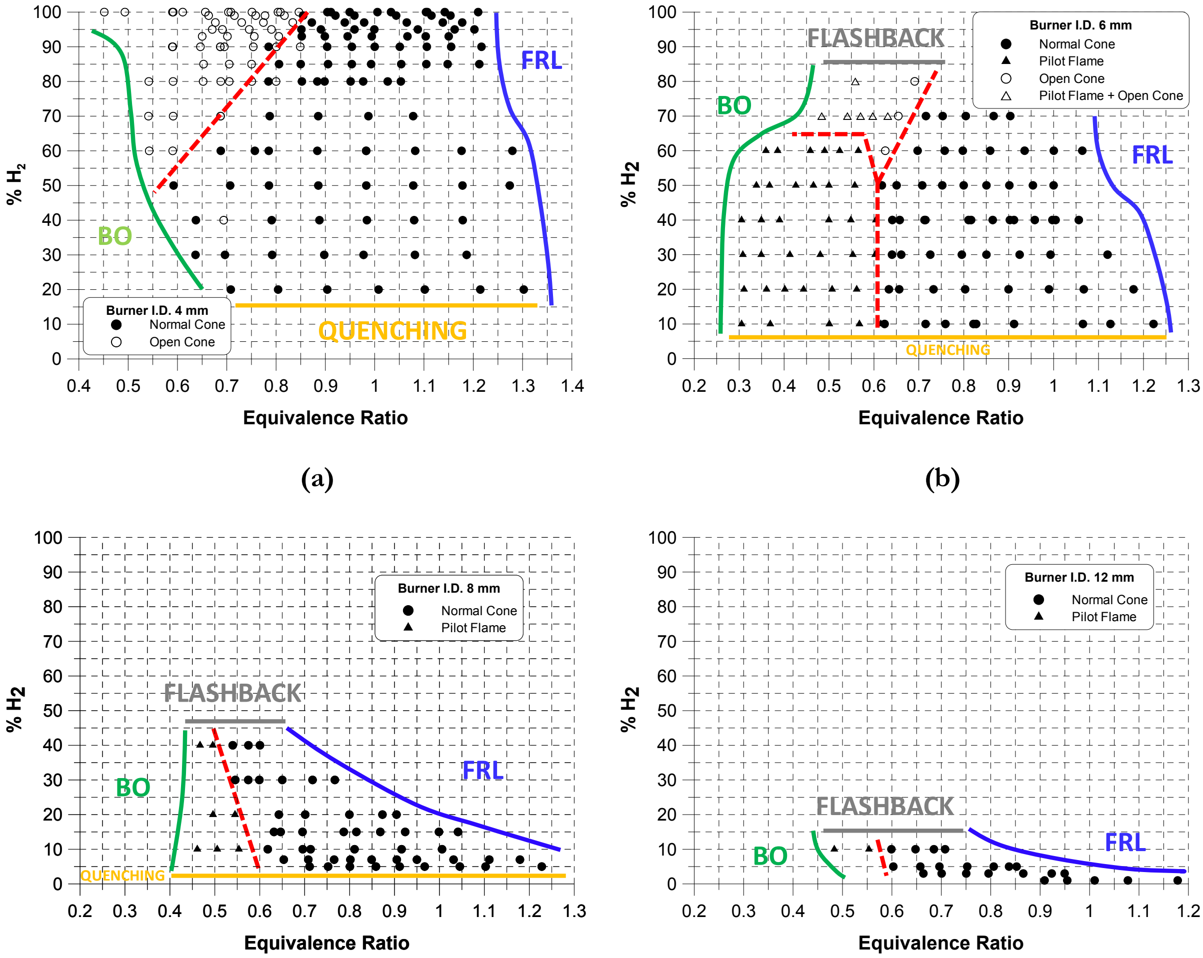

(a)

(b)

(c)

(d)

Figure VI.8 Test matrices for laminar flame speed determination of syngas flames following the OH* chemiluminescence methodology for the 4 mm (a), 6 mm (b), 8 mm (c) and 12 mm (d) I.D. burner tubes (Filled circles ●: "normal" conical flames, open circles ○: flame with open tip, filled triangle s ▲: flame stabilized with pilot flame, open triangles Δ: flame stabilized with pilot flame with open tip, BO: Blowoff, FRL: Flow Rate Limit).

An interesting point to be mentioned is that the flame tip opening phenomenon (open symbols on stability maps) was observed for lean flames with higher H_2 contents stabilized on the 4 and 6 mm I.D. burner tubes. This phenomenon is a direct illustration of curvature effects on nonequidiffusive mixtures. If the concave curvature towards the fresh reactants is focusing the heat at the flame apex (fresh reactants heated by a larger segment of the flame), the deficient reactants, in our case H_2+CO, is depleted at the flame tip due an opposite defocusing effect of the flame curvature (same volume of reactants for a larger segment of the flame). Therefore, the burning intensity at the flame tip is expected to be closely related to the mixture Lewis number *Le*. In the present case, flames displaying the open cone pattern are all characterized by Lewis numbers lower than unity which is manifested through a burning intensity decrease at the flame tip eventually leading to local extinction. This reduction in burning intensity is evident on the chemiluminescence images (see Figure VI.9). The flame tip opening has been previously observed for premixed flames including: rich propane and butane/air flames in [237-238] (also with diluents in ref. [239]), hydrogen/air flames in ref. [238] (also with diluents in ref. [239]), nitrogen-diluted methane and propane/air flames [240] as well as laminar diffusion flames of hydrogen/propane/air + inerts [241]. All aforementioned experimental studies showed a qualitative agreement with the non-unity Lewis number interpretation with tip weakening and eventually local extinction for mixtures with $Le < 1$ and enhancement of the tip burning intensity for mixtures with $Le > 1$. It is interesting to notice that according to the present experimental results, the flame tip opening of hydrogen/air flames arise on the lean side at E.R. ≈ 0.85-0.9 while ref. [238-239] reported a value located in the rich domain (E.R.≈ 1.1-1.15). A detailed review of the experimental apparatus used in ref. [239] indicates that, as compared to the present study, a smaller burner was used (3 mm I.D.), suggesting that the flame tip opening phenomenon is not uniquely appearing at a fixed equivalence ratio but also depends on flame geometrical parameters, such as the strength of the flame apex curvature, itself depending on the burner diameter and inlet flow rate. This flame tip opening phenomenon might represent a serious drawback for flame speed-related experiments since it would be reasonable to expect fuel leakage at the flame apex, and therefore, incomplete combustion. The latter hypothesis is questioned in the numerical study of Kozlovsky and Sivashinsky [242] who found that Bunsen flames characterized by low Lewis numbers are not necessarily subjected to fuel leakage at the tip and that the fuel is usually entirely consumed. In the present experiments, open tip flame cases were also analyzed and corresponding flame speed computed from truncated flame borders. These results should however be carefully considered since, for these weakly burning flame tips, the flame apex luminosity is strongly depending on the horizontal knife edge location and thus, ends of the flame borders close to the extinction region are left to the experimenter's own judgment.

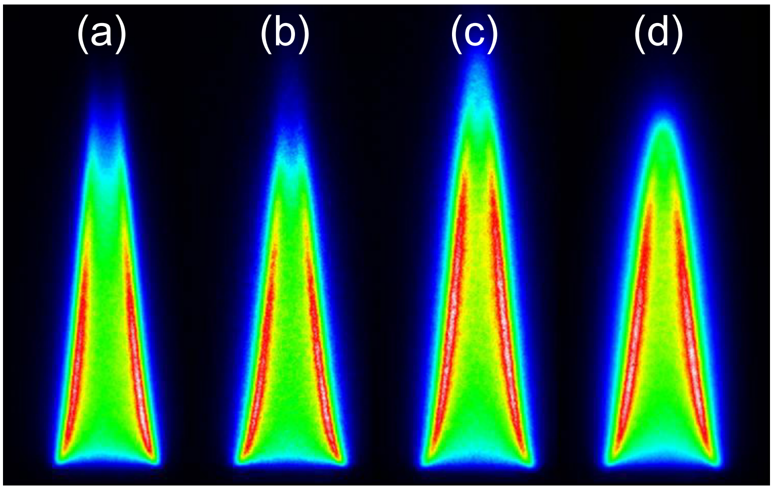

Figure VI.9 Syngas flames stabilized on the 4 mm I.D. straight tube burner (E.R.=0.6). Flame fuel compositions are respectively: 100 % H_2 (a) and 80/20 % (b), 60/40 % (c) and 40/60% (d) H_2/CO.

The flame surface area methodology has been first validated by investigating laminar flame speeds of various H_2/air mixtures with equivalence ratios ranging from 0.45 to 1.2. Measured flame speeds are compared in Figure VI.10 to results of the literature along with predictions calculated with the PREMIX code [27] and the mechanism of Li et al. [223]. Both open and closed tip flames are considered.

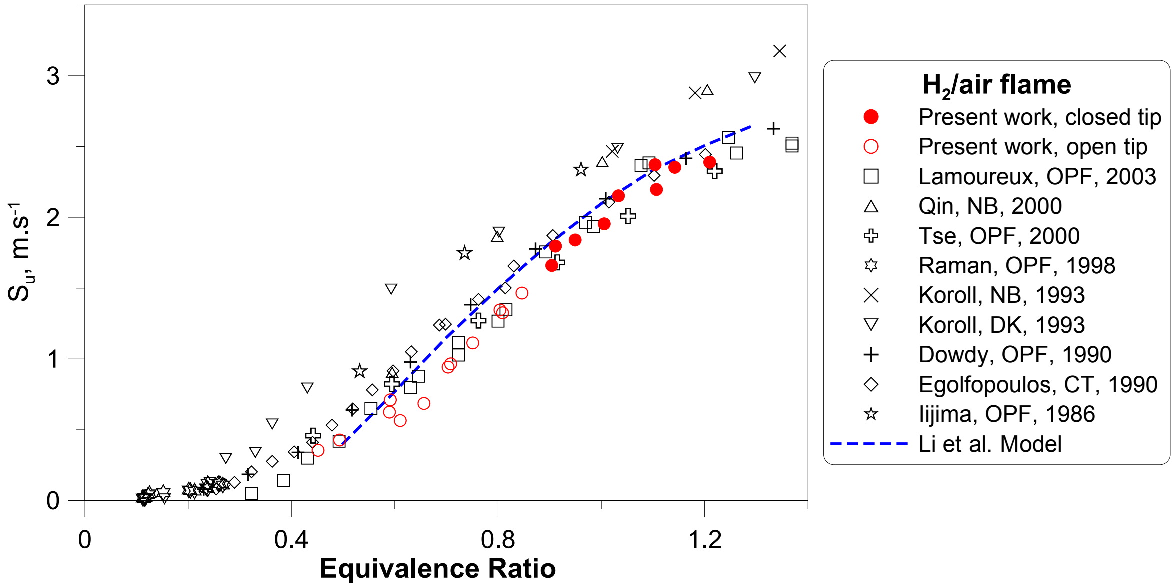

Figure VI.10 Validation of the OH* chemiluminescence methodology through comparison with experimental and numerical results for laminar flame speeds of H_2/air mixtures (Burner I.D.=4 mm). Experimental results are from Lamoureux [243], Qin [244], Tse [245], Raman [246], Koroll [247], Dowdy [248], Egolfopoulos [64], Iijima [174]. Model from Li et al. [230] (OPF: Outwardly Propagating Flame, NB: Nozzle Burner flame, DK: Double-Kernel flame, CT: Counterflow flame).

Important disparities among experimental results can be noticed. The works of Qin et al. [244], Koroll et al. [247] and Iijima et al. [174] yield flame speeds up to 50 cm.s^{-1} higher than the remaining datasets. Present results show an excellent agreement with the recent measurements of Lamoureux and coworkers [243] in the outwardly propagating flame configuration. If the agreement is also very good with datasets of Tse et al. [245], Dowdy et al. [248] and Egolfopoulos et al. [64] for flames with closed tips (E.R.= 0.7→ 1.2), results obtained for open flame cones are lower than aforementioned datasets. Although systematically lower, our measurements are also close to computations using the mechanism of Li and coworkers [223]. The overall good agreement of present results with the literature data as well as numerical predictions confirm the validity of the OH* chemiluminescence methodology.

As explained earlier, the latter has been applied to various H_2/CO blends. Laminar flame velocities of syngas mixtures with compositions ranging from 5/95 to 70/30 % H_2/CO are presented Figure VI.11. Apart from Fig. (c), results seem to indicate that measured flame speeds do not display any dependence with the burner tube diameter and that maximum discrepancies between measurements for the same mixtures but different burner I.D. are generally kept under 10 cm.s^{-1}. The abnormal important increase of flame speeds observed in Fig. (c) for the 4 mm burner I.D. is unclear. A general observation is that the laminar flame speed roughly displays a linear increase with equivalence ratio for all mixture compositions presented herein. If the use of the pilot flame considerably reduces the achieved equivalence ratio ranges, it has however a non-negligible effect on the flame since overlapped cases with and without pilot flame do not yield the same flame speed value, the pilot flame one being systematically higher (for instance, +6.7 $cm.s^{-1}$ for the 50/50 % H_2/CO mixture at E.R.=0.62 and +9$cm.s^{-1}$ for the 30/70 % H_2/CO mixtures at E.R.=0.65).

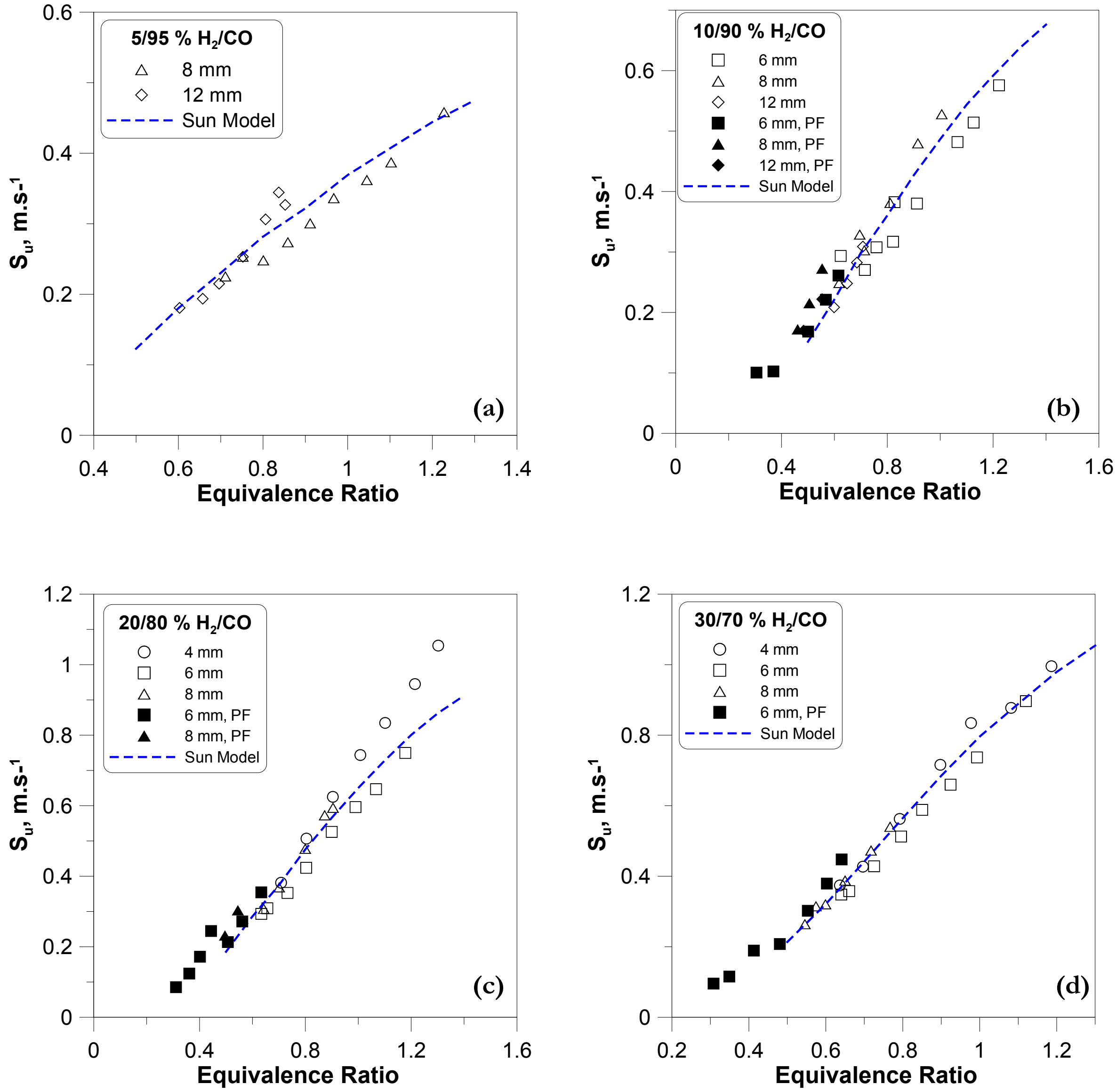

(Figure caption on the next page)

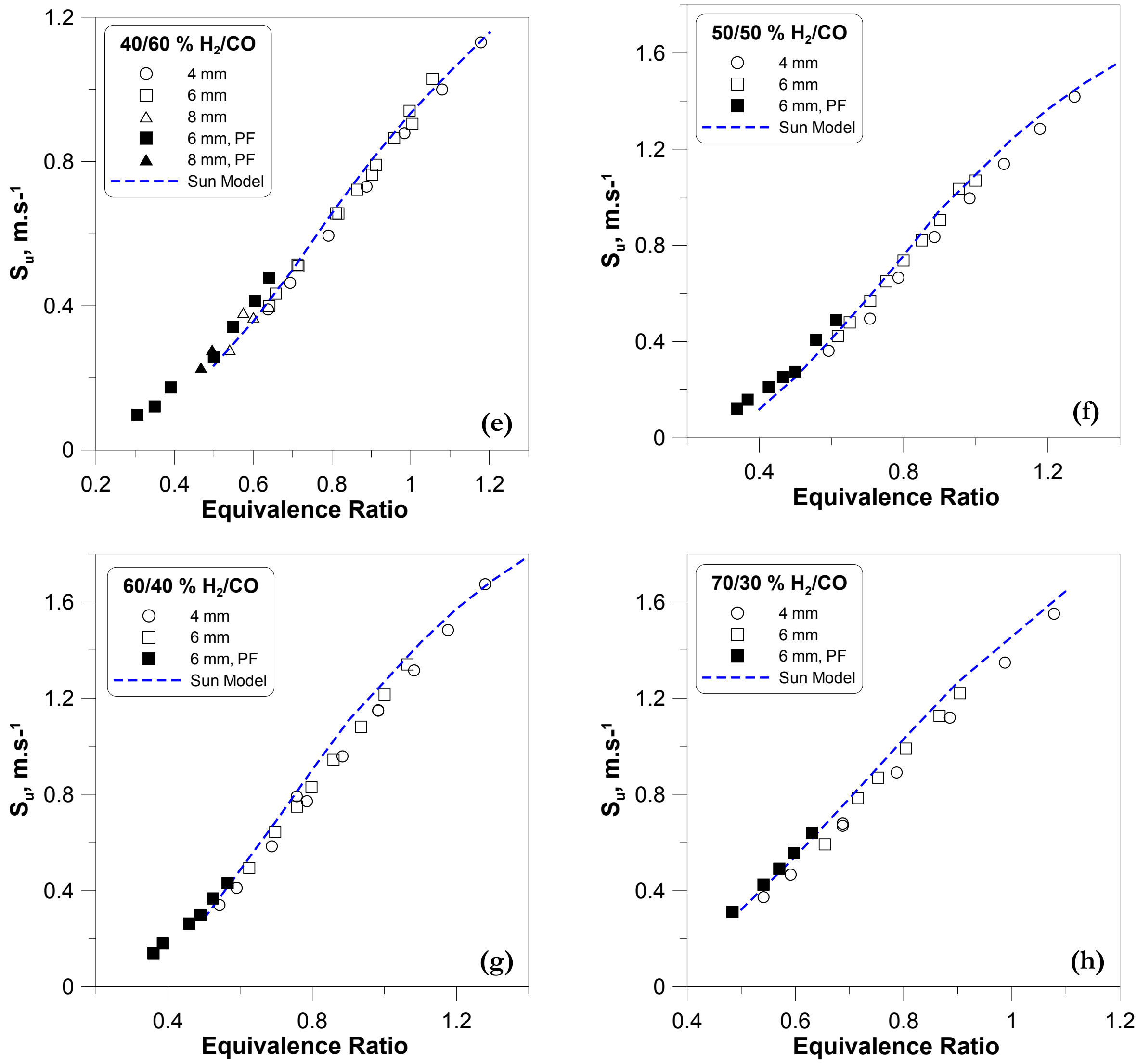

Figure VI.11 Laminar flame speed measurements for various syngas H_2/CO blends and burner internal diameters: (a) 5/95 %, (b) 10/90 %, (c) 20/80 %, (d) 30/70 %, (e) 40/60 %, (f) 50/50 %, (g) 60/40 % and (h) 70/30 % (Burner I.D.: 4, 6, 8 and 12 mm, Model from Sun et al. [200], PF: Pilot Flame). Results for flames with the open tips are not included.

Laminar flame speed of CO mixtures with small H_2 additions are shown in Figure VI.12. It is seen that mechanisms predictions capture fairly well the non-linear velocity increase with H_2 addition. Apart from the 5% H_2 case, measurements reported in the literature are rare, especially for the range 1 to 3 % that displays the maximum sensitivity to hydrogen addition. Note here that our measurements at 1 % closely agree with mechanism predictions.

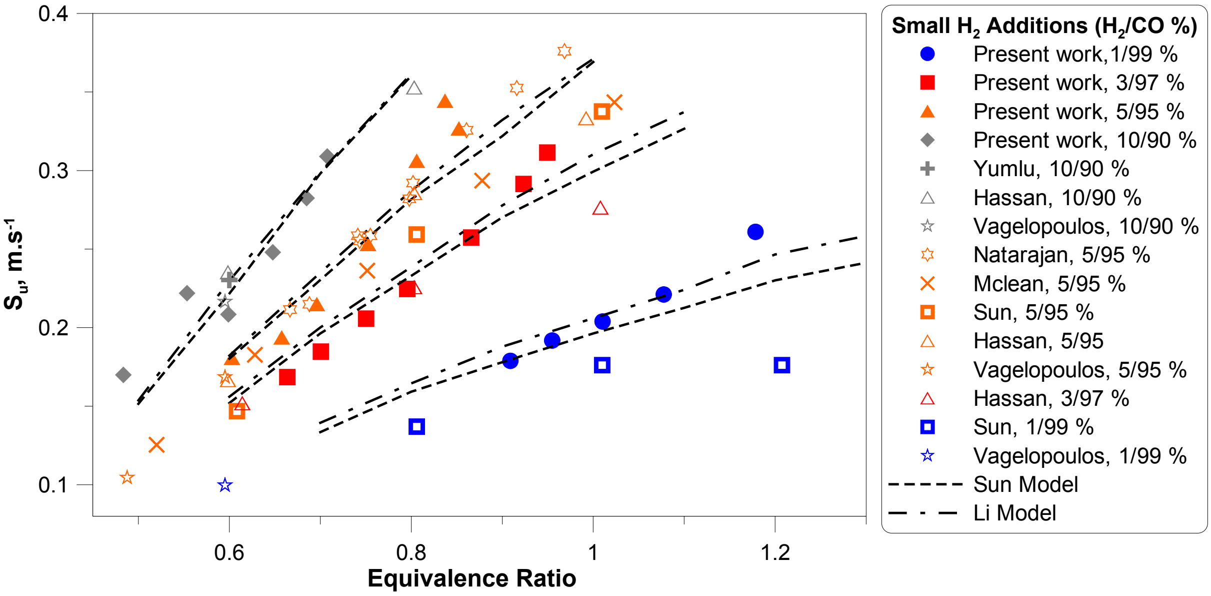

Figure VI.12 Laminar flame speeds of CO mixtures with small additions of H_2. Mixtures blends (H_2/CO %) are: 1/99 % (blue), 3/97 % (red), 5/95 % (orange) and 10/90 % (gray). Experimental data points are from Yumlu [207], Hassan [198], Vagelopoulos [70], Natarajan [211], McLean [199] and Sun [200]. Models are from Sun [200] and Li [230].

Comparison of both Chemiluminescence and Schlieren technique is provided in Figure VI.13. For all cases presented herein, the Schlieren technique leads to higher flame speed measurements up to 27% (Fig. a, E.R.=0.6) as compared the flame surface area method. This discrepancy can be reduced (≈ 9%) if the burner diameter is increased (Fig. b and c) and if higher flow rates are used (Fig. c). These observations strongly suggest that the direct calculation of U_0 from the total flow rate and burner area is inaccurate and that boundary layer effects are not negligible in this case. A local flow velocity measurement ahead of the flame would therefore be necessary to accurately evaluate the corresponding U_0 velocity. As such, the OH* chemiluminescence technique was preferred since it has been found that comprehensive results could be obtained independently of the burner diameters, without the use of complex velocimetry diagnostics.

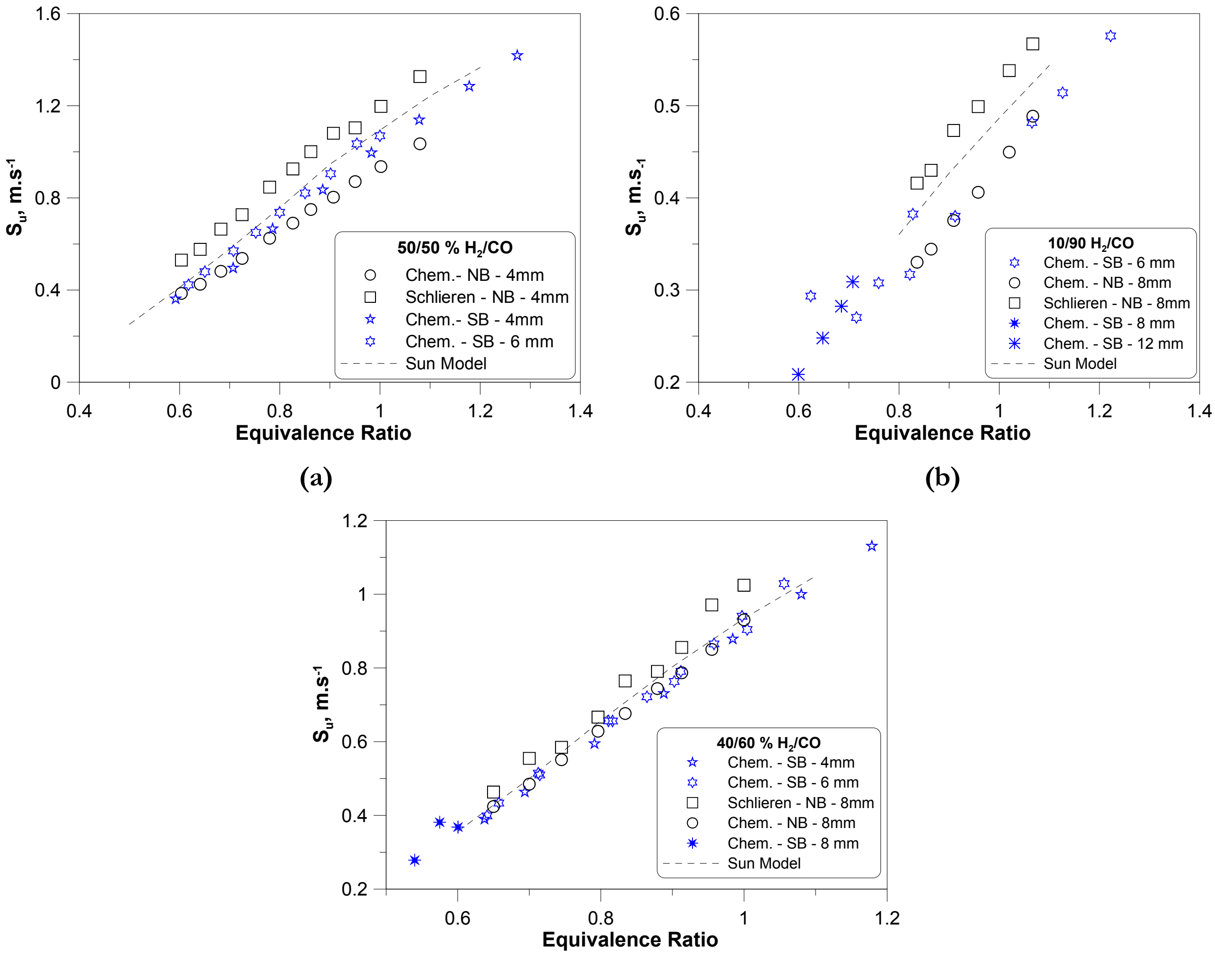

(a)

(b)

(c)

Figure VI.13 Comparison of the flame surface area (OH* chemiluminescence maximum intensity trace) and the cone angle (Schlieren) approaches for various syngas flames: (a) 50/50 %, (b) 10/90 %, (c) 40/60 % H_2/CO (Chem.: Chemiluminescence, NB: Nozzle Burner, SB: Straight Burner).

VI.3 PART II: The Outwardly Propagating Flame Approach

VI.3.1 Combustion Chamber Setup

The apparatus used in the present investigation is identical to the one presented in ref. [249]. The combustion vessel is a 24.32 L stainless steel cylindrical chamber (160 mm I.D., 300 mm height). Two sharpened-edge tungsten electrodes (base diameter: 1.2 mm) linked to a conventional capacitive discharge ignition system are used to provide the ignition energy. The latter can be changed by inputting a user-defined charging time, kept between 300 to 4000 µs for the present investigation. This charging time was adapted for each mixture of interest and trial tests were performed before experimental series to ensure that the ignition energy was close to the minimum one. Note that here the electrode plane is slightly tilted with respect to the plane of observation to avoid the recording of slight disturbances inherent to the ignition process. The spark gap could be varied and was usually set between 1 and 2 mm. The volumes of each individual mixture component (H_2-CO-Air) are sequentially injected in the combustion chamber thanks to dedicated Brooks 5850S thermal mass flow controllers (See Table V.3 for additional specifications) digitally piloted through a Labview program via a RS232 serial port. Gas volumes delivered by the flow controllers were periodically checked with an ACTARIS© wet meter (Measuring uncertainty 0.5%) and were found to be within 1.2% of the input values. The pressure and the temperature inside the chamber are measured thanks to a piezoelectric transducer and a type K thermocouple respectively. A fan located inside the vessel is ensuring a homogeneous mixing of reactants prior to ignition. Note here that efforts towards the minimization of stainless steel part of the CO delivery lines are reiterated. A CO SWAGELOK KCY regulator is used and the entire gas delivery network is made of Teflon tubing.

VI.3.2 Shadowgraph Diagnostics

Optical access to the chamber is provided through two opposite portholes (105 mm diameter). A continuous Stabilite 2017 argon ion laser (6W, λ = 457.9-514.5 nm) along with two planoconvex lenses ($L_1 \rightarrow d_1 = 15$ mm, $f_1 = 25$ mm; $L_2 \rightarrow d_2 = 70$ mm, $f_2 = 1000$ mm) are used to create the parallel light beam that crosses the combustion chamber. A transparent screen located at its back allows for the display of the shadowgraph images. Shadowgrams of outwardly propagating flames are recorded using a high speed CMOS APX camera operating at 6000 and 15000 frame/s for 512×512 and 256×256 pixel size frames respectively. The shutter speed is fixed at 1/40000 s. The spatial resolution achieved is close to 135 μm/pixel. The entire setup is shown in Figure VI.14.

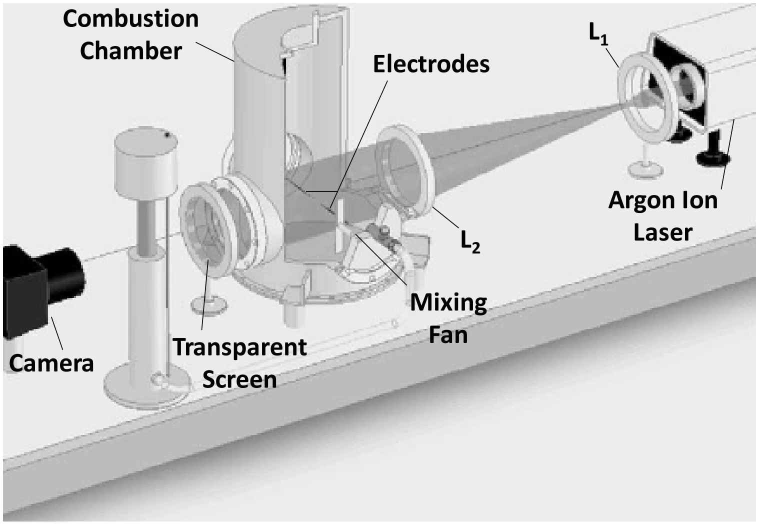

Figure VI.14 Schematic of the combustion chamber and shadowgraph system.

VI.3.3 Protocol for Data Acquisition

Prior to each run, the pressure and temperature were measured and a vacuum was created inside the combustion chamber. The stirring fan was activated and the mixture components were then sequentially introduced until complete filling. Note here that the sequential filling operation allows for the direct verification of the component partial pressures and thus any deviation from the input volumes could be easily detected. The fan was then stopped and pressure and temperature were measured again.

The initial pressure and temperature conditions were kept in the ranges of 1.04 ±0.035 bar and 295.3 ±3.7 K respectively. Few minutes were left before igniting the combustible mixture to make sure that quiescent flow conditions were achieved. The ignition sequence was then triggered and the flame front propagation evolution was recorded thanks to the synchronized high speed camera. 20 to 30 minutes were typically left between each run to allow for the cooling of the chamber walls.

VI.3.4 Data Processing

Figure VI.15 displays the temporal evolution of a 25/75 % H_2/CO flame front (E.R.=0.6). It is seen that the flame propagation is spherical starting from small radii (see t = 2ms) to larger ones (see t = 12 ms). A conventional assumption to simplify the flame front processing step is that the development of such flames is perfectly spherical and hence, flame fronts can be fitted by equations of a circle. This approach has been adopted by Tahtouh and coworkers in ref. [249]. Their flame edge detection program is here applied to the present shadowgraph images. This program is successively performing: i/ a background subtraction to enhance the flame front detection; ii/ a flame edge detection based on the maximum intensity of the flame front. Note that since shadowgrams respond to the second derivative of the refractive index n, i.e. $\partial^2 n/\partial x^2$ [250], the luminous outer part is located closer to the unburned side which is also the case for selected pixels of maximum intensity; iii/ the luminous edge best fit by performing an optimization algorithm based on the minimization of the distance between detected points and points belonging to the potential solution. Figure VI.16 shows a spherical flame front with its superimposed best fit (red circle). These processing steps are repeated for all recorded shadowgrams allowing for the extraction of the temporal evolution of the flame radius. Examples of such evolutions are given in Figure VI.17 for various equivalence ratios. It is seen that for the lean and moderately rich cases (E.R.=0.6, 1.0, 2.0) linear trends are observed. For the richest case (E.R.=5.0), a slower flame radius increase is observed during an initial phase of the flame propagation (up to t = 7 ms) but a linear trend is recovered in the later stages of the flame evolution. This observation is coherent with experimental and numerical works of Chen and coworkers [251]. The latter investigation showed that for mixtures with large Lewis numbers, the ignition energy as well as initial transient flame evolution have a significant impact on early flame trajectories. It was indeed demonstrated that for H_2/air mixtures at E.R.=4.5, the range for which the flame propagation velocity displays a linear dependence with stretch is drastically reduced as compared to mixtures with lower *Le*. Similar observations were reported by Kelley and coworkers [252] for hydrogen/air and butane /air flames at atmospheric and elevated pressures.

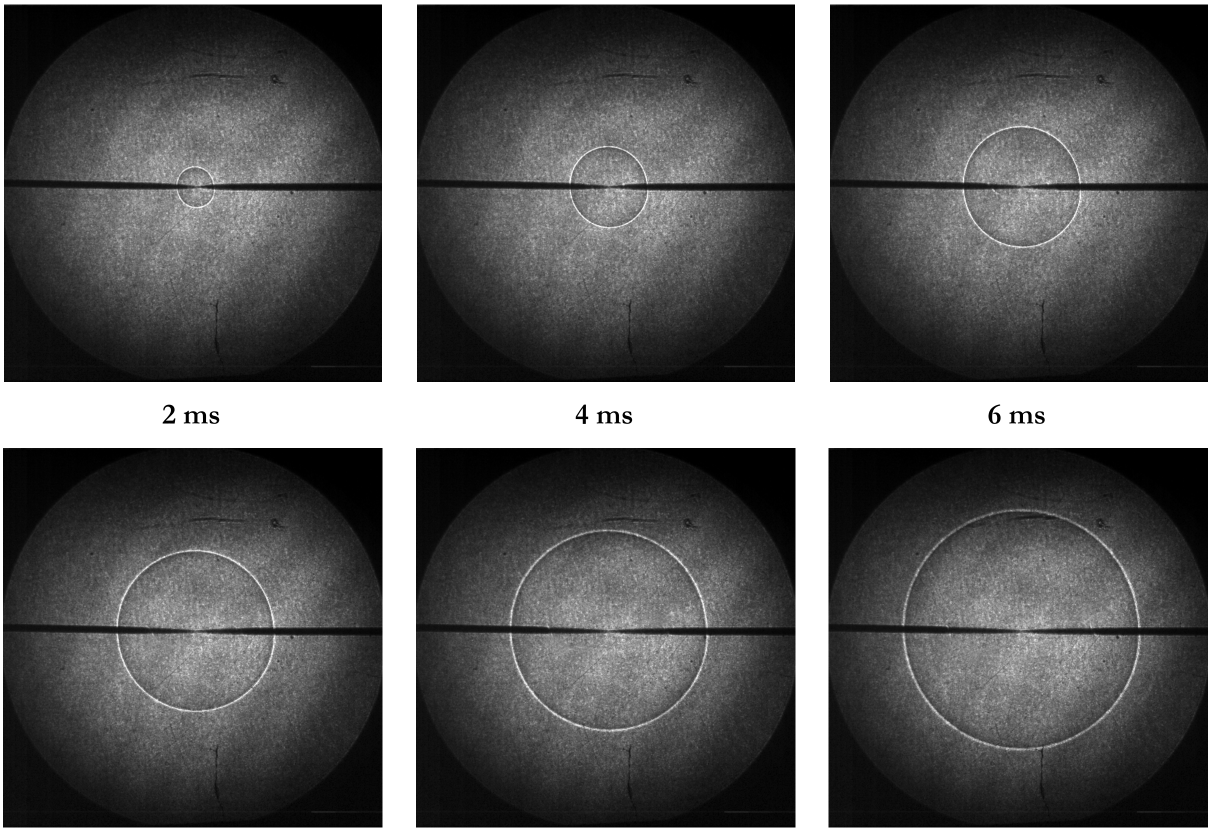

2 ms **4 ms** **6 ms**

8 ms **10 ms** **12 ms**

Figure VI.15 Temporal evolution of the flame front (25/75 % H_2/CO, E.R.=0.6, P=0.1 MPa, T = 300 K, 6000 images/s).

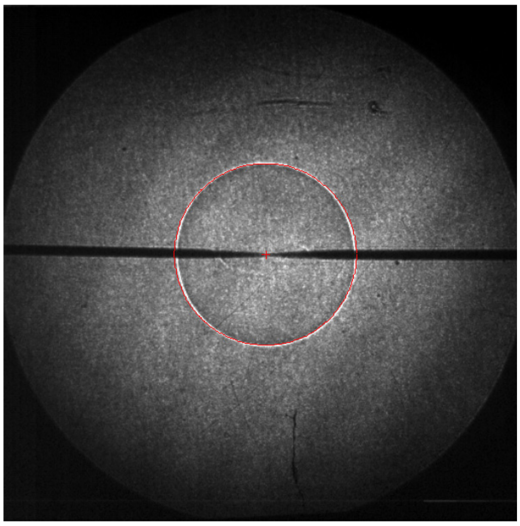

Figure VI.16 Illustration of the flame front edge detection (in red, circle best fit).

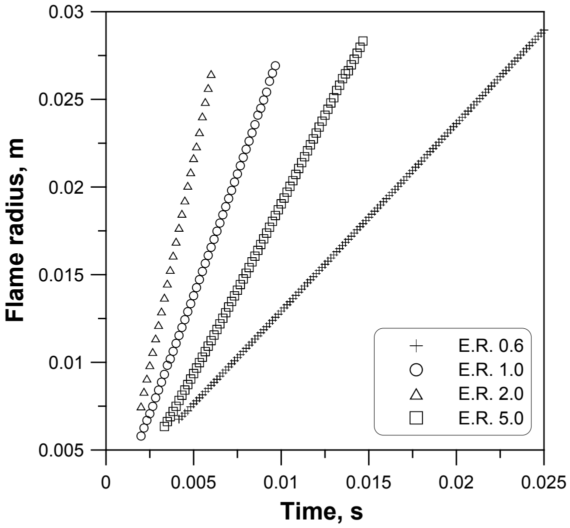

Figure VI.17 Temporal evolution of flame radii for different equivalence ratios (10%H_2 – 90% CO)

Similarly to the conventional counterflow technique, the classical outwardly propagating flame approach assumes that a linear relationship between the stretched propagation flame speed S_b and the applied stretch rate K exits. Such a relation between the flame speed and the magnitude of the flame front curvature was originally formulated in the pioneer works of Markstein [15] and further generalized in later theoretical and numerical studies [59, 253-254] for all stretch contributions (see Chapter I):

$$S_b = S_b^0 - L_b K \tag{VI-3}$$

with S_b^0, the unstretched propagation flame speed and L_b, the Markstein length for burned gases. The stretched propagation flame speed is related to the flame front radius as follows:

$$S_b = \frac{dr}{dt} \tag{VI-4}$$

It has been generally recognized that the flame stretch encompasses the combined effects of aerodynamic straining, curvature and flame motion [255]. Various forms for the expression of the stretch rate have been proposed in the past (See for instance [12-14]) and stretch rate expressions relevant to the classical flame configurations have been derived [13, 255]. In the case of the outwardly propagating flame configuration, the following stretch rate formulation, encompassing both flow straining and curvature effects, is conventionally used for spherically symmetric flames:

$$K = \frac{1}{A}\frac{dA}{dt} = \frac{2}{r}\frac{dr}{dt} \tag{VI-5}$$

with A, the flame surface. Temporal evolutions of the flame radii, as shown in Figure VI.17, can be used to yield the (K ; S_b) pairs and perform (in a simple approach!) a conventional linear regression to extract both the unstretched flame propagation speed S_b^0 and the Markstein length of burned gases L_b. In the case of a flame expansion at constant pressure, the laminar burning velocity S_u^0 is then deduced from the unstretched propagation flame speed using the burned to unburned gas density ratio:

$$S_u^0 = \frac{\rho_b}{\rho_u} S_b^0 \tag{VI-6}$$

with ρ_b, the density of burned gases and ρ_u, the density of unburned gases. This ratio is usually computed using classical programs such as EQUIL [256], allowing for the calculation of chemical equilibrium states.

A crucial point of the data processing step is the methodology used to extract both S_b^0 and L_b. Various methodologies have been proposed in the literature including for example: i/ the polynomial fitting of the temporal evolution of the flame front radius, followed by adequate differentiations; ii/ the direct optimization (with respect to the raw radius data points) of an integrated form of the flame front equation of motion, obtained combining both (VI-3) and (VI-5). Both methodologies are discussed in detail in the works of Tahtouh et al. and ref. [249] should be consulted for further information. In the present investigation, two different approaches have been tested:

- The recent linear extrapolation methodology proposed by Tahtouh and coworkers [249] based on the exact analytical solution of the differential equation of the flame front temporal evolution. It was demonstrated that this methodology yields an enhanced robustness and improved accuracy as compared to conventional linear processing schemes.

- The non-linear extrapolation methodology described by Kelley and Law in ref. [121], based on the integration of a non-linear expression of the stretched-affected flame propagation, originally proposed by Ronney and Sivashinsky [257]. The development of this approach was motivated by the apparent non-linearity of flame propagation velocities at higher stretch. This methodology was shown to provide an enhanced accuracy for the determination of fundamental flame speeds as compared to the conventional linear approaches, especially for nonequidiffusive mixtures. It is therefore of a prime interest to use this formulation for our H_2/CO mixtures, for which *Le* numbers are departing from unity as the H_2 content increases (See Table V.5).

  Both formulations are addressed below.

The Linear Formulation

For sake of clarity, the main steps of the linear methodology introduced in ref. [249] are recalled. Combining equations (VI-3) and (VI-5) yields the following expression:

$$\frac{dr}{dt} = S_b^0 - 2L_b \frac{1}{r}\frac{dr}{dt} \tag{VI-7}$$

The analytical solution of the differential equation (VI-7) is provided by:

$$r(t) = 2L_b W_0(Z) \tag{VI-8}$$

with *W*, the Lambert or Omega function, defined as the inverse function of $f(W) = We^W$, and *Z* defined as follows:

$$Z = \frac{e^{\frac{S_b^0 t + C_1}{2L_b}}}{2L_b} \tag{VI-9}$$

with C_1 a constant to be determined. The parameters S_b^0, L_b and C_1 can be found during an optimization process aiming at minimizing the following equation:

$$\sum_1^N \left(r_{original}\ (t) - r(t)\right)^2 = \sum_1^N \left(r_{original}\ (t) - 2L_b W_0(Z)\right)^2 \tag{VI-10}$$

with $r_{original}$, the experimental flame front radius at the time *t*, and *N*, the number of processing time steps. Note that here, expression (VI-8) can be differentiated to yield the stretched propagation flame speed S_b and its corresponding stretch rate *K*.

The Non-Linear Formulation

The non-linear methodology used in ref. [121] is recalled. The non-linear expression linking both the flame propagation velocity and the stretch rate is given by:

$$\left(\frac{S_b}{S_b^0}\right)^2 ln\left(\frac{S_b}{S_b^0}\right)^2 = -\frac{2L_b K}{S_b^0} \tag{VI-11}$$

Integrating (VI-11) leads to:

$$t = A^* \left[E_1(\ln \varepsilon^2) - \frac{1}{\varepsilon^2 \ln \varepsilon} \right] + C \tag{VI-12}$$

with A, E_1 and C being defined as:

$$A^* = \frac{2L_b}{S_b^0}\ , \qquad r = -\frac{2L_b}{\varepsilon \ln \varepsilon}\ , \qquad E_1(\varepsilon) = \int_{\varepsilon}^{\infty} \frac{e^{-z}}{z} dz \tag{VI-13}$$

with the variable $\varepsilon \in [1/e, 1[$ for $L_b > 0$ and $\varepsilon \in [1, \infty[$ for $L_b < 0$. Expression (VI-12) is used to perform constrained non-linear least square regression to find the three constants A^*, L_b and C. Recent investigations of Halter and coworkers [258] reported that the convergence of such an optimization process is difficult and highly dependent on initial estimates provided for the constant parameters S_b^0 and L_b. They recommended the calculations of "accurate" estimates by minimizing the following sum:

$$\sum_{1}^{N} \left| \left(\frac{S_b}{S_b^0}\right)^2 \ln \left(\frac{S_b}{S_b^0}\right)^2 + \frac{2L_b K}{S_b^0} \right| \tag{VI-14}$$

Obtained S_b^0 and L_b values were further used as input parameters for the iterative optimization procedure required in the methodology of Kelley and Law [121]. Note that extrapolation routines developed by Halter et al. [258] are used in the present investigation. Figure VI.18 illustrates aforementioned linear and non-linear extrapolation procedures on data points of a stoichiometric 10/90 % H_2/CO syngas mixture. It is seen that the non-linear extrapolation yield an unstretched flame propagation speed lower by 3.2 cm.s^{-1} as compared to the linear one. This difference is expected to increase for stronger nonequidiffusive mixtures as suggested by experimental results of Kelley and Law [121], for which discrepancies above 20 cm.s^{-1} were observed for a n-butane/air mixture at E.R.=0.8.

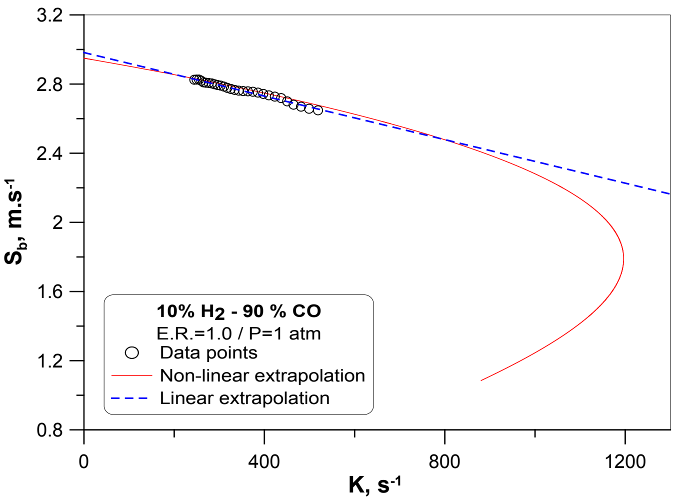

Figure VI.18 Example of the linear and non-linear extrapolation methodologies performed on experimental data points of a 10/90 % H_2/CO flame propagation speed evolution with stretch (E.R.=1.0).

VI.3.5 Data Uncertainty Analysis

During the present investigation, experimental runs were repeated 3 times in average. The corresponding standard deviations were found to be in a 0.09 to 7.82 cm.s^{-1} range. They are plotted in the form of vertical error bars in the following graphs.

VI.3.6 Results and Discussion

All measurements presented in this section were obtained using the non-linear methodology unless otherwise stated. It was generally found that both methodologies yielded the same laminar burning velocities, apart from specific cases that will be discussed later in this chapter.

The summary of flame speed measurements for all investigated syngas/air mixtures is presented in Figure VI.19 along with the predictions calculated with the Li mechanism [230]. It is seen that calculations generally overpredict the measurements up the curve extrema. The agreement is good for both 5/95 % and 10/90% H_2/CO mixtures for the very rich branch but measurements are higher than predictions for both 25/75 % and 50/50 % H_2/CO cases. The maximum difference is obtained for the 25/75 % composition at E.R.=5 with 17.6 cm.s^{-1}. Measurements for each individual composition are further compared to available results of the literature in the outwardly propagating flame configuration in Figure VI.20, Figure VI.21, Figure VI.22 and Figure VI.23.

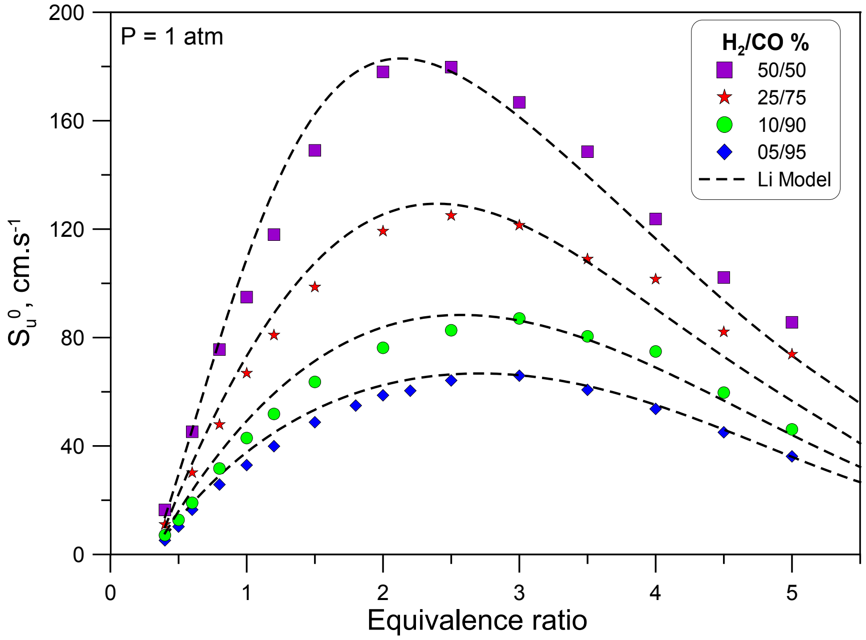

Figure VI.19 Results summary for laminar flame speeds of syngas mixtures determined in the outwardly propagating flame configuration with the non-linear methodology.

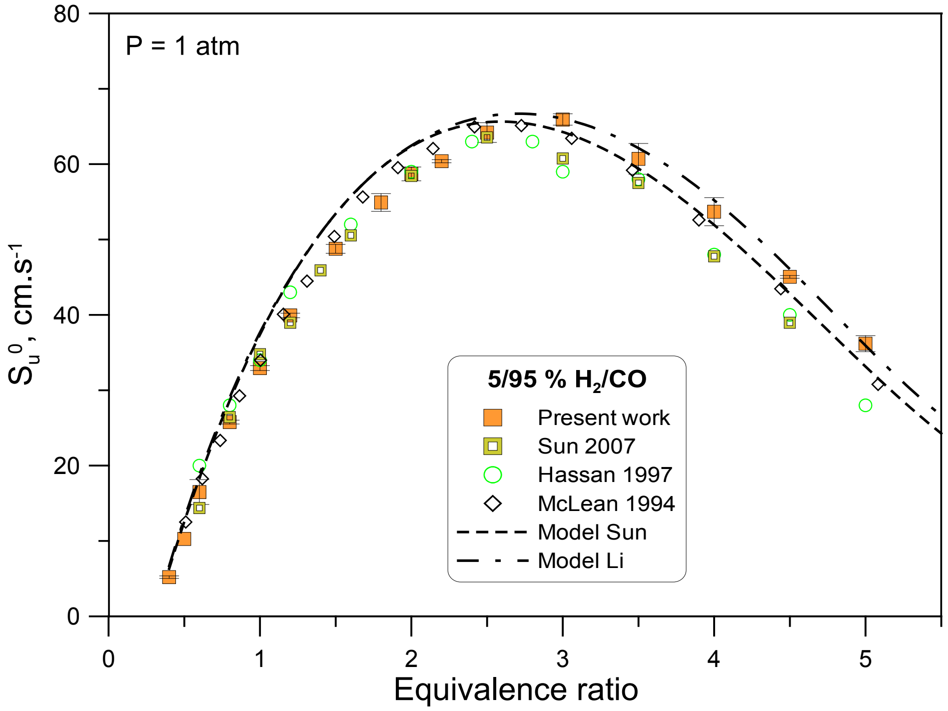

Figure VI.20 Laminar flame speeds of 5/95 % H_2/CO mixtures. Comparison with experimental datasets from Sun [200], Hassan [198], Mclean [199] and numerical predictions with the kinetic mechanisms of Sun [200] and Li [230].

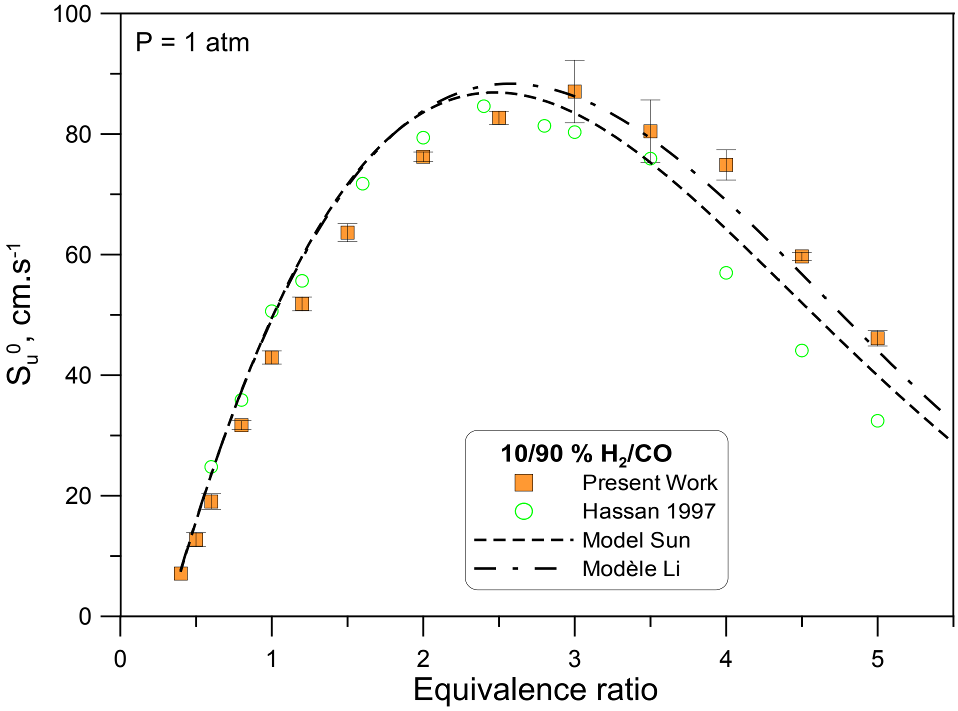

Figure VI.21 Laminar flame speeds of 10/90 % H_2/CO mixtures. Comparison with the experimental dataset of Hassan [198] and numerical predictions with the kinetic mechanisms of Sun [200] and Li [230].

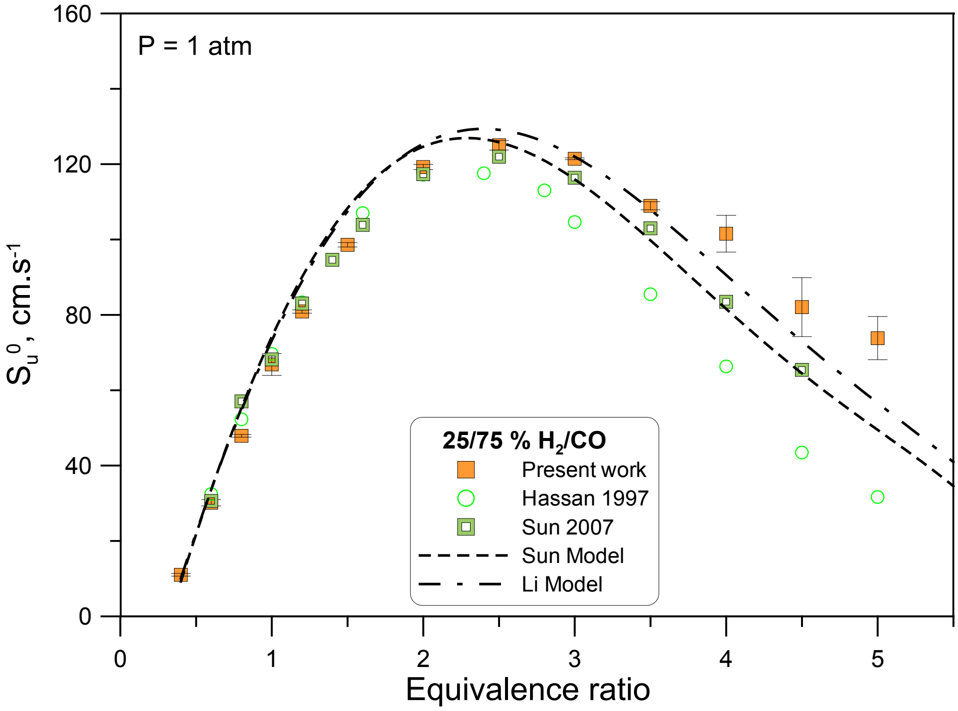

Figure VI.22 Laminar flame speeds of 25/75 % H_2/CO mixtures. Comparison with experimental datasets from Sun [200], Hassan [198] and numerical predictions with the kinetic mechanisms of Sun [200] and Li [230].

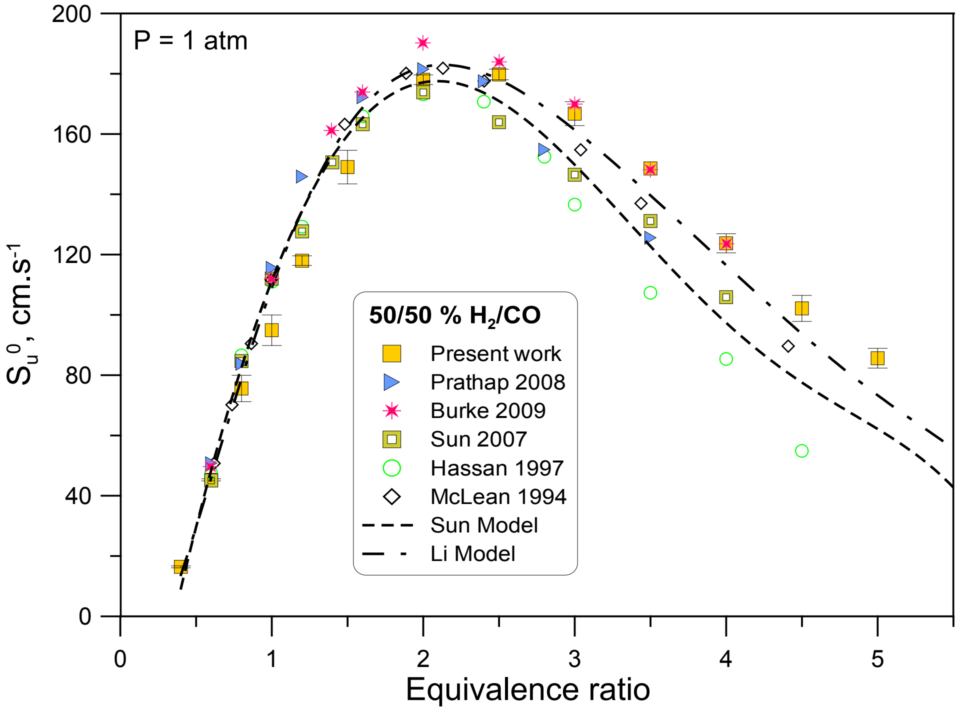

Figure VI.23 Laminar flame speeds of 50/50 % H_2/CO mixtures. Comparison with experimental datasets from Prathap [212], Burke [177], Sun [200], Hassan [198], McLean [199] and numerical predictions with the kinetic mechanisms of Sun [200] and Li [230].

For the 5/95 % H_2/CO case (Figure VI.20), the agreement is good for all series up to E.R.=2.5. Note that on the E.R. range 0.4-2.5, predictions given by the Li et al. [230] and Sun et al. [200] mechanisms seem to slightly overpredict all measurements. However disparities can be noticed on the rich side with lower velocities for both Sun et al. [200] and Hassan et al. [198] results with higher values given by the present investigation. Measurements reported by McLean and coworkers lay in an intermediate range. Notice here that results of the present investigation find an excellent agreement with computations using the mechanism of Li et al. [230] for the very rich cases (E.R.=4.5-5.0). A maximum discrepancy of 8.2 cm.s^{-1} is obtained at E.R.=5.0 between our results and those of Hassan et al. [198].

Disparities are further increased among experimental series for the 10/90 % H_2/CO case (Figure VI.21). If present results are still overestimated on the lean side up to E.R.=2.5, they do find a good agreement with predictions of the Li et al. mechanism [230]. Measurements of Hassan and coworkers [198] lay significantly lower than the present results with a maximum decay of 20.1 cm.s^{-1} obtained at E.R.=4.0.

The same observations hold for the 25/75 % H_2/CO case (see Figure VI.22) with an excellent agreement among experiments up to E.R.=2.0. Above, important differences can be seen for the three sets of measurements including the present one. Lowest velocities are found by Hassan and coworkers [198] and highest are given by the present investigation. The excellent agreement between measurements and numerical predictions of Sun et al. [200] is not surprising since their mechanism partly relies on their own measurements. Notice that results of the present works are, for the rich branch, higher than predictions obtained with the Li et al. [230] mechanism. At E.R.=4.5, we have $(S^{0}_{u\,\mathrm{HASSAN}} = 41\ \mathrm{cm.s^{-1}}) < (S^{0}_{u\,\mathrm{SUN}} = 65.4\ \mathrm{cm.s^{-1}}) < (S^{0}_{u\,\mathrm{PRESENT\ WORK}} = 82.1\ \mathrm{cm.s^{-1}})$.

Figure VI.23 shows the results obtained for the 50/50% H_2/CO mixtures. A good agreement can be seen for the very lean side, but some deviations occur for E.R.=1.0-1.5. On this range, present measurements give the lowest velocities as compared to Prathap et al. [212] and Sun et al. [200] datasets. The rich branch is still characterized by important disparities, especially between the present results and the data points of Hassan and coworkers [198] for which a 46.1 cm.s^{-1} difference at E.R.=4.5 can be observed. However, an excellent agreement is found between results of the present work and the recent measurements of Burke et al. [177]. Both are however largely underpredicted by the kinetic mechanism of Sun and coworkers [200] and to a lesser extent, by the mechanism of Li et al. [223].

It is important to underline that observed disparities for flame velocities of rich syngas mixtures are out of the range of the technique accuracy and repeatability: i/ the direct methodology accuracy i.e., the expected accuracy for a single measurement, is closely related to the extrapolation procedure employed to yield S^{0}_{b} (see the relevant discussion on the importance of extrapolation parameters for DPIV measurement accuracy in the previous chapter). It is expected to be on the order of few cm.s^{-1}; ii/ the repeatability, deduced from data series performed for the same experimental conditions, is found to be, in average, within a ±2 cm.s^{-1} range for the present experiments. As mentioned earlier, the largest deviation is ±7.8 cm.s^{-1} for the 25/75 % H_2/CO mixture at E.R.=4.5.

In an attempt to explain these important differences, few hypotheses should be reviewed. First, it is important to recognize that the carbonyl hypothesis should be seriously considered since it was established in the previous chapter that disparities between DPIV measurements and other experimental results could be explained by the presence of small amounts (up to 61 ppm) of iron pentacarbonyl in the studied syngas mixture (10/90 % H_2/CO). Moreover, the inhibition efficiency seemed to be enhanced at higher equivalence ratios with a progressive lowering of the rich branch of the velocity curve. Similar trends are observed for the experimental measurements presented in Figure VI.20, Figure VI.21, Figure VI.22, Figure VI.23, which could suggest that lower measurements (in particular those of Hassan and coworkers [198]) are under the influence of carbonyl contamination. Differences among experimental measurements could also be introduced by the processing methodologies developed for laminar flame speed extraction. However details on individual processing procedure used in the various reference cited above are scarce and they do not allow for a complete comparison with the processing approaches chosen in the present investigation. It is however, in our case, of a prime interest to compare both linear and non-linear approaches presented earlier. This is done for the 50/50% H_2/CO mixture in Figure VI.24. Three methodologies are considered for the comparison: i/ the non-linear method proposed by Kelley and Law [121], ii/ the linear method of Halter and coworkers [258] with an initial flame radius $Rf_{initial}$ (the first flame front radius considered in the processing procedure) kept at 8 mm; iii/ the linear method of Halter and coworkers [258] applying their processing criterion $\left|L_b/Rf_{initial}\right| < 0.18$. This empirical criterion recommends that a larger initial flame radius should be used for mixtures with larger Markstein lengths in order to ensure the validity of the linear approach. This is compatible with the conclusions of the investigation of Chen and coworkers [251]. It is seen in Figure VI.24 that almost no difference can be observed between the three approaches on the E.R.=0.4 to 4.0 range. Only flame velocities of very rich mixtures seem to be dependent on the employed methodology. The linear methodology without criterion yields the highest velocity values (110.2 $cm.s^{-1}$ at E.R.=4.5 and 93 $cm.s^{-1}$ at E.R.=5.0), the linear methodology with criterion intermediate ones (105 $cm.s^{-1}$ at E.R.=4.5 and 90.1 $cm.s^{-1}$ at E.R.=5.0) while the non-linear approach gives the lowest velocities (102.1 $cm.s^{-1}$ at E.R.=4.5 and 85.6 $cm.s^{-1}$ at E.R.=5.0). Thus, the extent of flame speed reduction using the non-linear approach compared to the conventional linear one (fixed initial flame radius) is 8.1 $cm.s^{-1}$ at E.R.=4.5 and 7.4 $cm.s^{-1}$ at E.R.=5.0. Note that here cases initially processed with $Rf_{initial}$= 8 mm that will not comply with the criterion of ref. [258] (and thus for which the linear extrapolation is not valid) are easily identified on a map such as the one presented in Figure VI.25. We indeed clearly see that data points at E.R.=4.5 and 5.0 are concerned.

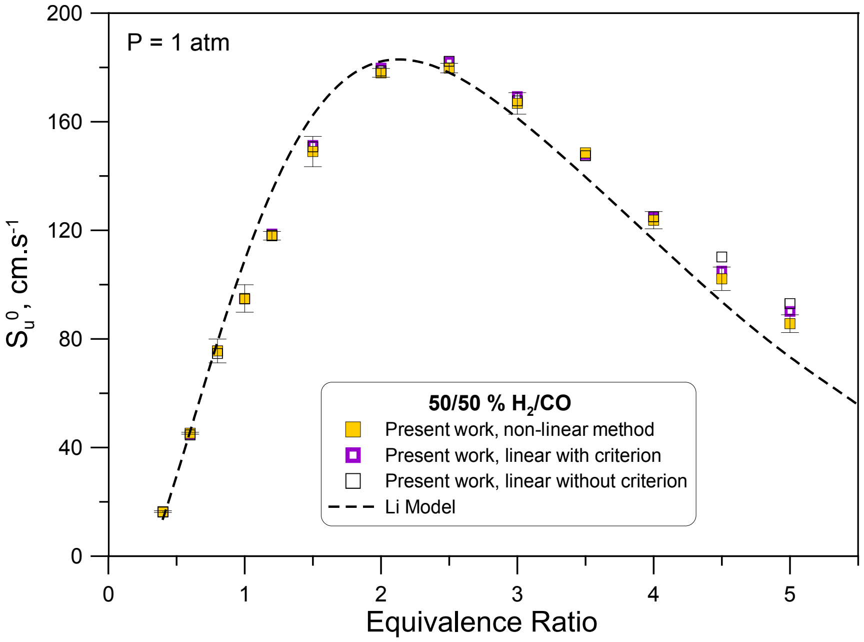

Figure VI.24 Laminar flame speeds of 50/50 % H_2/CO mixtures for the different extrapolation methodologies investigated.

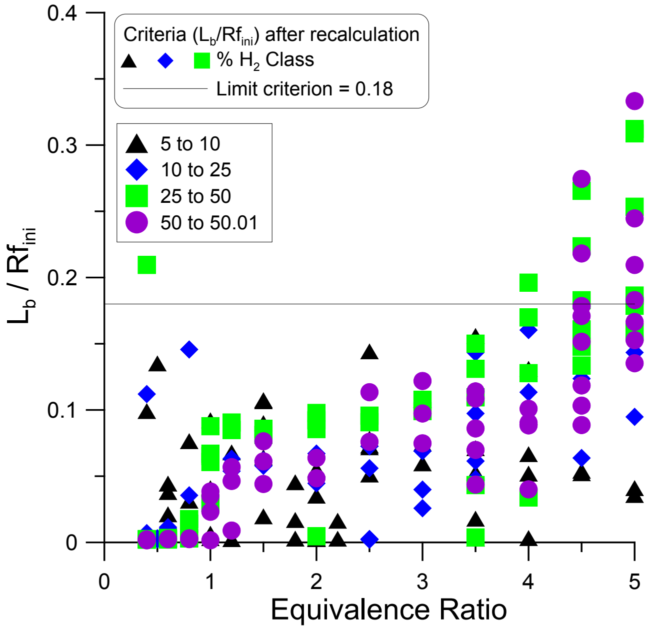

Figure VI.25 Evaluation of the L_b/Rf_{ini} criterion from [258] for experimental runs of the present investigation.

Markstein lengths for the different investigated mixtures are presented in Figure VI.26. Interestingly, all flames generally display a fairly poor sensitivity to stretch. The only exceptions are met for the 25/75 % and 50/50 % H_2/CO flames at E.R.=0.4-0.6 and 0.4-0.8 respectively, for which negative Markstein lengths are observed. This is in apparent contradiction with the effective Lewis number calculations provided in Table V.5 for lean mixtures, for which all L_{eff} numbers are above one. According to these predictions, positive Markstein numbers would have to be expected in these cases. Markstein lengths of the 50/50 % H_2/CO case are further compared to values of the literature in Figure VI.27. If our results are comprehensive with those of Brown et al. [209], Prathap data points [212] display a marked increase, starting at E.R.=2.5 up to 3.5. Our extracted Markstein lengths present a steep decrease in the ultra-lean domain (L_b=-2.9 E.R.=0.4) which needs to be confirmed by additional measurements. However, all datasets compared in Figure VI.27 suggest that Markstein lengths are becoming negative at lower equivalence ratios which in return indicates that mixture Lewis numbers should be under unity. This observation confirm that L_{eff} expressions (V-1) and (V-6), based on the mass fraction weighted average of individual fuel Le numbers, do not accurately describe the actual Lewis number of the investigated H_2/CO/air blends at lean conditions. The mixture L_{eff}' expression (VI-15) based on the mole fraction weighted average of both fuel Lewis numbers (see Figure V.13, square symbols, label: "X_i weighted") seems to yield a better adequacy with Markstein length results presented in Figure VI.26.

$$Le_{eff}' = 1 + X_{H_2}\left(Le_{H_2} - 1\right) + X_{CO}\left(Le_{CO} - 1\right) \qquad \text{(VI-15)}$$

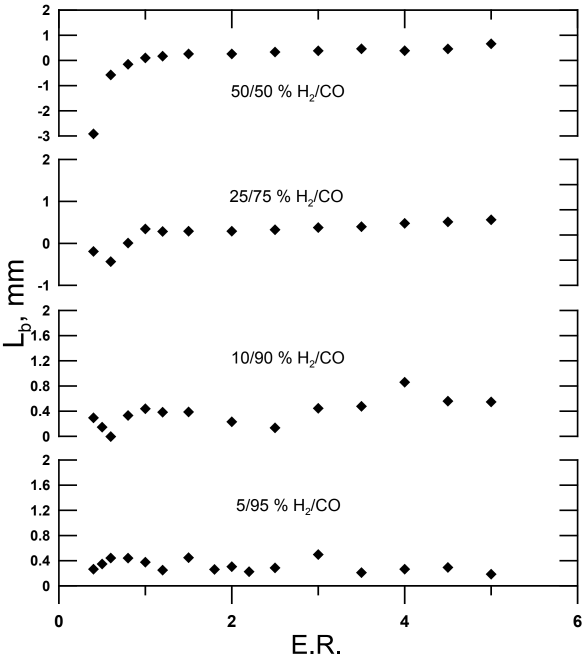

(a)

Figure VI.26 Comparison of Markstein lengths for investigated syngas mixtures.

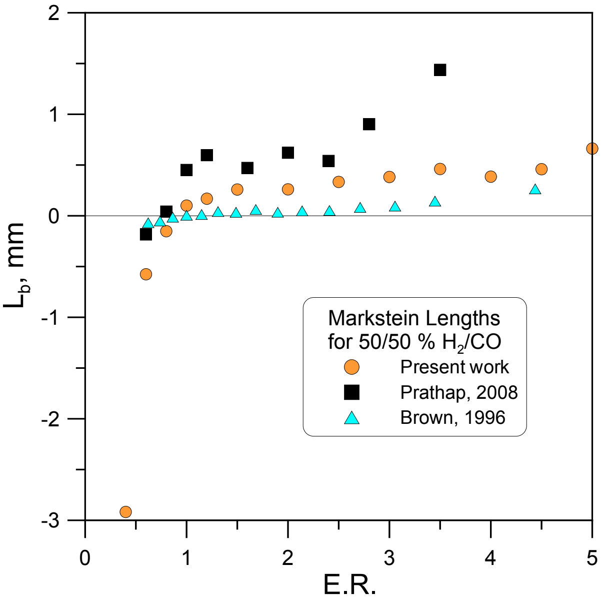

(b)

Figure VI.27 Comparison of Markstein lengths for the 50/50 % H_2/CO mixtures and experimental datasets from Prathap [212] and Brown [209].

VI.4 PART III: Comparison of Results from the Different Approaches

Results obtained in the counterflow, conical and outwardly propagating flames are confronted Figure VI.28 (5/95 % H_2/CO), Figure VI.29 (10/90 H_2/CO), Figure VI.30 (25/75 H_2/CO) and Figure VI.31 (50/50 H_2/CO). Note that vertical bars plotted in the graphs respectively correspond to: i/ the uncertainty on extrapolated flame speeds for DPIV measurements, ii/ standard deviations among series with the same experimental conditions for spherical flames measurements, iii/ standard deviations among series with close experimental conditions for conical flame measurements (data averages by ±0.05 E.R. steps). Taking into account the diversity of techniques compared in the present work, the agreement of all approaches is very good for very lean mixtures up to E.R.=1.0. The fact that Bunsen flame measurements (known to be influenced by curvature and heat loss effects) agree well with stretch compensated measurements is confirming the weak nonequidiffusive nature of lean to stoichiometric H_2/CO/Air blends with lower H_2 contents (%H_2 < 50%). Indeed curvature effects enhancing or reducing the burning rate at the flame cone apex are expected to be limited. Since both the present choice of the flame surface area (OH* chemiluminescence) and heat losses to the burner rim contribute to the decrease of the measured velocity, and noticing that no strong velocity reduction is obtained for these measurements, it is reasonable to assume that heat losses at the burner rim have a weak influence on the studied flames. Thus in the present case, the good agreement of conical flame measurements with stretch compensated ones is not due to compensating effects such as "heat loss at the burner rim - burning velocity enhancement at the flame tip" that could expected for mixtures with *Le* >> 1. Both stretched compensated methods find a reasonable agreement with discrepancies usually contained in a 10 cm.s^{-1} interval. Note that here, large error bars for DPIV measurements observed for the 10/90 % H_2/CO (E.R.=2.0, 3.0) and 50/50 % H_2/CO (E.R.=0.8) are due to the limited ranges of data points used in the extrapolation procedure as well as important lowest strain rate achieved. A significant reduction of these uncertainties could be achieved using a smaller burner (to widen investigated strain rates) as well as larger nozzle separation distances (to reach lower strain rates). Note here that counterflow and spherical flame measurements yield a reasonable agreement in the rich domain, both are however underpredicted by kinetic mechanisms with the gradual H_2 increase at very rich conditions, as seen in Figure VI.32.

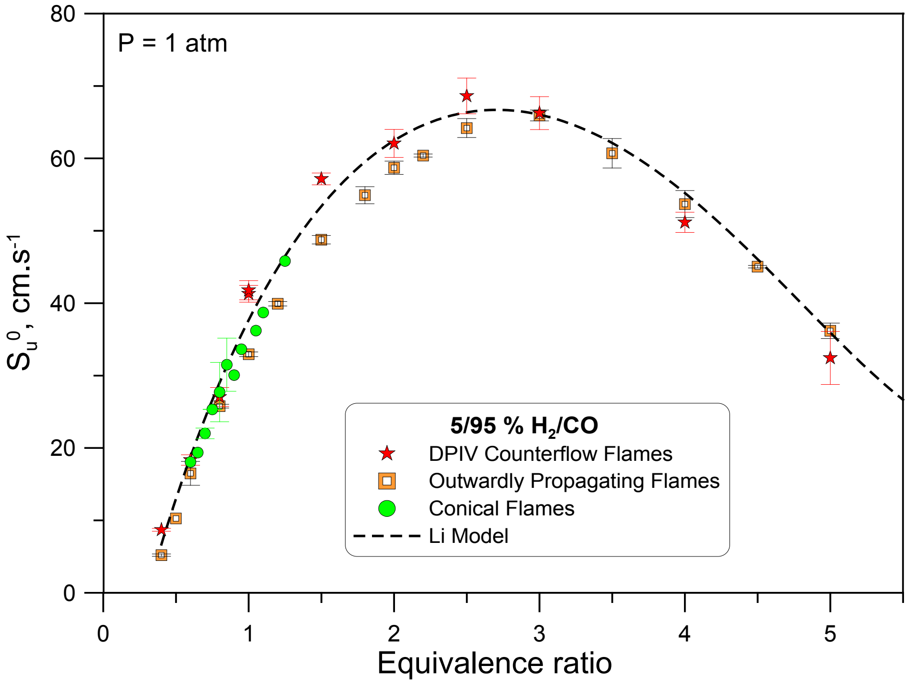

Figure VI.28 Laminar flame speed comparison of 5/95 % H_2/CO +air mixtures measured with the counterflow, outwardly propagating and conical flame techniques.

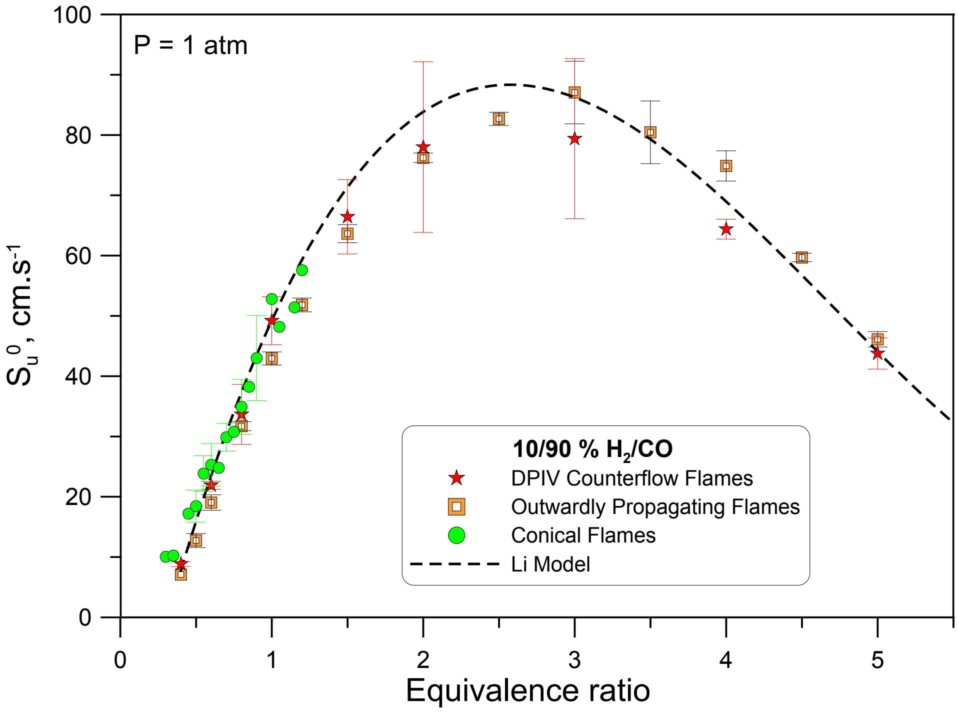

Figure VI.29 Laminar flame speed comparison of 10/90 % H_2/CO +air mixtures measured with the counterflow, outwardly propagating and conical flame techniques.

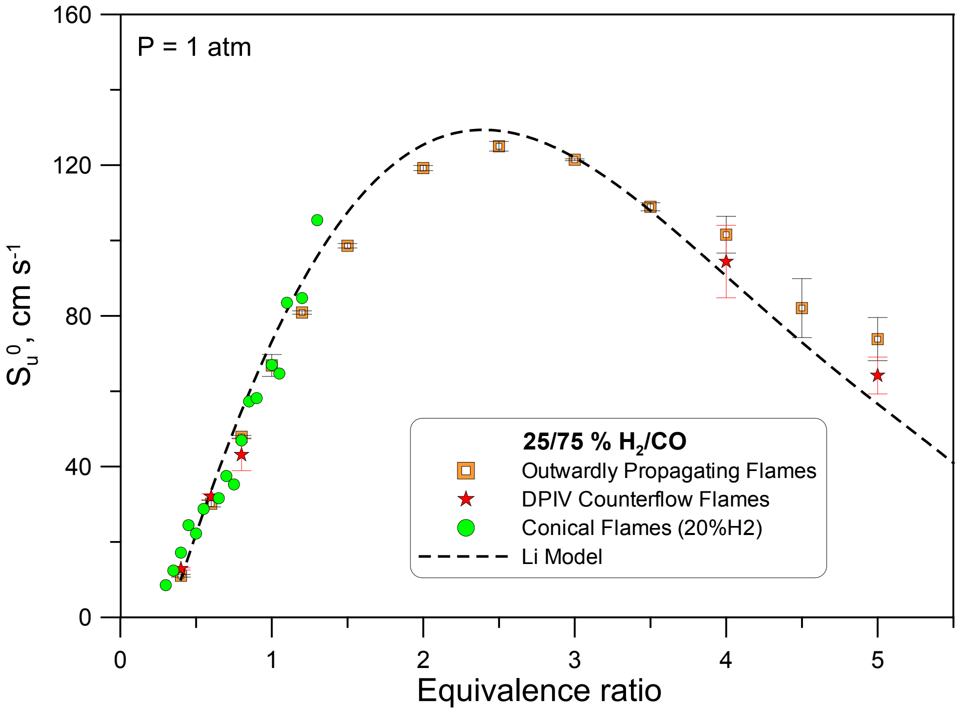

Figure VI.30 Laminar flame speed comparison of 25/75 % H_2/CO +air mixtures measured with the counterflow, outwardly propagating and conical flame techniques.

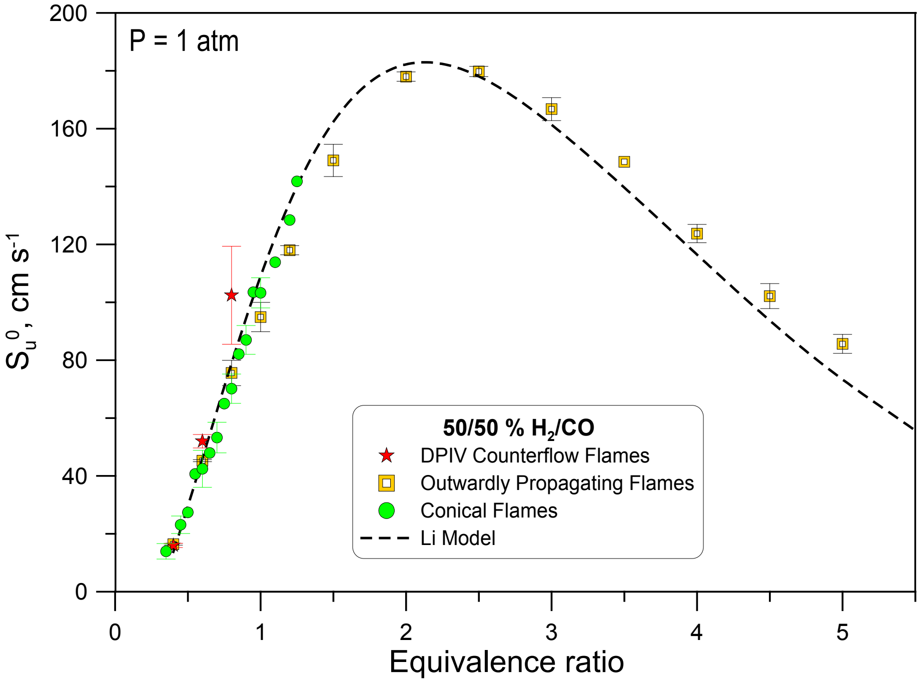

Figure VI.31 Laminar flame speed comparison of 50/50 % H_2/CO +air mixtures measured with the counterflow, outwardly propagating and conical flame techniques.

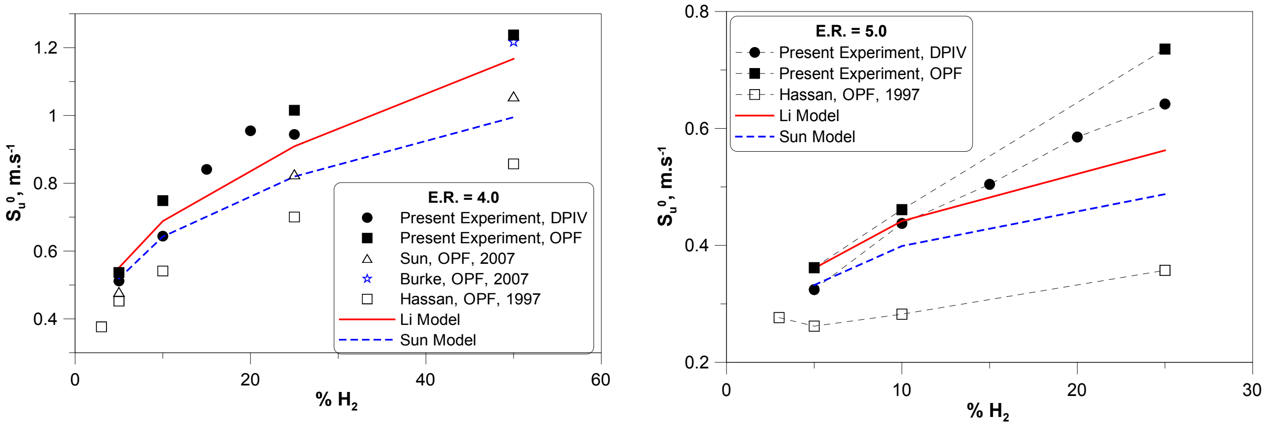

(a) **(b)**

Figure VI.32 Comparison of laminar flame speed measurements of H_2/CO mixtures with increasing amounts of H_2 obtained in the counterflow and outwardly propagating flame configurations: (a) E.R. = 4.0, (b) E.R. = 5.0. Experimental data points from Sun [200], Burke [213], Hassan [198]. Model: Li [230] and Sun [200].

VI.5 Summary

Laminar flame speeds of various syngas/air mixtures have been measured using the conical flame (PART I) and outwardly propagating flame (PART II) approaches. The developed flame surface area based on the maximum intensity of OH* chemiluminescence was found to give comprehensive results, which were in most cases independent of the straight burner I.D.s. The flame cone angle approach based on Schlieren images provided for all cases, higher velocity values. Discrepancies between both approaches were found to be reduced for large nozzle burner and higher flow rates. It was suggested that boundary layer effects might lead to erroneous estimations of the unburned gas velocity used as a direct input in the flame cone angle methodology for the laminar flame speed extraction. If the cone angle methodology is to be used, it is recommended to perform measurements on burners with large diameters and measure the local flow velocity close to the flame front thanks to velocimetry diagnostics such as PIV or LDV. Curvature effects were found to be important at higher H_2 contents due to the nonequidiffusive nature of investigated mixtures. In this region, a broad range of conical flames were found to suffer from the flame tip opening phenomenon which is characterized by a local extinction at the flame tip. Flame speed extraction using the flame surface area approach would require, in this case, additional experimental investigations to determine if fuel leakage is observed at the flame tip or not.

Laminar flame speeds of various syngas/air mixtures have also been investigated in the outwardly propagation flame approach using both state of art linear and non-linear processing methodologies (PART II). Important disparities on the order of few tens of $cm.s^{-1}$ were found among results of various experimental investigations in the rich flame domain for all syngas compositions. These disparities could be due to differences in processing methodologies but flame inhibition effects due to the contamination of syngas mixtures with carbonyl compounds seem to be highly relevant. Indeed, it was shown in the previous chapter that these inhibition effects are essentially concentrated on the rich side of the velocity bell-shaped curves. Extents of deviations between both linear and non-linear methodologies were found to be negligible for practically all flames investigated apart from very rich cases (E.R.=4.5-5) for which velocity reductions on the order of 8 $cm.s^{-1}$ are achieved. This result is coherent with recent investigations of mixture Lewis number and flame ignition energy effects on flame propagation. Extracted Markstein lengths showed that syngas mixtures with H_2 contents <50 % are fairly insensitive to strain and therefore are globally behaving like nonequidiffusive mixtures. It was found that a calculation of an effective mixture Lewis number L_{eff}, based on a mass fraction weighted average of the individual fuel Lewis numbers, does not yield a qualitative agreement with the experimental observations. Further investigations are required to confirm that a L_{eff} definition based on a mole fraction weighted average of the Lewis numbers of both fuel, would be more appropriate in the case of H_2/CO/air blends.

A comparison of the laminar flame speed results from the three investigated flame configurations (counterflow, outwardly propagating and conical flames) has been presented in PART III. DPIV measurements found an overall good agreement with the two other techniques with almost all measurements kept in a 10 $cm.s^{-1}$ interval. This further validates the counterflow-DPIV approach developed in the course of the present work. Note here that DPIV measurements accuracy is expected to be significantly improved for very fast mixtures if smaller nozzle diameter are used combined with larger separation distances. This will have for effect to widen the investigated strain rate ranges as well as allow for a decrease of the lowest achieved strain rates. The tradeoff between stability and large nozzle separation distance should be however carefully analyzed, and modifications of the burner counterflow burner apparatus have been engaged in this sense. Finally, it was found that both counterflow and outwardly propagating flame results were underestimated by tested kinetic mechanisms for rich flames (E.R.=4.0 and 5.0) and higher H_2 contents (H_2>10%).

Summary and Recommendations

Summary

The present work was oriented towards the following two main objectives: 1/ Develop and validate of a laminar flame speed measurement technique combining both the Digital Particle Image Velocimetry diagnostics with the counterflow flame configuration; 2/ Apply the developed approach to syngas (H_2/CO)/air flames and confront results to measurements obtained with two more conventional configurations, i.e. the conical and outwardly propagating flames.

A thorough literature review of investigations related to particle motion in seeded fluids has been proposed. The relevant Stokes drag and thermophoretic forces have been identified as key factors governing the particle motion in reactive stagnation flows, characterized by strong velocity and temperature gradients. Both Laser Doppler and Particle Image Velocimetry flame speed investigations have been reviewed for the stagnation flow configuration. They revealed that: 1/ flames are usually stabilized for weak strain rates with Karlovitz numbers *Ka* on the order of 0.1 (or lower); 2/ uncertainties related to the unstrained flame speed extrapolation procedure are rarely addressed; 3/ linear and non-linear extrapolation procedure yield unstrained flame speed within a 3 cm.s^{-1} interval; 4/ the apparent flame sensitivity to flow straining is depending on the reference plane chosen for the flame parameter extraction. The conventional reference at the unburned flame edge will almost always lead to an increase of the velocity with strain; 5/ the nozzle separation distance, or alternatively the burner-to-plate distance, is an important parameter. It is generally recommended that the ratio (nozzle separation distance)/(burner diameter) should be kept above one. Nozzle sepration distances of at least 14 mm were seen to be well adapted for the counterflow technique. All aforementioned points were carefully considered during the development of the present flame speed determination technique.

Principles of the Digital Particle Image Velocimetry (DPIV) have been recalled and the DPIV setup and specifications have been presented, including chosen processing algorithms. ZrO_2 particles with a primary particle size of 1.8 µm were selected and particle concentrations evaluated thanks to a home-developed program. These concentrations were found to be considerably lower than those shown to have thermal effects on flames. It was demonstrated that the peak locking phenomenon might affect the determination of the flame strain rates. It was recognized that a large number of data point should be considered while performing regression procedures on radial velocity profiles to cancel this potential bias. Programs were successfully developed in order to process instantaneous DPIV vector fields. It was shown that the radial strain rate determination is preferable to the conventional approach using the axial velocity profiles. The linear extrapolation approach adopted in the present investigation has been presented and used in a parametric study to illustrate the relative importance of several key parameters. For common cases, the predicted uncertainty is expected to be on the order of 2.5 cm.s^{-1}.

The developed DPIV approach has been applied to the well characterized methane/air mixtures in both stagnation plate and counterflow flame configuration. Since heat loss effects were experimentally found to be non-negligible at higher strain rates for investigated plate setups, the counterflow approach was retained for the laminar flame speed determination. Counterflow flame speed measurements were confronted to an extensive number of experimental datasets obtained for various flame configurations. Present measurements found a good agreement with works of the literature thus confirming the reliability and accuracy of the developed methodology. The stagnation plate and counterflow flame configurations were simulated for stoichiometric methane/air mixtures using both classical 1D and 2D-realistic approaches. It was demonstrated that for the plate setup case, the 1D approach fail to accurately predict flow velocity variations due to a simplifying assumption related to the radial pressure gradient. The 2-D simulations revealed that thermophoretic effect are indeed important but are only felt in the fast expansion zone of the flame and do not modify the velocity minimum taken as a reference in the present investigation. For the counterflow case, the agreement between both 1D and 2D approaches is improved.

Flame speeds of various syngas mixtures (from 5/95 % to 50/50% H_2/CO) have been investigated using the developed counterflow approach and a newly designed burner assembly. Measurements were confronted to the literature data as well as numerical predictions of two leading mechanisms developed for syngas combustion. An overall good agreement was found for the 5/95 % H_2/CO case, but important disparities were observed for the 10/90 % H_2/CO mixtures at rich conditions. It has been shown that flame inhibition effects of small amounts of iron pentacarbonyl could provide an effective flame speed reduction on the order of observed discrepancies. An increasing disagreement was found between numerical predictions given by tested kinetic mechanisms at higher equivalence ratio and H_2 contents. It has been shown that discrepancies among the models essentially result in the choice of different rate constant parameters for both $H+O_2=O+OH$ and $HO_2+H=OH+OH$ reactions. Both mechanisms were found to under predict DPIV measurements at higher H_2 contents.

To further validate syngas counterflow flame velocity measurements, complementary results using the conical and outwardly propagating approaches were performed. Counterflow measurements generally found an overall good agreement with the two other techniques with almost all measurements kept in a 10 cm.s^{-1} interval. It was noticed that both counterflow and outwardly propagating flame results were underestimated by tested kinetic mechanisms for rich flames (E.R.=4.0 and 5.0) and higher H_2 contents (H_2>10%). Markstein lengths, extracted from the outwardly propagating flame approach, showed that syngas mixtures with H_2 contents <50 % are fairly insensitive to stretch and therefore are globally behaving like nonequidiffusive mixtures.

Recommendations for Future Works

The following recommendations can be formulated:

- As mentioned earlier, the use of smaller nozzle I.D. burners along with a flexible upper burner will allow for the lowering of investigated strain rates and widening of their ranges, especially for the very fast syngas mixtures. A substantial gain in the extrapolated flame speed uncertainty is to be expected in this case. Modifications of the current setup are ongoing. Improvements of the seeding system to ensure a continuous and steady particle injection into the reactive flow will also be considered.

- High pressure laminar flame speed measurements of syngas mixtures are scarce. The syngas counterflow burner developed in the course of the present investigation is a perfect tool for such measurements to be performed. The burner being already housed in a high pressure chamber, only minor modifications are required. Adaptation of the present system to the measurements of burning velocities of liquid fuels is also seen to be very promising.
- It might be fruitful to combine DPIV measurements in the counterflow configuration with diagnostics allowing the flame temperature determination (For ex. Rayleigh scattering). As such, alternative planes of reference could be investigated to verify if flame sensitivities similar to those found in the outwardly propagating flame approach could be recovered.
- The counterflow measurement methodology presented in this work could potentially benefit from decreased post-processing times, for instance by directly implementing the developed data processing algorithms in the DPIV software, giving a real-time access to the flame reference velocity evolutions with strain.

References

1. (2009) Key World Energy Statistics. The International Energy Agency.
2. (2007) Climate Change 2007: Synthesis Report. The Intergovernmental Panel on Climate Change, Valencia, Spain.
3. (2009) How the energy sector can deliver on a climate agreement in Copenhagen. *Special early excerpt of the World Energy Outlook 2009 for the Bangkok UNFCCC meeting.* The International Energy Agency.
4. Richards, G.A., Mcmillian, M.M., Gemmen, R.S., Rogers, W.A. and Cully, S.R. (2001) Issues for low-emission, fuel-flexible power systems. *Progress in Energy and Combustion Science,* **27,** 141-169.
5. Moliere, M. (2002) Benefiting from the wide fuel capability of gas turbines: a review of application opportunities. In *ASME TURBO EXPO 2002*, 227-238, Amsterdam, The Netherlands.
6. De Biasi, V. (2003) FutureGen IGCC to convert coal into hydrogen and electric power. *Gas Turbine World,* **33,** 11-16.
7. Lieuwen, T. and Richards, G. (2006) Burning questions. *Mechanical Engineering,* **128,** 40-42.
8. Stiegel, G.J. (1999) Integrated Gasification Combined Cycle. U.S. Dpartment of Energy - Office of Fossil Energy, Federal Energy Technology Center.
9. Jones, R.M. and Shilling, N.Z. (2003) IGCC Gas Turbines for Refinery Applications. GE Power Systems, Schenectady, NY.
10. Poinsot, T. and Veynante, D. (2005) *Theoretical and numerical combustion,* Edwards, Philadelphia.
11. Jarosinski, J. and Veyssière, B. (2009) *Combustion Phenomena: Selected Mechanisms of Flame Formation, Propagation, and Extinction,* CRC Press.
12. Chung, S.H. and Law, C.K. (1984) An invariant derivation of flame stretch. *Combustion and Flame,* **55,** 123-125.
13. Matalon, M. (1983) On Flame Stretch. *Combustion Science and Technology,* **31,** 169-181.
14. Candel, S.M. and Poinsot, T.J. (1990) Flame Stretch and the Balance Equation for the Flame Area. *Combustion Science and Technology,* **70,** 1-15.
15. Markstein, G.H. (1951) Experimental and theoretical studies of flame-front stability. *Journal of the Aeronautical Sciences,* **18,** 199-209.
16. Clavin, P. and Joulin, G. (1983) Premixed flames in large scale and high intensity turbulent flow. *Journal de physique. Lettres,* **44,** 1-12.
17. Andrews, G.E. and Bradley, D. (1972) Determination of burning velocities: A critical review. *Combustion and Flame,* **18,** 133-153.
18. Kuo, K.K. (2005) *Principles of combustion,* John Wiley.
19. Botha, J.P. and Spalding, D.B. (1954) The Laminar Flame Speed of Propane/Air Mixtures with Heat Extraction from the Flame. *Proceedings of the Royal Society of London. Series A, Mathematical and Physical Sciences,* **225,** 71-96.
20. Van Maaren, A., Thung, D.S. and De Goey, L.R.H. (1994) Measurement of Flame Temperature and Adiabatic Burning Velocity of Methane/Air Mixtures. *Combustion Science and Technology,* **96,** 327-344.
21. De Goey, L.P.H., Van Maaren, A. and Quax, R.M. (1993) Stabilization of Adiabatic Premixed Laminar Flames on a Flat Flame Burner. *Combustion Science and Technology,* **92,** 201-207.
22. Bosschaart, K.J. (2002) Analysis of the heat flux method for measuring burning velocities. Ph.D. thesis, Technische Universiteit Eindhoven, The Netherlands.
23. Wu, C.K. and Law, C.K. (1984) On the Determination of Laminar Flame Speeds From Stretched Flames. *Symposium (International) on Combustion,* **20,** 1941-1949.

24. Bradley, D., Gaskell, P.H. and Gu, X.J. (1996) Burning velocities, markstein lengths, and flame quenching for spherical methane-air flames: A computational study. *Combustion and Flame,* **104,** 176-198.

25. Gu, X.J., Haq, M.Z., Lawes, M. and Woolley, R. (2000) Laminar burning velocity and Markstein lengths of methane-air mixtures. *Combustion and Flame,* **121,** 41-58.

26. Groot, G.R.A., Van Oijen, J.A., De Goey, L.P.H., Seshadri, K. and Peters, N. (2002) The effects of strain and curvature on the mass burning rate of premixed laminar flames. *Combustion Theory and Modelling,* **6,** 675-695.

27. Kee, R.J., Grcar, J.F., Smooke, M.D. and Miller, J.A. (1985) A Fortran Program for Modeling Steady Laminar One-Dimensional Premixed Flames. Report SAND85-8240. Sandia National Laboratories Livermore, CA.

28. Lutz, A.E., Kee, R.J., Grcar, J.F. and Rupley, F.M. (1996) OPPDIF: A Fortran Program for Computing Opposed-flow Diffusion Flames, Report 96-8243. Sandia National Laboratories, Livermore, CA.

29. Kee, R.J., Miller, J.A., Evans, G.H. and Dixon-Lewis, G. (1988) A computational model of the structure and extinction of strained, opposed flow, premixed methane-air flames. *Symposium (International) on Combustion,* **22,** 1479-1494.

30. Dixon-Lewis, G. (1991) Structure of Laminar Flames. *Symposium (International) on Combustion,* **23,** 305-324.

31. Bird, R.B., Stewart, W.E. and Lightfoot, E.N. (1960) *Transport Phenomena,* John Wiley & Sons, New York.

32. Mathur, S., Tondon, P.K. and Saxena, S.C. (1967) Thermal conductivity of binary, ternary and quaternary mixtures of rare gases. *Molecular Physics: An International Journal at the Interface Between Chemistry and Physics,* **12,** 569-579.

33. Hjelmfelt, J.A.T. and Mockros, L.F. (1966) Motion of discrete particles in turbulent fluid. *Applied Scientific Research,* **16,** 149-161.

34. Durst, F., Melling, A. and Whitelaw, J.H. (1981) *Principles and practice of laser-Doppler anemometry,* Academic Press, London; New York.

35. Sung, C.J., Law, C.K. and Axelbaum, R.L. (1994) Thermophoretic Effects on Seeding Particles in LDV Measurements of Flames. *Combustion Science and Technology,* **99,** 119-132.

36. Melling, A. (1997) Tracer particles and seeding for particle image velocimetry. *Measurement Science and Technology,* **8,** 1406-1416.

37. Mei, R. (1996) Velocity fidelity of flow tracer particles. *Experiments in Fluids,* **22,** 1-13.

38. Egolfopoulos, F.N. and Campbell, C.S. (1999) Dynamics and structure of dusty reacting flows: inert particles in strained, laminar, premixed flames. *Combustion and Flame,* **117,** 206-226.

39. Allen, M.D. and Raabe, O.G. (1985) Slip Correction Measurements of Spherical Solid Aerosol Particles in an Improved Millikan Apparatus. *Aerosol Science and Technology,* **4,** 269-286.

40. Sung, C.J., Kistler, J.S., Nishioka, M. and Law, C.K. (1996) Further studies on effects of thermophoresis on seeding particles in LDV measurements of strained flames. *Combustion and Flame,* **105,** 189-201.

41. Bergthorson, J. and Dimotakis, P. (2006) Particle velocimetry in high-gradient/high-curvature flows. *Experiments in Fluids,* **41,** 255-263.

42. Raffel, M., Willert, C., Wereley, S. and Kompenhans, J. (2007) *Particle Image Velocimetry: a practical guide,* Springer, Berlin.

43. Rosner, D.E., Mackowski, D.W., Tassopoulos, M., Castillo, J. and Garcia-Ybarra, P. (1992) Effects of heat transfer on the dynamics and transport of small particles suspended in gases. *Industrial and Engineering Chemistry Research,* **31,** 760-769.

44. Gomez, A. and Rosner, D.E. (1993) Thermophoretic Effects on Particles in Counterflow Laminar Diffusion Flames. *Combustion Science and Technology,* **89,** 335-362.

45. Brock, J.R. (1962) On the theory of thermal forces acting on aerosol particles. *Journal of Colloid Science,* **17,** 768-780.

46. Talbot, L., Cheng, R.K., Schefer, R.W. and Willis, D.R. (1980) Thermophoresis of Particles in a Heated Boundary Layer. *Journal of Fluid Mechanics,* **101,** 737-758.

47. Williams, M.M.R. (1986) Thermophoretic forces acting on a spheroid. *Journal of Physics D: Applied Physics,* **19,** 1631-1642.

48. Garcia-Ybarra, P. and Rosner, D.E. (1989) Thermophoretic properties of nonspherical particles and large molecules. *AIChE Journal,* **35,** 139-147.

49. Williams, M.M.R. (1987) The thermophoretic forces acting on a bispherical system. *Journal of Physics D: Applied Physics,* **20,** 354-359.

50. Zheng, F. (2002) Thermophoresis of spherical and non-spherical particles: a review of theories and experiments. *Advances in Colloid and Interface Science,* **97,** 253-276.

51. Sung, C.J. and Law, C.K. (1993) On the Structure and Response of Aerodynamically-Strained Planar Premixed Flames. In *Aerospace Sciences Meeting and Exhibit, 31st,* AIAA, Reno, NV; United States.

52. Chelliah, H.K., Law, C.K., Ueada, T., Smooke, M.D. and Williams, F.A. (1991) An Experimental and Theoritical Investigation of the Dilution, Pressure, and Flow-Field Effects on the Extinction Condition of Methane-Air-Nitrogen Diffusion Flames. *Symposium (International) on Combustion,* **23,** 503-511.

53. Pandya, T.P. and Weinberg, F.J. (1964) The Structure of Flat, Counter-Flow Diffusion Flames *Proceedings of the Royal Society of London. Series A, Mathematical and Physical Sciences,* **279,** 544-561.

54. Kim, B.S., Travelho, J., Jagoda, J.I. and Zinn, B.T. (1985) Soot Formation in an opposed flow polymer diffusion flame. *Symposium (International) on Combustion,* **20,** 1113-1120.

55. Goodwin, D.G. (2003) An open-source, extensible software suite for CVD process simulation. In *Proceedings of CVD XVI and EuroCVD Fourteen*: Electrochemical Society, 155–162.

56. Bergthorson, J.M. (2005) Experiments and modeling of impinging jets and premixed hydrocarbon stagnation flames. Ph.D. thesis, California Institute of Technology.

57. Law, C.K., Ishizuka, S. and Mizomoto, M. (1981) Lean-limit extinction of propane/air mixtures in the stagnation-point flow. *Symposium (International) on Combustion,* **18,** 1791-1798.

58. Yu, G., Law, C.K. and Wu, C.K. (1986) Laminar Flame Speeds of Hydrocarbons + Air Mixtures With Hydrogen Addition. *Combustion and Flame,* **63,** 339-347.

59. Matalon, M. and Matkowsky, B.J. (1982) Flames as gasdynamic discontinuities. *Journal of Fluid Mechanics Digital Archive,* **124,** 239-259.

60. Law, C.K., Zhu, D.L. and Yu, G. (1986) Propagation and Extinction of Stretched Premixed Flames. *Symposium (International) on Combustion,* **21,** 1419-1426.

61. Clavin, P. and Williams, F.A. (1982) Effects of Molecular Diffusion and Thermal Expansion on the Structure and Dynamics of Premixed Flames in Turbulent Flows of Large Scale and Low Intensity. *Journal Fluid Mechanics,* **116,** 251-282.

62. Zhu, D.L., Egolfopoulos, F.N. and Law, C.K. (1988) Experimental and Numerical Determination of Laminar Flame Speeds of Methane/(Ar,N2,CO2)-Air Mixtures as Function of Stoichiometry, Pressure, and Flame Temperature. *Symposium (International) on Combustion,* **22,** 1537-1545.

63. Egolfopoulos, F.N., Cho, P. and Law, C.K. (1989) Laminar flame speeds of methane-air mixtures under reduced and elevated pressures. *Combustion and Flame,* **76,** 375-391.

64. Egolfopoulos, F.N. and Law, C.K. (1990) An Experimental and Computational Study of the Burning Rates of Ultra-Lean to Moderate-Rich H2/O2/N2 Laminar Flames with Pressure Variations. *Symposium (International) on Combustion,* **23,** 333-340.

65. Egolfopoulos, F.N., Zhu, D.L. and Law, C.K. (1990) Experimental and Numerical Determination of Laminar Flame Speeds: Mixtures of C2-Hydrocarbons With Oxygen and Nitrogen. *Symposium (International) on Combustion* **23,** 471-478.

66. Egolfopoulos, F.N., Du, D.X. and Law, C.K. (1992) A Comprehensive Study of Methanol Kinetics in Freely-Propagating and Burner-Stabilized Flames, Flow and Static Reactors, and Shock Tubes. *Combustion Science and Technology,* **83,** 33-75.

67. Egolfopoulos, F.N., Du, D.X. and Law, C.K. (1992) A Study on Ethanol Oxidation Kinetics in Laminar Premixed Flames, Flow Reactors, and Schock Tubes. *Symposium (International) on Combustion,* **24,** 833-841.

68. Tien, J.H. and Matalon, M. (1991) On the burning velocity of stretched flames. *Combustion and Flame,* **84,** 238-248.

69. Yang, M.H. and Puri, I.K. (1993) Experimental investigation of stretched premixed flames burning mixtures of methane and methyl chloride in air and comparison with numerical simulations. *Combustion and Flame,* **94,** 25-34.

70. Vagelopoulos, C.M. and Egolfopoulos, F.N. (1994) Laminar flame speeds and extinction strains rates of mixtures of carbon monoxide with hydrogen, methane, and air. *Symposium (International) on Combustion,* **25,** 1317-1323.

71. Vagelopoulos, C.M., Egolfopoulos, F.N. and Law, C.K. (1994) Further considerations on the determination of laminar flame speeds with the counterflow twin flame technique. *Symposium (International) on Combustion,* **25,** 1341-1347.

72. Davis, S.G., Wang, H., Brézinsky, K. and Law, C.K. (1996) Laminar Flame Speeds and Oxidation Kinetics of Benzene-Air and Toluene-Air Flames. *Symposium (International) on Combustion,* **26,** 1025-1033.

73. Davis, S.G. and Law, C.K. (1998) Determination of and Fuel Structure Effects on Laminar Flame Speeds of C1 to C8 Hydrocarbons. *Combustion Science and Technology,* **140,** 427-449.

74. Davis, S.G. and Law, C.K. (1998) Laminar Flame Speeds and Oxidation Kinetics Of iso-Octane-Air and n-Heptane-Air Flames. *Symposium (International) on Combustion,* **27,** 521-527.

75. Davis, S.G., Law, C.K. and Wang, H. (1998) Experimental and kinetic modeling study of propyne oxidation. *Symposium (International) on Combustion,* **1,** 305-312.

76. Davis, S.G., Law, C.K. and Wang, H. (1999) Propene pyrolysis and oxidation kinetics in a flow reactor and laminar flames. *Combustion and Flame,* **119,** 375-399.

77. Davis, S.G. (1998) An experimental and kinetic modeling study of the pyrolysis and oxidation of selected carbon(3-8) hydrocarbons. Ph.D. thesis, Princeton University.

78. Wang, C.-H. and Wang, W.-B. (1997) The Measurements of the Laminar Flame Propagation Velocity of Premixed-Prevaporized Liquid Fuels. *Journal of the Chinese Society of Mechanical Engineers* **18,** 75-83.

79. Wang, C.-H., Ueng, G.-J. and Tsay, M.-S. (1998) Experimental determination of the laminar burning velocities and extinction stretch rates of benzene/air flames. *Combustion and Flame,* **113,** 242-248.

80. Wang, H., Hahn, T.O., Sung, C.J. and Law, C.K. (1996) Detailed oxidation kinetics and flame inhibition effects of chloromethane. *Combustion and Flame,* **105,** 291-307.

81. Leylegian, J.C., Zhu, D.L., Law, C.K. and Wang, H. (1998) Experiments and Numerical Simulation on the Laminar Flame Speeds of Dichloromethane and Trichloromethane. *Combustion and Flame,* **114,** 285-293.

82. Leylegian, J.C., Law, C.K. and Wang, H. (1998) Laminar Flame Speeds and Oxidation Kinetics of Tetrachloromethane. *Symposium (International) on Combustion,* **27,** 529-536.

83. Saso, Y., Zhu, D.L., Wang, H., Law, C.K. and Saito, N. (1998) Laminar Burning Velocities of Trifluoromethane-Methane Mixtures: Experiment and Numerical Simulation. *Combustion and Flame,* **114,** 457-468.

84. Leylegian, J.C., Sun, H.Y. and Law, C.K. (2005) Laminar flame speeds and kinetic modeling of hydrogen/chlorine combustion. *Combustion and Flame,* **143,** 199-210.

85. Natarajan, J., Lieuwen, T. and Seitzman, J. (2007) Laminar flame speeds of H2/CO mixtures: Effect of CO2 dilution, preheat temperature, and pressure. *Combustion and Flame,* **151,** 104-119.

86. Natarajan, J. (2008) Experimental and Numerical Investigation of Laminar Flame Speeds of H2/CO/CO2/N2 Mixtures. Ph.D. thesis, Georgia Institute of Technology.

87. Natarajan, J., Lieuwen, T. and Seitzman, J. (2007) Laminar flame speeds and strain sensitivities of mixtures of H2 with CO, CO2, N2 at elevated temperatures. In *ASME Turbo Expo: Power for Land, Sea and Air*, May 14-17, Montreal, CANADA.

88. Natarajan, J., Lieuwen, T. and Seitzman, J. (2007) Experimental and Numerical Investigation of Strained Laminar Flame Speeds for H2/O2/N2 Mixtures at Elevated Temperature. In *5th US Combustion Meeting*, March 25-28, University of California at San Diego.

89. Vagelopoulos, C.M. and Egolfopoulos, F.N. (1998) Direct experimental determination of laminar flame speeds. *Symposium (International) on Combustion,* **27,** 513-519.

90. Hirasawa, T., Sung, C.J., Joshi, A., Yang, Z., Wang, H. and Law, C.K. (2002) Determination of laminar flame speeds using digital particle image velocimetry: Binary fuel blends of ethylene, n-butane, and toluene. *Proceedings of the Combustion Institute,* **29,** 1427-1433.

91. Hirasawa, T., Sung, C.J., Joshi, A., Yang, Z., Wang, H. and Law, C.K. (2001) Determination of Laminar Flame Speeds of Ethylene/n-Butane/Air Flames Using Digital Particle Image Velocimetry. In *2nd Joint Meeting of the U.S. Section of the Combustion Institute*, March 25-28, Oakland, California.

92. Ibarreta, A.F., Sung, C.-J., Hirasawa, T. and Wang, H. (2005) Burning velocity measurements of microgravity spherical sooting premixed flames using rainbow Schlieren deflectometry. *Combustion and Flame,* **140,** 93-102.

93. Ibarreta, A.F., Sung, C.-J., Hirasawa, T. and Wang, H. (2004) Burning velocity measurements of sooting premixed flames. In *42nd AIAA Aerospace Sciences Meeting and Exhibit*, Reno, Nevada.

94. Dong, Y., Vagelopoulos, C.M., Spedding, G.R. and Egolfopoulos, F.N. (2002) Measurement of laminar flame speeds through digital particle image velocimetry: Mixtures of methane and ethane with hydrogen, oxygen, nitrogen, and helium. *Proceedings of the Combustion Institute,* **29,** 1419-1426.

95. Huang, Y., Sung, C.J. and Eng, J.A. (2003) Laminar Flame Speeds of Primary Reference Fuels and Reformer Gas Mixtures. In *Third Joint Meeting of the U.S. Sections of the Combustion Institute*, Chicago.

96. Huang, Y. (2003) On flame propagation of primary reference fuels and reformer gas: Implications for improving cold-start performance of a SI engine. Ph.D. thesis, Case Western Reserve University.

97. Huang, Y., Sung, C.J. and Eng, J.A. (2004) Laminar flame speeds of primary reference fuels and reformer gas mixtures. *Combustion and Flame,* **139,** 239-251.

98. Huang, Y., Sung, C.J. and Eng, J.A. (2004) Determination of laminar flame speeds of primary reference fuel and reformer gas mixtures using digital particle image velocimetry. In *42nd AIAA Aerospace Sciences Meeting and Exhibit*: American Institute of Aeronautics and Astronautics Inc., Reston, 3398-3408, Reno, NV, United States.

99. Huang, Y., Sung, C.J. and Eng, J.A. (2003) Laminar Flame Speeds of Primary Reference Fuels. In *The 2003 Fall Technical Meeting of the Eastern States Sections of the Combustion Institute*, University Park, PA.

100. Freeh, J.E.K., K., Huang, Y. and Sung, C.J. (2004) Laminar Flame Speeds of Preheated iso-Octane/Air and n-Decane/Air Flames Using Digital Particle Image Velocimetry. In *40th AIAA/ASME/SAE/ASEE Joint Propulsion Conference and Exhibit*, July 11-14, Fort Lauderdale, Florida.

101. Zhao, Z., Kazakov, A. and Dryer, F.L. (2004) Measurements of dimethyl ether/air mixture burning velocities by using particle image velocimetry. *Combustion and Flame,* **139,** 52-60.

102. Zhao, Z., Kazakov, A. and Dryer, F.L. (2001) Laminar Flame Speed Study of DME/Air Mixtures Using Particle Image Velocimetry. In *Fall Technical Eastern Section*: Combustion Institute, 416-419.

103. Zhao, Z., Kazakov, A., Li, J. and Dryer, F.L. (2004) The initial temperature and N2 dilution effect on the laminar flame speed of propane/air. *Combustion Science and Technology,* **176,** 1705-1723.

104. Zhao, Z., Juan, L.I., Kazakov, A., Dryer, F.L. and Zeppieri, S.P. (2005) Burning velocities and a high-temperature skeletal kinetic model for n-decane. *Combustion Science and Technology,* **177,** 89-106.

105. Zhao, Z. (2005) Experimental and numerical studies of burning velocities and kinetic modeling for practical and surrogate fuels. Ph.D. thesis, Princeton University.

106. Kumar, K., Freeh, J.E., Sung, C.J. and Huang, Y. (2007) Laminar Flame Speeds of Preheated iso-Octane/O2/N2 and n-Heptane/O2/N2 Mixtures. *Journal of Propulsion and Power,* **23,** 428-436.

107. Kumar, K. and Sung, C.-J. (2007) Laminar flame speeds and extinction limits of preheated n-decane/O2/N2 and n-dodecane/O2/N2 mixtures. *Combustion and Flame,* **151,** 209-224.

108. Kumar, K., Huang, Y. and Sung, C.J. (2005) Laminar Flame Speeds of Preheated n-Decane/Air and n-Dodecane/Air Mixtures. In *Fourth Joint Meeting of the U.S. Sections of the Combustion Institute*, Philadelphia, PA.

109. Kumar, K., Mittal, G., Sung, C.-J. and Law, C.K. (2008) An experimental investigation of ethylene/O2/diluent mixtures: Laminar flame speeds with preheat and ignition delays at high pressures. *Combustion and Flame,* **153,** 343-354.

110. Kumar, K., Mittal, G., Sung, C.J. and Law, C.K. (2007) An Experimental Investigation on Ethylene/Oxygen/Diluent Mixtures: Laminar Flames Speeds with Preheat and Ignition Delays at High Pressures. In *5th US Combustion Meeting*, University of California, San Diego.

111. Kumar, K. (2007) Global combustion responses of practical hydrocarbon fuels: n-heptane, iso-octane, n-decane, n-dodecane and ethylene. Ph.D. thesis, Case Western Reserve University.

112. Daneshyar, H., Mendes-Lopes, J.M.C. and Ludford, G.S.S. (1982) Effect of Strain Fields on Burning Rate. *Symposium (International) on Combustion,* **19,** 413-421.

113. Mendes-Lopes, J.M.C. and Daneshyar, H. (1985) Influence of strain fields on flame propagation. *Combustion and Flame,* **60,** 29-48.

114. Smith, D.B., Taylor, S.C. and Williams, A. (1989) Problems with Defining and Measuring Burning Velocities. In *Joint Meeting of the British and French Sections of the Combustion Institute*, 151-154, Rouen, France.

115. Dixon-Lewis, G. and Islam, S.M. (1982) Flame Modelling and Burning Velocity Measurement. *Symposium (International) on Combustion,* **19,** 283-291.

116. Deshaies, B. and Cambray, P. (1990) The velocity of a premixed flame as a function of the flame stretch: An experimental study. *Combustion and Flame,* **82,** 361-375.

117. Matalon, M. (1994) Modeling Flame Phenomena. In *1994 Fall Technical Meeting, Eastern States of the Combustion Institute*, Surfside Holiday Inn, Clearwater Beach, FL.

118. Eteng, E., Ludford, G.S.S. and Matalon, M. (1986) Displacement effect of a flame in a stagnation-point flow. *Physics of Fluids,* **29,** 2172-2180.

119. Chao, B.H., Egolfopoulos, F.N. and Law, C.K. (1997) Structure and propagation of premixed flame in nozzle-generated counterflow. *Combustion and Flame,* **109,** 620-638.

120. Kelley, A.P. and Law, C.K. (2007) Nonlinear Effects in the Experimental Determination of Laminar Flame Properties from Stretched Flames. In *Eastern State Fall Technical Meeting Chemical & Physical Processes in Combustion*, University of Virginia.

121. Kelley, A.P. and Law, C.K. (2009) Nonlinear effects in the extraction of laminar flame speeds from expanding spherical flames. *Combustion and Flame,* **156,** 1844-1851.

122. Sun, C.J., Sung, C.J., He, L. and Law, C.K. (1999) Dynamics of weakly stretched flames: Quantitative description and extraction of global flame parameters. *Combustion and Flame,* **118,** 108-128.

123. Davis, S.G., Quinard, J. and Searby, G. (2001) A numerical investigation of stretch effects in counterflow, premixed laminar flames. *Combustion Theory and Modelling,* **5,** 353-362.

124. Davis, S.G., Quinard, J. and Searby, G. (2002) Determination of Markstein numbers in counterflow premixed flames. *Combustion and Flame,* **130,** 112-122.

125. Davis, S.G., Quinard, J. and Searby, G. (2002) Markstein numbers in counterflow, methane- and propane- air flames: a computational study. *Combustion and Flame,* **130,** 123-136.

126. Davis, S.G. and Searby, G. (2002) The Use of Counterflow Flames for the Evaluation of Burning Velocities and Stretch Effects in Hydrogen/Air Mixtures. *Combustion Science and Technology,* **174,** 93-110.

127. Egolfopoulos, F.N. (1994) Geometric and Radiation Effects on Steady and Unsteady Strained Laminar Flames. *Symposium (International) on Combustion* **25,** 1375-1381.

128. Milson, A. and Chigier, N.A. (1973) Studies of methane and methane-air flames impinging on a cold plate. *Combustion and Flame,* **21,** 295-305.

129. Smith, H.W., Schmitz, R.A. and Ladd, R.G. (1971) Combustion of a Premixed System in Stagnation Flow.I. Theoretical. *Combustion Science and Technology,* **4,** 131-142.

130. Fang, M., Schmitz, R.A. and Ladd, R.G. (1971) Combustion of a Premixed System in Stagnation Flow - II. Experiments with Carbon Monoxide Oxidation. *Combustion Science and Technology,* **4,** 143-148.

131. Ishizuka, S. and Law, C.K. (1982) Experimental study on extinction and stability of stretched premixed flames. *Symposium (International) on Combustion,* **19,** 327-335.

132. Ishizuka, S., Miyasaka, K. and Law, C.K. (1982) Effects of heat loss, preferential diffusion, and flame stretch on flame-front instability and extinction of propane/air mixtures. *Combustion and Flame,* **45,** 293-308.

133. Vlachos, D.G., Schmidt, L.D. and Aris, R. (1993) Ignition and extinction of flames near surfaces: Combustion of H2 in air. *Combustion and Flame,* **95,** 313-335.

134. Vlachos, D.G., Schmidt, L.D. and Aris, R. (1994) Products in methane combustion near surfaces. *AIChE Journal,* **40,** 1018-1025.

135. Egolfopoulos, F.N., Zhang, H. and Zhang, Z. (1997) Wall effects on the propagation and extinction of steady, strained, laminar premixed flames. *Combustion and Flame,* **109,** 237-252.

136. Zhang, H. (1999) An experimental and numerical study of the effects of heat loss and unsteadiness on laminar strained flames. Ph.D. thesis, University of Southern California.

137. Mendes-Lopes, J.M.C. (1983) Influence of strain fields on flame propagation. Ph.D. thesis, University of Cambridge.

138. Vagelopoulos, C.M. (1999) An experimental and numerical study on the stability and propagation of laminar premixed flames. Ph.D. thesis, University of Southern California.

139. Cuenot, B., Egolfopoulos, F.N. and Poinsot, T. (1999) Direct numerical simulations of stagnation-flow premixed flames: The phenomenon of transition from planar to Bunsen flame. In *1999 Fall Meeting of the Western States Section of the Combustion Institute.*

140. Westerweel, J. (1993) Digital particle image velocimetry: Theory and application. Ph.D. thesis, Technische Universiteit Delft, the Netherlands.

141. Westerweel, J. (1997) Fundamentals of digital particle image velocimetry. *Measurement Science and Technology,* **8,** 1379-1392.

142. Willert, C.E. and Gharib, M. (1991) Digital particle image velocimetry. *Experiments in Fluids,* **10,** 181-193.

143. Keane, R.D. and Adrian, R.J. (1990) Optimization of particle image velocimeters. I. Double pulsed systems. *Measurement Science and Technology,* **1,** 1202-1215.

144. Keane, R.D. and Adrian, R.J. (1991) Optimization of particle image velocimeters: II. Multiple pulsed systems. *Measurement Science and Technology,* **2,** 963-974.

145. Grant, I. (1997) Particle image velocimetry: a review. *Proceeding of the Institution of Mechanical Engineers, Part C: Journal of Mechanical Engineering Science,* **211,** 55-76.

146. Westerweel, J., Dabiri, D. and Gharib, M. (1997) The effect of a discrete window offset on the accuracy of cross-correlation analysis of digital PIV recordings. *Experiments in Fluids,* **23,** 20-28.

147. Scarano, F. (2002) Iterative image deformation methods in PIV. *Measurement Science and Technology,* **13,** R1-R19.

148. Smith, G.P., Golden, D.M., Frenklach, M., Moriarty, N.W., Eiteneer, B., Goldenberg, M., Bowman, C.T., Hanson, R.K., Song, S., Gardiner, W.C., Lissianski, V.V. and Qin, Z. (2006) GRI Mech. 3.0, http://www.me.berkeley.edu/gri_mech/.

149. Stella, A., Guj, G., Kompenhans, J., Raffel, M. and Richard, H. (2001) Application of particle image velocimetry to combusting flows: design considerations and uncertainty assessment. *Experiments in Fluids,* **30,** 167-180.

150. Yao, W., Guangsheng, G., Fei, W. and Jun, W. (2002) Fluidization and agglomerate structure of SiO2 nanoparticles. *Powder Technology,* **124,** 152-159.

151. Andac, M.G., Egolfopoulos, F.N., Campbell, C.S. and Lauvergne, R. (2000) Effects of Inert Dust Clouds on the Extinction of Strained, Laminar, Flames at Normal and Micro-gravity. *Symposium (International) on Combustion,* **28,** 2921-2929.

152. Andac, M.G., Egolfopoulos, F.N. and Campbell, C.S. (2002) Premixed flame extinction by inert particles in normal- and micro-gravity. *Combustion and Flame,* **129,** 179-191.

153. Keane, R.D. and Adrian, R.J. (1992) Theory of cross-correlation analysis of PIV images. *Applied Scientific Research* **49,** 191-215.

154. Nogueira, J., Lecuona, A. and Rodríguez, P.A. (2001) Identification of a new source of peak locking, analysis and its removal in conventional and super-resolution PIV techniques. *Experiments in Fluids,* **30,** 309-316.

155. Christensen, K.T. (2004) The influence of peak-locking errors on turbulence statistics computed from PIV ensembles. *Experiments in Fluids,* **36,** 484-497.

156. Gui, L. and Wereley, S.T. (2002) A correlation-based continuous window-shift technique to reduce the peak-locking effect in digital PIV image evaluation. *Experiments in Fluids,* **32,** 506-517.

157. Chen, J. and Katz, J. (2005) Elimination of peak-locking error in PIV analysis using the correlation mapping method. *Measurement Science and Technology,* **16,** 1605-1618.

158. Cholemari, M. (2007) Modeling and correction of peak-locking in digital PIV. *Experiments in Fluids,* **42,** 913-922.

159. Wernet, M.P. (2000) A flow field investigation in the diffuser of a high-speed centrifugal compressor using digital particle imaging velocimetry. *Measurement Science and Technology,* **11,** 1007-1022.

160. Press, W.H. (1996) *FORTRAN numerical recipes - in Fortran 77,* Cambridge University Press.

161. Rolon, J.C. (1988) Etude Théorique et Expérimentale de la Flamme de Diffusion à Contre-Courant. Ph.D. thesis, Ecole Centrale Paris.

162. Cohen, M.J. and Ritchie, N.J.B. (1962) Low speed three-dimensional contraction design. *Journal of the royal aeronautical society* **66,** 231-236.

163. Hsieh, W.-D. and Lin, T.-H. (2005) Methane flames in a jet impinging onto a wall. *Energy Conversion and Management,* **46,** 727-739.

164. Huang, Z., Zhang, Y., Zeng, K., Liu, B., Wang, Q. and Jiang, D. (2006) Measurements of laminar burning velocities for natural gas-hydrogen-air mixtures. *Combustion and Flame,* **146,** 302-311.

165. Halter, F., Chauveau, C., Djebaïli-Chaumeix, N. and Gökalp, I. (2005) Characterization of the effects of pressure and hydrogen concentration on laminar burning velocities of methane-hydrogen-air mixtures. *Proceedings of the Combustion Institute,* **30,** 201-208.

166. Qin, X. and Ju, Y. (2005) Measurements of burning velocities of dimethyl ether and air premixed flames at elevated pressures. *Proceedings of the Combustion Institute,* **30,** 233-240.

167. Liao, S.Y., Jiang, D.M. and Cheng, Q. (2004) Determination of laminar burning velocities for natural gas. *Fuel,* **83,** 1247-1250.

168. Tanoue, K., Shimada, F. and Hamatake, T. (2003) The Effects of Flame Stretch on Outwardly Propagating Flames. *JSME international journal. Series B, Fluids and thermal engineering,* **46,** 416-424.

169. Rozenchan, G., Zhu, D.L., Law, C.K. and Tse, S.D. (2002) Outward propagation, burning velocities, and chemical effects of methane flames up to 60 ATM. *Proceedings of the Combustion Institute,* **29,** 1461-1470.

170. Elia, M., Ulinski, M. and Metghalchi, M. (2001) Laminar Burning Velocity of Methane-Air-Diluent Mixtures. *Journal of Engineering for Gas Turbines and Power,* **123,** 190-196.

171. Hassan, M.I., Aung, K.T. and Faeth, G.M. (1998) Measured and predicted properties of laminar premixed methane/air flames at various pressures. *Combustion and Flame,* **115,** 539-550.

172. Aung, K.T., Tseng, L.K., Ismail, M.A. and Faeth, G.M. (1995) Response to comment by S.C. Taylor and D.B. Smith on "laminar burning velocities and Markstein numbers of hydrocarbon/air flames". *Combustion and Flame,* **102,** 526-530.

173. Taylor, S.C. and Smith, D.B. (1995) Comment on "laminar burning velocities and Markstein numbers of hydrocarbon/air flames" by L.-K. Tseng, M.A. Ismail, and G.M. Faeth. *Combustion and Flame,* **102,** 523-525.

174. Iijima, T. and Takeno, T. (1986) Effects of temperature and pressure on burning velocity. *Combustion and Flame,* **65,** 35-43.

175. Sharma, S.P., Agrawal, D.D. and Gupta, C.P. (1981) The pressure and temperature dependance of burning velocity in a spherical combustion bomb. *Symposium (International) on Combustion* **18,** 493-501.

176. Agrawal, D.D. (1981) Experimental determination of burning velocity of methane-air mixtures in a constant volume vessel. *Combustion and Flame,* **42,** 243-252.

177. Burke, M.P., Chen, Z., Ju, Y. and Dryer, F.L. (2009) Effect of cylindrical confinement on the determination of laminar flame speeds using outwardly propagating flames. *Combustion and Flame,* **156,** 771-779.

178. Dyakov, I.V., Konnov, A.A., De Ruyck, J., Bosschaart, K.J., Brock, E.C.M. and De Goey, L.P.H. (2001) Measurement of adiabatic burning velocity in methane-oxygen-nitrogen mixtures. *Combustion Science and Technology,* **172,** 81-96.

179. Law, C.K. (2006) *Combustion physics,* Cambridge University Press.

180. El Bakali, A., Pillier, L., Desgroux, P., Lefort, B., Gasnot, L., Pauwels, J.F. and Da Costa, I. (2006) NO prediction in natural gas flames using GDF-Kin®3.0 mechanism NCN and HCN contribution to prompt-NO formation. *Fuel,* **85,** 896-909.

181. Konnov, A.A. (2009) Implementation of the NCN pathway of prompt-NO formation in the detailed reaction mechanism. *Combustion and Flame,* **156,** 2093-2105.

182. Le Cong, T. (2007) Etude expérimentale et modélisation de la cinétique de combustion de combustibles gazeux : Méthane, gaz naturel et mélanges contenant de l'hydrogène, du monoxyde de carbone, du dioxyde de carbone et de l'eau. Ph.D. thesis, Orléans, France.

183. Turànyi, T., Zalotai, L., Dóbé, S. and Bérces, T. (2002) Effect of the uncertainty of kinetic and thermodynamic data on methane flame simulation results. *Physical Chemistry Chemical Physics,* **4,** 2568-2578.

184. Lim, J. (1998) A study of the effects of preheat and steam addition on the flame structure and NO formation in laminar counterflow flames. Ph.D. thesis, Purdue University.

185. Wu, C.Y., Chao, Y.C., Cheng, T.S., Chen, C.P. and Ho, C.T. (2009) Effects of CO addition on the characteristics of laminar premixed CH4/air opposed-jet flames. *Combustion and Flame,* **156,** 362-373.

186. Tomboulides, A.G., Lee, J.C.Y. and Orszag, S.A. (1997) Numerical Simulation of Low Mach Number Reactive Flows. *Journal of Scientific Computing,* **12,** 139-167.

187. Frouzakis, C.E., Lee, J., Tomboulides, A.G. and Boulouchos, K. (1998) Two-Dimensional Direct Numerical Simulation of Opposed-Jet Hydrogen-Air Diffusion Flame. *Symposium (International) on Combustion,* **27,** 571–577.

188. Amantini, G., Frank, J.H., Smooke, M.D. and Gomez, A. (2007) Computational and experimental study of steady axisymmetric non-premixed methane counterflow flames. *Combustion Theory and Modelling,* **11,** 47-72.

189. Oh, C.B., Lee, C.E. and Park, J. (2004) Numerical investigation of extinction in a counterflow nonpremixed flame perturbed by a vortex. *Combustion and Flame,* **138,** 225-241.

190. Katta, V.R., Carter, C.D., Fiechtner, G.J., Roquemore, W.M., Gord, J.R. and Rolon, J.C. (1998) Interaction of a vortex with a flat flame formed between opposing jets of hydrogen and air. *Symposium (International) on Combustion,* **27,** 587-594.

191. Katta, V.R., Hsu, K.Y. and Roquemore, W.M. (1998) Local extinction in an unsteady methane-air jet diffusion flame. *Symposium (International) on Combustion,* **27,** 1121-1129.

192. Katta, V.R., Meyer, T.R., Brown, M.S., Gord, J.R. and Roquemore, W.M. (2004) Extinction criterion for unsteady, opposing-jet diffusion flames. *Combustion and Flame,* **137,** 198-221.

193. Oh, C.B., Hamins, A., Bundy, M. and Park, J. (2008) The two-dimensional structure of low strain rate counterflow nonpremixed-methane flames in normal and microgravity. *Combustion Theory and Modelling,* **12,** 283-302.

194. Frouzakis, C.E., Tomboulides, A.G., Lee, J. and Boulouchos, K. (2002) Transient phenomena during diffusion/edge flame transitions in an opposed-jet hydrogen/air burner. *Proceedings of the Combustion Institute,* **29,** 1581-1587.

195. Lee, J., Frouzakis, C.E. and Boulouchos, K. (2000) Two-dimensional numerical simulation of opposed-jet hydrogen/air flames/transition from a diffusion to an edge flame. *Symposium (International) on Combustion,* **28,** 801-806.

196. Smooke, M. and Giovangigli, V. (1995) Simplified transport and reduced chemistry models of premixed and nonpremixed combustion. In *Modeling in Combustion Science*, 79-106, Springer, Berlin/Heidelberg.

197. Hirschfelder, J.O., Curtiss, C.F. and Bird, R.B. (1954) *Molecular Theory of Gases and Liquids,* Wiley, New York.

198. Hassan, M.I., Aung, K.T. and Faeth, G.M. (1997) Properties of Laminar Premixed CO/H2/Air Flames at Various Pressures. *Journal of Propulsion and Power,* **13,** 239-245.

199. Mclean, I.C., Smith, D.B. and Taylor, S.C. (1994) The use of carbon monoxide/hydrogen burning velocities to examine the rate of the CO+OH reaction. *Symposium (International) on Combustion,* **25,** 749-757.

200. Sun, H., Yang, S.I., Jomaas, G. and Law, C.K. (2007) High-pressure laminar flame speeds and kinetic modeling of carbon monoxide/hydrogen combustion. *Proceedings of the Combustion Institute,* **31,** 439-446.

201. Chaos, M. and Dryer, F.L. (2008) Syngas Combustion Kinetics and Applications. *Combustion Science and Technology,* **180,** 1053-1096.

202. Natarajan, J., Kochar, Y., Lieuwen, T. and Seitzman, J. (2009) Pressure and preheat dependence of laminar flame speeds of H2/CO/CO2/O2/He mixtures. *Proceedings of the Combustion Institute,* **32,** 1261-1268.

203. Bunkute, B. and Moss, J.B. (2007) Laminar Burning Velocities of Carbon Monoxide/Hydrogen – Air Mixtures at High Temperatures and Pressures. In *Third european combustion meeting ECM 2007.*

204. Badami, G.N. and Egerton, A. (1955) The Determination of Burning Velocities of Slow Flames. *Proceedings of the Royal Society of London. Series A, Mathematical and Physical Sciences,* **228,** 297-322.

205. Scholte, T.G. and Vaags, P.B. (1959) The influence of small quantities of hydrogen and hydrogen compounds on the burning velocity of carbon monoxide-air flames. *Combustion and Flame,* **3,** 503-510.

206. Scholte, T.G. and Vaags, P.B. (1959) Burning velocities of mixtures of hydrogen, carbon monoxide and methane with air. *Combustion and Flame,* **3,** 511-524.

207. Yumlu, V.S. (1967) Prediction of burning velocities of carbon monoxide-hydrogen-air flames. *Combustion and Flame,* **11,** 190-194.

208. Günther, R. and Janisch, G. (1971) Messwerte der Flammengeschwindigkeit von Gasen und Gasgemischen. *Chemie-Ing.-Techn.,* **43**.

209. Brown, M.J., Mclean, I.C., Smith, D.B. and Taylor, S.C. (1996) Markstein lenghts of CO/H2/Air flames using expanding spherical flames. *Symposium (International) on Combustion,* **26,** 875-881.

210. Serrano, C., Hernandez, J.J., Mandilas, C., Sheppard, C.G.W. and Woolley, R. (2007) Laminar burning behaviour of biomass gasification-derived producer gas. *International Journal of Hydrogen Energy,* **33,** 851-862.

211. Natarajan, J., Nandula, S., Lieuwen, T. and Seitzman, J. (2005) Laminar flame speed of synthetic gas fuel mixtures. In *ASME Turbo Expo 2005: Power for Land, Sea and Air*, June 6-9, Reno-Tahoe, Nevada, USA.

212. Prathap, C., Ray, A. and Ravi, M.R. (2008) Investigation of nitrogen dilution effects on the laminar burning velocity and flame stability of syngas fuel at atmospheric condition. *Combustion and Flame,* **155,** 145-160.

213. Burke, M.P., Qin, X., Ju, Y. and Dryer, F.L. (2007) Measurements of Hydrogen Syngas Flame Speeds at Elevated Pressures. In *5th US Combustion Meeting*, March 25-28, University of California at San Diego.

214. Dong, C., Zhou, Q., Zhao, Q., Zhang, Y., Xu, T. and Hui, S. (2009) Experimental study on the laminar flame speed of hydrogen/carbon monoxide/air mixtures. *Fuel,* **88,** 1858-1863.

215. Natarajan, J., Kochar, Y., Lieuwen, T. and Seitzman, J. (2008) Laminar Flame Speed Measurements of H2/CO/CO2 Mixtures Up to 15 atm and 600 K Preheat Temperature. In *ASME Turbo Expo 2008: Power for Land, Sea and Air GT2008*, Berlin, Germany.

216. Durox, D., Schuller, T. and Candel, S. (2002) Self-induced instability of a premixed jet flame impinging on a plate. *Proceedings of the Combustion Institute,* **29,** 69-75.

217. Higman, C. and Van Der Burgt, M. (2003) *Gasification,* Elsevier/Gulf Professional Pub., Burlington, MA.

218. Rumminger, M.D. and Linteris, G.T. (2000) Inhibition of premixed carbon monoxide-hydrogen-oxygen-nitrogen flames by iron pentacarbonyl. *Combustion and Flame,* **120,** 451-464.

219. Egerton, A. and Rudrakanchana, S. (1954) The Combustion of Some Organo-Metallic Compounds. *Proceedings of the Royal Society of London. Series A, Mathematical and Physical Sciences,* **225,** 427-443.

220. Williams, T.C. and Shaddix, C.R. (2007) Contamination of Carbon Monoxide with Metal Carbonyls: Implications for Combustion Research. *Combustion Science and Technology,* **179,** 1225-1230.

221. Konnov, A.A., Ãlvarez, G.P., Rybitskaya, I.V. and Ruyck, J.D. (2009) The Effects of Enrichment by Carbon Monoxide on Adiabatic Burning Velocity and Nitric Oxide Formation in Methane Flames. *Combustion Science and Technology,* **181,** 117-135.

222. Pearse, R.W.B. and Gaydon, A.G. (1976) *The Identification of Molecular Spectra,* Wiley, London, New York.

223. Li, J., Zhao, Z., Kazakov, A., Chaos, M., Dryer, F.L. and Scire, J.J. (2007) A comprehensive kinetic mechanism for CO, CH2O, and CH3OH combustion. *International Journal of Chemical Kinetics,* **39,** 109-136.

224. Law, C.K. (1989) Dynamics of Stretched Flames. *Symposium (International) on Combustion,* **22,** 1381-1402.

225. Law, C.K., Jomaas, G. and Bechtold, J.K. (2005) Cellular instabilities of expanding hydrogen/propane spherical flames at elevated pressures: theory and experiment. *Proceedings of the Combustion Institute,* **30,** 159-167.

226. Matalon, M., Cui, C. and Bechtold, J.K. (2003) Hydrodynamic theory of premixed flames: effects of stoichiometry, variable transport coefficients and arbitrary reaction orders. *Journal of Fluid Mechanics,* **487,** 179-210.

227. Matalon, M. (2009) Flame dynamics. *Proceedings of the Combustion Institute,* **32,** 57-82.

228. Rumminger, M.D., Reinelt, D., Babushok, V. and Linteris, G.T. (1999) Numerical study of the inhibition of premixed and diffusion flames by iron pentacarbonyl. *Combustion and Flame,* **116,** 207-219.

229. Tepe, R.K., Vassallo, D., Jacksier, T. and Barnes, R.M. (1999) Iron pentacarbonyl determination in carbon monoxide. *Spectrochimica Acta Part B: Atomic Spectroscopy,* **54,** 1861-1868.

230. Li, J., Zhao, Z., Kazakov, A., Chaos, M., Dryer, F.L. and Scire, J., James J. (2007) A comprehensive kinetic mechanism for CO, CH2O, and CH3OH combustion. *International Journal of Chemical Kinetics,* **39,** 109-136.

231. Hessler, J.P. (1998) Calculation of Reactive Cross Sections and Microcanonical Rates from Kinetic and Thermochemical Data. *The Journal of Physical Chemistry A,* **102,** 4517-4526.

232. Hwang, S.M., Ryu, S.-O., Witt, K.J.D. and Rabinowitz, M.J. (2005) High temperature rate coefficient measurements of H + O2 chain-branching and chain-terminating reaction. *Chemical Physics Letters,* **408,** 107-111.

233. Mueller, M.A., Kim, T.J., Yetter, R.A. and Dryer, F.L. (1999) Flow reactor studies and kinetic modeling of the H2/O2 reaction. *International Journal of Chemical Kinetics,* **31,** 113-125.

234. Dash, C.J. (1992) One-dimensionnal tomography: a comparision of Abel, onion-peeling and filterd backprojection methods. *Applied Optics,* **31,** 1146-1152.

235. Lewis, B. and Von Elbe, G. (1987) *Combustion, flames, and explosions of gases,* 3rd Ed., Academic Press.

236. Echekki, T. and Mungal, M.G. (1990) Flame speed measurements at the tip of a slot burner: effect of flame curvature and hydrodynamic stretch. *Symposium (International) on Combustion,* **23,** 455-461.

237. Law, C.K., Ishizuka, S. and Cho, P. (1982) On the opening of premixed Bunsen flame tips. *Combustion Science and Technology,* **28,** 89-96.

238. Mizomoto, M., Asaka, Y., Ikai, S. and Law, C.K. (1985) Effects of preferential diffusion on the burning intensity of curved flames. *Symposium (International) on Combustion,* **20,** 1933-1939.

239. Mizomoto, M. and Yoshida, H. (1987) Effects of Lewis number on the burning intensity of Bunsen flames. *Combustion and Flame,* **70,** 47-60.

240. Sakai, Y., Konishi, K. and Ishihara, A. (1996) Tip opening and burning intensity of Bunsen flames diluted with nitrogen. *JSME International Journal, Series B: Fluids and Thermal Engineering,* **39,** 164-170.

241. Ishizuka, S. (1982) An experimental study on the opening of laminar diffusion flame tips. *Symposium (International) on Combustion,* **19,** 319-326.

242. Kozlovsky, G. and Sivashinsky, G.I. (1994) On open and closed tips of bunsen burner flames. *Theoretical and Computational Fluid Dynamics,* **6,** 181-192.

243. Lamoureux, N., Djebaili-Chaumeix, N. and Paillard, C.E. (2003) Laminar flame velocity determination for H2-air-He-CO2 mixtures using the spherical bomb method. *Experimental Thermal and Fluid Science,* **27,** 385-393.

244. Qin, X., Kobayashi, H. and Niioka, T. (2000) Laminar burning velocity of hydrogen-air premixed flames at elevated pressure. *Experimental Thermal and Fluid Science,* **21,** 58-63.

245. Tse, S.D., Zhu, D.L. and Law, C.K. (2000) Morphology and Burning Rates of Expanding Spherical Flames in H2/O2/Inert Mixtures up to 60 Atmosphere. *Symposium (International) on Combustion,* **28,** 1793-1800.

246. Raman, K.S. (1998) Laminar Burning Velocities of Lean Hydrogen-Air Mixtures, Report FM97-15. Explosion Dynamics Laboratory, California Institute of Technology, Pasadena, CA.

247. Koroll, G.W., Kumar, R.K. and Bowles, E.M. (1993) Burning velocities of hydrogen-air mixtures. *Combustion and Flame,* **94,** 330-340.

248. Dowdy, D.R. (1990) The Use of Expanding Spherical Flames to Determine Burning Velocities and Stretch Effects in Hydrogen/Air Mixtures. *Symposium (International) on Combustion,* **23,** 325-332.

249. Tahtouh, T., Halter, F. and Mounaïm-Rousselle, C. (2009) Measurement of laminar burning speeds and Markstein lengths using a novel methodology. *Combustion and Flame,* **156,** 1735-1743.

250. Settles, G.S. (2001) *Schlieren and shadowgraph techniques : visualizing phenomena in transparent media,* Springer-Verlag, Berlin, New York.

251. Chen, Z., Burke, M.P. and Ju, Y. (2009) Effects of Lewis number and ignition energy on the determination of laminar flame speed using propagating spherical flames. *Proceedings of the Combustion Institute,* **32,** 1253-1260.

252. Kelley, A.P., Jomaas, G. and Law, C.K. (2009) Critical radius for sustained propagation of spark-ignited spherical flames. *Combustion and Flame,* **156,** 1006-1013.

253. Matalon, M. and Matkowsky, B.J. (1983) Flames in Fluids: Their Interaction and Stability. *Combustion Science and Technology,* **34,** 295-316.

254. Clavin, P. (1985) Dynamic behavior of premixed flame fronts in laminar and turbulent flows. *Progress in Energy and Combustion Science,* **11,** 1-59.

255. Law, C.K. and Sung, C.J. (2000) Structure, aerodynamics, and geometry of premixed flamelets. *Progress in Energy and Combustion Science,* **26,** 459-505.

256. Kee, R.J., Rupley, F.M., Miller, J.A., Coltrin, M.E., Grcar, J.F., Meeks, E., Moffat, H.K., Lutz, A.E., Dixon-Lewis, G., Smooke, M.D., Warnatz, J., Evans, G.H., Larson, R.S., Mitchell, R.E., Petzold, L.R., Reynolds, W.C., Caracotsios, M., Stewart, W.E., Glarborg, P., Wang, C., Adigun, O., Houf, W.G., Chou, C.P. and Miller, S.F. (2003) Chemkin Collection. Reaction Design, Inc., San Diego, CA.

257. Ronney, P.D. and Sivashinsky, G.I. (1989) A Theoretical Study of Propagation and Extinction of Nonsteady Spherical Flame Fronts. *SIAM Journal on Applied Mathematics,* **49,** 1029-1046.

258. Halter, H., Tahtouh, T. and Mounaïm-Rousselle, C. (2009) Nonlinear effects of stretch on the flame front propagation. *Submitted to Combustion and Flame.*

List of Symbols

Dimensions: [M] Mass, [L] Length, [T] Time, [K] Temperature.

Chapter I

Ch.I - Roman Capitals		**Units**	**Dimension**
A	Infinitesimal element of the flame surface	m^2	[L^2]
C_p	Mixture mass heat capacity	J.kg^{-1}.K^{-1}	[L^{2}T^{-2}K^{-1}]
$C_{p,k}$	Mass heat capacity of species k	J.kg^{-1}.K^{-1}	[L^{2}T^{-2}K^{-1}]
D_T	Mixture thermal diffusivity	m^2.s^{-1}	[L^{2}T^{-1}]
$D_{l,k}$	Binary diffusion coefficient for the l^{th} and k^{th} species	m^2.s^{-1}	[L^{2}T^{-1}]
D_{mol}	Species diffusivity	m^2.s^{-1}	[L^{2}T^{-1}]
$F(x)$	Stream function related to the gas normal velocity	kg.m^{-2}.s^{-1}	[ML^{-2}T^{-1}]
$G(x)$	Stream function related to the gas tangential velocity	kg.m^{-3}.s^{-1}	[ML^{-3}T^{-1}]
H	Normalized radial pressure gradient	Pa.m^{-2}	[ML^{-3}T^{-2}]
$J_{k,i}$	Diffusion mass flux (PREMIX-OPPDIF formalism)	kg.m^{-2}.s^{-1}	[ML^{-2}T^{-1}]
$J'_{k,i}$	Diffusion mass flux (Fluent formalism)	kg.m^{-2}.s^{-1}	[ML^{-2}T^{-1}]
K	Stretch rate	s^{-1}	[T^{-1}]
Ka	Karlovitz number	-	-
L	Markstein Length	-	-
Le	Lewis number	-	-
Ma	Markstein number	-	-
N	Number of chemical species	-	-
Q	Heat source term	J.m^{-3}.s^{-1}	[ML^{-1}T^{-3}]
R	Perfect gas constant	J.K^{-1}.mol^{-1}	[ML^{2}T^{-2}K^{-1}]
R_c	Conical flame radius (Distance from the centerline axis to the flame surface)	m	[L]
R_s	Spherical flame radius	m	[L]
S_u	Stretched laminar flame speed	m.s^{-1}	[LT^{-1}]
S_u^0	Fundamental flame speed	m.s^{-1}	[LT^{-1}]
$S_{u,ref}$	Reference flame speed (for counterflow flames)	m.s^{-1}	[LT^{-1}]
T	Temperature	K	[K]
$V_{k,i}$	Diffusion velocity of the species k in the direction i	m.s^{-1}	[LT^{-1}]
W	Mean molecular weight of the mixture	kg.mol^{-1}	[M]
W_k	Molar mass of the species k	kg.mol^{-1}	[M]
X_k	Molar fraction of the species k	-	-
Y_k	Mass fraction of the species k	-	-

Ch.I - Lower-Case Roman		**Units**	**Dimension**
a	Radial velocity gradient in counterflow flames	s^{-1}	[T^{-1}]
a_p	Fully developed potential flow velocity gradient	s^{-1}	[T^{-1}]
d_k	Diffusion coefficient of the species k (PREMIX-OPPDIF formalism)	m^2.s^{-1}	[L^{2}T^{-1}]
d'_k	Diffusion coefficient of the species k (Fluent formalism)	m^2.s^{-1}	[L^{2}T^{-1}]
$f_{k,j}$	Volume force acting on species in the direction j	m.s^{-2}	[LT^{-2}]
h_k	Specific enthalpy of the species k	J.kg^{-1}	[L^{2}T^{-2}]
$\boldsymbol{n}$	Normal to the flame front oriented towards fresh gases	-	-
p	Pressure	Pa	[ML^{-1}T^{-2}]
r	Radius in cylindrical coordinates	m	[L]

t	Time	s	[T]
$\boldsymbol{u}$	Local flame velocity vector evaluated on the flame temperature isolevel	m.s^{-1}	[LT^{-1}]
u	Gas normal velocity component	m.s^{-1}	[LT^{-1}]
u_n	Absolute speed at which the flame front is moving with respect to the laboratory frame	m.s^{-1}	[LT^{-1}]
u_i	Flow velocity in the direction *i*	m.s^{-1}	[LT^{-1}]
$\boldsymbol{v}$	Local flow velocity vector evaluated at a chosen fresh gases temperature isolevel	m.s^{-1}	[LT^{-1}]
v	Gas Tangential velocity component	m.s^{-1}	[LT^{-1}]
v_n	Fresh gas inlet speed with respect to the laboratory frame	m.s^{-1}	[LT^{-1}]
$\boldsymbol{v_s}$	Tangential velocity component of the flow velocity at the flame surface	m.s^{-1}	[LT^{-1}]
$\boldsymbol{v_{s,t}}$	Defined in expression I-2	m.s^{-1}	[LT^{-1}]
v_z	Axial velocity in the cylindrical coordinate system	m.s^{-1}	[LT^{-1}]
x	Component in rectangular coordinates	m	[L]
x_i	Component in rectangular coordinates in the *i* direction	m	[L]
y	Component in rectangular coordinates	m	[L]
z	Axial component in cylindrical coordinates	m	[L]

Ch.I - Greek		**Units**	**Dimension**
α	Flame cone angle	-	-
β	Reduced activation energy	-	-
γ	Gas expansion parameter	-	-
δ	Flame thickness (Thermal diffusivity definition)	m	[L]
δ_{ij}	Kronecker symbol	-	-
$\varepsilon(x)$	Non-constant coefficient of the first order differential equation for the density in the stagnation flow configuration (see expression I-33 and I-34)	m^{-1}	[L^{-1}]
$\phi_{k,l}$	Mixture averaged viscosity function (see I-38 and I-39)	-	-
λ	Mixture thermal conductivity	W.m^{-1}.K^{-1}	[MLT^{-3}K^{-1}]
λ_k	Thermal conductivity of the species *k*	W.m^{-1}.K^{-1}	[MLT^{-3}K^{-1}]
μ	Dynamic viscosity	Pa.s	[ML^{-1}T^{-1}]
μ_k	Dynamic viscosity of the species *k*	Pa.s	[ML^{-1}T^{-1}]
θ	Angle in cylindrical coordinates	-	-
ρ	Mixture density	kg.m^{-3}	[ML^{-3}]
ρ_b	Burned gas density	kg.m^{-3}	[ML^{-3}]
ρ_u	Unburned gas density	kg.m^{-3}	[ML^{-3}]
τ_{ij}	Viscous tensor	Pa	[ML^{-1}T^{-2}]
$\dot{\omega}_k$	Reaction rate of species *k*	kg.m^{-3}.s^{-1}	[ML^{-3}T^{-1}]
$\dot{\omega}_T$	Heat release	J.m^{-3}.s^{-1}	[ML^{-1}T^{-3}]

Chapter II

Ch.II - Roman Capitals		**Units**	**Dimension**
B	Particle mobility	s.kg^{-1}	[M^{-1}T]
C	Cunningham slip correction factor	-	-
C_m	Constant in the thermophoretic force formulation II-16	-	-
C_s	Constant in the thermophoretic force formulation II-16	-	-
C_t	Constant in the thermophoretic force formulation II-16	-	-

D	Burner diameter	m	[L]
D_t	Thermophoretic diffusivity	$m^2.s^{-1}$	$[L^2T^{-1}]$
F_G	Gravitational force	N	$[MLT^{-2}]$
F_{SD}	Stokes drag force	N	$[MLT^{-2}]$
FVL	Fractional velocity lag	%	-
G	Stream function related to the gas tangential velocity	$kg.m^{-3}.s^{-1}$	$[ML^{-3}T^{-1}]$
K	Strain rate	s^{-1}	[T]
Ka	Karlovitz number	-	-
Kn	Knudsen number	-	-
L	Distance between nozzles (or alternatively twice the burner to stagnation plate distance)	m	[L]
Le	Lewis number	-	-
L_{sp}	Burner-to-plate separation distance	m	[L]
L_u	Unburned Markstein length	m	[L]
Ma	Markstein length	-	-
P	Pressure	Pa	$[ML^{-1}T^{-2}]$
Re_p	Particle Reynolds number	-	-
S_b	Axial flow velocity	$m.s^{-1}$	$[LT^{-1}]$
S_b^0	Downstream fundamental flame speed (extracted from the burned gas side)	$m.s^{-1}$	$[LT^{-1}]$
S_u	Upstream flame speed	$m.s^{-1}$	$[LT^{-1}]$
S_u^0	Fundamental flame speed	$m.s^{-1}$	$[LT^{-1}]$
$S_{u,ref}$	Reference flame speed	$m.s^{-1}$	$[LT^{-1}]$
T	Temperature	K	[T]
T_0	Mean gas temperature in the vicinity of the particle	K	[T]
Ze	Zeldovich number	-	-

Ch.II - Lower-Case Roman		**Units**	**Dimension**
a	Radial velocity gradient	s^{-1}	$[T^{-1}]$
$\bar{c}$	Mean velocity of the gaseous molecules	$m.s^{-1}$	$[LT^{-1}]$
d_p	Particle diameter	m	[L]
g	Gravitational acceleration under normal gravity conditions	$m.s^{-2}$	$[LT^{-2}]$
k_f	Fluid thermal conductivity	$W.m^{-1}.K^{-1}$	$[MLT^{-3}K^{-1}]$
k_p	Particle thermal conductivity	$W.m^{-1}.K^{-1}$	$[MLT^{-3}K^{-1}]$
m_p	Particle mass	kg	[M]
v_f	Fluid velocity	$m.s^{-1}$	$[LT^{-1}]$
v_p	Particle velocity	$m.s^{-1}$	$[LT^{-1}]$
v_t	Particle drift velocity induce by the thermophoretic force	$m.s^{-1}$	$[LT^{-1}]$
t	Time	s	[T]

Ch.II - Greek		**Units**	**Dimension**
α	Coefficient of the Cunningham slip correction factor (Knudsen-Weber formulation)	-	-
β	Coefficient of the Cunningham slip correction factor (Knudsen-Weber formulation)	-	-
δ	Flame thickness	m	[L]
Δ	Thermal expansion factor in expression II-20	-	-
γ	Coefficient of the Cunningham slip correction factor (Knudsen-Weber formulation)	-	-
ϕ	Dimensionless parameter given by the gas kinetic theory	-	-

	(see expression II-9)		
λ	Mean free path of gaseous molecules	m	[L]
μ	Fluid dynamic viscosity	Pa.s	[ML^{-1}T^{-1}]
η	Kinematic viscosity	m^2.s^{-1}	[L^{2}T^{-1}]
ρ_f	Fuid density	kg.m^{-3}	[ML^{-3}]
ρ_p	Particle density	kg.m^{-3}	[ML^{-3}]
σ	Thermal expansion parameter	-	-
τ_s	Particle relaxation time	s	[T]

Chapter III

Ch.III - Roman Capitals		**Units**	**Dimension**
$C(x,y)$	Discrete cross-correlation function	-	-
D_0	PIV detectability threshold	-	-
D_T	Mixture thermal diffusivity	m^2.s^{-1}	[L^{2}T^{-1}]
$I(i,j)$	(i^{th}, j^{th}) pixel intensity within the interrogation spot on the first frame	-	-
$I'(i,j)$	(i^{th}, j^{th}) pixel intensity within the interrogation spot on the second frame	-	-
K	Strain rate (determined from the axial velocity profile)	s^{-1}	[T]
K_{low}	Lowest strain rate achieved for a PIV series	s^{-1}	[T]
K_r	Strain rate (determined from the radial velocity profile)	s^{-1}	[T]
L	Burner-to-burner separation distance	m	[L]
L_{sp}	Burner-to-plate separation distance	m	[L]
M	PIV optical system magnification	-	-
N	Size in pixels of a square interrogation spot	Pixel	-
N_{dp}	Number of points per PIV series	-	-
N_p	Particle image density	-	-
S_u^0	Fundamental flame speed	m.s^{-1}	[LT^{-1}]
$S_{u,ref}$	Reference flame speed	m.s^{-1}	[LT^{-1}]
T	Temperature	K	[K]
T_b	Burned gas temperature	K	[K]
T_u	Unburned gas temperature	K	[K]
U	Normal velocity	m.s^{-1}	[LT^{-1}]
V	Tangential velocity	m.s^{-1}	[LT^{-1}]
X	Normal coordinate	m	[L]
Y	Tangential coordinate	m	[L]
Ze	Zeldovich number	-	-

Ch.III - Lower-Case Roman		**Units**	**Dimension**
d_p	Particle diameter	m	[L]
d_{spot}	Interrogation spot size (CCD side)	m	[L]
f	Lens focal distance	m	[L]
i	Pixel coordinate within an interrogation spot (*i* direction)	-	-
$\tilde{\imath}$	*i*-component of the highest peak location on the cross-correlation map		
j	Pixel coordinate within an interrogation spot (*j* direction)	-	-
$\tilde{\jmath}$	*j*-component of the highest peak location on the cross-correlation map	-	-

w	Transverse velocity component of a seeding particle	$m.s^{-1}$	$[LT^{-1}]$
x	Component of the cross-correlation “hypothetical” displacement vector (*i* direction)	Pixel	-
x_0	Total displacement component (*i* direction)	Pixel	-
y	Component of the cross-correlation “hypothetical” displacement vector (*j* direction)	Pixel	-
y_0	Total displacement component (*j* direction)	Pixel	-
r	Radius in cylindrical coordinates	m	[L]

Ch.III - Greek		**Units**	**Dimension**
δ	Flame thickness (Thermal diffusion definition)	m	[L]
δ_{ch}	Flame thickness (Chemical reaction zone definition)	m	[L]
δ_{th}	Flame thickness (Temperature gradient definition)	m	[L]
ΔK_r	Strain rate range achieved for combined PIV series	s^{-1}	[T]
Δt	Laser pulse delay	s	[T]
Δu	Velocity gradient within an interrogation spot	$m.s^{-1}$	$[LT^{-1}]$
Δx	Particle displacement within an interrogation spot	m	[L]
Δz	Particle transverse displacement	m	[L]
Δz_0	Laser sheet thickness	m	[L]
σ	Standard deviation	cf. related variable	cf. related variable
ρ_p	Particle density	$kg.m^{-3}$	$[ML^{-3}]$

Chapter IV

Ch.IV - Roman Capitals		**Units**	**Dimension**
A_0	Cross section area at the nozzle burner exit	m^2	$[L^2]$
A_u	Upstream unburned streamtube area	m^2	$[L^2]$
A_T	Streamtube area at the beginning of the flame thermal zone	m^2	$[L^2]$
C	Cunningham slip correction factor	-	-
C_m	Constant in the thermophoretic coefficient (formulation IV-7)	-	-
C_s	Constant in the thermophoretic coefficient (formulation IV-7)	-	-
C_t	Constant in the thermophoretic coefficient (formulation IV-7)	-	-
C_{th}	Thermophoretic coefficient	J	$[ML^2T^{-2}]$
D	Burner diameter	m	[L]
F_D	Aerodynamic drag coefficient	s^{-1}	$[T^{-1}]$
$F(x)$	Stream function related to the gas normal velocity	$kg.m^{-2}.s^{-1}$	$[ML^{-2}T^{-1}]$
$G(x)$	Stream function related to the gas tangential velocity	$kg.m^{-3}.s^{-1}$	$[ML^{-3}T^{-1}]$
H	Normalized radial pressure gradient	$Pa.m^{-2}$	$[ML^{-3}T^{-2}]$
K	Strain rate (determined from the axial velocity profile)	s^{-1}	[T]
K_g	General formulation of the strain rate including variable density effects	s^{-1}	[T]
Kn	Knudsen number	-	-
K_r	Strain rate (determined from the radial velocity profile)	s^{-1}	[T]
L	Burner-to-burner separation distance	m	[L]
Le	Lewis number	-	-
L_{sp}	Burner-to-plate separation distance	m	[L]

Q	Volumetric flow rate	$m^3.s^{-1}$	$[L^3T^{-1}]$
R_0	Center nozzle radius for the 7 mm I.D. burner	m	[L]
S_u	Upstream flame speed	$m.s^{-1}$	$[LT^{-1}]$
S_u^0	Fundamental flame speed	$m.s^{-1}$	$[LT^{-1}]$
$S_{u,ref}$	Reference flame speed	$m.s^{-1}$	$[LT^{-1}]$
T	Temperature	K	[K]
T_p	Particle temperature	K	[K]
T_0	Mean gas temperature in the vicinity of the particle	K	[T]
T_∞	Ambient temperature far from the stainless steel plate	K	[K]
T_w	Disk wall temperature	K	[K]
U, u	Normal velocity	$m.s^{-1}$	$[LT^{-1}]$
U_0	Mean velocity at the nozzle burner exit	$m.s^{-1}$	$[LT^{-1}]$
X, x	Normal coordinate	m	[L]
Y, y	Tangential coordinate	m	[L]
Y_{N_2}	Mass fraction of N_2	-	-
Y_{CO}	Mass fraction of CO	-	-

Ch.IV - Lower-Case Roman		**Units**	**Dimension**
a	Radial velocity gradient	s^{-1}	$[T^{-1}]$
a_{th}	Particle acceleration due to the thermophoretic force	$m.s^{-2}$	$[LT^{-2}]$
d_p	Particle diameter	m	[L]
g_x	Gravity acceleration	$m.s^{-2}$	$[LT^{-2}]$
m_p	Particle mass	kg	[M]
p	Pressure	Pa	$[ML^{-1}T^{-2}]$
q_{rad}	Radiative heat flux of the stainless steel stagnation plate	$W.m^{-2}$	$[MT^{-3}]$
r	Radius in cylindrical coordinates	m	[L]
u_f	Fluid velocity (normal direction)	$m.s^{-1}$	$[LT^{-1}]$
u_p	Particle velocity (normal direction)	$m.s^{-1}$	$[LT^{-1}]$
x_p	Particle position	m	[L]
t	Time	s	[T]

Ch.IV - Greek		**Units**	**Dimension**
Δt	Laser pulse delay	s	[T]
ϵ	Effective emissivity of the stainless steel plate	-	-
λ	Mixture thermal conductivity	$W.m^{-1}.K^{-1}$	$[MLT^{-3}K^{-1}]$
k_f	Fluid thermal conductivity	$W.m^{-1}.K^{-1}$	$[MLT^{-3}K^{-1}]$
k_p	Particle thermal conductivity	$W.m^{-1}.K^{-1}$	$[MLT^{-3}K^{-1}]$
μ	Mixture dynamic viscosity	Pa.s	$[ML^{-1}T^{-1}]$
η	Mixture kinematic viscosity	$m^2.s^{-1}$	$[L^2T^{-1}]$
ρ	Mixture density	$kg.m^{-3}$	$[ML^{-3}]$
ρ_f	Fuid density	$kg.m^{-3}$	$[ML^{-3}]$
ρ_p	Particle density	$kg.m^{-3}$	$[ML^{-3}]$
σ	Stefan-Boltzmann constant	$W.m^{-2}.K^{-4}$	$[MT^{-3}K^{-4}]$

Chapter V

Ch.V - Roman Capitals		**Units**	**Dimension**
D_T	Mixture thermal diffusivity	$m^2.s^{-1}$	$[L^2T^{-1}]$

Ka	Karlovitz number	-	-
K_r	Strain rate (determined from the radial velocity profile)	s^{-1}	[T]
Le	Lewis number	-	-
Le_{CO}	CO-based Lewis number	-	-
L_{eff}	Effective Lewis number (Y_i weighted)	-	-
Le_{H_2}	H_2-based Lewis number	-	-
Le_{O_2}	O_2-based Lewis number	-	-
L_{sp}	Burner-to-plate separation distance	m	[L]
Q	Heat of reaction	J.kg^{-1}	$[L^2T^{-2}]$
P	Pressure	Pa	$[ML^{-1}T^{-2}]$
S_u^0	Fundamental flame speed	m.s^{-1}	$[LT^{-1}]$
$S_{u,ref}$	Reference flame speed	m.s^{-1}	$[LT^{-1}]$
T	Temperature	K	[K]
T_u	Unburned gas temperature	K	[K]
Y_{CO}	CO mass fraction (relative to the total fuel mass)	-	-
Y_{H_2}	H_2 mass fraction (relative to the total fuel mass)	-	-
X_i	Molar fraction of the species *i*	-	-
Y_i	Mass fraction of the species *i*	-	-

Ch.V - Lower-Case Roman		**Units**	**Dimension**
c_p	Mixture specific heat	J.kg^{-1}.K^{-1}	$[L^2T^{-2}K^{-1}]$
f	Focal length	m	[L]
q	Total nondimensionnal heat release	-	-
q_{CO}	CO-based nondimensionnal heat release parameter	-	-
q_{H_2}	H_2-based nondimensionnal heat release parameter	-	-

Ch.V - Greek		**Units**	**Dimension**
δ	Flame thickness	m	[L]
λ	Wavelength	m	[L]
ρ_b	Burned gas density	kg.m^{-3}	$[ML^{-3}]$
ρ_u	Unburned gas density	kg.m^{-3}	$[ML^{-3}]$
σ	Thermal expansion ratio	-	-
$\sigma_{S_u^0}$	Fundamental flame speed standard deviation	m.s^{-1}	$[LT^{-1}]$

Chapter VI

Ch.VI - Roman Capitals		**Units**	**Dimension**
A	Total flame surface area	m^2	$[L^2]$
A^*	Fitting constant	s	[T]
C	Fitting constant	s	[T]
C_1	Constant	m	[L]
K	Stretch rate	s^{-1}	[T]
L_b	Markstein length for burned gases	m	[L]
Le	Lewis number	-	-
$Le_{eff}{}'$	Effective Lewis number (X_i weighted)	-	-
Le_{CO}	CO-based Lewis number	-	-
Le_{H_2}	H_2-based Lewis number		
N	Number of processing time step	-	-

P	Pressure	Pa	[ML^{-1}T^{-2}]
$\dot{Q}$	Total volumetric flow rate	m^{3}.s^{-1}	[L^{3}T^{-1}]
$Rf_{initial}$	First flame front radius considered in the processing procedure	m	[L]
S_b	Stretched propagation flame speed	m.s^{-1}	[LT^{-1}]
S_b^0	Unstretched propagation flame speed	m.s^{-1}	[LT^{-1}]
S_u	Laminar flame speed (unburned side)	m.s^{-1}	[LT^{-1}]
S_u^0	Fundamental flame speed	m.s^{-1}	[LT^{-1}]
T	Temperature	K	[K]
U	Gas normal velocity	m.s^{-1}	[LT^{-1}]
U_0	Mean velocity at the nozzle burner exit	m.s^{-1}	[LT^{-1}]
W	Lambert or Omega function	-	-
X_{CO}	CO molar fraction	-	-
X_{H_2}	H_2 molar fraction	-	-
Z	Variable of the Lambert function	m^{-1}	[L]

Ch.VI - Lower-Case Roman		**Units**	**Dimension**
d_i	Diameter of lens *i*	m	[L]
f	Focal length	m	[L]
f_i	Focal length of lens *i*	m	[L]
$f\#$	Lens *f* number	-	-
n	Refractive index	-	-
r	Spherical flame radius	m	[L]
$r_{original}\ (t)$	Experimental flame front radius at the time *t*	m	[L]
t	Time	s	[T]
z	Dummy variable of integration	-	-

Ch.VI - Greek		**Units**	**Dimension**
α	Half cone angle of the flame	°	-
ε	Optimization variable	-	-
λ	Wavelength	m	[L]
ρ_b	Burned gas density	kg.m^{-3}	[ML^{-3}]
ρ_u	Unburned gas density	kg.m^{-3}	[ML^{-3}]

List of Abbreviations

BC	Burner Configuration
BID	Burner exit Inside Diameter
BO	Blowoff
CA	Cone Angle
CCD	Charge-Coupled Device
CFD	Computational Fluid Dynamics
CF	Conical Flame
CFR	Coflowing inert Flow Rate
Chemi.	Chemiluminescence
Conf.	Configuration
$cste$	Constant
CT	Counterflow setup
CTF	Counterflow Flames
C. Type	Correlation Type
DDE	Dynamic Data Exchange
DESIG.	Designation
DK	Double Kernel
DPIV	Digital Particle Image Velocimetry
E.R.	Equivalence Ratio
FF	Flat Flame
FFT	Fast Fourier Transform
FRL	Flow Rate Limit
FSA	Flame Surface Area
GSP	Gas Stagnation Plane
Gt	Giga tons
HBW	Half Band Width
HF	Heat Flux
HHV	Higher Heating Value
ICCD	Intensified Couple-Charge Device
I.C.S.	Interrogation Cell Size
I.D.	Internal Diameter
IGCC	Integrated Gasification Combined Cycle
IPCC	Intergovernmental Panel on Climate Change
LDV (LDA)	Laser Doppler Velocimetry (Laser Doppler Anemometry)
MANUF.	Manufacturer
MB	Mixture Blend
MFR	Main Flow Rate
NB	Nozzle Burner
NO_x	Nitrogen Oxides
O.J.	Opposed Jets
OPF	Outwardly Propagating Flame
PIV	Particle Image Velocimetry
PSP	Particle Stagnation Plane
R.A.	Recursive Algorithm
Reac.	Number of reactions
Ref.	Reference
SEM	Scanning Electron Microscopy

S.J.	Single Jet
SP	Stagnation Plate
Spec.	Number of species
SPF	Stagnation Plate Flame
S.R.	Spatial Resolution
Tran. Meth.	Transition Methodology
1D	One-dimensional
2D	Two-dimensional

Nicolas BOUVET

Étude des Vitesses Fondamentales des Flammes Laminaires Prémélangées: Application aux Mélanges Méthane/Air et Syngas (H_2/CO)/Air

Résumé :

Cette étude est consacrée à l'élaboration d'une méthodologie de détermination des vitesses fondamentales des flammes laminaires, en utilisant un diagnostic de Vélocimétrie par Imagerie de Particules (PIV). Ce dernier est appliqué aux écoulements réactifs avec point de stagnation, permettant la stabilisation de flammes planes, stationnaires et en conditions quasi adiabatiques. Les effets d'étirements subits par la flamme sont également quantifiables et parfaitement maîtrisés. L'approche ici développée a tout d'abord été appliquée aux mélanges méthane/air pour validation. Une comparaison exhaustive des résultats obtenus avec les données de la littérature est effectuée. Les codes de combustion 1D (PREMIX, OPPDIF) et 2D (Fluent©) ont été utilisés afin de confirmer la fiabilité et la précision de l'approche proposée. Une attention particulière a été accordée à la caractérisation du mouvement des particules ensemencées dans les écoulements réactifs divergents, avec notamment la prise en considération de la force de thermophorèse. La méthode développée a ensuite été appliquée à la détermination des vitesses de flammes laminaires de divers mélanges de syngas (H_2+CO). Une étude comparative sur ces mélanges a été conduite en utilisant des approches expérimentales multiples comprenant : les flammes à contre-courant, les flammes à propagation sphérique ainsi que les flammes stabilisées coniques. Les résultats obtenus pour chaque approche ont été confrontés et la sensibilité à l'étirement des flammes de syngas a été caractérisée pour une large gamme de richesses (E.R.=0.4 to 5.0) et de compositions de mélanges (5/95 to 50/50 % H_2/CO).

Mots clés : Combustion, Syngas, Vitesse Fondamentale de Flamme, Étirement, Vélocimétrie par Imagerie de Particules, Flammes à Contre courant, Flammes Sphériques, Flammes Coniques.

Experimental and Numerical Studies of the Fundamental Flame Speeds of Methane/Air and Syngas (H_2/CO)/Air Mixtures

Summary :

In the context of CO_2 emission reduction, the present study is devoted to the development of a laminar flame speed measurement methodology, using the Digital Particle Image Velocimetry (DPIV) diagnostic. The latter is applied to stagnation flow flames, seen to have considerable assets for such studies. Indeed, flames stabilized in these diverging flows are planar, steady and in near-adiabatic conditions, while subtraction of strain effects on flame is intrinsically allowed. The methodology developed herein has been applied to the well-characterized methane/air mixtures for validation. An extensive comparison with the literature datasets has been provided. Both 1D (PREMIX, OPPDIF) as well as 2D (Fluent©) numerical tools have been used to confirm the reliability and accuracy of the developed approach. A particular attention has been given to the characterization of the seeding particle motion within the diverging flow, with consideration of the often-neglected thermophoretic force. Fundamental flame velocities of various syngas (H_2+CO) mixtures have been investigated using multiple experimental approaches including the aforementioned counterflow methodology as well as spherical and conical flame configurations. Performed measurements from the different approaches have been confronted and flame sensitivities to stretch have been characterized for a wide range of equivalence ratios (E.R.=0.4 to 5.0) and mixture compositions (5/95 to 50/50 % H_2/CO).

Keywords : Combustion, Syngas, Fundamental Flame Speed, Stretch Rate, Particle Image Velocimetry, Counterflow Flames, Outwardly Propagating Flames, Conical Flames.

Institut de Combustion, Aérothermique,
Réactivité et Environnement - ICARE
1 C, Avenue de la Recherche Scientifique,
45071 Orléans Cedex 2